SCIENTIFIC POSTERS

116 Performance of Alternative Pathway Non-US International Medical Graduates in Neuroradiology Fellowships as Assessed by Program Directors.

Fatemeh Dehghani Firouzabadi MD[1], Fahimul Huda MD[1], Caline Azzi MD[2], Meisam Hoseinyazdi MD[2], David Yousem MD[2], Nana Yaw Ohene- Baah MD[1]
[1]University of Louisville School of Medicine, Louisville, Kentucky, USA. [2]Johns Hopkins School of MedicineUniversity of Louisville School of Medicine, Baltimore, Maryland, USA

Purpose

AAMC data indicates that by 2033, the U.S. could face a shortage of up to 139,000 physicians, including thousands of radiologists. A previous report from 75 Diagnostic Radiology (DR) Program Directors (PDs) found that 53% of PDs noted no performance differences between IMGs and U.S. MDs (USMD) in radiology training programs while an equal percentage said IMGs performed better and worse than USMDs. Many IMGs pursue the ABR's Alternate Pathway for entering the US radiology community by spending 4 years of training/research/faculty positions in US radiology departments in order to be eligible for the American Board of Radiology (ABR) DR boards. This study aims to evaluate the performance of neuroradiology clinical fellows enrolled in the ABR Alternate Pathway versus U.S. DR residency graduates.

Materials & Methods

Data were collected from the ABR and neuroradiology fellowship PDs. Surveys evaluated clinical performance, research productivity, and board examination pass rates. A survey (https://qualtricsxmqpxgnlmnq.qualtrics.com/jfe/form/SV_9zskxVq61wgvyrs) was distributed in January and February 2025, with three additional reminders spaced one month apart for non-respondents. Data collection is ongoing.

Results

Among those neuroradiology PDs responding (n = 36/80), 72% accept candidates in the ABR Alternate Pathway, while 28% do not. Regarding research skills, 46% of programs rated Alternate Pathway candidates (APCs) as stronger than U.S. DR graduates, 8% rated them as weaker, and 46% rated them as similar. For clinical skills, 4% of programs rated APCs as better, 21% as worse, and 75% as equal to U.S. DR graduates. In terms of teaching ability, 21% of programs rated APCs as better, 17% as worse, and 62% as similar. When comparing subspecialty certification exam (CAQ) pass rates, 0% of programs rated APCs as better than U.S. DR graduates, 5% as worse, and 95% as equivalent. Actual exam performance data indicated that APCs had comparable or higher first-attempt pass rates than U.S. DR graduates. PDs reported that 33% of APCs passed the ABR Diagnostic Radiology Qualifying/Core Exam on the first attempt, compared to 26% of U.S. DR graduates. However, a substantial proportion of PDs responded "I don't know" to these questions—50% for APCs versus 37% for U.S. DR graduates. Similarly, for the CAQ exam, PDs reported a 48% first-time pass rate for APCs versus 46% for U.S. DR graduates, with 48% of PDs selecting "I don't know" for APCs compared to 37% for U.S. DR graduates.

Conclusion

Preliminary data suggest that ABR APCs perform comparably to U.S. DR graduates in clinical duties, research, teaching, and board examination success, supporting their favorable role in potentially addressing the projected radiologist shortage in the United States. As the U.S. faces a growing shortage of radiologists, incorporating non-U.S. IMGs through the ABR Alternate Pathway offers a viable solution to workforce gaps without compromising clinical, research, or educational standards. The comparable performance of APCs to U.S. DR residency graduates supports broader utilization and integration of this pathway in radiology training programs, ensuring sustained delivery of high-quality radiologic care nationwide.

References

1. Khoshpouri P, Mohseni A, Dabiri M, Ansari G, Zadeh FS, Ataeinia B, Saadat N, Sherbaf FG, Yousem DM. International Medical Graduates in Radiology Residencies: Demographics, Performance, and Visa Issues. Acad Radiol. 2023 Dec;30(12):3124-3134. doi: 10.1016/j.acra.2023.04.008. Epub 2023 May 12. PMID: 37183141.
2. Fatemeh Dehghani Firouzabadi, Mina Hesami, Ali Sheikhy, Mahla Radmard, Mona Dabiri, Sara Ramezanpour, David M. Yousem. Representation of International Medical Graduates Among Diagnostic Radiology Chairs, Neuroradiology Chiefs, and Program Directors, Academic Radiology, Volume 31, Issue 9, 2024, Pages 3844-3850
3. Huda F, Rozenshtein A, Bedi H. The American Board of Radiology's Alternate Pathway for Diagnostic Radiology: What the Programs and the Applicants Need to Know. Acad Radiol. 2022 Mar;29(3):465-468. doi: 10.1016/j.acra.2021.09.017. Epub 2021 Oct 8. PMID: 34629263.

---

150 Utilizing 4D-CT radiomic features for differentiation of parathyroid adenomas from lymph nodes and thyroid nodules

Asim Dhungana BA[1], Chime Ezenekwe BS[1], Michael H Zhang MD[2], Irfan Hussain MD[3], Daniel T Ginat MD[3]
[1]University of Chicago Pritzker School of Medicine, Chicago, IL, USA. [2]Department of Radiology, Northwestern Medicine, Chicago, IL, USA.
[3]Department of Radiology, University of Chicago, Chicago, IL, USA

Purpose

Minimally invasive parathyroidectomy (MIP) requires high fidelity localization of parathyroid adenomas through pre-operative imaging, commonly four-dimensional computed tomography (4D-CT).[1] Texture analysis extracts high-order mathematical features from an image and may be applied to 4D-CT for quantitative differentiation of lymph nodes and thyroid nodules from parathyroid adenomas.[2] The aim of this study is to correlate 4D-CT radiomic data of lymph nodes and thyroid nodules to pathology-proven parathyroid adenomas to identify and quantify texture features that predict parathyroid adenomas.

Materials & Methods

This is a retrospective cohort study of 144 patients with history of hyperparathyroidism, pre-operative parathyroid 4D-CT scan, subsequent parathyroidectomy, and pathology-proven parathyroid adenoma and/or thyroid nodule diagnosed between 2013 and 2023 at the University of Chicago Medical Center (UCMC). Patients with thyroidectomy, unsuccessful parathyroid resection, or indeterminate localization of the parathyroid adenoma of interest were excluded. Three anatomical structures (parathyroid adenoma, lymph node, and thyroid nodule) were manually segmented on 25-second arterial phase axial sections of the 4D-CT scans (**Figure 1**). Radiomic data were extracted for shape, first-order, and second-order classes (107 total features) for each of the structures in each patient using the open-source software package PyRadiomics.[3] A series of t-tests were conducted to assess for radiomic features with statistically significant differences in lymph nodes or thyroid nodules when compared to parathyroid adenomas. A multivariable logistic regression model for discrimination of parathyroid adenomas was trained on a subset of the dataset and assessed

on a hold-out test subset. Given the limited size of the overall dataset, we also assessed model stability by resampling the training/test sets and performing model training/testing across 200 random seeds, examining the final feature set and AUC at each bootstrap iteration to generate 95% confidence intervals.

Results

We identified 51 patients at UCMC between 2013 and 2023 with a history of parathyroidectomy for a pathology-proven parathyroid adenoma and/or thyroid nodule meeting inclusion criteria. Patients were predominantly female (67%) and White (57%) and had a mean age of 61 years. Other represented races include Black (29%) and Asian (6%). All patients had a segmented cervical lymph node, 49 (96%) patients had a parathyroid adenoma, and 18 (35%) patients had a thyroid nodule. When comparing parathyroid adenomas and lymph nodes, 14/18 first-order features and 44/75 second-order features were statistically significantly different ($p < 0.05$), of which 13/18 first-order features and 16/75 second-order features were potent discriminators ($p < 0.0001$). No features were significantly different between parathyroid adenomas and thyroid nodules. A multivariable logistic regression model for discrimination of parathyroid adenomas from lymph nodes achieved strong predictive performance (AUC 0.95, 95% CI 0.86 – 1, **Figure 2**).

Conclusion

Parathyroid adenomas and lymph nodes have statistically distinct radiomic textural signatures on arterial phase 4D-CT, with the most significant differences found in first-order textural features. We have also demonstrated the strong performance of a limited logistic regression model trained on this dataset. These findings may facilitate the development of other future machine learning models for automated differentiation of parathyroid adenomas, further enhancing uptake of MIP and improving clinical outcomes.

References

1. Bunch PM, Randolph GW, Brooks JA, et al. Parathyroid 4D CT: What the Surgeon Wants to Know. *RadioGraphics* 2020;40:1383–94.
2. Jategaonkar AA, Lerner DK, Cooke P, et al. Implementation of a 4-dimensional computed tomography protocol for parathyroid adenoma localization. *Am J Otolaryngol* 2021;42:102907.
3. van Griethuysen JJ, Fedorov A, Parmar C, et al. Computational Radiomics System to Decode the Radiographic Phenotype. *Cancer Res* 2017;77:e104–7.

Images/Tables

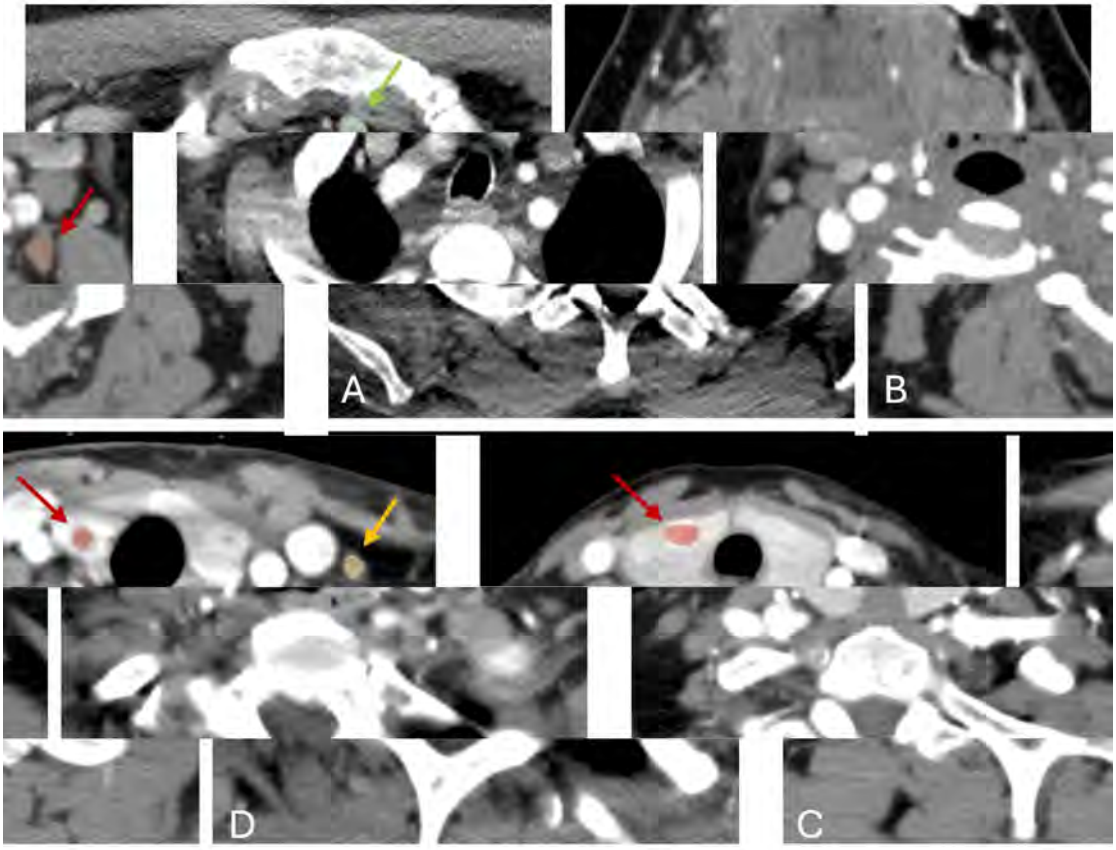

ctural Segmentation. Representative examples of region-of-interest (ROI) on arterial phase four-dimensional CT imaging axial slices for **A)** parathyroid ymph node, **C)** thyroid nodule, and **D)** thyroid nodule (red) and lymph node same slice. Indicator arrows are also shown pointing out these structures.

Figure 1: Stru segmentations adenoma, **B)** (yellow) on the

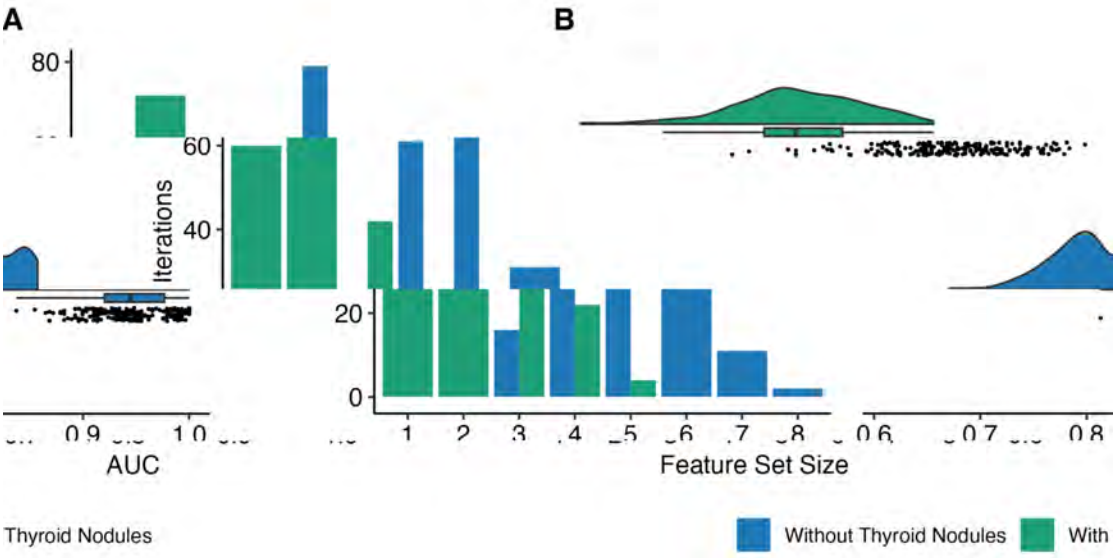

Logistic Regression Model. Across 200 ion of feature set size and **B)** the distribution own for models either including or excluding .

Figure 2: Performance Stability Analysis of bootstrap iterations, shown are **A)** the distribut of area under the curve (AUC). Results are sh thyroid nodules in the training and testing sets

207 Does One Size Fit All for Brain Tumor Segmentation? Assessing the Performance of Segmentation Models Trained on Glioblastoma for the Evaluation of Intracranial Metastatic Disease

Peter I Kamel MD[1], George Biros PhD[2], Dihua Yu MD, PhD[1], Max Wintermark MD, MS, MBA[1]
[1]MD Anderson Cancer Center, Houston, TX, USA. [2]The University of Texas at Austin, Austin, TX, USA

Purpose

Historically, brain tumor segmentation models such as those trained for the RSNA-ASNR-MICCAI Brain Tumor Segmentation (BraTS) Challenge have focused on primary brain tumors such as glioblastomas. The purpose of this project was to evaluate the performance of such models trained on primary brain tumors for the detection and segmentation of intracranial metastases.

Materials & Methods

A self-configuring nnU-Net model was trained on 1,251 T1 post-contrast MRIs reflecting the entirety of the BraTS pre-treatment glioma segmentation challenge. Performance of the model was assessed on 200 T1 post-contrast MRI exams containing 993 metastatic lesions. Each lesion was assessed for binary detection by the algorithm and segmentation Dice score. Performance was compared by lesion size and primary tumor type via two-tailed t-test.

Results

For a model averaging a Dice score of 0.791 ± 0.005 on the BraTS glioblastoma dataset, performance significantly decreased in the evaluation of metastatic lesions, particularly for small lesions. For all sizes and types, only 34.7% (345 / 993) of lesions were detected with an average Dice score for detected lesions of 0.452 ± 0.362. Performance was heavily dependent on lesion size with lesions <1 cc only detected 19.0% of the time, compared to 95.6% for lesions ≥ 1 cc ($p < 0.001$). Dice scores increased with size of the lesion upwards to 0.831 for lesions ≥ 10 cc. Significant differences were also noted in the detection rate and segmentation by primary tumor type with melanoma metastases demonstrating the lowest segmentation scores.

Conclusion

Models trained only on primary brain tumors perform much worse in the evaluation of metastatic disease, missing small lesions and demonstrating differences in performance by primary tumor type. This highlights the need for metastasis-specific models over those trained for the segmentation of primary brain tumors.

References

Moawad AW, Janas A, Baid U, Ramakrishnan D, Saluja R, Ashraf N, Maleki N, Jekel L, Yordanov N, Fehringer P, Gkampenis A, Amiruddin R, Manteghinejad A, Adewole M, Albrecht J, Anazodo U, Aneja S, Anwar SM, Bergquist T, Chiang V, Chung V, Conte GM, Dako F, Eddy J, Ezhov I, Khalili N, Farahani K, Iglesias JE, Jiang Z, Johanson E, Kazerooni AF, Kofler F, Krantchev K, LaBella D, Van Leemput K, Li HB, Linguraru MG, Liu X, Meier Z, Menze BH, Moy H, Osenberg K, Piraud M, Reitman Z, Shinohara RT, Wang C, Wiestler B, Wiggins W, Shafique U, Willms K, Avesta A, Bousabarah K, Chakrabarty S, Gennaro N, Holler W, Kaur M, LaMontagne P, Lin M, Lost J, Marcus DS, Maresca R, Merkaj S, Cassinelli Pedersen G, von Reppert M, Sotiras A, Teytelboym O, Tillmans N, Westerhoff M, Youssef A, Godfrey D, Floyd S, Rauschecker A, Villanueva-Meyer J, Pflüger I, Cho J, Bendszus M, Brugnara G, Cramer J, Perez-Carillo GJG, Johnson DR, Kam A, Kwan BYM, Lai L, Lall NU, Memon F, Krycia M, Patro SN, Petrovic B, So TY, Thompson G, Wu L, Schrickel EB, Bansal A, Barkhof F, Besada C, Chu S, Druzgal J, Dusoi A, Farage L, Feltrin F, Fong A, Fung SH, Gray RI, Ikuta I, Iv M, Postma AA, Mahajan A, Joyner D, Krumpelman C, Letourneau-Guillon L, Lincoln CM, Maros ME, Miller E, Morón FEA, Nimchinsky EA, Ozsarlak O, Patel U, Rohatgi S, Saha A, Sayah A, Schwartz ED, Shih R, Shiroishi MS, Small JE, Tanwar M, Valerie J, Weinberg BD, White ML, Young R, Zohrabian VM, Azizova A, Brüßeler MMT, Ghonim M, Ghonim M, Okar A, Pasquini L, Sharifi Y, Singh G, Sollmann N, Soumala T, Taherzadeh M, Vollmuth P, Foltyn-Dumitru M, Malhotra A, Abayazeed AH, Dellepiane F, Lohmann P, Pérez-García VM, Elhalawani H, de Verdier MC, Al-Rubaiey S, Armindo RD, Ashraf K, Asla MM, Badawy M, Bisschop J, Lomer NB, Bukatz J, Chen J, Cimflova P, Corr F, Crawley A, Deptula L, Elakhdar T, Shawali IH, Faghani S, Frick A, Gulati V, Haider MA, Hierro F, Dahl RH, Jacobs SM, Hsieh KJ, Kandemirli SG, Kersting K, Kida L, Kollia S, Koukoulithras I, Li X, Abouelatta A, Mansour A, Maria-Zamfirescu RC, Marsiglia M, Mateo-Camacho YS, McArthur M, McDonnell O, McHugh M, Moassefi M, Morsi SM, Munteanu A, Nandolia KK, Naqvi SR, Nikanpour Y, Alnoury M, Nouh AMA, Pappafava F, Patel MD, Petrucci S, Rawie E, Raymond S, Roohani B, Sabouhi S, Sanchez-Garcia LM, Shaked Z, Suthar PP, Altes T, Isufi E, Dhemesh Y, Gass J, Thacker J, Tarabishy AR, Turner B, Vacca S, Vilanilam GK, Warren D, Weiss D, Worede F, Yousry S, Lerebo W, Aristizabal A, Karargyris A, Kassem H, Pati S, Sheller M, Link KEE, Calabrese E, Tahon NH, Nada A, Velichko YS, Bakas S, Rudie JD, Aboian M. The Brain Tumor Segmentation - Metastases (BraTS-METS) Challenge 2023: Brain Metastasis Segmentation on Pre-treatment MRI. ArXiv [Preprint]. 2024 Dec 9:arXiv:2306.00838v3. PMID: 37396600; PMCID: PMC10312806.

Images/Tables

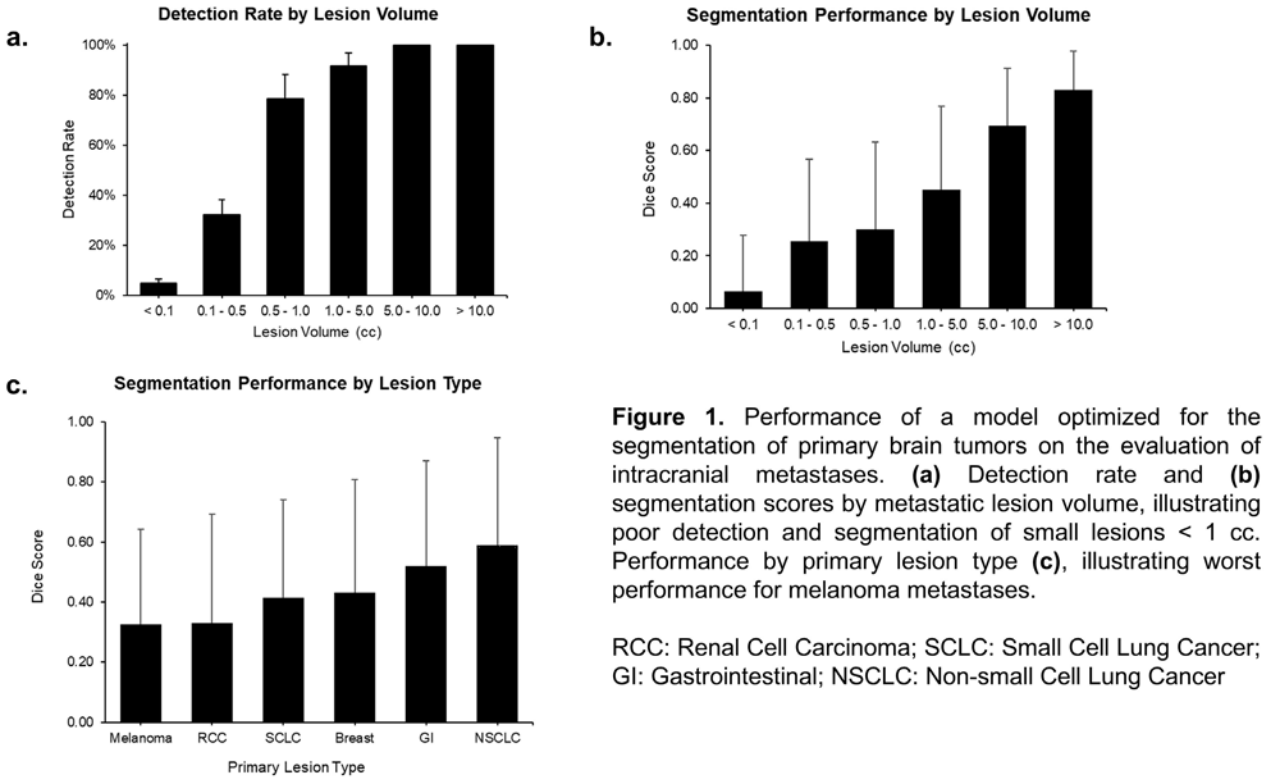

Figure 1. Performance of a model optimized for the segmentation of primary brain tumors on the evaluation of intracranial metastases. **(a)** Detection rate and **(b)** segmentation scores by metastatic lesion volume, illustrating poor detection and segmentation of small lesions < 1 cc. Performance by primary lesion type **(c)**, illustrating worst performance for melanoma metastases.

RCC: Renal Cell Carcinoma; SCLC: Small Cell Lung Cancer; GI: Gastrointestinal; NSCLC: Non-small Cell Lung Cancer

---

216 Evaluating the Utility of 3D-Volumetric Tumor Segmentation for RANO Intracranial Treatment Response Assessment

Peter I Kamel MD, Komal Shah MD, Max Wintermark MD, MS, MBA
MD Anderson Cancer Center, Houston, TX, USA

Purpose

3D volumetric segmentation has increasingly emerged in tumor assessment with machine learning demonstrating high performance in localizing, segmenting, and providing volumetric evaluation of brain tumors. It is unclear however if such methods can be translated into clinically applicable tools for assessing treatment response in neuro-oncology. This study aims to assess whether automated 3D volumetric tumor segmentation can accurately be used to assess treatment response according to the Response Assessment in Neuro-Oncology (RANO) criteria.

Materials & Methods

A self-configuring nnU-Net model was trained for segmentation on 2,872 pre- and post-treatment glioma MRIs with annotated ground truth. A separate longitudinal dataset of 91 patients (totaling 638 imaging timepoints) was then preprocessed, including construction and co-registration of subject-specific atlases for lesion tracking. The pre-trained nnU-Net model was used to automatically segment regions of enhancing tumor on the longitudinal dataset. After excluding patients classified as having progression based on T2/FLAIR changes or clinical criteria, 234 pairwise comparisons remained. Using auto-segmented volumetric assessment, comparisons were classified into Complete Response (CR), Partial Response (PR), Stable Disease (SD), and Progressive Disease (PD) according to RANO criteria based on measurable and non-measurable enhancing disease, lesion volume, and appearance of new lesions. Model results were compared to radiologist ground truth assessment and evaluated for accuracy, sensitivity, and specificity.

Results

Overall, the model was 71.4% accurate (95% CI: 65.3 – 76.8%) in classifying progressive versus non-progressive disease with sensitivity of 63.5% (54.6 – 71.7%) and specificity of 79.3% (71.0 – 85.7%). False negatives were commonly due to missed small non-measurable or non-target lesions in segmentation (**Figure 1**). The most common cause of false positive classification of progression was incorrect segmentation of lesions such as surrounding the surgical resection cavity (**Figure 2**). Subgroup analysis demonstrated highest classification of CR with accuracy of 73.9% (68.0 – 79.1%), sensitivity of 87.0% (67.9 – 95.5%), specificity of 72.5% (66.1 – 78.0%), though with frequent misclassification of SD as CR.

Conclusion

3D-volumetric segmentation will likely play an increasing role in treatment response assessment, though is still met with limitations in clinical translation into fully automated response assessment due to the accuracy of segmentation and complexity of response criteria assessment.

References

Wen PY, van den Bent M, Youssef G, Cloughesy TF, Ellingson BM, Weller M, Galanis E, Barboriak DP, de Groot J, Gilbert MR, Huang R, Lassman AB, Mehta M, Molinaro AM, Preusser M, Rahman R, Shankar LK, Stupp R, Villanueva-Meyer JE, Wick W, Macdonald DR, Reardon DA, Vogelbaum MA, Chang SM. RANO 2.0: Update to the Response Assessment in Neuro-Oncology Criteria for High- and Low-Grade Gliomas in Adults. J Clin Oncol. 2023 Nov 20;41(33):5187-5199. doi: 10.1200/JCO.23.01059. Epub 2023 Sep 29. PMID: 37774317; PMCID: PMC10860967.

Images/Tables

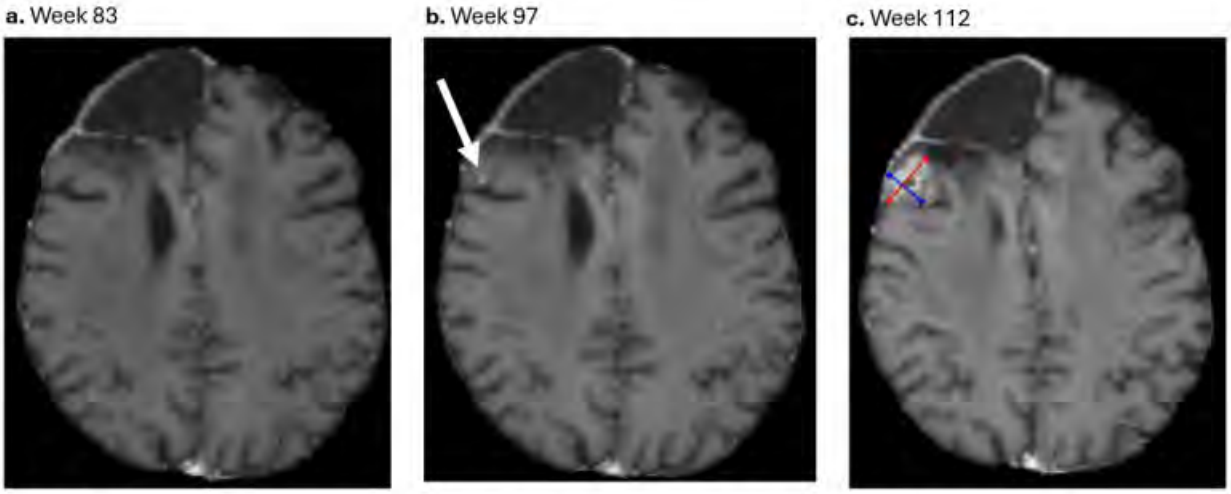

Figure 1. (a) Postoperative examination following tumor resection showing no evidence of disease **(b)** Follow-up MRI examination showing a new small area of enhancement. This new lesion was classified as "Progressive Disease" in ground truth interpretation, though was missed by the segmentation model and incorrectly classified as "Stable Disease". **(c)** Subsequent follow-up MRI, annotated and measured by the model, and correctly classified as "Progressive Disease".

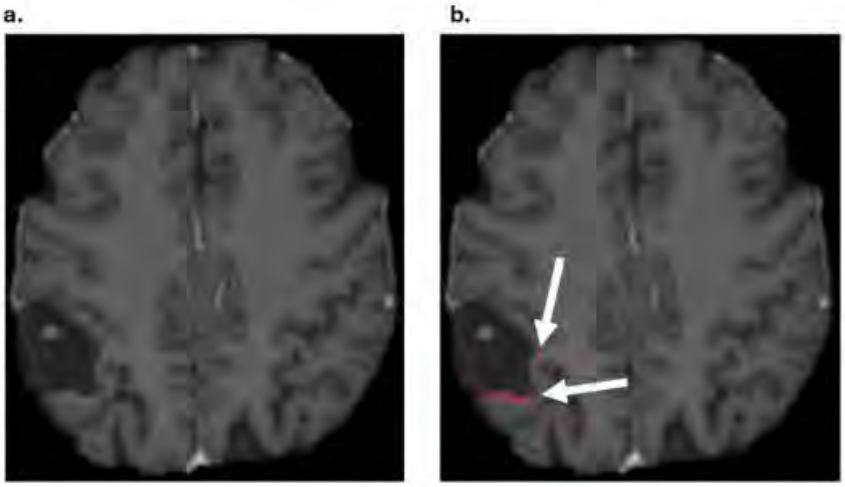

Figure 2. Example of false positive classification of disease progression. (a) Postoperative MRI showing smooth postsurgical enhancement along the margins of the resection cavity. **(b)** Incorrect segmentation of the enhancement as new lesions, leading to incorrect classification as "Progressive Disease".

---

237 **Peroneal and Tibial Intraneural Ganglion Cysts: Imaging Characteristics at Presentation and Postoperative Recurrence**

Cullen Fleming MD
UCSF, San Francisco, CA, USA

Purpose

Intraneural ganglion cysts are an uncommon pathology that results from joint fluid dissecting within the epineurium of peripheral nerves. While much of the literature to date focusing on pathogenesis and surgical management, there is a paucity characterizing the MR imaging characteristics at presentation & postoperative recurrence. This study aims to more fully characterize the MRI appearance of intraneural ganglion cysts about the knee at presentation and recurrence so that practitioners may more comfortably and confidently diagnose them at time of imaging.

Materials & Methods

We conducted a retrospective chart review from 2015 to 2025 to identify patients with pathology and surgically proven intraneural ganglion cysts about the knee. The corresponding MRIs, EMGs, operative reports, and clinical notes were reviewed to fully characterise the patient's lesion, symptoms, and interventions.

Results

The imaging at time of presentation was available for 9 patients with a median age of 56. A joint connection was present in all patients, with 7 involving the peroneal articular branch and 2 involving the tibial articular branch. All cysts demonstrated a lobular morphology which increased in diameter with cranial extension.

Of these patients, 5 experienced a total of 9 postoperative recurrences. At representation, the majority of patients reported recurrence of their original symptoms. All recurrences occurred along the same articular branch as the original presentation. All but one patient experienced increased cranial extent of the cyst at time of recurrence; however, maximum diameter of the cysts were highly variable. There was a single case of the cyst extending across the tibial nerve into the common peroneal nerve.

Both pre- and post-operatively, all cysts were T2 hyperintense, at or slightly below that of joint space fluid, and T1 dark, at or slightly below that of muscle, with thin enhancing walls. No cysts contained septations, internal debris, nodularity, or a solid component.

Conclusion

Intraneural ganglion cysts are rare but the uncertainty around their diagnosis can be reduced by recognizing their consistent MR imaging characteristics both pre- and post-operatively.

References

1. Spinner RJ, Hébert-Blouin M-N, Amrami KK, et al. Peroneal and Tibial Intraneural Ganglion Cysts in the Knee Region. Operative Neurosurgery 2010;67:ons71–8.
2. Desy NM, Wang H, Elshiekh MAI, et al. Intraneural ganglion cysts: a systematic review and reinterpretation of the world's literature. J Neurosurg 2016;125:615–30.

Images/Tables

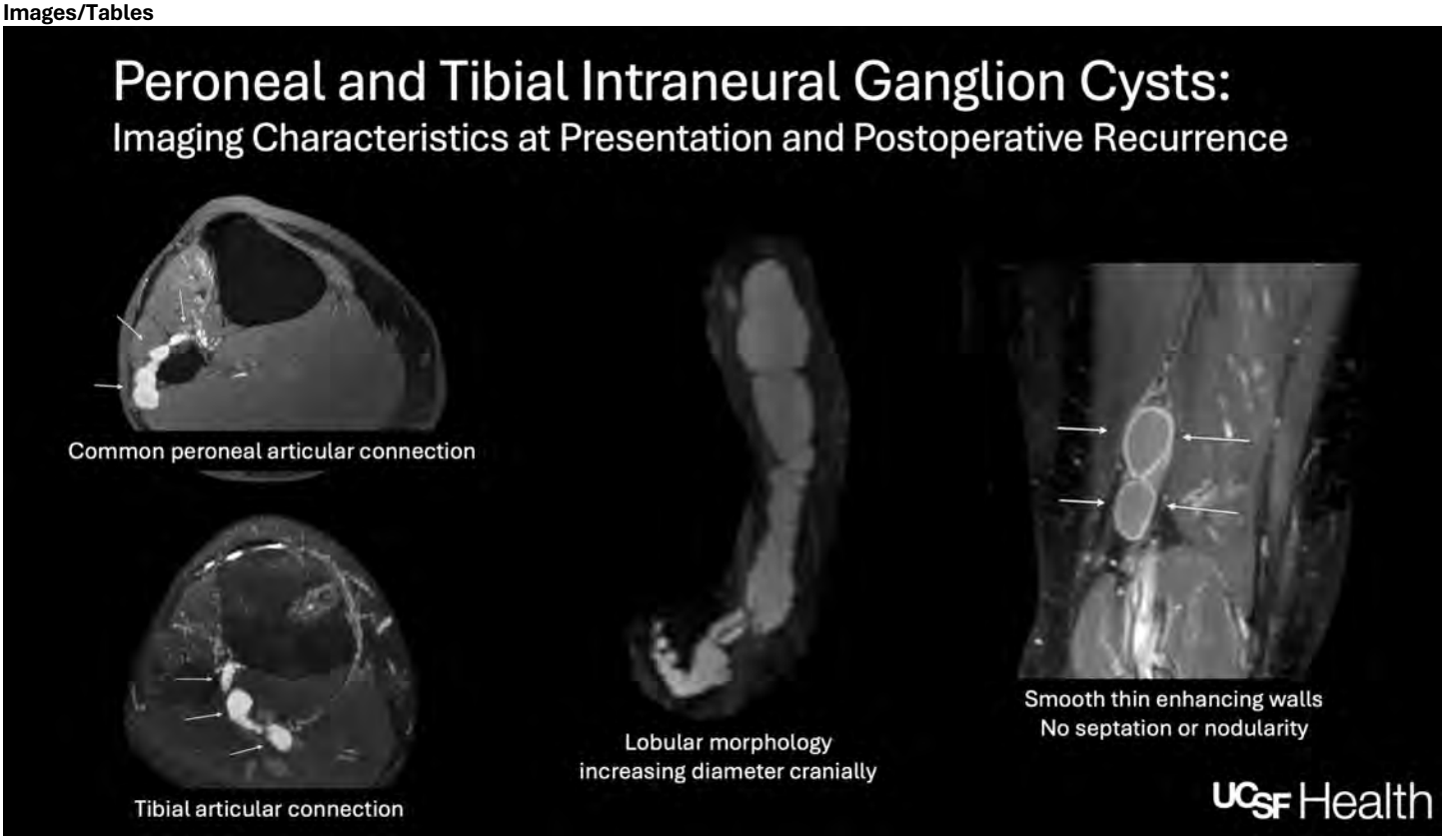

290 Manual Editing Improves FreeSurfer Segmentation Quality

Damon Motamedi MD[1], Haley E Wiskoski BS[2], Summan Zahra MBBS[3], Juan C Arias MD[3], Scott R French[3], Gavin Culwell[3], Loi Do[3], Edward Bedrick PhD[4], Kevin Johnson BS[1], Simeon Smith MD[1], Maria Altbach PhD[5], Gene E Alexander PhD[6], Craig C Weinkauf MD[3], Raza Mushtaq MD[7]

[1]University of Arizona Department of Radiology and Imaging Sciences, Tucson, AZ, USA. [2]University of Arizona Department of Biomedical Engineering, Tucson, AZ, USA. [3]University of Arizona, Division of Vascular Surgery, Tucson, AZ, USA. [4]University of Arizona, Department of Epidemiology and Biostatistics, Mel and Enid Zuckerman College of Public Health, Tucson, AZ, USA. [5]University of Arizona Department of Radiology and Imaging Sciences, Department of Biomedical Engineering, Tucson, AZ, USA. [6]University of Arizona, Department of Psychology, Department of Psychiatry, Arizona Alzheimer's Disease Consortium, Evelyn F. McKnight Brain Institute, Tucson, AZ, USA. [7]Barrow Neurological Institute, Department of Neuroradiology, Phoenix, AZ, USA

Purpose

FreeSurfer morphometrics are widely used in the dementia and aging fields. FreeSurfer is susceptible to segmentation errors and one method to overcome such errors is with manual editing. There is no consensus regarding the need/importance of manual editing and across studies there is great variation in whether editing is performed and what type. This results in significant limitations for interpreting and comparing studies evaluating brain morphometry. To address this, we applied a concise, criteria-based 4-point expert grading rubric to FreeSurfer reconstructions evaluated before and after manual editing.

Materials & Methods

Thirty adults underwent FreeSurfer reconstruction with two pipelines per subject (T1-only and T1+T2-SPACE). For each pipeline, reconstructions were evaluated before and after manual edits, yielding 120 datasets. Two neuroradiologists and one radiology resident, blinded to pipeline and edit status, graded each dataset in FreeView on a 1–4 scale using explicit criteria:

- 4 (Excellent): virtually no errors; ≤3 consecutive slices; full ribbon capture.
- 3 (Good): localized errors >3 slices in ≤2 lobes; mild pial over/underestimation.

- 2 (Fair): errors >3 slices in ≥3 lobes or markedly overextended pial surface.
- 1 (Poor): severe localized/global errors expected to bias morphometrics

Scores were averaged per dataset. A 2×2 repeated-measures ANOVA (within-subject factors: Editing Status and Scan Type) tested main effects; aligned rank-transform ANOVA verified robustness for ordinal data. Post-hoc pairwise tests used Tukey adjustment (α=0.05). Agreement was summarized with intraclass correlation (ICC) and pairwise Cohen's κ.

Results

Manual editing produced a significant improvement in expert-graded quality. The ANOVA showed a strong main effect of Editing (p<0.001), replicated in the nonparametric analysis (p<0.001). Within-pipeline paired comparisons confirmed higher post-edit scores in both pipelines:

- T1-only: +0.65 increase (from 2.57±0.60 to 2.94±0.712), p<0.0001.
- T1+T2-SPACE: +0.80 increase (from 2.14±0.49 to 3.22±0.54), p<0.0001.

Aggregated across pipelines, the mean improvement was approximately +0.73 grade points. Inter-rater agreement was strong (ICC=0.823, 95% CI 0.759–0.872). Pairwise Cohen's kappa (κ) values were 0.809 for Rater 1–2, 0.475 for Rater 1–3, and 0.484 for Rater 2–3, indicating agreement ranging from moderate to substantial agreement.

Conclusion

Our data demonstrate that manual editing significantly improves FreeSurfer segmentation quality. These data suggest editing should be considered, particularly in the medial temporal lobe that is prone to segmentation errors. This approach promotes transparent cohort assembly and helps limit segmentation-driven bias in morphometric analyses. Future work could compare cross-study analyses and editing time efficiency to further understand the costs and benefits of manual editing implementation.

References

Brinkmann, BH, Guragain, H, Kenney-Jung, D, et al. Segmentation errors and intertest reliability in automated and manually traced hippocampal volumes. *Annals of clinical and translational neurology* 2019; 6(9), 1807–1814. https://doi.org/10.1002/acn3.50885

Waters, AB, Mace, RA, Sawyer, KS, et al. Identifying errors in Freesurfer automated skull stripping and the incremental utility of manual intervention. *Brain imaging and behavior* 2019; 13(5), 1281–1291. https://doi.org/10.1007/s11682-018-9951-8

Images/Tables

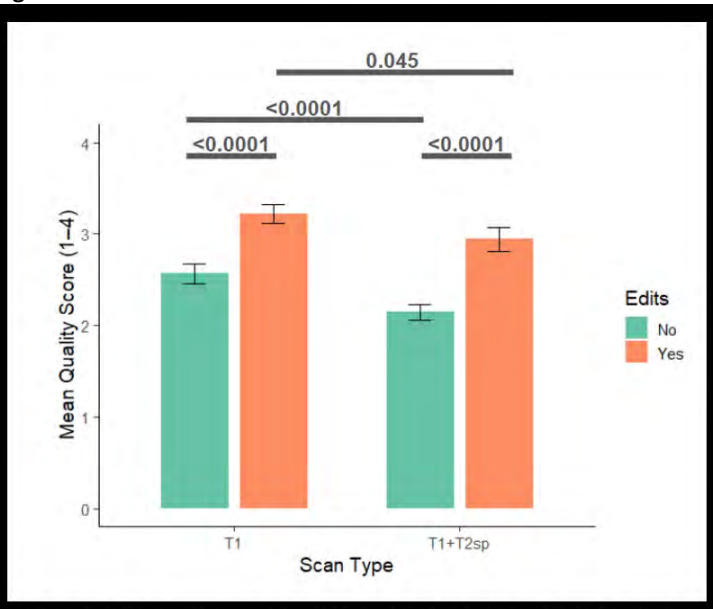

Expert grading results reveal manual editing significantly improves segmentation quality. Mean quality scores (1 = poor, 4 = excellent) are shown for T1-Only and T1+T2sp reconstructions before (green) and after (orange) manual editing. Mean and standard deviations are shown. Brackets indicate post-hoc analysis p-values. Prior to editing, T1-Only reconstructions had a significantly higher quality score than T1+T2sp. Manual editing significantly improved quality for both scan types with T1+T2sp achieving comparable quality to edited T1-Only.

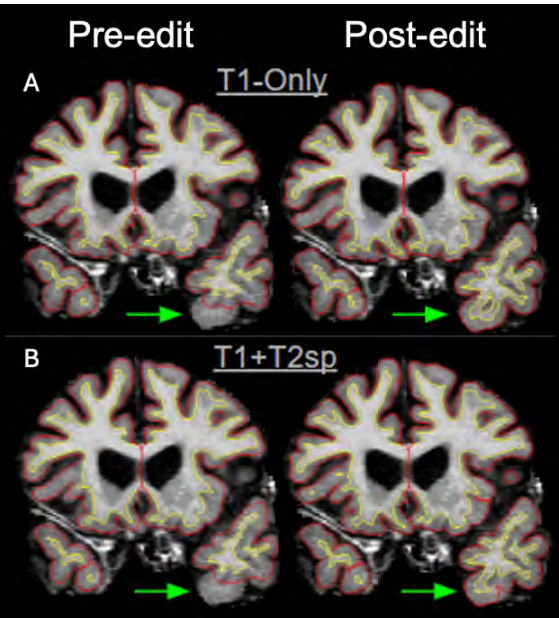

Representative showing correction of surface errors after manual editing. Pre-edit (left) versus post-edit (right) reconstructions of pial and WM surface boundaries derived from T1-Only (**A**) and T1+T2sp (**B**). These systematic differences illustrate how input contrast choice influences automated delineation of cortical surfaces.

---

300 Cavum Septum Pellucidum Enlargement in Special Operations Forces Members Is Associated with Lifetime Exposure to Large Explosives

Sara De Giorgi[1], Andrea Diociasi[2], Rehab Naeem Khalid[1], Phoebe Degn[3], Katelyn Elizabeth Rand[3], Seba Gabali[3], Ronald Hirschberg[3], Scott Sorg[4], Michael Lev[5], Rajiv Gupta[1]

[1]Department of Radiology, Massachusetts General Hospital 55 Fruit Street, Boston, MA 02114, USA, Boston, MA, USA. [2]Department of Internal Medicine (DiMI), University of Genoa, genova, italy, Italy. [3]Home Base Program, Massachusetts General Hospital, Boston, MA, USA. [4]Home Base Program & Harvard Medical School, Boston, MA, USA. [5]Department of Radiology, Massachusetts General Hospital, Boston, MA, USA

Purpose

Cavum septum pellucidum (CSP) is a common neuroimaging finding linked to repetitive head trauma, yet its relationship to blast exposure among the military population remains elusive. Here, we investigated whether lifetime exposure to different types of blast is associated with CSP morphology among Special Operations Forces (SOF) personnel.

Materials & Methods

We retrospectively analyzed 323 SOF members from the Comprehensive Brain Health and Trauma Program at Home Base who completed high-resolution 3T MRI and the Blast Exposure Threshold Survey (BETS), which quantifies lifetime exposure to explosive weapons across five blast exposure categories (BEC1-BEC5). CSP grade and length were assessed using validated criteria on coronal 3D T1-weighted Magnetization Prepared Rapid Gradient Echo (MPRAGE) scans. A CSP length-to-septum length ratio (CSP ratio) was calculated to adjust for anatomical variation. Blast exposure counts (BEC1-BEC5) were log-transformed to correct skewness and are referred to as log-BEC1-5.

Variance inflation factor analysis indicated low multicollinearity among predictors (log-BEC1-5 and age), and variable selection using Least Absolute Shrinkage and Selection Operator regression identified log-BEC5 (exposure to large explosives) as the only retained predictor. In fully adjusted models, only log-BEC5 remained significantly associated with CSP measureoutcomes and was therefore the focus of subsequent analyses. Participants were stratified by BEC5 = 0 vs BEC5 > 0, and associations with CSP measuroutcomes were assessed using group comparisons, multivariable regression, and dose-response models.

Results

Variance inflation factor analysis indicated low multicollinearity among predictors. LASSO regression identified log-BEC5 as the only retained predictor. In fully adjusted models, only log-BEC5 remained significantly associated with CSP measures and was therefore the focus of subsequent analyses.

Among 323 participants (mean age 42.7 ± 8.8 years), 273 (84%) reported any BEC5 exposure. SOF members with BEC5 > 0 had significantly greater CSP presence (42.1% vs 22.0%, p = 0.007) and longer CSP length (median 3 mm vs 2 mm, p = 0.002). In age-adjusted models, BEC5 > 0 was associated with greater odds of CSP presence (OR = 2.58, 95% CI 1.26–5.25, p = 0.009) and a 1.45 mm increase in CSP length (p = 0.004). In continuous models, each one-unit increase in log-BEC5 was associated with a 0.31 mm increase in CSP length (p = 0.008) and a 0.0059 increase in CSP ratio (p = 0.008).

Conclusion

These findings indicate a statistically significant association between cumulative exposure to heavy explosives and CSP enlargement, suggesting that CSP may serve as a potential imaging marker of blast-related neurotrauma.

References

- **Modica LCM, Egnoto MJ, Statz JK, et al.** Development of a blast exposure estimator from a Department of Defense-wide survey study on military service members. *J Neurotrauma* 2021;38(12):1654–1661. doi:10.1089/neu.2020.7405
- **Gardner RC, Hess CP, Brus-Ramer M, et al.** Cavum septum pellucidum in retired American pro-football players. *J Neurotrauma* 2016;33(1):157–161. doi:10.1089/neu.2014.3805
- **Koerte IK, Hufschmidt J, Muehlmann M, et al.** Cavum septi pellucidi in symptomatic former professional football players. *J Neurotrauma* 2016;33(4):346–353. doi:10.1089/neu.2015.3880
- **Shively SB, Horkayne-Szakaly I, Jones RV, et al.** Characterisation of interface astroglial scarring in the human brain after blast exposure: a post-mortem case series. *Lancet Neurol* 2016;15(9):944–953. doi:10.1016/S1474-4422(16)30057-6
- **Kamps S, Hempel HL, Van Amerongen S, et al.** Enlarged cavum septum pellucidum as a neuroimaging signature of head impact exposure. *Brain Communications* 2025;7(2):fcaf085. doi:10.1093/braincomms/fcaf085

Images/Tables

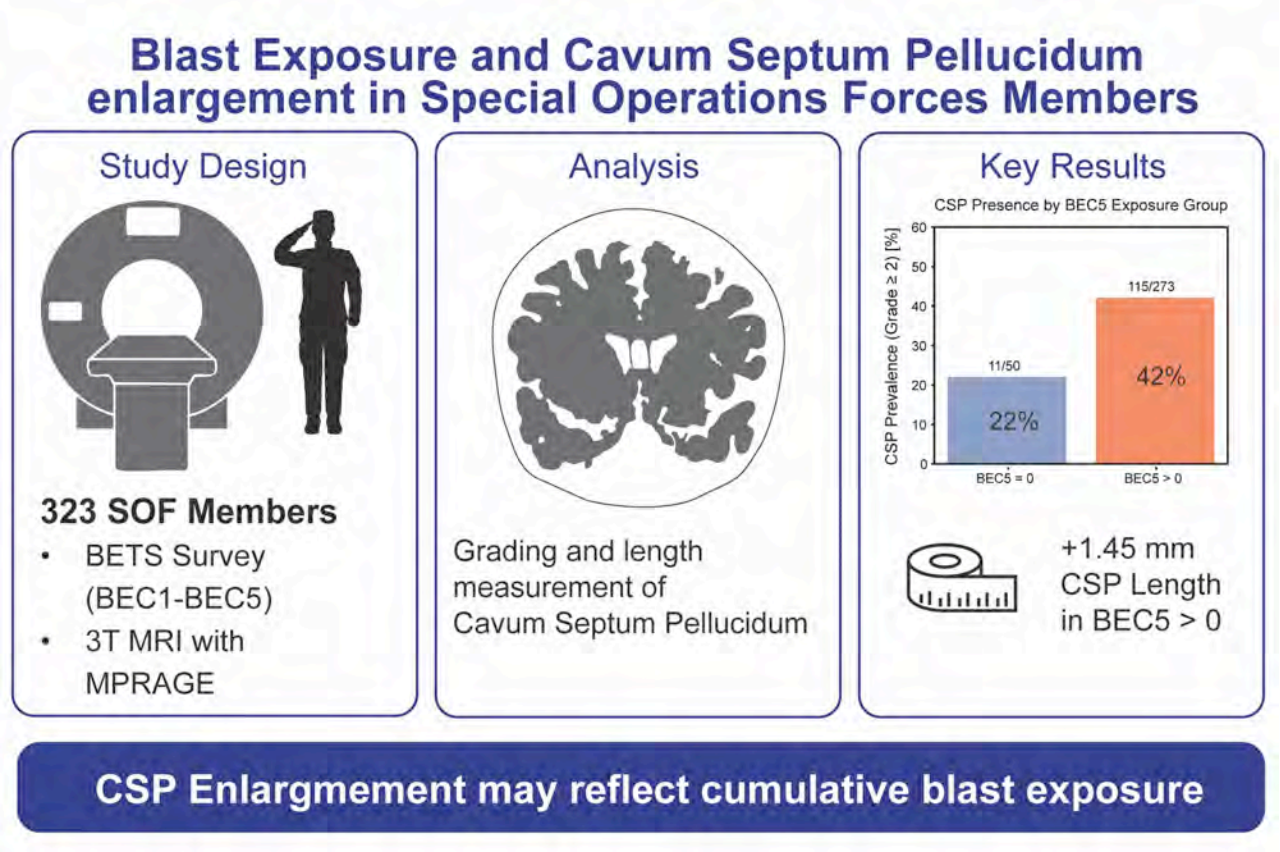

382 Architectural Innovation Meets Clinical Application: Validating Alzevita, a 3DAttResUNet++ segmentation model, for Hippocampal MRI Analysis.

Shelly Patel MPharm, Pushpendra Sisodia, Heather Barkwill
Topia MedTech, London, London, United Kingdom

Purpose

This study validates Alzevita, an AI-driven tool for automated hippocampal segmentation and Alzheimer's disease classification, using a clinically representative dataset. The goal is to assess its accuracy and reliability for integration into the dementia care pathway, supporting early diagnosis and longitudinal monitoring.

Materials & Methods

We evaluated Alzevita using 298 independent 3D T1-weighted MRI scans obtained from the Alzheimer's Disease Neuroimaging Initiative (ADNI) database. The dataset was curated to ensure diversity in age (55–90 years, mean 76 ± 7 years), clinical subgroups (ADNI-Control, ADNI-MCI, ADNI-AD), gender, magnetic field strength (1.5T and 3T), slice thickness (1 mm and 1.2 mm), and geographic regions (East, West, Central USA, and Canada). Preprocessing included noise reduction and feature normalisation. Manual hippocampal segmentations were performed by three certified radiologists following the EADC-ADNI Harmonised Protocol. To address inter-observer variability, consensus ground truth masks were generated using the STAPLE algorithm, which probabilistically estimates the most accurate segmentation by modelling individual rater performance. Segmentation accuracy was assessed using Dice Similarity Coefficient and Hausdorff distance. Diagnostic performance was evaluated through sensitivity, specificity, area under the curve (AUC), and F1 Score. Volumetric reliability was measured via correlation with expert annotations, Relative Volume Difference (RVD), and Bland–Altman analysis.

Results

Alzevita achieved a Dice Score of 0.86 and a Hausdorff distance of 1.51 mm, indicating precise hippocampal segmentation with minimal boundary error. It distinguished Alzheimer's cases from healthy controls with a sensitivity of 0.89 and specificity of 0.99, minimising misclassification risk. The AUC was 0.95, and the F1 Score was 0.86, confirming strong diagnostic consistency. Hippocampal volume estimates showed a high correlation with expert manual annotations ($r = 0.93$), and the RVD was 10.64%, well below the 24.6% threshold for longitudinal monitoring. Bland–Altman analysis revealed a mean volume difference of 0.485 cm^3, indicating minimal systematic bias.

Alzevita demonstrated consistent performance across key clinical and imaging subgroups. Diagnostic accuracy remained stable across Alzheimer's, MCI, and control groups, with no gender-based disparities observed. The model showed robust reliability across different MRI field strengths (1.5T vs 3T) and maintained segmentation precision across varying slice thicknesses (1 mm vs 1.2 mm), confirming its generalisability across diverse patient populations and imaging conditions.

Conclusion

Alzevita demonstrates robust performance in hippocampal segmentation and Alzheimer's classification across a clinically diverse validation cohort. Its high accuracy, reliability, and alignment with expert measurements support its integration into clinical workflows. For clinicians, Alzevita offers dependable decision support; for patients, it enables earlier and more accurate diagnosis; and for healthcare systems, it provides a scalable solution to enhance efficiency and continuity of dementia care.

References

Frisoni GB, Jack CR Jr, Bocchetta M, Bauer C, Frederiksen KS, Liu Y, et al. The EADC-ADNI harmonized protocol for manual hippocampal segmentation on magnetic resonance: Evidence of validity. Alzheimers Dement 2015;11(2):111–25

458 Positron Emission Tomography and CSF marker comparisons: Amyloid and Tau in Alzheimer's Disease Study

Maryam Fotouhi MD, Nasim Sheikh-Bahaei MD, PhD
Department of Radiology, Keck School of Medicine, University of Southern California, Los Angeles, CA, USA

Purpose

The optimal sequence of biomarker positivity in Alzheimer's disease remains contested, with significant implications for diagnosis, clinical trial enrollment, and therapeutic intervention windows. In this study, we examine the association between cerebrospinal fluid (CSF) and positron emission tomography (PET) assessments of amyloid and tau pathology, exploring the existence of a consistent temporal sequence and identifying variables contributing to discordance patterns.

Materials & Methods

Participants were included from the Alzheimer's Disease Neuroimaging Initiative (ADNI); of 1724 individuals with Florbetaben and Florbetapir amyloid PET imaging, 1290 had both CSF Aβ42 and amyloid-PET, while of 931 individuals with Flortaucipir tau-PET, 504 had both CSF pTau-181 and tau-PET within one year. Amyloid status was classified based on the Youden index as positive (A+) if either Aβ42 was below 977 pg/mL or amyloid-PET centiloid was ≥18 for florbetaben, ≥20 for florbetapir; cases were negative (A-) if both measures were negative. Tau status was classified as positive (T+) if any tau biomarker was elevated: CSF pTau-181 (≥24 pg/mL), entorhinal tau PET (SUVR ≥1.21), or meta-temporal tau-PET (SUVR ≥1.25). Regional tau PET SUVRs were adjusted for intensity using inferior cerebellar grey matter as a reference. Two tau-PET thresholding methodologies were evaluated: the Youden index (inclusive, exhibiting greater sensitivity) and the Mean/SD threshold (restrictive, demonstrating enhanced specificity). Discordance was characterized as a discrepancy between CSF and PET modalities acquired within one year (CSF+/PET- or CSF-/PET+). Statistical analyses were performed using ANOVA with Tukey's HSD and Kruskal-Wallis tests, applying Bonferroni correction, with significance determined at $\alpha=0.05$.

Results

CSF pTau and Tau-PET Positivity Discordance: Based on Youden threshold, 79 (15.7%) cases showed entorhinal and 62 (12.3%) cases meta-temporal tau-PET positivity (T+) despite negative CSF pTau-181 results. Discordance decreased by implementing a more stringent threshold. The CSF-/PET+ group demonstrated mean pTau-181 of 18.09 pg/mL (95%CI:17.32-18.87), substantially below positivity threshold, yet both discordant groups showed elevated amyloid-PET burden (31.7 vs. 43.2 centiloids).

Regional Tau-PET Discordance: Among 931 cases, 131 (14.1%) showed entorhinal positivity preceding meta-temporal positivity (Ent+/Tem-), while 52 (5.6%) exhibited the reverse pattern (Ent-/Tem+). The Ent+/Tem- group demonstrated worse cognitive outcomes (ADAS-Cog13: 13.5 vs. 10.7, $p=0.035$), higher CSF pTau-181 (23.0 vs. 18.7 pg/mL, $p=0.009$), and trends toward greater amyloid burden.

CSF Amyloid and Amyloid-PET Discordance: 142 cases showed CSF+ but PET- amyloid status with remarkably low centiloid values (2.7, 95%CI:1.0-4.4) and preserved cognition (CDR-SB progressing from 0.3 to 1.7). Conversely, 119 CSF-/PET+ cases had mean CSF Aβ42 of 1344 pg/mL (95%CI:1269-1420), well above conventional positivity thresholds and higher APOE ε4 carrier frequency (42% vs. 33%).

Conclusion

There is discordance between PET and CSF biomarkers for amyloid and tau, and the rates differ substantially with the threshold selection. These results call into question the idea of an immutable temporal progression in which CSF abnormalities precede PET in every instance of positivity. The patterns of discordance, on the other hand, point to the modality-specific identification of independent disease processes: whereas CSF index dynamic molecular pathology, PET will show accumulated pathology with defined spatial distributions.

References

1. Royse SK, Minhas DS, Lopresti BJ, et al. Validation of amyloid PET positivity thresholds in centiloids: a multisite PET study approach. Alzheimer's Res Ther. 2021;13(1):99. DOI: https://doi.org/10.1186/s13195-021-00836-1

2. Jagust WJ, Koeppe RA, Rabinovici GD, et al. The ADNI PET Core at 20. Alzheimer's Dement. 2024; 20: 7340–7349. DOI: https://doi.org/10.1002/alz.14165

3. Blennow K, Shaw LM, Stomrud E, et al. Predicting clinical decline and conversion to Alzheimer's disease or dementia using novel Elecsys Aβ(1–42), pTau and tTau CSF immunoassays. Sci Rep. 2019;9(1):19024. DOI: https://doi.org/10.1038/s41598-019-54204-z

4. Knopman DS, Weigand SD, Wiste HJ, et al. Discrepancies between CSF biomarker and PET determinations of elevated brain amyloid and their prognostic significance. Alzheimer's Dement. 2025; 21:e70468. DOI: https://doi.org/10.1002/alz.70468

5. Zeltzer E, Schonhaut DR, Mundada NS, et al. Concordance Between Amyloid-PET Quantification and Real-World Visual Reads. JAMA Neurol. 2025;82(9):952–962. DOI: https://doi.org/10.1001/jamaneurol.2025.2218

Images/Tables

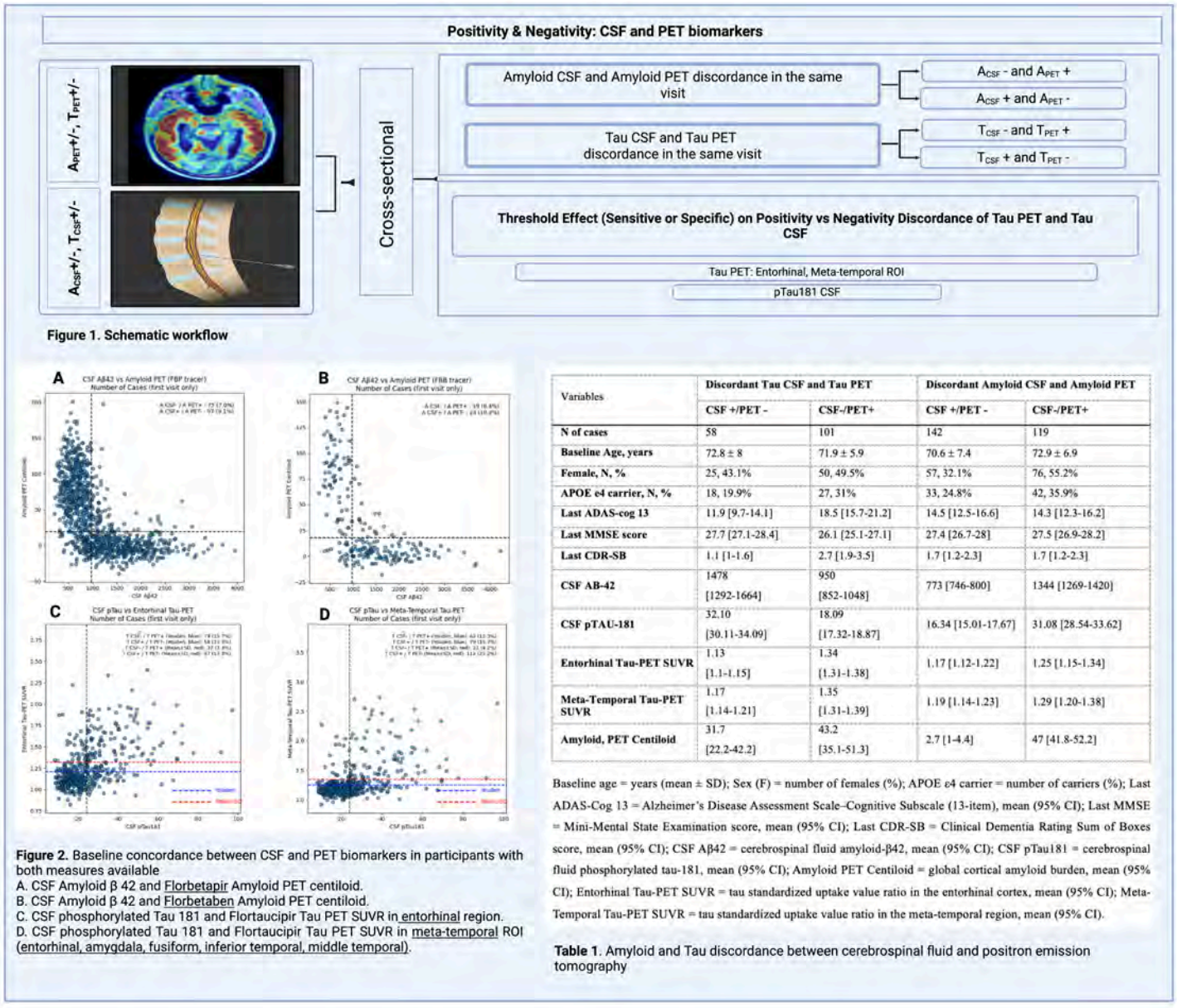

Figure 1. Schematic workflow

Figure 2. Baseline concordance between CSF and PET biomarkers in participants with both measures available
A. CSF Amyloid β 42 and Florbetapir Amyloid PET centiloid.
B. CSF Amyloid β 42 and Florbetaben Amyloid PET centiloid.
C. CSF phosphorylated Tau 181 and Flortaucipir Tau PET SUVR in entorhinal region.
D. CSF phosphorylated Tau 181 and Flortaucipir Tau PET SUVR in meta-temporal ROI (entorhinal, amygdala, fusiform, inferior temporal, middle temporal).

Variables	Discordant Tau CSF and Tau PET		Discordant Amyloid CSF and Amyloid PET	
	CSF +/PET -	CSF-/PET+	CSF +/PET -	CSF-/PET+
N of cases	58	101	142	119
Baseline Age, years	72.8 ± 8	71.9 ± 5.9	70.6 ± 7.4	72.9 ± 6.9
Female, N, %	25, 43.1%	50, 49.5%	57, 32.1%	76, 55.2%
APOE ε4 carrier, N, %	18, 19.9%	27, 31%	33, 24.8%	42, 35.9%
Last ADAS-cog 13	11.9 [9.7-14.1]	18.5 [15.7-21.2]	14.5 [12.5-16.6]	14.3 [12.3-16.2]
Last MMSE score	27.7 [27.1-28.4]	26.1 [25.1-27.1]	27.4 [26.7-28]	27.5 [26.9-28.2]
Last CDR-SB	1.1 [1-1.6]	2.7 [1.9-3.5]	1.7 [1.2-2.3]	1.7 [1.2-2.3]
CSF AB-42	1478 [1292-1664]	950 [852-1048]	773 [746-800]	1344 [1269-1420]
CSF pTAU-181	32.10 [30.11-34.09]	18.09 [17.32-18.87]	16.34 [15.01-17.67]	31.08 [28.54-33.62]
Entorhinal Tau-PET SUVR	1.13 [1.1-1.15]	1.34 [1.31-1.38]	1.17 [1.12-1.22]	1.25 [1.15-1.34]
Meta-Temporal Tau-PET SUVR	1.17 [1.14-1.21]	1.35 [1.31-1.39]	1.19 [1.14-1.23]	1.29 [1.20-1.38]
Amyloid, PET Centiloid	31.7 [22.2-42.2]	43.2 [35.1-51.3]	2.7 [1-4.4]	47 [41.8-52.2]

Baseline age = years (mean ± SD); Sex (F) = number of females (%); APOE ε4 carrier = number of carriers (%); Last ADAS-Cog 13 = Alzheimer's Disease Assessment Scale–Cognitive Subscale (13-item), mean (95% CI); Last MMSE = Mini-Mental State Examination score, mean (95% CI); Last CDR-SB = Clinical Dementia Rating Sum of Boxes score, mean (95% CI); CSF Aβ42 = cerebrospinal fluid amyloid-β42, mean (95% CI); CSF pTau181 = cerebrospinal fluid phosphorylated tau-181, mean (95% CI); Amyloid PET Centiloid = global cortical amyloid burden, mean (95% CI); Entorhinal Tau-PET SUVR = tau standardized uptake value ratio in the entorhinal cortex, mean (95% CI); Meta-Temporal Tau-PET SUVR = tau standardized uptake value ratio in the meta-temporal region, mean (95% CI).

Table 1. Amyloid and Tau discordance between cerebrospinal fluid and positron emission tomography

474 Automated MR Imaging Characterization and Spatial Mapping of Diffuse Midline Glioma

Atlas Haddadi Avval M.D., Nabaan Mir B.S., Evan Bloch B.S., Andreas M Rauschecker M.D. Ph.D.
UCSF, San Francisco, CA, USA

Purpose

Diffuse midline gliomas (DMGs) are highly aggressive pediatric and young adult tumors with limited treatment options and poor prognosis [1]. While qualitative MRI studies have described certain imaging patterns, large-scale quantitative characterization remains limited. We aimed to comprehensively quantify MRI features of DMGs across a large cohort using an automated feature extraction pipeline, as well as map the spatial distributions among the whole cohort and subgroups of patients.

Materials & Methods

A total of 254 patients diagnosed with DMG were retrospectively identified. Inclusion for further analysis required pre-treatment brain MRI containing at least T1-weighted (T1), post-contrast T1-weighted (T1c), T2-weighted (T2), and FLAIR sequences; advanced sequences (SWI, ADC, and CBF) were analyzed when available. Demographic, clinical, histopathologic, and molecular data were extracted from medical records, and subgroups of sex, age, and method of diagnosis (biopsy vs. imaging-only) were identified. Deep learning–based tumor segmentation was performed, and masks were registered to the SRI-24 atlas, enabling voxel-wise spatial map generation across patients and subgroups. Quantitative feature extraction was performed using Pyalfe (v0.1.1), an open-source Python framework that computes volumetric, signal-based, and anatomical distribution features across multiple MRI modalities [2]. Subgroup-level analyses compared features using the Mann–Whitney U and Kruskal–Wallis tests ($p < 0.05$ was considered significant).

Results

Among the 254 patients (mean age 16.4 ± 15.4 years; 52% male), 224 had complete MRI data. Most tumors were biopsy-confirmed (93%), and 89% of cases harbored the H3K27M mutation. Spatial mapping revealed that pons, thalamus, and midbrain were commonly involved regions. Younger patients (≤5 years) demonstrated a greater pontine and midline predominance, whereas older patients exhibited frequent cerebellar and more widespread extension (Fig. 1). Quantitative feature analysis demonstrated that relative MRI signal intensities (T1, T2, FLAIR, SWI, ADC, and CBF) were largely consistent across subgroups, with only minor exceptions observed in T1 by sex and age (p-value of 0.03 and 0.04, respectively) and T2 by diagnostic method (p-value of 0.02). In contrast, lesion topography showed marked subgroup variability. Imaging-diagnosed tumors exhibited higher involvement of the brainstem and cerebellum, whereas biopsy-confirmed cases demonstrated greater cortical and gray matter extension (p-values<0.05), reaffirming the spatial mapping results (Table 1).

Conclusion

This study represents one of the largest quantitative imaging analyses of diffuse midline gliomas to date. By combining deep learning–based spatial mapping with automated radiomic feature extraction, we provide an objective, reproducible framework for characterizing DMG topography and MRI-derived phenotypes across clinical and molecular subgroups. These results highlight distinct spatial patterns associated with patient subgroups, and the potential of quantifying imaging features in clinical MRI to refine DMG phenotyping and support future prognostic modeling.

References

1. Miguel Llordes G, Medina Pérez VM, Curto Simón B, et al. Epidemiology, Diagnostic Strategies, and Therapeutic Advances in Diffuse Midline Glioma. *J Clin Med* 2023;12
2. Eghbali R, Nedelec P, Weiss D, et al. Automated Lesion and Feature Extraction Pipeline for Brain MRIs with Interpretability. *Neuroinformatics* 2025;23:2

Images/Tables

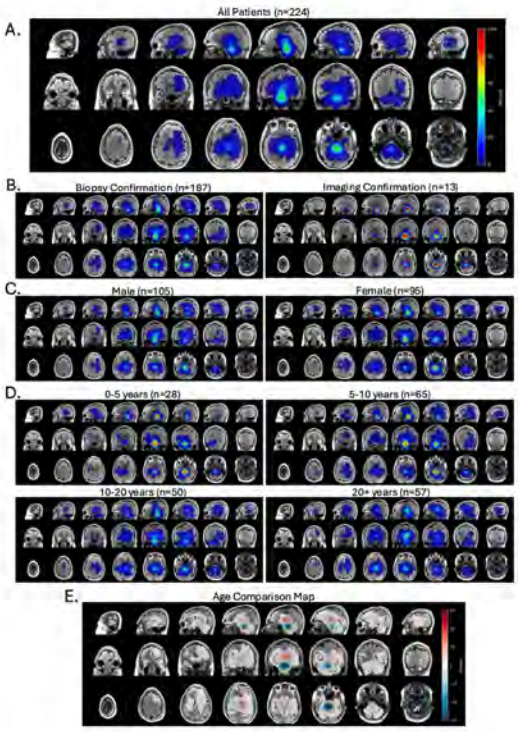

Figure 1. Spatial maps of Diffuse Midline Gliomas in the whole cohort (A) and among diagnostic confirmation method (B), sex (C), and age (D) subgroups. Part (E) shows the subtraction of the two age group extremities, highlighting the areas of difference.

Table 1. Quantitative pre-treatment MRI features of Diffuse Midline Glioma in the whole cohort and within different diagnosis method, sex, and age subgroups of patients. Significant p-values are highlighted in bold.

Feature		All patients (n=254)	Diagnosis Method			Sex			Age				
			Imaging (n=19)	Biopsy (n=235)	P-value	Female (n=123)	Male (n=131)	P-value	Age 0-5 (n=35)	Age 5-10 (n=87)	Age 10-20 (n=61)	Age 20+ (n=71)	P-value
Lesion volume		31,608.14 ± 33,584.91	24,909.03 ± 13,929.28	30,098.80 ± 30,745.80	0.902	28,805.26 ± 26,952.99	30,501.31 ± 32,292.92	0.688	27,938.88 ± 15,407.39	30,870.40 ± 34,143.33	27,553.12 ± 27,671.42	30,616.08 ± 30,637.21	0.597
Contrast enhancement (%)		19.83 ± 25.15	30.26 ± 32.90	20.22 ± 24.88	0.594	20.88 ± 25.60	21.27 ± 25.95	0.770	28.24 ± 28.76	19.34 ± 23.51	21.19 ± 30.59	19.86 ± 22.81	0.359
Relative Signal in	T1	0.79 ± 0.14	0.86 ± 0.15	0.78 ± 0.13	0.053	0.76 ± 0.13	0.80 ± 0.14	**0.029**	0.76 ± 0.14	0.75 ± 0.12	0.81 ± 0.13	0.81 ± 0.15	**0.044**
	T2	1.95 ± 3.61	1.41 ± 0.45	2.02 ± 3.91	**0.025**	2.24 ± 5.33	1.71 ± 0.50	0.488	1.73 ± 0.51	2.43 ± 6.11	1.60 ± 0.26	1.76 ± 0.63	0.441
	FLAIR	1.68 ± 0.34	1.65 ± 0.30	1.68 ± 0.36	0.684	1.65 ± 0.33	1.71 ± 0.37	0.154	1.74 ± 0.56	1.63 ± 0.19	1.64 ± 0.24	1.75 ± 0.46	0.505
	SWI	5.66 ± 77.87	258.57 ± 450.44	-1.72 ± 23.07	0.888	-4.23 ± 32.75	14.93 ± 106.05	0.084	-17.44 ± 61.87	1.03 ± 6.05	0.17 ± 3.50	24.10 ± 135.53	0.273
Absolute signal* in	ADC (5^{th})	815.19 ± 949.01	651.48 ± 323.66	830.92 ± 1,004.74	0.776	888.62 ± 1,062.48	758.21 ± 902.95	0.637	742.45 ± 323.26	962.48 ± 1,278.65	796.60 ± 1,282.71	721.63 ± 262.37	0.264
	ADC (mean)	1,300.59 ± 1,495.41	1,099.88 ± 533.11	1,322.12 ± 1,586.62	0.767	1,458.42 ± 1,801.92	1,168.95 ± 1,261.40	0.233	1,183.91 ± 458.41	1,582.10 ± 2,184.16	1,241.33 ± 1,770.04	1,121.68 ± 385.41	0.145
	ADC (median)	1,252.61 ± 1,485.30	1,060.81 ± 505.85	1,272.31 ± 1,576.29	0.613	1,396.61 ± 1,767.26	1,131.80 ± 1,286.01	0.276	1,143.43 ± 445.54	1,528.80 ± 2,140.98	1,188.42 ± 1,800.93	1,075.93 ± 409.66	0.096
	ADC (95^{th})	1,972.45 ± 2,125.87	1,675.13 ± 954.83	2,008.72 ± 2,249.75	0.896	2,246.22 ± 2,669.63	1,746.75 ± 1,613.72	0.259	1,822.50 ± 783.89	2,324.34 ± 3,235.82	1,928.22 ± 2,213.48	1,749.18 ± 681.91	0.669
	CBF (mean)	602.34 ± 526.54	1,217.17 ± 72.99	607.48 ± 531.45	0.138	630.26 ± 586.33	633.82 ± 506.33	0.662	889.59 ± 389.44	785.04 ± 553.46	520.96 ± 522.35	503.69 ± 538.48	0.196
	CBF (median)	597.52 ± 532.45	1,224.24 ± 88.58	602.26 ± 537.60	0.138	628.76 ± 588.37	626.87 ± 516.41	0.737	890.79 ± 391.27	775.74 ± 556.21	511.66 ± 527.25	502.98 ± 551.08	0.180
Lesion Percentage Volume in:	Cortical Grey Matter	7.22 ± 10.49	1.47 ± 1.98	7.30 ± 10.49	**0.007**	6.93 ± 10.84	6.72 ± 9.59	0.695	4.31 ± 7.20	4.55 ± 7.20	7.80 ± 10.98	10.28 ± 12.97	**0.010**
	Basal Ganglia	12.53 ± 18.21	3.57 ± 3.67	12.75 ± 18.71	0.316	8.67 ± 15.92	15.17 ± 19.57	**0.038**	5.13 ± 9.97	4.81 ± 6.88	15.73 ± 18.44	21.88 ± 24.06	**0.000**
	White Matter	17.39 ± 22.22	2.05 ± 3.01	17.47 ± 21.72	**0.002**	14.21 ± 20.72	18.11 ± 21.67	0.183	8.64 ± 15.19	9.97 ± 17.93	23.72 ± 23.93	21.99 ± 22.19	**0.000**
	Brain Stem	28.66 ± 27.60	49.83 ± 23.13	27.68 ± 27.18	**0.002**	28.60 ± 25.06	30.38 ± 29.76	0.876	35.00 ± 21.86	36.69 ± 24.27	26.40 ± 28.95	19.75 ± 29.97	**0.001**
	Cerebellum	26.47 ± 27.01	40.65 ± 23.34	26.60 ± 27.43	**0.022**	33.82 ± 27.76	21.94 ± 25.75	**0.002**	42.35 ± 26.44	37.65 ± 24.41	16.52 ± 20.18	16.76 ± 28.86	**0.000**
	Corpus Callosum	2.09 ± 5.05	0.10 ± 0.39	2.27 ± 5.40	**0.003**	1.60 ± 3.88	2.57 ± 6.20	0.167	0.84 ± 2.50	1.38 ± 3.90	3.36 ± 8.35	2.61 ± 4.01	**0.011**
	Frontal lobe	18.61 ± 26.35	1.64 ± 3.27	18.24 ± 25.27	**0.002**	14.76 ± 23.98	18.89 ± 25.22	0.525	6.69 ± 11.81	10.67 ± 21.09	23.14 ± 28.26	24.88 ± 26.84	**0.002**
	Parietal lobe	7.93 ± 13.29	0.22 ± 0.37	8.34 ± 13.68	**0.008**	6.15 ± 12.84	9.13 ± 13.62	0.168	4.29 ± 9.78	3.35 ± 9.52	10.09 ± 11.79	13.14 ± 17.49	**0.001**
	Temporal lobe	6.80 ± 14.31	0.72 ± 1.41	7.20 ± 14.91	**0.012**	6.72 ± 15.23	6.60 ± 13.61	0.593	3.25 ± 6.61	3.96 ± 12.39	8.91 ± 14.66	10.07 ± 18.15	**0.000**
	Occipital lobe	5.71 ± 8.83	0.59 ± 0.90	6.05 ± 8.87	**0.009**	4.37 ± 7.84	6.77 ± 9.22	**0.018**	3.54 ± 6.37	2.06 ± 3.91	7.83 ± 9.46	9.53 ± 11.13	**0.000**

497 Quantitative ADC Mapping of T2W/FLAIR Abnormalities Enhances Differentiation of True Progression from Pseudoprogression in IDH-Wildtype Glioblastoma

Doonyaporn Wongsawaeng MD[1], Nanthapob Chanthaphan MD[1], Achiraya Teyateeti MD[2], Sith Sathornsumetee MD[3], Chanon Ngamsombat MD[1]
[1]Division of Diagnostic Radiology, Department of Radiology, Faculty of Medicine Siriraj Hospital, Mahidol University, Bangkoknoi, Bangkok, Thailand.
[2]Division of Radiation Oncology, Department of Radiology, Faculty of Medicine Siriraj Hospital, Mahidol University, Bangkoknoi, Bangkok, Thailand.
[3]Division of Neurology, Department of Medicine, Faculty of Medicine Siriraj Hospital, Mahidol University, Bangkoknoi, Bangkok, Thailand

Purpose

Diffusion MRI could aid to differentiate between glioma progression and treatment-related abnormalities (1). Some factor such as corticosteroid administration interfere enhancing tumor volume and diffusion MRI measurement (2). We investigated whether apparent diffusion coefficient (ADC) values derived from abnormal T2W/FLAIR regions can distinguish true tumor progression (TP) from pseudoprogression (PsP) in IDH-WT glioblastoma.

Materials & Methods

Thirty-eight IDH-WT glioblastoma patients who received standard of care Stupp protocol were retrospectively reviewed. Fourteen patients developed presumed disease progression and were classified as TP (n=10) and PsP (n=4) group by RANO criteria or histopathology. MRI scans including DWI sequence (single shot spin-echo EPI with b values of 0 and 1000 s/mm^2), T2W/FLAIR and T1W post-Gd were analyzed. ADC was measured within a manually defined ROI in various regions including contrast-enhanced tumor (CET) exclude/include necrosis, only necrosis, T2W/FLAIR tumor exclude/ include edema, perilesional edema only as well as contralateral normal appearing white matter (WM) by using Horos (Version 3.3.6; Horos Project; https://horosproject.org/). ADC metrics were normalized (rADC) to WM. Mean ADC and rADC values each regions were compared between two groups using independent sample t-tests. P-value < 0.05 was considered significant.

Results

TP showed significantly lower mean ADC and rADC values compared with PsP group on T2W/FLAIR tumor (equal to or larger than CET area), CET include necrosis and necrosis only (Figure 1A and 1B). No statistically significant difference was found between the two groups on CET exclude necrosis, T2W/FLAIR tumor include edema, and perilesional edema only. However, there was a trend toward lower mean ADC and rADC values in TP compared to PsP group.

Conclusion

ADC analysis of T2W/FLAIR abnormalities, non-invasive biomarker, potentially enables differentiating TP from PsP in IDH-WT glioblastoma. Incorporating this metric into standard post-treatment MRI could optimize response assessment and patient management.

References

1. Van den Elshout R, Scheenen TWJ, Driessen CML, et al. Diffusion imaging could aid to differentiate between glioma progression and treatment-related abnormalities: a meta-analysis. Insights Imaging. 2022;13(1):158. https://doi.org/10.1186/s13244-022-01295-4.
2. Sanvito F, Kim A, Raymond C, et al. Impact of corticosteroid administration on contrast-enhancing volume and diffusion MRI in treatment naive glioblastoma. Neuro Oncol. 2025. https://doi.org/10.1093/neuonc/noaf136.

Images/Tables

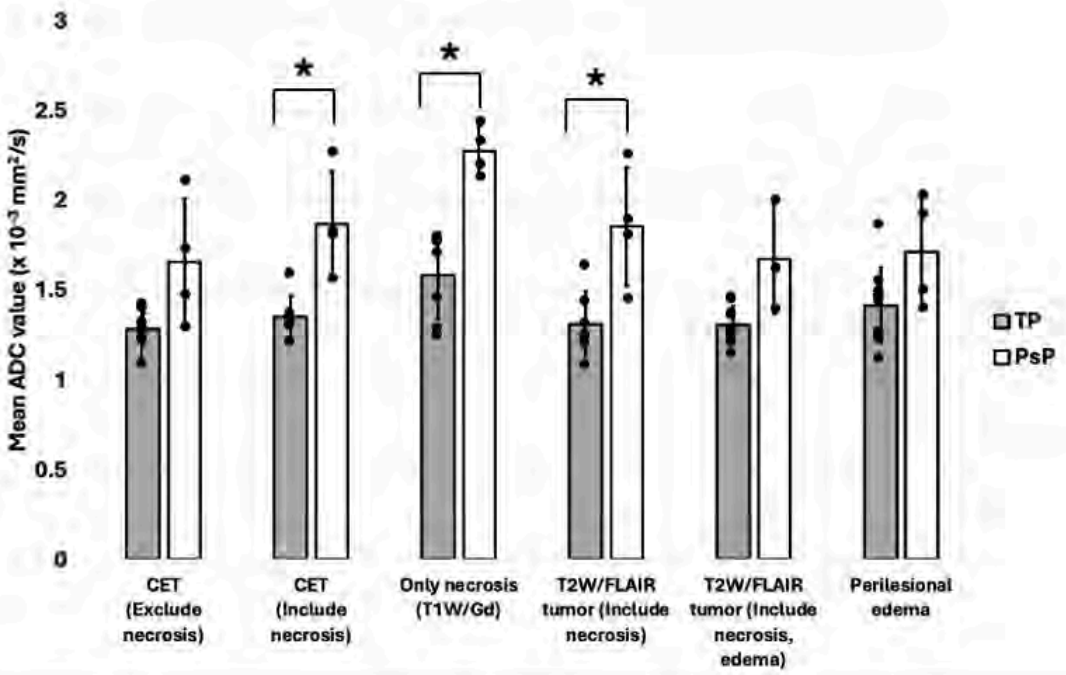

Figure 1A: Comparison of mean ADC value measured from various regions including contrast-enhanced tumor (CET) exclude/include necrosis, only necrosis, T2W/FLAIR tumor exclude/include perilesional edema and perilesional edema only at presumed disease progression time point between true progression (TP) and pseudoprogression (PsP) patients. * Indicates P-value < 0.05

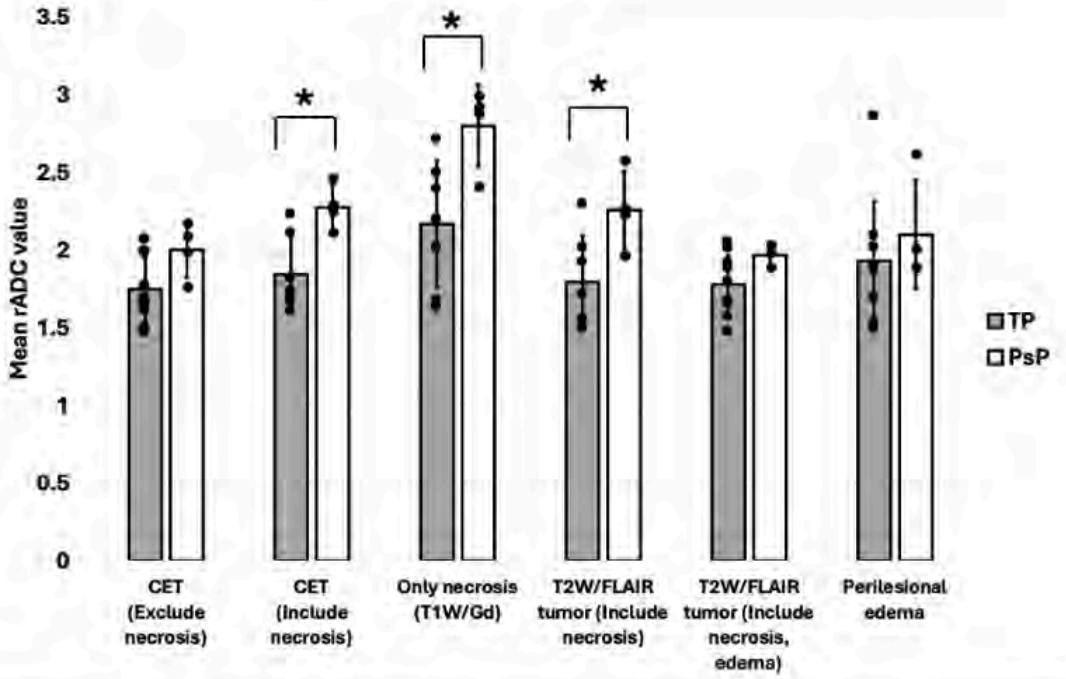

Figure 1B: Comparison of mean rADC value measured from various regions including contrast-enhanced tumor (CET) exclude/include necrosis, only necrosis, T2W/FLAIR tumor exclude/include perilesional edema and perilesional edema only at presumed disease progression time point between true progression (TP) and pseudoprogression (PsP) patients. * Indicates P-value < 0.05

502 Portable Low-Field MRI for Rapid Detection and Monitoring of ARIA in Lecanemab-Treated Alzheimer's Disease Patients: A Pilot Study

Shenghua Zhu MD, PhD, Nima Omid-Fard MD, Jarrel Seah MBBS, Saurabh Rohatgi MD, Jeremy Ford MD, Javier Romero MD
Mass General Hospital, Boston, MA, USA

Purpose

Cerebral edema and sulcal effusions, also known as amyloid-related imaging abnormalities (ARIA-E), are complications of anti-amyloid therapy and require frequent monitoring. However, timely high-field (HF) MRI may not be available; portable low-field (LF) MRI could enable point-of-care surveillance. To determine the diagnostic performance of portable 0.064 T LF MRI for detecting and quantifying ARIA-E in lecanemab-treated patients, using temporally paired HF-MRI as the reference standard.

Materials & Methods

Twenty lecanemab-treated Alzheimer's patients (November 2023 to February 2025) underwent 20 LF-MRI examinations at 0.064 T; the closest 3 T HF-MRI served as reference. Three blinded neuroradiologists scored LF-MRI for ARIA-E. Lesion size and volume were manually segmented on both modalities and correlated.

Results

Seven ARIA-E events developed in 6 of 20 patients and 5 of 7 active ARIA-E were correctly detected on LF-MRI. 15 of 20 ARIA-negative cases were accurately classified. LF-MRI measurements strongly matched HF-MRI (maximum dimension $r = 0.908$, $p < 0.0001$; volume $r = 0.968$, $p < 0.0001$).

Conclusion

Portable 0.064 T MRI reliably confirmed absence or presence of ARIA-E in this pilot cohort and produced quantitative metrics comparable to HF-MRI, supporting its use for rapid clinic-based monitoring. Larger studies should validate sensitivity and optimize protocols.

References

1. 2024 Alzheimer's disease facts and figures. *Alzheimers Dement* 2024; 20:3708-3821
2. van Dyck CH, Swanson CJ, Aisen P, et al. Lecanemab in Early Alzheimer's Disease. *N Engl J Med* 2023; 388:9-21
3. Mazurek MH, Cahn BA, Yuen MM, et al. Portable, bedside, low-field magnetic resonance imaging for evaluation of intracerebral hemorrhage. *Nat Commun* 2021; 12:5119
4. Sheth KN, Mazurek MH, Yuen MM, et al. Assessment of Brain Injury Using Portable, Low-Field Magnetic Resonance Imaging at the Bedside of Critically Ill Patients. *JAMA Neurol* 2020; 78:41-47

Images/Tables

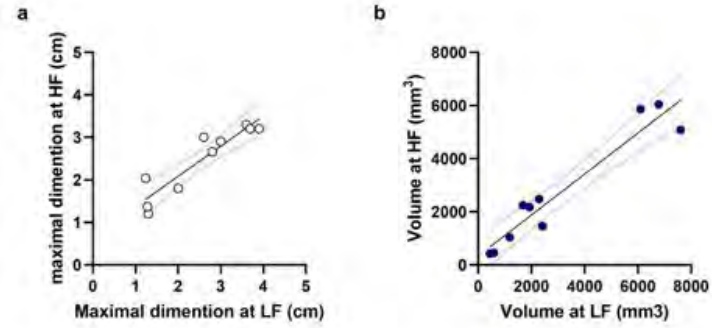

Figure1. Scatter plots comparing the maximal dimension (in cm), volume of ARIA-E (in mm^3) derived from High field (HF) MRI and Low field (LF) MRI scans are shown. The individual data points are shown adjacent to the box plots.

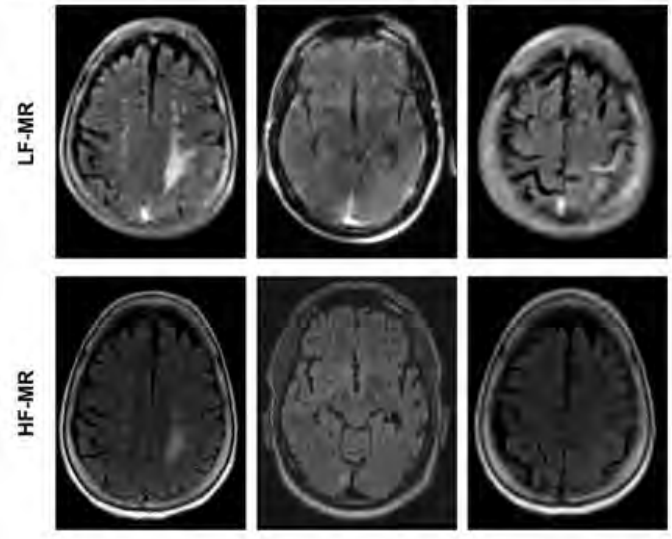

Figure 2. Representative ARIA-E on FLAIR images at low field (LF) and high field (HF) in patients with Alzheimer's disease (AD) received lecanemab.

508 Tract-Specific White Matter Changes Linked to Eye-Hand Coordination Deficits After MCA Stroke

Boniface Yarabe MD, Alaleh Alivar PhD, Mahya Beheshti MD, Patryk Filipiak PhD, Santiago Coelho PhD, Els Fieremans PhD, Yvonne Lui MD, John R Rizzo MD, Sohae Chung PhD
NYU Langone Health, New York, New York, USA

Purpose

Eye-hand coordination (EHC) is critical to upper-limb recovery after middle cerebral artery (MCA) stroke, yet remains under-addressed in rehabilitation [1]. We hypothesize that EHC deficits arise from tract-specific white matter (WM) microstructural injury within visuomotor networks. In this preliminary study, we use advanced diffusion MRI to identify and quantify tract-level alterations underpinning EHC after MCA stroke, laying the groundwork for EHC-targeted interventions.

Materials & Methods

Seven MCA-stroke patients with EHC deficits (62±12 years) and six age-matched controls (61±10 years) underwent multi-shell, multi-dimensional diffusion MRI on a 3T scanner (Prisma, Siemens). We derived: fractional anisotropy (FA), mean/axial/radial diffusion and kurtosis (MD/AD/RD, MK/AK/RK), and Standard Model [2] indices including intra-axonal diffusivity (Da), extra-axonal parallel and perpendicular diffusivities ($D_{e\parallel}$, $D_{e\perp}$), and axonal water fraction (f), capturing biologically interpretable intra-/extra-axonal properties. Tractography (ODF-FP) reconstructed ten WM tracts with emphasis on visuomotor pathways: superior longitudinal fasciculi (SLF I-III), optic radiations (OR), and inferior fronto-occipital fasciculi (IFOF). Infarcts were segmented on T2-FLAIR in ITK-SNAP; lesion voxels were excluded from analysis. Tracts-wise means from the stroke-affected and contralateral hemispheres were compared separately with controls using independent t-tests (significance at $p<0.001$).

Results

Patients exhibited impaired upper-limb performance: median Jebsen-Taylor Hand Function Test (JTHFT) scores were 82 ipsilesionally and 73 contralesionally (higher = worse).

Along-tract diffusion analysis demonstrated significant patients-controls differences in visuomotor pathways (Fig.1; SLF I-III, OR, IFOF). In SLF I and III, reduced f and MK indicated axonal loss with diminished tissue complexity. In the IFOF, reduced FA and Da suggested decreased directional coherence and axonal injury. Notably, Da differentiated affected from unaffected IFOF where FA did not, supporting greater specificity of Da for post-stroke axonal loss. These findings indicate vulnerability of EHC-related association fibers after MCA stroke and highlight Da's sensitivity to WM injury beyond infarct regions.

Conclusion

Preliminary data show tract-specific microstructural alterations in visuomotor association pathways after MCA stroke that relate to impaired EHC. In particular, IFOF Da differed both between patients and controls and between affected and contralateral hemispheres, highlighting the value of compartment-specific diffusion metrics. Abnormalities extended beyond infarct regions, indicating network-level injury that lesion mapping alone may miss. Da appears sensitive to post-stroke axonal compromise and may serve as a tract-specific imaging biomarker to guide EHC-focused rehabilitation and monitor recovery.

References

1. Rizzo, J.-R., Hosseini, M., Wong, E., et al. The intersection between ocular and manual motor control: eye–hand coordination in acquired brain injury. Frontiers in neurology, 2017. 8: p. 227.
2. Novikov, D. S., Fieremans, E., Jespersen, S. N., et al. Quantifying brain microstructure with diffusion MRI: Theory and parameter estimation. *NMR in Biomedicine*, 2019, *32*(4), e3998.

Images/Tables

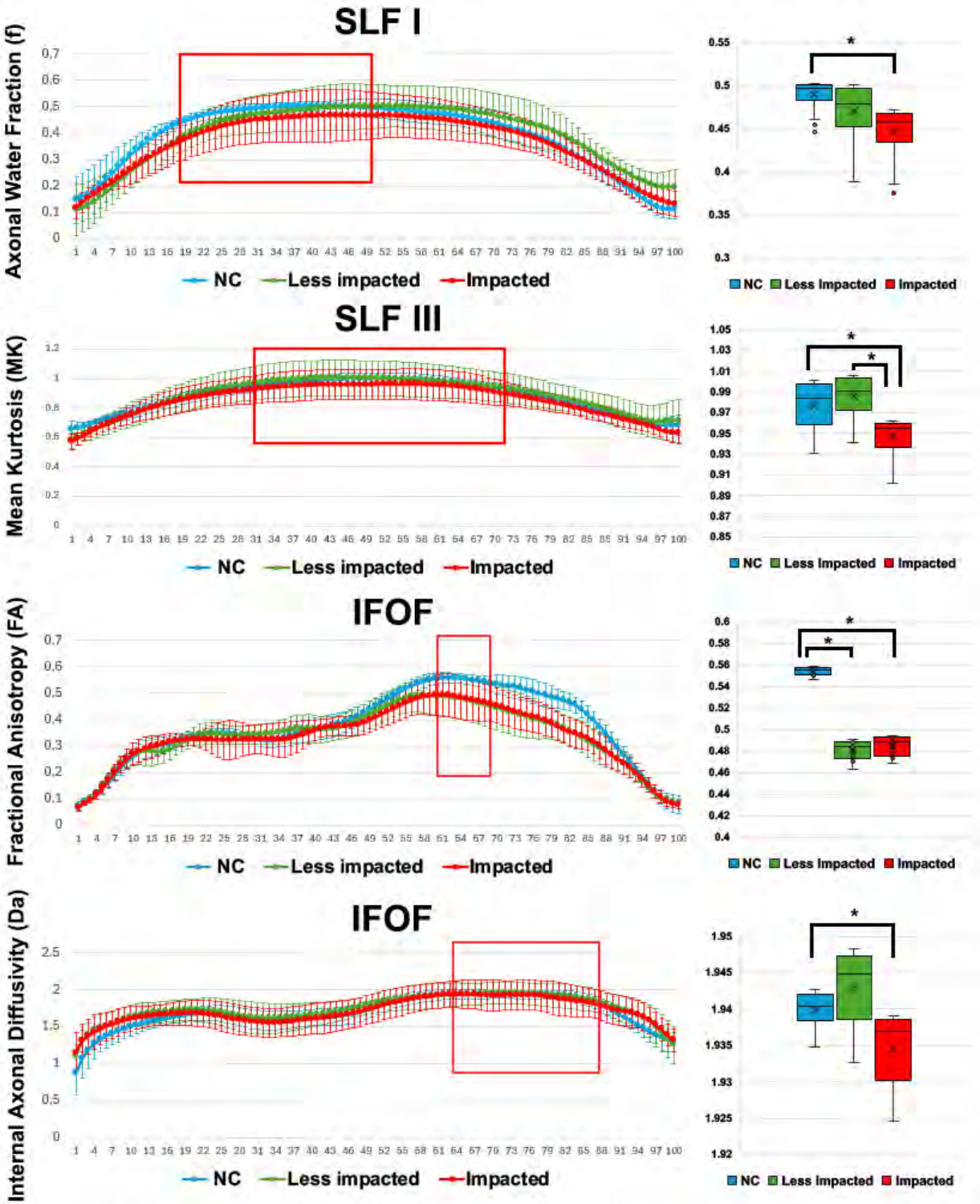

Figure 1. Highly significant microstructural differences between groups (normal controls, less-impacted, stroke-impacted tracts) were found in SLF I (lower axonal water fraction), SLF III (lower MK), and IFOF (lower FA, lower Da), suggesting selective vulnerability of EHC-related tracts following MCA stroke. (*p<0.001)
Note that the plotted values were computed along the fascicles and the x-axis in each subfigure represents 100 sampling points distributed evenly from the anterior (1) to the posterior (100) end of a fascicle.

537 Deep learning based segmentation of arteries and veins on single-phase CTA using CTP source training data for contrast phase augmentation

Henk van Voorst MD, PhD[1], Daniel de Wilde BSc[1], Maya Alexandra Schwarz BSc[1], Jamie Kesten BSc[1], Pere Canals PhD[1], Ish Talati MD[1], Praneeta Konduri PhD[1], Donghoon Kim PhD[1], Nicol Yuen MSc[1], Soren Christensen PhD[1], Greg Albers MD[1], Gagan Sharma MSc[2], Mark Parsons MD[3], Greg Zaharchuk MD, PhD[1], Maarten Lansberg MD, PhD[1], Jeremy J Heit MD, PhD[1]

[1]Stanford, Palo Alto, CA, USA. [2]University of Melbourne, Melbourne, NSW, Australia. [3]University of New South Wales, Sydney, NSW, Australia

Purpose

Automated segmentation of arteries and veins on single-phase brain CT angiography (CTA) could support vascular disease diagnostics (1) and the comprehensive evaluation of arterial and venous flow patterns in acute ischemic stroke (2). However, separating arteries from veins on CTA is challenging because of the similarity in vascular contrast opacification. The appearance of contrast fluid flowing through vessels over time is available in CT perfusion (CTP) source data and enables accurate deep-learning-guided artery and vein segmentation (3). We aimed to study the use of thin-slice (<1mm) CTP source data to generate multiple single-phase CTA instances with ground-truth artery-vein segmentations for training deep learning models.

Materials & Methods

We used a training dataset of 44 CTP source scans and test sets from external centers comprising 17 CTP source scans to simulate CTAs at various contrast phases and 10 real CTAs with varying arterial and venous collateral scores. CTAs were simulated from CTP source data by taking the exposure-dose-weighted average across three consecutive frames. Arteries and veins were semi-automatically segmented using CTP source data (3). Manual ground truth segmentations were acquired for CTAs. Simulated CTAs were defined by time differences with 2-second increments ranging from -6 to +6 seconds from the arterial peak defined in a main intracranial artery (M1/ICA). We trained nnUNet-based deep learning models on peak arterial simulated CTA (t0-model) and simulated CTAs with randomly sampled time differences – 0 and +/- 2, 4, 6 seconds – for each epoch to augment contrast appearance (t246-model). For both deep learning models, we compared the mean (95% confidence interval) Dice Similarity Coefficient (DSC) for artery and vein segmentation using ANOVA and t-tests.

Results

In the simulated CTA test set, artery segmentation performance decreased while vein segmentation increased for larger phase delays. Arterial segmentation DSC varied between 0.90(0.89-0.90) and 0.85(0.83-0.86) for the deep learning model using contrast phase augmentation (t246) and between 0.86(0.85-0.88) and 0.79(0.77-0.81) when only peak arterial simulated CTA (t0) was used (t246 vs t0 $p<1e-5$). Similarly, vein segmentation DSC varied between 0.85(0.82-0.88) and 0.92(0.90-0.94) with contrast phase augmentation (t246) and between 0.86(0.85-0.88) and 0.79(0.77-0.81) without contrast phase augmentation (t246 vs t0 $p<0.0001$). In the real CTA test set, arterial segmentation DSC was 0.75(0.73-0.77) with contrast phase augmentation and 0.70(0.68-0.73) without (t246 vs t0 $p<0.05$). Vein segmentation DSC for real CTAs was 0.87(0.85-0.88) with contrast phase augmentation and 0.83(0.81-0.85) without.

Conclusion

CTP source data can be used to efficiently simulate CTAs and acquire corresponding ground-truth artery and vein segmentations, thereby significantly reducing annotation time and enabling contrast-phase augmentation. Deep learning models trained using these simulated CTAs achieved state-of-the-art artery and vein segmentations, with improved performance under contrast-augmented training regimes on external test sets comprising simulated and real CTAs.

References

1. Aziz, Y. N., Sriwastwa, A., Nael, K., et al. (2025). Automated Vessel Occlusion Software in Acute Ischemic Stroke: Pearls and Pitfalls. Stroke.
2. Faizy, T. D., Mlynash, M., Kabiri, R., et al. (2022). The cerebral collateral cascade: comprehensive blood flow in ischemic stroke. Neurology, 98(23), e2296-e2306.
3. Meijs, M., Pegge, S. A., Vos, M. H., et al. (2020). Cerebral artery and vein segmentation in four-dimensional CT angiography using convolutional neural networks. Radiology: Artificial Intelligence, 2(4), e190178.

Images/Tables

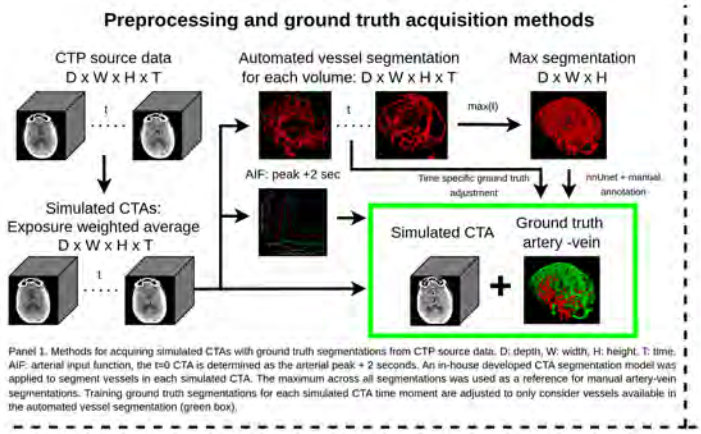

Panel 1. Methods for acquiring simulated CTAs with ground truth segmentations from CTP source data. D: depth, W: width, H: height, T: time. AIF: arterial input function, the t=0 CTA is determined as the arterial peak + 2 seconds. An in-house developed CTA segmentation model was applied to segment vessels in each simulated CTA. The maximum across all segmentations was used as a reference for manual artery-vein segmentations. Training ground truth segmentations for each simulated CTA time moment are adjusted to only consider vessels available in the automated vessel segmentation (green box).

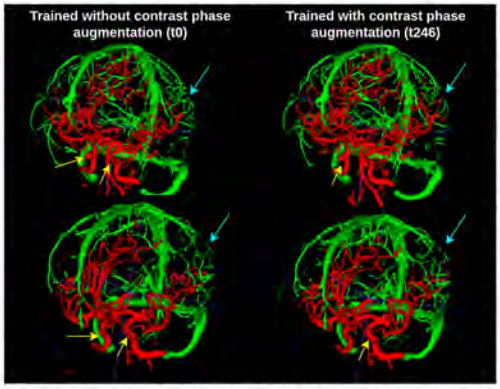

Panel 2. Examples of artery and vein segmentations on real CTAs. Compared to the method trained with contrast phase augmentation, the model trained without contrast phase augmentation missed parts of the internal carotid artery close to the skull (yellow arrows) and the distal small vessels (blue arrows). For large veins and venous sinuses both method show comparable segmentations. The model trained with contrast phase augmentation segmented smaller veins better (blue arrows).

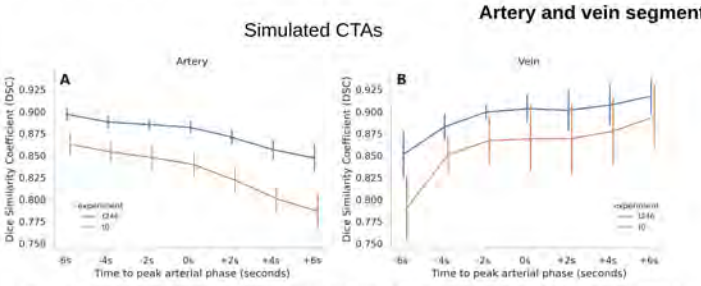

Panel 3 A/B: Simulated CTAs for 2-second increments from the simulated peak arterial CTA derived from 17 CTP source data scans, vertical lines represent 95%CI. Contrast phase augmentation (t246) during training outperformed the use of only peak arterial simulated CTAs (t0) (A:p<0.001, B:p<0.03)

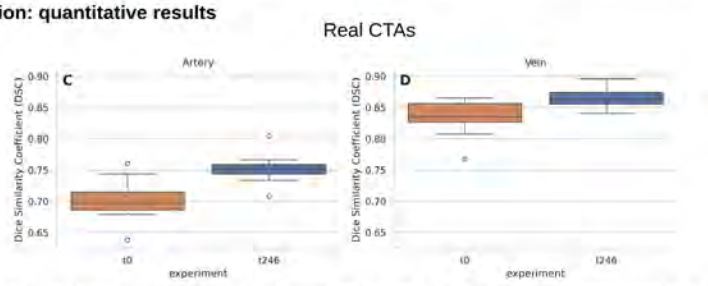

Panel 3 C/D: Segmentation performance boxplot for 10 real CTAs. Contrast phase augmentation (t246) outperformed the use of only peak arterial CTAs (t0) (A: p<0.05, B: p<0.05)

613 Timing of Antithrombotic Therapy Resumption After Surgical Evacuation of Chronic Subdural Hematoma: A Propensity Score-Matched Analysis

Hamza Adel Salim M.D.[1], Sami O Dakhel M.S.[2], Muhammed Amir Essibayi MD, MSc[3], Ahmed Y Azzam MD, MEng[4], Huanwen Chen M.D.[5], Dheeraj Gandhi M.D.[5], Adam A Dmytriw MD, MPH, MSc[6], Vivek S Yedavalli MD, MS, FAHA[7], Marco Colasurdo M.D.[8], Ajay Malhorta MBBS, MD, MMM, FACR[9], David J Altschul M.D.[3], Dhairya A Lakhani M.D.[10]

[1]MD Anderson Medical Center, Houston, Texas, USA. [2]Rowan-Virtua School of Osteopathic Medicine, Stratford, New Jersey, USA. [3]Montefiore Medical Center, Albert Einstein College of Medicine, New York, New York, USA. [4]ASIDE Healthcare, Lewes, Delaware, USA. [5]University of Maryland Medical Center, Baltimore, Maryland, USA. [6]Massachusetts General Hospital & Brigham and Women's Hospital, Harvard University, Boston, Massachusetts, USA. [7]Johns Hopkins University, Baltimore, Maryland, USA. [8]Oregon Health & Science University, Portland, Oregon, USA. [9]Yale University, New Haven, Connecticut, USA. [10]Rockefeller Neuroscience Institute, West Virginia University, Morgantown, West Virginia, USA

Purpose

Chronic subdural hematoma (cSDH) is a common neurosurgical condition in elderly patients, driven by angiogenic and inflammatory membrane activity rather than acute trauma. These mechanisms are now recognized as central to cSDH pathophysiology rather than coagulopathy alone[1]. While burr-hole drainage remains the standard treatment, adjunctive endovascular and medical strategies continue to evolve[2]. The timing of postoperative antithrombotic resumption remains heterogeneous across institutions[3]. Early restart may prevent thromboembolic complications but has historically raised concern for recurrence4,5.

Materials & Methods

We conducted a retrospective cohort study using the TriNetX US Collaborative Network (2003–2025), identifying adults undergoing surgical drainage of cSDH. Exposure groups were defined by timing of postoperative antithrombotic therapy: ≤7 days, 8–14 days, 15–28 days, and no therapy within 3 months. Outcomes included 180-day all-cause mortality (primary) and reoperation for recurrence (secondary). Propensity score matching was applied to balance demographics, comorbidities, and preoperative therapy.

Results

Among 11,608 patients, 906 resumed therapy ≤7 days, 402 at 8–14 days, 198 at 15–28 days, and 10,102 received none. Early resumption (≤7 days) reduced mortality versus no therapy (18.4% vs. 26.5%; OR 0.62, 95% CI 0.50–0.79; P<0.001) without higher reoperation risk (7.8% vs. 9.1%; P=0.34). Similar mortality reduction was observed with 8–14 days (OR 0.68, P=0.025) and 15–28 days (OR 0.53, P=0.014). Head-to-head comparison of ≤7 vs. 8–14 days showed no significant differences in mortality or reoperation.

Conclusion

Early resumption of antithrombotic therapy within 7–14 days after cSDH evacuation was associated with lower mortality and no increase in recurrence, supporting a risk-stratified approach consistent with recent consensus guidelines[1] and observational data[4,5]. Delays beyond four weeks may unnecessarily increase thromboembolic mortality[3]. Prospective, randomized trials are needed to refine optimal restart windows and align with emerging multimodal management strategies2.

References

1. Kan P, Fiorella D, Dabus G, et al. ARISE I consensus statement on the management of chronic subdural hematoma. *Stroke* 2024;55:1438–48. DOI: https://doi.org/10.1161/STROKEAHA.123.044129

2. Fiorella D, Monteith SJ, Hanel R, et al. Embolization of the middle meningeal artery for chronic subdural hematoma. *N Engl J Med* 2025;392:855–64. DOI: https://doi.org/10.1056/NEJMoa2409845

3. Phan K, Abi-Hanna D, Kerferd J, et al. Resumption of antithrombotic agents in chronic subdural hematoma: a systematic review and meta-analysis. *World Neurosurg* 2018;109:e792–e799. DOI: https://doi.org/10.1016/j.wneu.2017.10.091
4. Guha D, Coyne S, Macdonald RL. Timing of the resumption of antithrombotic agents following surgical evacuation of chronic subdural hematomas: a retrospective cohort study. *J Neurosurg* 2016;124:750–59. DOI: https://doi.org/10.3171/2015.2.JNS141889
5. Amano T, Matsuo S, Miyamatsu Y, et al. Impact of antithrombotic therapy on surgical treatment in patients with chronic subdural hematoma. *J Clin Neurosci* 2020;74:55–60. DOI: https://doi.org/10.1016/j.jocn.2020.01.076

Images/Tables

Table 1. Baseline Characteristics of Chronic Subdural Hematoma Patients by Antithrombotic Therapy Timing

Characteristic	Antithrombotic ≤1 week (n=848)	No Antithrombotic (n=848)	SMD	Antithrombotic 8-14 days (n=393)	No Antithrombotic (n=393)	SMD	Antithrombotic 15-28 days (n=189)	No Antithrombotic (n=189)	SMD
Demographics									
Age at index, mean ± SD	67.1 ± 15.4	68.7 ± 14.1	0.109	65.5 ± 16.9	66.8 ± 15.8	0.081	62.6 ± 18.9	63.8 ± 16.7	0.066
Male sex, n (%)	544 (64.2)	534 (63.0)	0.025	262 (66.7)	282 (71.8)	0.110	129 (68.3)	123 (65.1)	0.067
White race, n (%)	575 (67.8)	577 (68.0)	0.005	275 (70.0)	270 (68.7)	0.028	136 (72.0)	139 (73.5)	0.036
Comorbidities									
Hypertension, n (%)	605 (71.3)	611 (72.1)	0.016	276 (70.2)	276 (70.2)	<0.001	134 (70.9)	140 (74.1)	0.071
Diabetes mellitus, n (%)	283 (33.4)	289 (34.1)	0.015	123 (31.3)	132 (33.6)	0.049	51 (27.0)	46 (24.3)	0.061
Chronic kidney disease, n (%)	118 (13.9)	122 (14.4)	0.014	58 (14.8)	52 (13.2)	0.044	22 (11.6)	16 (8.5)	0.106
Atrial fibrillation, n (%)	221 (26.1)	256 (30.2)	0.092	101 (25.7)	106 (27.0)	0.029	50 (26.5)	57 (30.2)	0.082
Ischemic heart disease, n (%)	292 (34.4)	297 (35.0)	0.012	147 (37.4)	149 (37.9)	0.011	60 (31.7)	69 (36.5)	0.101
Tobacco use history, n (%)	168 (19.8)	159 (18.8)	0.027	73 (18.6)	71 (18.1)	0.013	37 (19.6)	44 (23.3)	0.090
Neoplasms, n (%)	119 (14.0)	126 (14.9)	0.023	69 (17.6)	65 (16.5)	0.027	34 (18.0)	21 (11.1)	0.196
Headache, n (%)	101 (11.9)	106 (12.5)	0.018	48 (12.2)	51 (13.0)	0.023	25 (13.2)	26 (13.8)	0.015
Gait abnormalities, n (%)	90 (10.6)	97 (11.4)	0.026	46 (11.7)	41 (10.4)	0.041	30 (15.9)	29 (15.3)	0.015
Coagulation disorders, n (%)	241 (28.4)	267 (31.5)	0.067	110 (28.0)	109 (27.7)	0.006	65 (34.4)	67 (35.4)	0.022
Subdural hematoma type									
Chronic, n (%)	272 (32.1)	283 (33.4)	0.028	106 (27.0)	110 (28.0)	0.023	48 (25.4)	45 (23.8)	0.037
Unspecified, n (%)	700 (82.5)	700 (82.5)	<0.001	336 (85.5)	315 (80.2)	0.142	178 (94.2)	180 (95.2)	0.047
Subacute, n (%)	101 (11.9)	106 (12.5)	0.018	52 (13.2)	56 (14.2)	0.030	14 (7.4)	17 (9.0)	0.058
Prior antithrombotic therapy									
Anticoagulants, n (%)	477 (56.3)	543 (64.0)	0.159	317 (80.7)	314 (79.9)	0.019	178 (94.2)	175 (92.6)	0.064
Antiplatelet agents, n (%)	710 (83.7)	711 (83.8)	0.003	308 (78.4)	309 (78.6)	0.006	101 (53.4)	107 (56.6)	0.064

Data presented as n (%) for categorical variables and mean ± standard deviation for continuous variables. SMD = standardized mean difference. Values represent post-matching cohorts for each timing comparison vs. no antithrombotic therapy control group. *Antithrombotic medications included: aspirin, clopidogrel, warfarin, rivaroxaban, apixaban, dabigatran, ticagrelor, prasugrel, and dipyridamole.*

Table 2. Clinical Outcomes by Antithrombotic Therapy Timing After cSDH Surgery

Comparison	Mortality, n (%)	Mortality OR (95% CI)	P-value	Repeat Surgery, n (%)	Repeat Surgery OR (95% CI)	P-value
Within 7 days vs. none	156/848 (18.40) vs. 225/848 (26.50)	0.62 (0.50–0.79)	<0.001	66/848 (7.80) vs. 77/848 (9.10)	0.85 (0.60–1.19)	0.34
Within 7 days vs. 8–14 days	67/388 (17.30) vs. 75/388 (19.30)	0.87 (0.61–1.25)	0.46	38/388 (9.80) vs. 28/388 (7.20)	1.40 (0.84–2.32)	0.20
8–14 days vs. none	73/393 (18.60) vs. 99/393 (25.20)	0.68 (0.48–0.95)	0.025	29/393 (7.40) vs. 39/393 (9.90)	0.72 (0.44–1.20)	0.21
15–28 days vs. none	28/189 (14.80) vs. 47/189 (24.90)	0.53 (0.31–0.88)	0.014	Surgery outcome not reported	—	—

Data presented as n/N (%) for event rates. All comparisons use propensity score-matched cohorts. OR = odds ratio; CI = confidence interval; cSDH = chronic subdural hematoma.

638 Results of the QUANTI CNS Phase 3 Study: Efficacy and Safety of Gadoquatrane in Patients Undergoing Contrast-enhanced MRI of the CNS at Reduced Gadolinium Dose Compared to Macrocyclic GBCAs.

Benjamin P Liu MD[1], Alex Liu PhD[2], Mark A Klemens MD[3], Birte M Hofmann DVM[3], Petra Palkowitsch MD[3]

[1]Northwestern University Feinberg School of Medicine, Chicago, IL, USA. [2]Clinical Data & Analytics, Bayer Pharma R&D, Whippany, NJ, USA. [3]Bayer AG, Pharma, Radiology R&D, Berlin, Germany, Germany

Purpose

Gadoquatrane is a novel tetrameric macrocyclic gadolinium (Gd)-based contrast agent (GBCA) which exhibits high relaxivity. This characteristic allows for a reduction in the Gd dose for contrast-enhanced (CE) MRI while maintaining a similar signal intensity level compared to current macrocyclic GBCAs. The QUANTI CNS study is a phase 3 study investigating efficacy and safety of gadoquatrane, at a dose of 0.04 mmol gadolinium (Gd)/kg body weight (bw) compared to 0.1 mmol Gd/kg bw of macrocyclic GBCAs (gadobutrol, gadoterate meglumine and gadoteridol) in CE-MRI of the central nervous system (CNS) in adults.

Materials & Methods

QUANTI CNS is a multicenter, randomized, prospective double-blind, cross-over study, conducted between July 2023 and May 2024 in 15 countries. Adult patients with known or suspected CNS pathology underwent two CE-MRIs, one with gadoquatrane and the other with a comparator GBCA, administered in random order with a washout period of 3 to 14 days in between. MRIs were evaluated in a blinded independent central review by three neuroradiologists. Safety parameters, such as adverse events and laboratory parameters, were assessed for both MRI periods.

Results

Out of 303 patients receiving at least one contrast administration, 294 completed both MRIs. Among these participants, 58% were female, and the mean age was 55.5 years. The study met the primary objectives by showing combined (pre-and post-contrast) gadoquatrane MRI to be non-inferior to combined comparator MRI and superior to pre-contrast MRI, based on the three visualization parameters: contrast enhancement, delineation, and morphology.

The mean scores vs. combined comparator MRI for all three parameters and three readers were similar with differences close to zero and below the non-inferiority margin of 0.35. Combined gadoquatrane MRI demonstrated significant improvements in all visualization parameters compared to pre-contrast images ($p < .0001$) for all three readers. The key secondary endpoints, sensitivity and specificity for the detection of lesions, were shown to be non-inferior to comparator MRI.

The safety profile (adverse events (AEs), serious AEs, safety parameters) was similar for gadoquatrane and comparators.

Conclusion

Gadoquatrane at a dose of 0.04 mmol Gd/kg bw, which corresponds to a 60% reduced gadolinium dose compared to GBCA at 0.1 mmol Gd/kg bw, is non-inferior for CE-MRI of the CNS with a similar safety profile and is superior to pre-contrast MRI.

References

1. Lohrke J, Berger M, Frenzel T, et al. Preclinical profile of gadoquatrane: a novel tetrameric, macrocyclic high relaxivity gadolinium-based contrast agent. Invest Radiol 2022;57(10):629–638. doi:10.1097/RLI.0000000000000889.

2. Hofmann BM, Riecke K, Klein S, et al. Pharmacokinetics, safety, and tolerability of the novel tetrameric, high-relaxivity, macrocyclic gadolinium-based contrast agent gadoquatrane in healthy adults. Invest Radiol 2024;59(2):140–149. doi:10.1097/RLI.0000000000001043.

3. Hofmann BM, Riecke K, Klein S, et al. Relationship of dose and signal enhancement properties of gadoquatrane, a new tetrameric, macrocyclic gadolinium-based contrast agent, compared with gadobutrol: A randomized crossover study in healthy adults. Invest Radiol 2024. doi:10.1097/RLI.0000000000001098.

Images/Tables

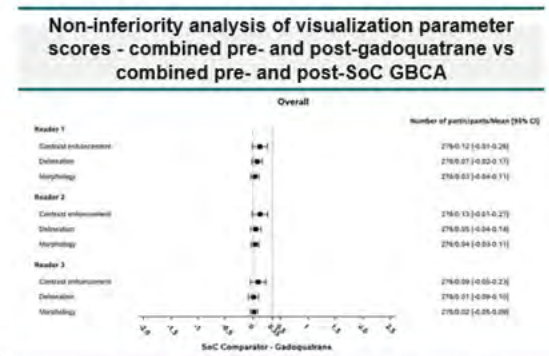

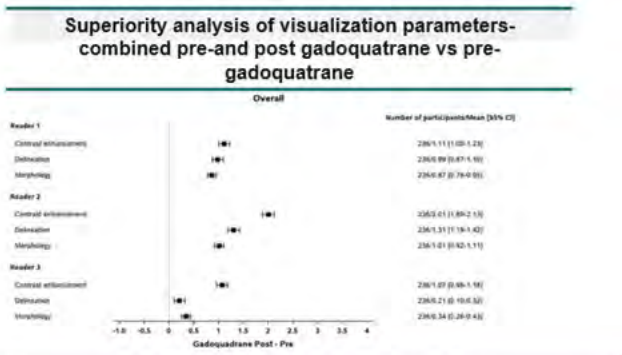

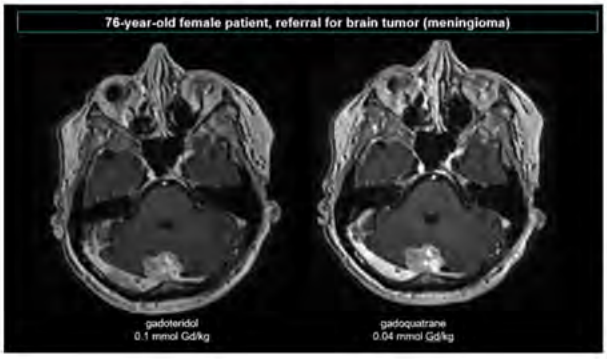

667 Quantitative Histogram-Based MRI Biomarkers Distinguish IDH-Mutant from IDH-Wild-Type High-Grade Gliomas

Archith Rajan PhD[1], Ajay Kumar MD,PhD[1], Stephen Bagley MD,MSCE[2], Richard Phillips MD, PhD[3], Lisa Desiderio RT (R) (MR) CCRC[1], Steven Brem MD[4], Laurie A. Loevner MD[1], Suyash Mohan MD[1], Sanjeev Chawla PhD[1]

[1]Division of Neuroradiology, Department of Radiology, Perelman School of Medicine at the University of Pennsylvania, Philadelphia, Pennsylvania, USA. [2]Abramson Cancer Center, Perelman School of Medicine at the University of Pennsylvania, Philadelphia, Pennsylvania, USA. [3]Department of Neurology, Perelman School of Medicine, University of Pennsylvania, Philadelphia, PA, USA. [4]Department of Neurosurgery, Perelman School of Medicine at the University of Pennsylvania, Philadelphia, Pennsylvania, USA

Purpose

Isocitrate dehydrogenase (IDH) mutations serve as critical biomarkers in gliomas, influencing prognosis and therapeutic strategies, and are present in approximately 70% of WHO grade 2–3 gliomas and 10% of grade-4 gliomas (1). While the detection of 2-hydroxyglutarate (2-HG) via advanced MR spectroscopy has enabled non-invasive identification of IDH mutations, its clinical adoption remains limited due to variable metabolite expression and technical complexity (2). Alternative imaging biomarkers are therefore essential, particularly for distinguishing the rare yet clinically important IDH-mutant grade-4 astrocytoma (G-4-Astro) from its IDH-wild-type glioblastoma (GBM) counterparts. Conventional region-of-interest (ROI) analysis of diffusion and perfusion MRI has been tried (3), but it often fails to accurately reflect intratumoral heterogeneity, whereas histogram analysis may provide a superior spatial characterization (4,5). The purpose of the current study was to investigate the potential of histogram analysis of diffusion tensor imaging (DTI) and dynamic-susceptibility contrast-perfusion weighted imaging (DSC-PWI) derived parameters in differentiating G-4-Astro from GBM.

Materials & Methods

A cohort of 51 treatment-naïve patients (14 G-4-Astro; 37 GBM) underwent 3T MRI, including DTI and DSC-PWI. Imaging parameters—mean diffusivity (MD), fractional anisotropy (FA), linear (CL), planar (CP), and spherical (CS) anisotropy, and normalized cerebral blood volume (rCBV)—were extracted from contrast-enhancing tumor regions. The representative anatomical images, DTI and DSC-PWI-derived parameters, histology, and immunohistochemistry from a G-4-Astro and GBM are shown in **Figure A**. Histogram analysis was performed using five statistical descriptors (mean, variance, skewness, kurtosis, and median), resulting in 30 quantitative features. Group differences were assessed using Mann–Whitney U-tests ($p < 0.05$), with significant features entered into a multivariate logistic regression model and evaluated via ROC analysis.

Results

The histogram profiles for the imaging parameters are shown in **Figure B**. Several histogram features, including kurtosis of rCBV, skewness, and median of rCBV and MD, significantly differentiated G-4-Astro from GBM. The best logistic regression model included the following features: kurtosis: rCBV, MD; skewness: MD, rCBV; median: MD, CP, rCBV. An area under the curve (AUC) of 0.86 was achieved, with a sensitivity of 72% and specificity of 87% (**Figure C**), indicating robust classification performance.

Conclusion

Multiparametric histogram analysis of DTI and DSC-PWI data offers a promising, non-invasive approach to distinguish IDH-mutant grade-4 astrocytomas from IDH-wild-type GBMs. By capturing tumor microstructural and perfusion heterogeneity, this method holds potential for improving diagnostic precision and informing targeted therapeutic strategies.

References

1. Yan H, Parsons DW, Jin G, et al. IDH1 and IDH2 mutations in gliomas. N Engl J Med. 2009 Feb 19;360(8):765-73.
2. Natsumeda M, Igarashi H, Motohashi K, et al. Advances and Challenges in Assessing 2-Hydroxyglutarate in Gliomas by Magnetic Resonance Spectroscopy: A Short Review. Neuropsychiatry (London) 2018; 8(6): 1831-1838.
3. Xing Z, Yang X, She D, et al. Noninvasive Assessment of IDH Mutational Status in World Health Organization Grade II and III Astrocytomas Using DWI and DSC-PWI Combined with Conventional MR Imaging. Am J Neuroradiol. 2017 Jun;38(6):1138-1144.
4. Law M, Young R, Babb J, et al. Histogram analysis versus region of interest analysis of dynamic susceptibility contrast perfusion MR imaging data in the grading of cerebral gliomas. Am J Neuroradiol. 2007 Apr;28(4):761-6.
5. Just N. Improving tumour heterogeneity MRI assessment with histograms. Br J Cancer. 2014 Dec 9;111(12):2205-13.

Images/Tables

Figure: Representative MRI, histology, and immunohistochemistry in
profiles from an IDH mutant grade-4 Astrocytoma and an IDH-wild
from the multivariate logistic regression model (C)

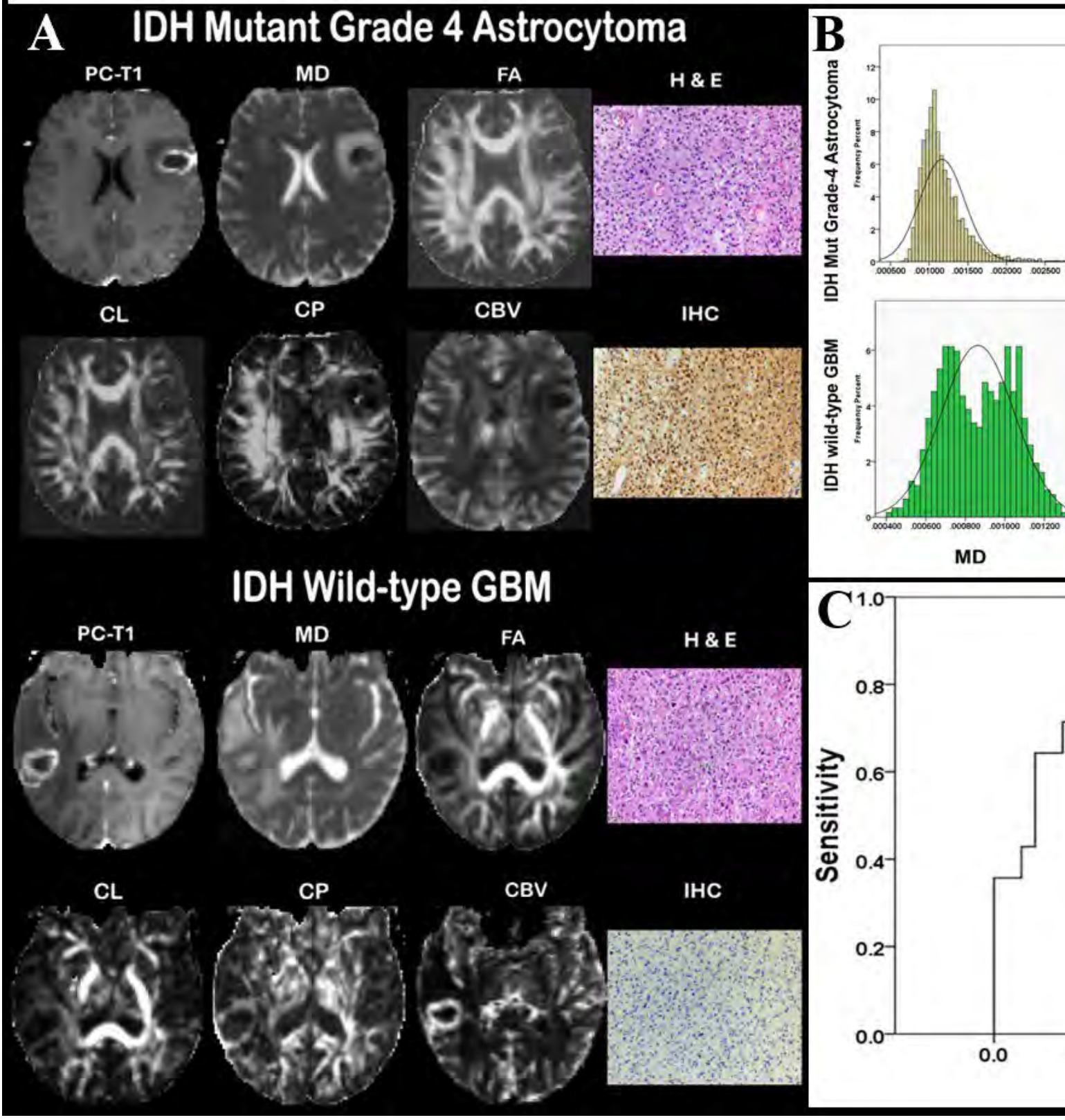

673 **Longitudinal MRI Characterization of Amyloid-Related Imaging Abnormalities Following Lecanemab Discontinuation: Temporal Evolution and Genotype-Specific Patterns**

Hana Farzaneh MD[1], Christina Younan BS[1], Esteban Calle MD[1], Saurabh Rohatgi MD[1], Jeremy N Ford MD, MS, MBA[1], Zhu Shenghua MD, PhD[1], Nima Omid-Fard MD[1], Maryam Vejdani jahromi MD, PhD[1], Odette Ganem[1], Chelsea B. Scott MSc[2], Rafael Martinez MD[1], Marvin Relerford BS[1], Javier Romero MD[1]

[1]Mass General Hospital, Boston, MA, USA. [2]University of Virginia School of Medicine, Charlottesville, VA, USA

Purpose

To delineate the temporal progression of Amyloid-Related Imaging Abnormalities (ARIA-E and ARIA-H) following the cessation of lecanemab in patients with Alzheimer's disease (AD), utilizing longitudinal MRI, with a focus on volumetric regression and hemorrhagic progression across APOE genotypes.

Materials & Methods

This IRB-approved retrospective study included 16 consecutive AD patients who discontinued lecanemab after ARIA-E detection. MRIs were obtained at baseline, at ARIA-E onset, and during two follow-up scans (~2 months after discontinuation). ARIA-E lesions were manually segmented on 3D FLAIR for volumetric analysis. ARIA-H microhemorrhages and superficial siderosis were assessed using susceptibility-weighted imaging (SWI) and gradient-echo (GRE) sequences. Non-parametric bootstrapping (10,000 iterations) generated 95% confidence intervals (CIs) for changes in lesion volume and count, stratified by APOE genotype.

Results

After stopping treatment, ARIA-E volumes significantly decreased. By the second follow-up, 9 of 16 patients (56.3%) experienced complete resolution. The average percentage change in ARIA-E volume from the initial ARIA-positive state to the first follow-up was −52.1% (95% CI, −84.4 to +23.0); from the first to the second follow-up, it was −86.5% (95% CI, −94.1 to −72.1); overall, the total reduction was −94.6% (95% CI, −99.0 to −79.7). Carriers of the APOE ε4/ε4 genotype had a higher initial edema burden and slower recovery. ARIA-H was observed in 10 patients (62.5%), mainly between detection and the first follow-up, and superficial siderosis was seen in 7 patients (43.8%).

Conclusion

ARIA-E regresses substantially after lecanemab discontinuation, with 95% ARIA-E volume reduction and the majority of patients (56.3%) achieving complete resolution within two months. APOE ε4 carriage is linked to greater edema burden and slower recovery. The temporal overlap between ARIA-E regression and new ARIA-H suggests ARIA-H may represent a downstream phenomenon, highlighting the need for ongoing post-treatment imaging surveillance.

References

Hampel, H., et al., Amyloid-related imaging abnormalities (ARIA): radiological, biological and clinical characteristics. Brain, 2023. 146(11): p. 4414-4424.

Images/Tables

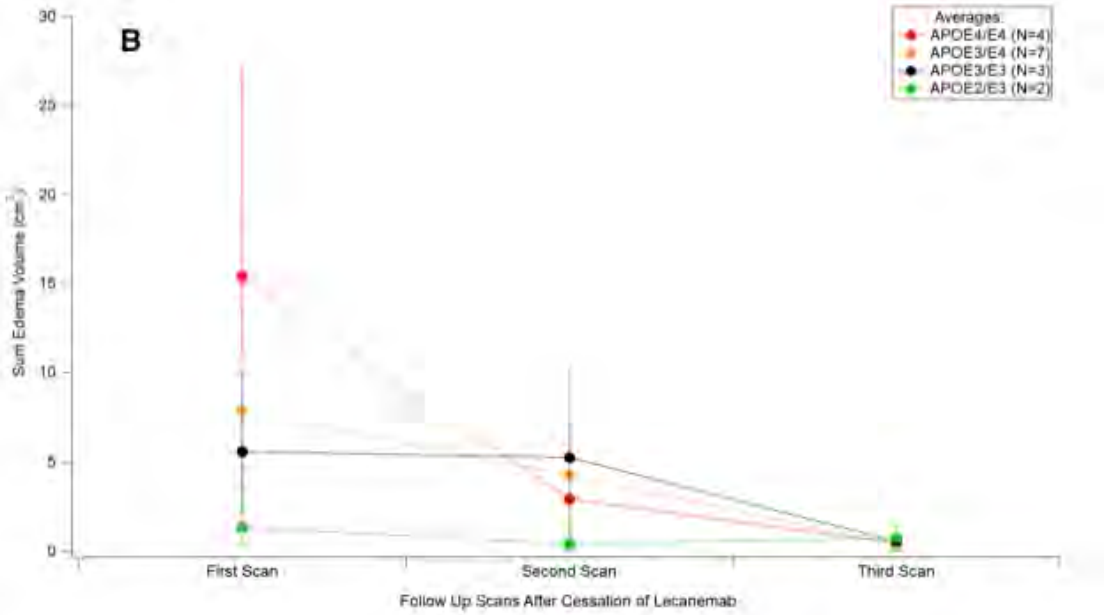

Figure: ARIA-E Volume Trajectories Following Lecanemab Discontinuation

(A) Individual ARIA-E lesion volumes (cm^3) across three consecutive 3D FLAIR scans (n=16). Black lines denote individual trajectories; the red line indicates the group mean with shading representing the standard error. The first, second, and third scans represent ARIA-E detection, first follow up, and second follow-up, respectively. (B) Mean ARIA-E volumes stratified by APOE genotype: ε4/4 (n=4, red), ε3/4 (n=7, orange), ε3/3 (n=3, black), and ε2/3 (n=2, green). Error bars indicate the standard error of the mean.

675 Visceral Fat and Insulin Resistance as Predictors of Cerebral Blood Flow in Midlife: Insights from Arterial Spin Labeling

Soheil Mohammadi[1], Mahsa Dolatshahi[1], Paul K. Commean[1], Weiying Dai[2], Farzaneh Rahmani[1], LaKisha Lloyd[1], Mahshid Naghashzadeh[1], Mobina Amanollahi[1], Mona Mirbeyk[1], Bettina Mittendorfer[3], Claude B. Sirlin[4], Tammie L.S. Benzinger[1], Joseph E. Ippolito[1], John C. Morris[5], Cyrus A. Raji[1]
[1]Mallinckrodt Institute of Radiology, Washington University in St. Louis, St. Louis, MO, USA. [2]Binghamton University, New York, New York, USA. [3]Departments of Medicine and Nutrition & Exercise Physiology, University of Missouri, School of Medicine,, Colombia, MO, USA. [4]Liver Imaging Group, Department of Radiology, University of California-San Diego, San Diego, CA, USA. [5]Department of Neurology, Washington University in St. Louis, St. Louis, MO, USA

Purpose

Midlife obesity and increased adiposity are well-established risk factors for Alzheimer's disease (AD)[1], with vascular dysfunction and reduced cerebral perfusion contributing to neurodegeneration in AD. This study aimed to investigate the relationships between body mass index (BMI), abdominal visceral adipose tissue (VAT), subcutaneous adipose tissue (SAT), waist circumference, triglycerides (TG), high-density lipoprotein (HDL), low-density lipoprotein (LDL), cholesterol-to-HDL ratio, insulin resistance, and HbA1C with cerebral blood flow (CBF) in cognitively normal, middle-aged individuals.

Materials & Methods

A total of 87 cognitively normal, middle-aged adults (mean age 49.97 years; 66.7% female; 55.2% with obesity; mean BMI 31.65 kg/m^2) underwent abdominal and brain MRI, brain PET, and metabolic assessments. Cerebral blood flow (CBF) was measured using a 3D pseudo-continuous arterial spin labeling (pCASL) sequence with a single post-labeling delay of 2.025 seconds. ASL difference and absolute CBF (aCBF) maps were generated in SPM12 using a single-compartment model, co-registered to gray matter segmentations, normalized to MNI space, and spatially smoothed with a 6 mm FWHM Gaussian kernel. Region-of-interest (ROI) masks for the amygdala, hippocampus, posterior cingulate, precuneus, parahippocampal, medial orbitofrontal, middle temporal, and calcarine cortices were created using the AAL3 atlas in MATLAB and applied to the aCBF maps. Multiple linear regression analyses were performed to examine associations between metabolic metrics and aCBF. Mediation analyses tested whether HDL, triglycerides, or HOMA-IR mediated the relationship between BMI and aCBF. Voxel-wise analyses were also conducted using metabolic metrics as independent predictors. All analyses were adjusted for age and corrected for multiple comparisons using the false discovery rate (FDR) method.

Results

Higher BMI, VAT, triglycerides, and HOMA-IR were consistently linked to lower CBF in multiple regions, including the hippocampus, amygdala, calcarine cortex, middle temporal gyrus, and posterior cingulate. In contrast, higher HDL levels were positively associated with aCBF in these areas. SAT, waist circumference, and LDL showed no significant associations with aCBF (Table 1). Mediation analyses indicated that the relationship between BMI and aCBF, both globally and within ROIs, was significantly mediated by triglycerides, HDL, and HOMA-IR (Table 2). Voxel-wise analyses revealed that higher BMI, waist circumference, VAT, cholesterol-to-HDL ratio, HbA1C, and HOMA-IR were associated with lower aCBF, whereas higher HDL was linked to higher aCBF in clusters across the temporal, occipital, and frontal lobes, after correction for false discovery rate (Figures 1–3).

Conclusion

Obesity and increased VAT are associated with reduced cerebral blood flow in both the whole brain and AD-related regions of interest. These findings highlight the impact of obesity, particularly visceral fat, on brain hypoperfusion and its potential contribution to increased AD risk beginning in midlife. The results indicate that aCBF is influenced by insulin resistance and obesity, specifically driven by VAT rather than SAT. Moreover, given HDL's mediating role in the relationship between BMI and aCBF, it is plausible that obesity contributes to reduced cerebral perfusion through atherosclerotic mechanisms.

References

1. Livingston G, Huntley J, Liu KY, et al. Dementia prevention, intervention, and care: 2024 report of the Lancet standing Commission. *Lancet* 2024; **404**(10452): 572-628.

Images/Tables

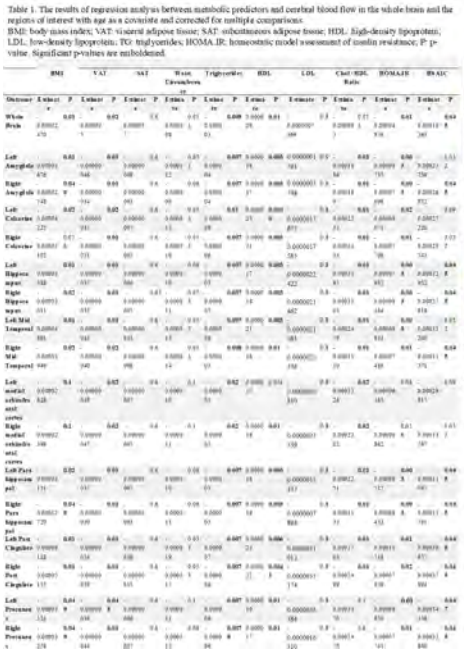

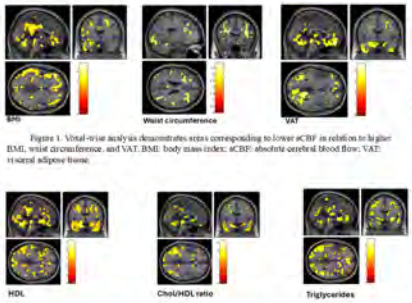

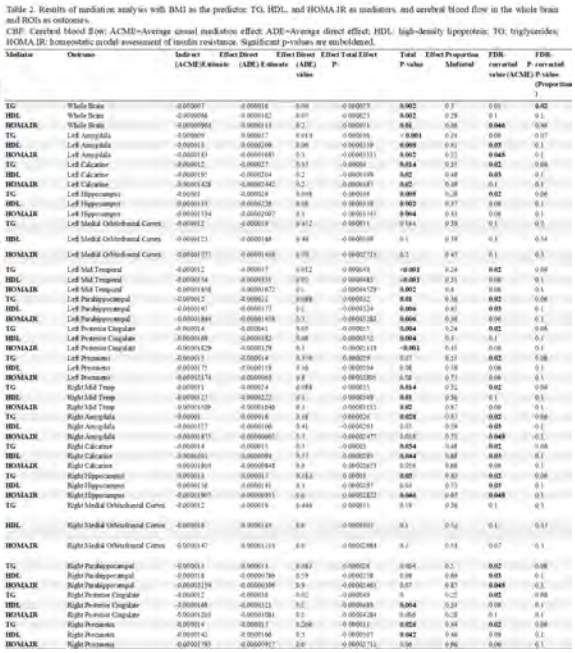

677 Systematic Evaluation of the MELD Graph Pipeline: A Deep Learning Framework for MRI-Based Detection of Focal Cortical Dysplasia

Mateus A Esmeraldo MD[1], Stefanie Chambers MD[2], Yanniklas Kravutske MD[2], Eduardo P Reis MD[1], Gregor Kasprian MD[2], Bruno P Soares MD[1]
[1]Stanford University, Stanford, CA, USA. [2]Medical University of Vienna, Vienna, Vienna, Austria

Purpose

Focal cortical dysplasia (FCD) is one of the most common causes of drug-resistant focal epilepsy in children and a leading indication for epilepsy surgery [1]. Early and accurate lesion detection is critical for favorable surgical outcomes, however, lesions are often subtle and difficult to identify on imaging. Artificial intelligence tools such as the multicenter MELD Graph algorithm have shown promising results in this task, achieving 72% sensitivity and 56% specificity in FCD detection and providing interpretable, user-friendly reports [2]. However, AI models often face challenges when translated into routine clinical practice, particularly due to limited performance in heterogeneous real-world data. Based on our institutional experience, a significant proportion of missed cases and false positives appear to result from pipeline errors, such as inadequate cortical identification and segmentation, rather than solely from failures of the FCD detection algorithm. In this context, the present study aims to conduct a critical evaluation and error analysis of the newly released MELD Graph algorithm [2].

Materials & Methods

A total of 64 subjects were analyzed, including 32 patients with histologically confirmed focal cortical dysplasia (FCD) type II and 32 controls, obtained from two publicly available presurgical MRI datasets [3,4]. All subjects had 3D T1-weighted images available, and 3D T2-FLAIR images were available for 36 subjects (14 patients and 22 controls). The remaining 2D FLAIR scans were excluded due to incompatibility with the MELD Graph pipeline. Expert-curated lesion masks provided within the open datasets served as the ground truth. To simulate real-world application, the MELD Graph pipeline was applied without data harmonization, retraining, or parameter adjustment. Each case was carefully visually inspected by a neuroradiologist using the original images and the preprocessing files to identify potential errors in the processing steps performed by FreeSurfer [5], which is part of the MELD Graph pipeline.

Results

Error analysis identified 8 false-positive and 6 false-negative cases among the 32 patients with FCD. Of these 14 total errors, 10 (71%) were due to algorithmic limitations, and 4 (29%) resulted from cortical segmentation errors by FreeSurfer. In controls, 24 of 25 false positives (96%) arose from algorithmic limitations, and 1 of 25 (4%) from a FreeSurfer segmentation error. No errors were clearly related to image quality or to preprocessing issues other than segmentation. Regional analysis revealed that in patients, 6 of 10 failures (60%) were localized to the temporal lobe, of which 3 (50%) were attributable to FreeSurfer segmentation failures; in controls, 15 of 25 false positives (60%) were also located in the temporal lobe, including one FreeSurfer-related segmentation failure (Figure 1).

Conclusion

Most MELD Graph failures were attributable to algorithmic limitations, but a substantial proportion in the patient group (29%) were linked to FreeSurfer segmentation errors. These findings highlight that segmentation problems are a meaningful and underrecognized contributor to MELD Graph's overall error profile. Targeted improvements to the FreeSurfer cortical identification or the adoption of modern cortical segmentation methods leveraging deep learning could significantly enhance FCD detection.

References

1. Walger L, Schmitz MH, Bauer T, et al. A public benchmark for human performance in the detection of focal cortical dysplasia. Epilepsia Open. 2025;10(3):778-786. doi:10.1002/epi4.70028
2. Ripart M, Spitzer H, Williams LZJ, et al. Detection of Epileptogenic Focal Cortical Dysplasia Using Graph Neural Networks: A MELD Study. JAMA Neurol. Published online February 24, 2025. doi:10.1001/jamaneurol.2024.5406
3. Taylor PN, Wang Y, Simpson C, et al. The Imaging Database for Epilepsy And Surgery (IDEAS). Epilepsia. 2025;66(2):471-481. doi:10.1111/epi.18192
4. Schuch F, Walger L, Schmitz M, et al. An open presurgery MRI dataset of people with epilepsy and focal cortical dysplasia type II. Sci Data. 2023;10(1):475. Published 2023 Jul 20. doi:10.1038/s41597-023-02386-7
5. Fischl B. (2012). FreeSurfer. NeuroImage, 62(2), 774–781. https://doi.org/10.1016/j.neuroimage.2012.01.021

Images/Tables

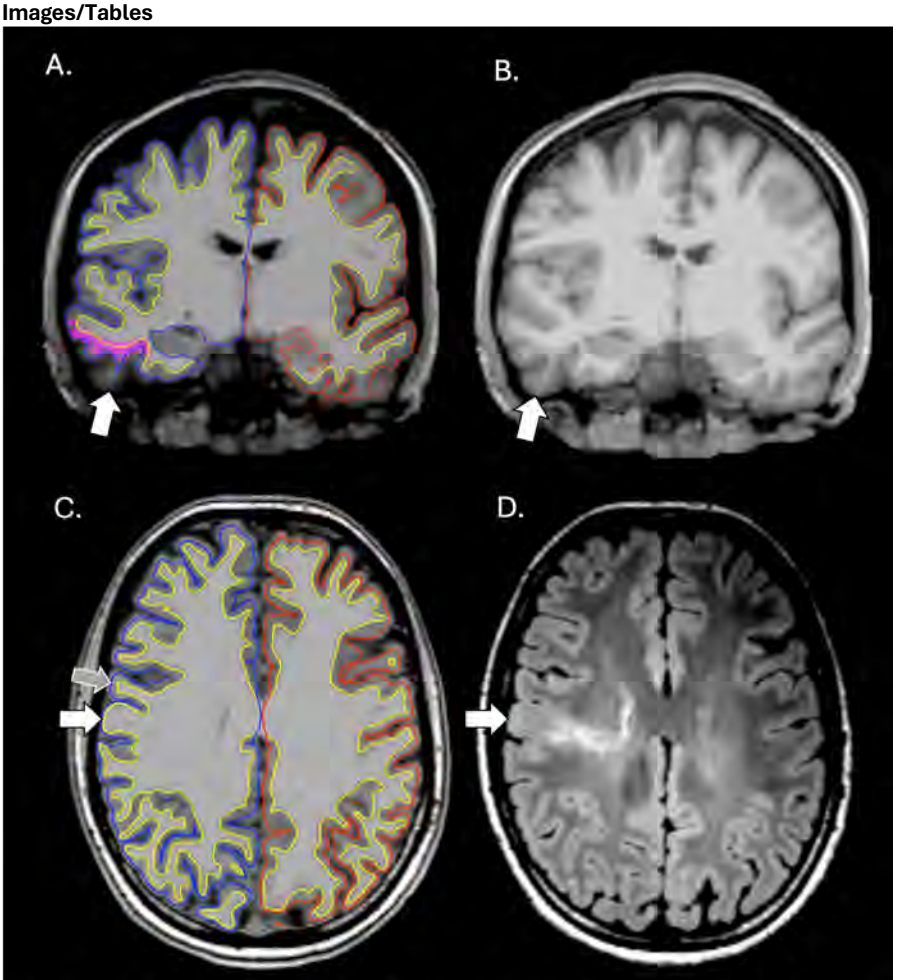

Figure: Example of cortical segmentation errors by FreeSurfer. (A) Coronal T1-weighted MR image showing segmented pial (blue, right hemisphere; red, left hemisphere) and white matter (yellow) surfaces generated by FreeSurfer. The white arrow indicates a segmentation failure of the cortical ribbon in the inferior temporal region of the right temporal lobe, resulting in an incorrect prediction of a cluster suspected of focal cortical dysplasia (FCD) by MELD Graph (purple). (B) Corresponding T1-weighted image without segmentation overlays, shown for anatomical reference. (C) The white arrow highlights extension of the predicted white matter surface (yellow) to the outer margin of a dysplastic gyrus. Because the cortex is defined as the region between the white matter (yellow) and pial (blue) surfaces, the dysplastic cortex was excluded from the cortical segmentation, preventing analysis by MELD Graph. The gray arrow indicates an adjacent normal gyrus that was properly segmented. (D) Corresponding FLAIR image showing the dysplastic gyrus (arrow) with blurring of the gray–white matter junction and a subcortical white matter hyperintensity extending toward the ventricular margin, consistent with the transmantle sign, classically linked to focal cortical dysplasia type IIb.

703 Amyloid–Tau Dissociation Patterns: Insights from Correlative Tau PET and Centiloid Analysis in a Single-Center Cohort

Ghazal Shadmani MD
Washington University in Saint Louis, Saint Louis, MO, USA

Purpose

To evaluate the relationship between tau PET uptake characteristics—both semi-quantitative intensity Standardized Uptake Value (SUV) and spatial extent—and β-amyloid burden as measured by Centiloid scores from amyloid PET.

Materials & Methods

Eighty-four consecutive patients (mean age 74.9 ± 6.2 years; 43 men, 41 women) underwent tau PET imaging at a single tertiary center. Each study was visually categorized as *Negative*, *Weakly positive*, or *Positive*. For every case, the highest standardized uptake value (SUV) and the extent of cortical tau involvement (number of regions with uptake) were recorded.

Centiloid scores, reflecting quantitative β-amyloid deposition from amyloid PET, were available for a subset of 27 patients who underwent corresponding amyloid imaging.

Pearson correlation analyses assessed relationships among SUV, extent of uptake, and Centiloid score. Descriptive statistics were used to characterize concordant and discordant amyloid/tau patterns, and group means were compared across visual categories.

Results

SUV and extent of tau uptake increased progressively from *negative* to *weakly positive* to *positive* visual categories.

In the subset with amyloid quantification, both SUV ($r = 0.55$) and extent of involvement ($r = 0.50$) correlated positively with Centiloid score, indicating that higher tau uptake intensity and wider distribution were associated with greater β-amyloid burden.

Importantly, four patients (15%) exhibited elevated Centiloid scores (> 20; mean 77.6 ± 20.1, range 47.7–96.9) despite negative tau PET, representing an amyloid-positive/tau-negative ($A^{+}T^{-}$) pattern consistent with pre-tangle amyloid accumulation preceding measurable cortical tau deposition.

No significant associations were found between age or sex and any imaging metric.

Conclusion

Greater tau PET uptake in both intensity and extent correlates with β-amyloid Centiloid burden, reinforcing the interconnected progression of amyloid and tau pathology. The identification of a distinct amyloid-positive/tau-negative subgroup underscores the early sequence of amyloid accumulation and may represent a target window for disease-modifying therapy and longitudinal biomarker tracking.

References

1.Jack CR Jr, Bennett DA, Blennow K, et al. NIA-AA Research Framework: toward a biological definition of Alzheimer's disease. *Alzheimer's Dement* 2018;14:535–562.

2. Ossenkoppele R, Schonhaut DR, Schöll M, et al. Tau PET patterns mirror clinical and neuroanatomical variability in Alzheimer's disease. *Brain* 2016;139:1551–1567.

3. Pontecorvo MJ, Devous MD Sr, Kennedy I, et al. A multicenter longitudinal study of flortaucipir (18F) in normal aging, mild cognitive impairment, and Alzheimer's disease dementia. *J Nucl Med* 2019;60:561–569.

Images/Tables

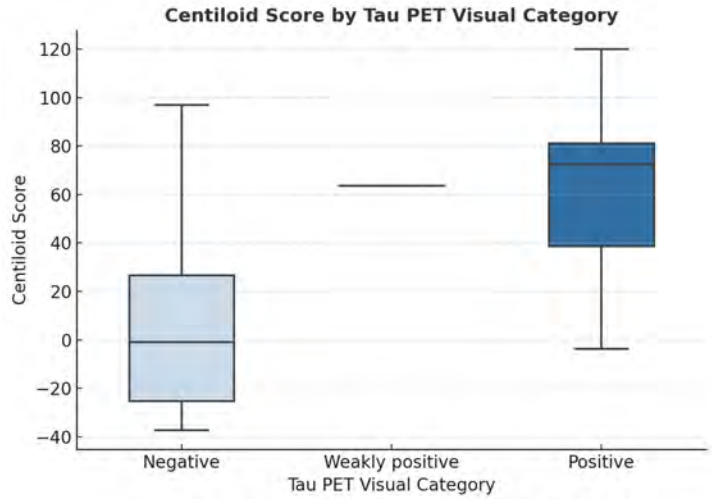

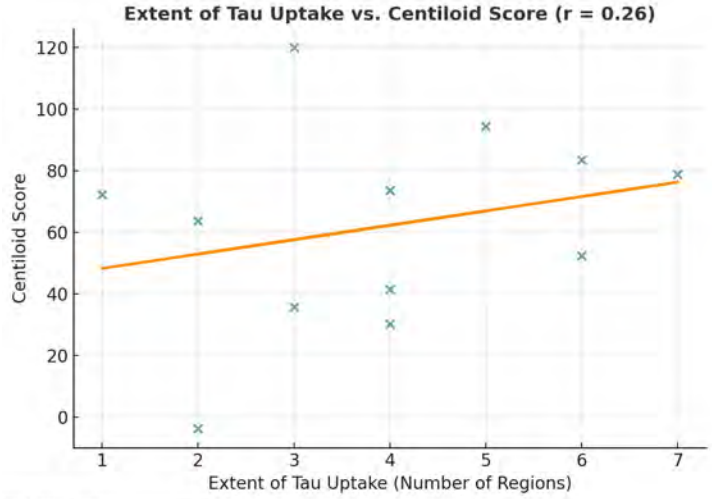

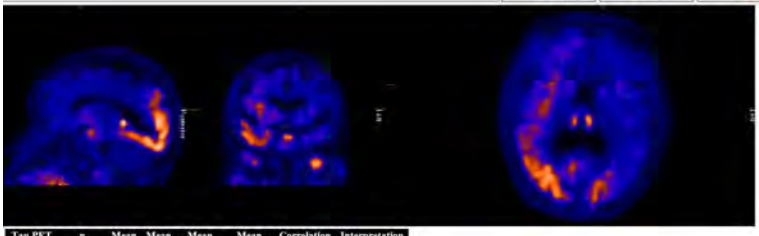

Tau PET Visual Category	n (Total)	Mean Age (y)	Mean SUV ± SD	Mean Extent (Regions ± SD)	Mean Centiloid ± SD	Correlation with Centiloid (r)	Interpretation / Notes
Negative	49	74.5 ± 6.1	0.0 ± 0.0	—	9.5 ± 45.6 (n=15)	—	Majority amyloid-negative; includes 4 **A⁺T⁺** cases with Centiloid 47.7–96.9
Weakly positive	2	73.8 ± 5.0	2.6 ± 0.1	2.0 ± 0.0	63.7 (n=1)	—	Low-level tau uptake, intermediate amyloid load
Positive	33	76.0 ± 6.5	2.4 ± 1.2	4.1 ± 1.8	61.8 ± 34.5 (n=11)	—	High tau intensity and extent, high β-amyloid burden
All Patients (n=84)	—	74.9 ± 6.2	1.0 ± 1.4	3.1 ± 1.9	—	**SUV–Centiloid:** r = 0.55 **Extent–Centiloid:** r = 0.50	Tau PET metrics correlate with β-amyloid load
A⁺T⁺ Subgroup	4 (15% of Centiloid subset)	74.0 ± 5.9	0.0 ± 0.0	—	77.6 ± **20.1 (range 47.7–96.9)**	—	**Amyloid-positive / Tau-negative:** pre-tangle amyloid accumulation (early AD)

734 Auto calculated cerebral fluid to brain volume ratio improve classification of cognitive impairment

Shin Ohno MD[1], Siavash Shirzadeh Barough MD[2], Abhay Moghekar MBSS[2], Haris Sair MD[2]
[1]Juntendo university, Bunkyo-ku, Tokyo, Japan. [2]Johns Hopkins School of Medicine, Baltimore, Maryland, USA

Purpose

There are several neuroimaging biomarkers for cognitive impairment, such as SPARE-AD and SPARE-BA[1]. In this study, we quantified the volumes of cerebral fissures and ventricle between the anterior and posterior commissures using a deep learning-based automated method and calculated the ratio of cerebral fluid (CF) volume to the brain volume.

Materials & Methods

2606 T1 MPRAGE Scans from Baltimore Longitudinal Study of Aging (BLSA) were preprocessed using N4 Bias Correction and then were registered to MNI152 space. BrainSignsNet model [2] was used to extract coordinates of anatomical landmarks including Anterior and Posterior Commissures (AC and PC) recognized and coronal slices between the two commissures were extracted for the subsequent analysis. In the segmentation phase, a UNet-based segmentation model generated a brain mask, a ventricle mask, bilateral Sylvian fissures masks, and mask of bilateral cerebral sulci superior to Sylvian fissure. Then, we calculated the ratio of CF volume to brain volume between AC and PC. We used t-tests and ANOVA for comparison of the ratio in different numerical variables, Pearson correlation and linear regression were used to evaluate the ratio with continuous variables like age and cognitive measures (MMSE) We compared the predictive performance of the ratio to that of SPARE-AD and SPARE-BA Using Root Mean Square Error (RMSE) We evaluated the accuracy of cognitive status classification using logistic regression.

Results

-Demographics

We extracted 1032 subjects with 2606 MRI scans. Mean age was 75.2 ± 11.6 (SD). Females were 556 (53.7%), and Male were 476 (46.3%). There were 2,064 cognitively normal individuals (at the time of scan), 277 with MCI, 228 with dementia, and 37 with cognitive impairment not classified as MCI or dementia.

-Statistical Associations of the composite ratio score

One-way ANOVA revealed significant differences in the ratio score across cognitive diagnostic groups ($F(3, 2872) = 166.28$, $p < 0.0001$). After adjusting for age and sex using ANCOVA, the group effect remained significant ($F(3, 2870) = 46.75$, $p < 0.0001$), indicating that the ratio robustly differentiates cognitive status.

Both age and sex were independently associated with the ratio score. Linear regression showed a strong positive association with age ($\beta = 0.0002$, $p < 0.0001$) and a significant sex effect, with females exhibiting a lower ratio than males ($\beta = -0.0028$, $p < 0.0001$). A Welch's *t*-test confirmed a significant sex difference in the ratio ($t = 18.15$, $p < 0.0001$).

-Predictive Performance

We next evaluated the predictive performance of the age and sex-adjusted ratio, in comparison to established neuroimaging biomarkers SPARE-AD and SPARE-BA, for both cognitive status classification and prediction of global cognition as measured by MMSE. For MMSE prediction using linear regression, the ratio explained 7.0% of the variance ($R^2 = 0.070$; RMSE = 1.605), outperforming both SPARE-AD ($R^2 = 0.058$; RMSE = 1.615) and SPARE-BA ($R^2 = 0.052$; RMSE = 1.620).

Conclusion

We developed a novel ratio reflecting brain atrophy. It showed a robust performance in predicting MMSE and cognitive status over traditional brain aging and atrophy markers, and potential to serve as another neuroimaging biomarker.

References

1. Davatzikos C, Bhatt P, Shaw LM, et al. Prediction of MCI to AD conversion, via MRI, CSF biomarkers, and pattern classification. Neurobiol Aging. 2011 Dec;32(12):2322.e19-27. DOI: 10.1016/j.neurobiolaging.2010.05.023.
2. Slavish Shirzadeh Barough, Catalina Ventura, View ORCID ProfileMurat Bilgel, et al. BrainSignsNET: Deep Learning-Based 3D Anatomical Landmark Detection in Human Brain Imaging. medRxiv. 2025 Aug. DOI: https://doi.org/10.1101/2025.07.31.25332457.

---

744 Per-Voxel Quantitative ADC Mapping of Large Core Infarction Following Mechanical Thrombectomy as a Measure of Infarct Depth

Lulu Bi BA[1], Xinye Yang BS[2], Zhicheng Jiao PhD[2], Grayson Baird PhD[2], Gnaneswari Karayi BA[1], Revyn Kim BA[1], David Hong BS[1], Miranda Gonzales BA[1], Joshua Feler MD[2], Radmehr Torabi MD[2], Krisztina Moldovan MD[2], Elias Shaaya MD[2], Mahesh V Jayaraman MD[2], Dylan N Wolman MD[2]
[1]The Warren Alpert Medical School of Brown University, Providence, RI, USA. [2]Rhode Island Hospital, Providence, RI, USA

Purpose

Mechanical thrombectomy (MT) is the standard of care for acute ischemic stroke (AIS) due to large vessel occlusion (LVO). Recent trials have demonstrated a surprising treatment effect of MT despite large ischemic cores (≥70 mL), leading to a paradigm shift in our estimation of residual function within the ischemic core.[1,2,3,4] We propose that one component of the treatment effect of MT in large ischemic core patients may be attributable to differences in the extent of infarction within affected tissue, or what we will term the *depth* of infarction, which traditional volumetric assessments alone fail to capture. Apparent diffusion coefficient (ADC) values are a per-voxel quantitative measure of diffusion restriction and are decreased in acute infarcts, with lower values potentially representing greater local cytotoxic or ionic edema. We therefore hypothesize that decreasing ADC values within the infarct bed may additively predict poorer long term neurologic outcomes alongside overall infarct volume in large core infarct patients.

Materials & Methods

We performed a retrospective review of a prospectively maintained thrombectomy database at a single comprehensive stroke center from 2022-2025. Inclusion criteria were AIS patients age>18 who underwent MT for anterior circulation LVO with a 24-hour post-thrombectomy DWI of sufficient quality for analysis. Clinical metrics were collected, including pre-procedure modified Rankin Scale (mRS) and 90-day mRS. DWI sequences for each patient were manually segmented to create an infarct map which was mirrored to the corresponding ADC sequence. Overall infarct volume and per-voxel ADC values were collated for each patient. mRS scores (0-6) were modeled by infarct volume and ADC values using generalized linear mixed modeling where observations were nested within patients with the SAS Software. Additionally, ADC values were binned (0-120, 121-220, 221-320, 321-420, 421-520, 521-620, 621-720, 721-820) and a color lookup table was applied for ease of visualization.

Results

A total of 98 patients were included, 38 with large core infarcts (71-100 cc) and 60 with very large core infarcts (>101 cc). As seen in Figure 1A, for every 100,000 cubic mm increase in infarct volume, the odds of a 1-point 90-day mRS increase were 3.03 (95%CI [1.11, 8.26], p=0.032). In addition, for every 1000 unit decrease in ADC values by volume, the odds of being in a higher 90-day mRS category increased by 3.6-fold (OR: 3.6, 95%CI [3.5, 3.72], p<0.0001; Figure 1B), but this effect was of lesser magnitude than volume alone (Figure 1C). When considering binned ADC values, the odds of a 1-point 90-day mRS increase were 3.7 (95% CI [3.6, 3.8] for bin 1 (0-120) compared to bin 8 (820), p<0.0001 (Figure 1D). Figure 2 demonstrates qualitative assessment of ADC heterogeneity by color mapping of the infarct within a selected patient.

Conclusion

While the effect of infarct volume predominated in this cohort enriched in very large infarct patients, per-voxel ADC mapping had a statistically significant but relatively minor contributory effect upon outcome prediction, with deeper infarction correlating to poorer outcomes. However, data truncation by our enriched dataset limits application of these findings to the entire spectrum of moderate to large ischemic core patients.

References

1. Bendszus M, Fiehler J, Subtil F, et al. Endovascular Thrombectomy for Acute Ischaemic Stroke with Established Large Infarct: Multicentre, Open-Label, Randomised Trial. *Lancet* 2023;402:1753–1763. DOI: 10.1016/S0140-6736(23)02032-9
2. Huo X, Ma G, Tong X, et al. Trial of Endovascular Therapy for Acute Ischemic Stroke with Large Infarct. *N Engl J Med* 2023;388:1272–1283. DOI: 10.1056/NEJMoa2213379
3. Sarraj A, Hassan AE, Abraham MG, et al. Trial of Endovascular Thrombectomy for Large Ischemic Strokes. *N Engl J Med* 2023;388:1259-1271. DOI: 10.1056/NEJMoa2214403
4. Yoshimura S, Sakai N, Yamagami H, et al. Endovascular Therapy for Acute Stroke with a Large Ischemic Region. *N Engl J Med* 2022;386:1303–1313. DOI: 10.1056/NEJMoa211819

Images/Tables

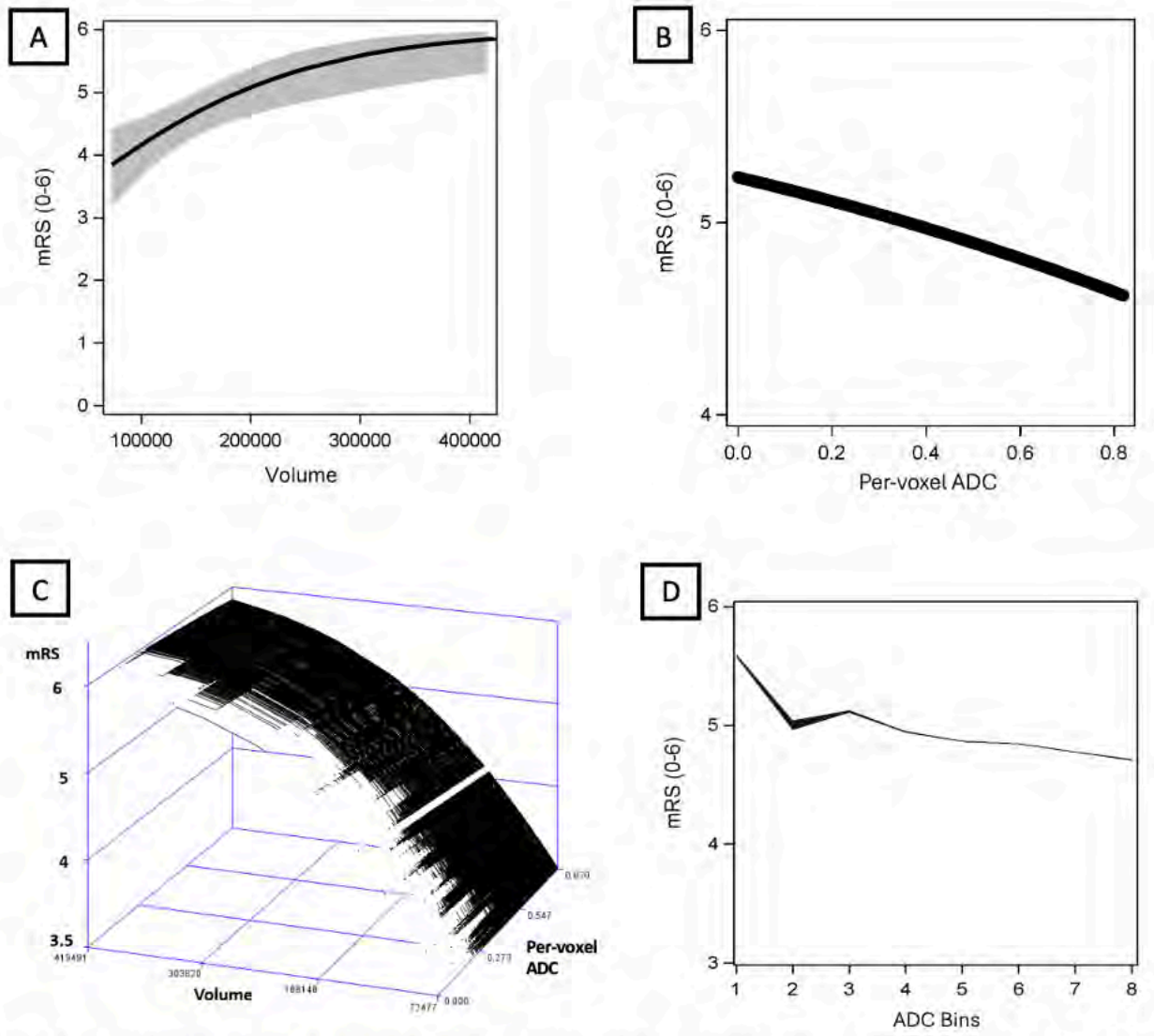

Figure 1. **A** demonstrates the association between overall infarct volume and 90-day mRS. **B** shows the association between per-voxel ADC values and 90-day mRS. **C** three-dimensionally plots the association between per-voxel ADC values, overall infarct volume, and 90-day mRS. **D** demonstrates the association between ADC bins and 90-day mRS.

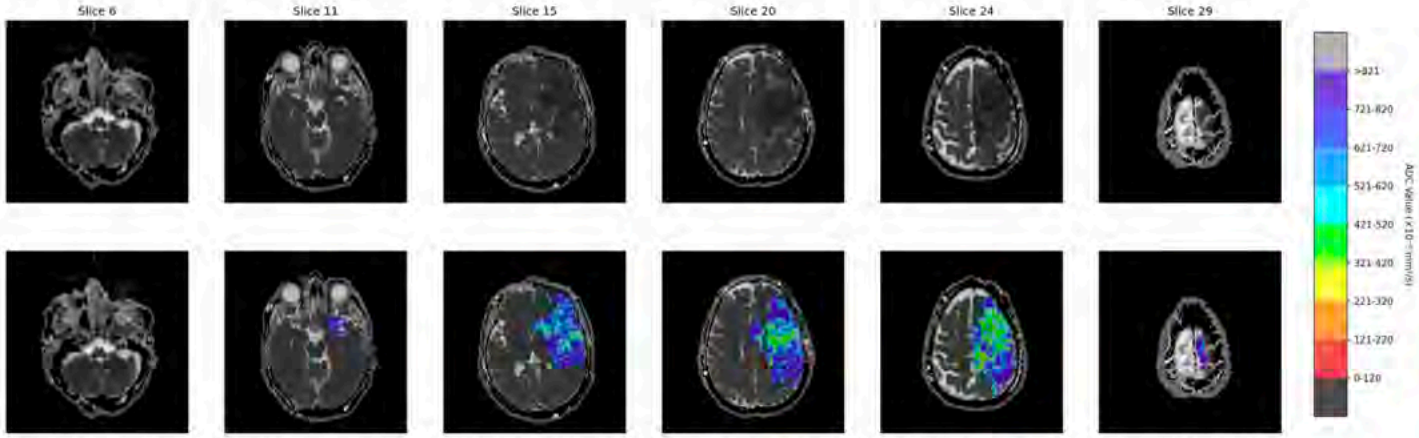

Figure 2. ADC color maps in a patient with a very large (>101cc) LVO, who had a 90-day mRS of 4.

785 Qualitative Evaluation of Distortion Correction and Deep Learning-based Phase Correction for DW-MRI in Head and Neck Cancers

Jaemin Shin PhD[1], Ramesh Paudyal PhD[2], Vaios Hatzoglou MD[2], Suchandrima Banerjee PhD[3], Eve LoCastro MS[2], Maggie Fung MS[1], Muhammad Awais PhD[2], Nancy Lee MD[2], Amita Shukla-Dave PhD[2]

[1]GE HealthCare, New York, NY, USA. [2]Memorial Sloan Kettering Cancer Center, New York, NY, USA. [3]GE HealthCare, Menlo Park, CA, USA

Purpose

Qualitative assessments of diffusion-weighted (DW) MRI enable tumor detection, characterization, and evaluation of treatment response in patients with head and neck (HN) cancer[1]. Motion and susceptibility artifacts are a challenge in HN MRI, leading to signal loss and distortion[2]. Previous studies reported that multishot (MUSE) DW-EPI enables higher resolution with reduced distortion over standard single-shot (SS)-EPI in the HN region[1,3], and that adding reverse polarity gradient (RPG) further reduces distortions[1]. AIR Recon DL (ARDL) reduces noise and Gibbs ringing[4], and a newly proposed DL-based phase correction (DLPC) enables robust complex averaging across shots[5-8]. This study qualitatively evaluates the efficacy of RPG-based distortion correction (DC) and the incremental effect of DLPC using three pipelines in multi-b-value MUSE DW-EPI of HN tumors.

Materials & Methods

Seventeen HN cancer patients (median age 59 years, 11M/6F) were retrospectively enrolled between July and October 2025 were enrolled. Standard T_1/T_2w imaging was followed by multishot Multiplexed Sensitivity Encoding (MUSE) DW-EPI on a 3 T MRI scanner (SIGNA Premier, GE Healthcare) using a 24-channel head and neck unit at post-trement. MUSE parameters were TR/TE=3000/60 (minimum) ms, the field of view=20-24 cm, matrix=128×128, slices=8-10, slice thickness=4mm, number of shots=2, number of excitation=2, and b=0,50,1000 s/mm^2. ARDL denoising was applied on complex MR data during reconstruction for all datasets. DLPC was applied to generate high quality phase maps for complex averaging[5,7]. RPG-based DC was applied to reconstructed images using displacement maps from dual-polarity images[9]. MUSE images were reconstructed in three sets using (1) baseline, (2) with RPG, and (3) with DLPC + RPG.

An experienced neuroradiologist rated image quality on a five-point scale (5 = excellent; 1 = unacceptable) as detailed else[1] . Signal-to-noise ratio (SNR) was calculated as μ/σ (μ = mean signal from the metastatic nodes; σ = background SD). Wilcoxon tests compared scores ($P < 0.05$).

Results

Ninety-six MUSE set (b = 0, 1000 s/mm^2) are reported (baseline n = 30; with RPG n = 32; with DLPC+RPG n = 34). Mean SNRs were 28 (baseline), 32 (with RPG), and 81 (with DLPC+RPG). Mean quality scores (±SD) were 2.73 ± 0.46 (baseline), 3.44 ± 0.73 (with RPG), and 4.24 ± 1.03 (with DLPC+RPG), with significant differences for both b-values ($P < 0.05$). The combined ARDL + DLPC with RPG achieved 53% excellent (5) and 29% good (4) ratings, whereas baseline scored 1-3. Representative images for three reconstructions are shown in Figure 1, and mean rating scores across both b-values are illustrated in Figure 2. Adding RPG increased mean scores by 31%, confirming the benefit of distortion correction. Adding DLPC further increased mean scores by 26%, indicating improved per-shot phase stabilization and complex averaging. Overall improvement with DLPC+RPG was 55% with a large SNR gain.

Conclusion

While ARDL improves SNR and sharpness, RPG provides substantial distortion correction and DLPC further improves phase stability and image quality. The combined ARDL + DLPC with RPG reduces artifacts, increases SNR, and yields predominantly excellent or good ratings across b-values, supporting more reliable HN tumor characterization and treatment monitoring.

References

1. Konar AS, Fung M, Paudyal R, Oh JH, Mazaheri Y, Hatzoglou V, Shukla-Dave A. Diffusion-weighted echo planar imaging using multiplexed sensitivity encoding and reverse polarity gradient in head and neck cancer: an initial study. Tomography. 2020;6(2):231.
2. Schakel T, Hoogduin JM, Terhaard CHJ, Philippens MEP. Technical Note: Diffusion-weighted MRI with minimal distortion in head-and-neck radiotherapy using a turbo spin echo acquisition method. Med Phys. Aug 2017;44(8):4188-4193. doi:10.1002/mp.12363
3. Chen NK, Guidon A, Chang HC, Song AW. A robust multi-shot scan strategy for high-resolution diffusion weighted MRI enabled by multiplexed sensitivity-encoding (MUSE). Neuroimage. May 15 2013;72:41-7. doi:10.1016/j.neuroimage.2013.01.038
4. Lebel RM. Performance characterization of a novel deep learning-based MR image reconstruction pipeline. arXiv preprint arXiv:200806559. 2020;
5. Wang X, Lan P, Wang K, Zhu A, Nastaren A, Guidon A. Deep Learning based Phase Correction and Denoising for Accurate ADC Quantification, 2025, Honolulu, HI, USA: ISMRM Annual Meeting; 4197.
6. Wang X, Litwiller D, Guidon A, et al. Robust Complex Signal Averaging for Diffusion Weighted Imaging, 2023, Toronto, Canada: ISMRM;3963.
7. Lan P, Wang X, Guidon A. Improved Brachial Plexus and C-Spine DTI using Deep Learning-based Phase Correction, 2025, Hawai'I, USA: ISMRM;2975
8. Chien N, Cho Y-H, Wang M-Y, et al. Deep learning based multi-shot breast diffusion MRI: Improving imaging quality and reduced distortion. European Journal of Radiology. 2025;193:112419. doi:10.1016/j.ejrad.2025.112419
9. Holland, Dominic, Joshua M. Kuperman, and Anders M. Dale. "Efficient correction of inhomogeneous static magnetic field-induced distortion in Echo Planar Imaging." Neuroimage 50, no. 1 (2010): 175-183.

Images/Tables

Figure 1.

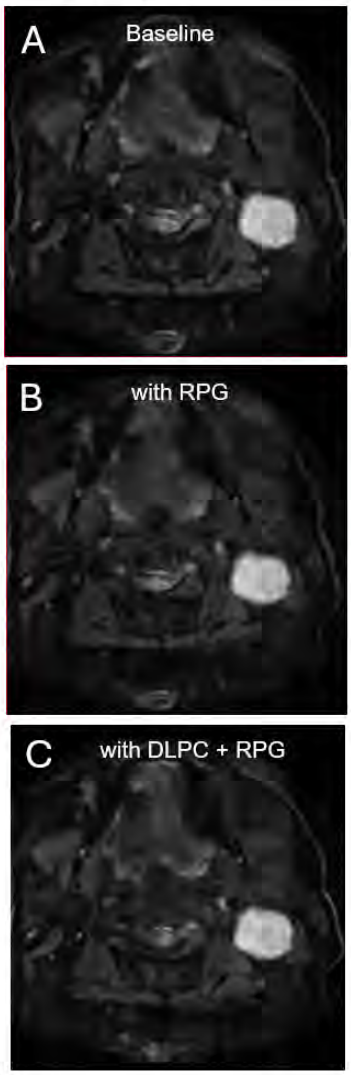

Table 1.

Diagnostic quality Image rating score	DW image b = 0 (s/mm^2)			DW image b = 1000 (s/mm^2)		
	A: Baseline	B: with RPG	C: with DLPC+RPG	A: Baseline	B: with RPG	C: with DLPC+RPG
Excellent (5)	0 (0%)	0 (0%)	9 (53%)	0(0%)	9 (56%)	9 (53%)
Good (4)	0 (0%)	9 (56%)	5 (29%)	0(0%)	5 (31%)	5 (29%)
Acceptable (3)	11 (73%)	5 (31%)	1 (6%)	11(73%)	1 (6%)	1 (6%)
Poor and unacceptable (2 and 1)	4 (27%)	2 (13%)	2 (26%)	4 (27%)	2 (13%)	2 (26%)

Figure 2.

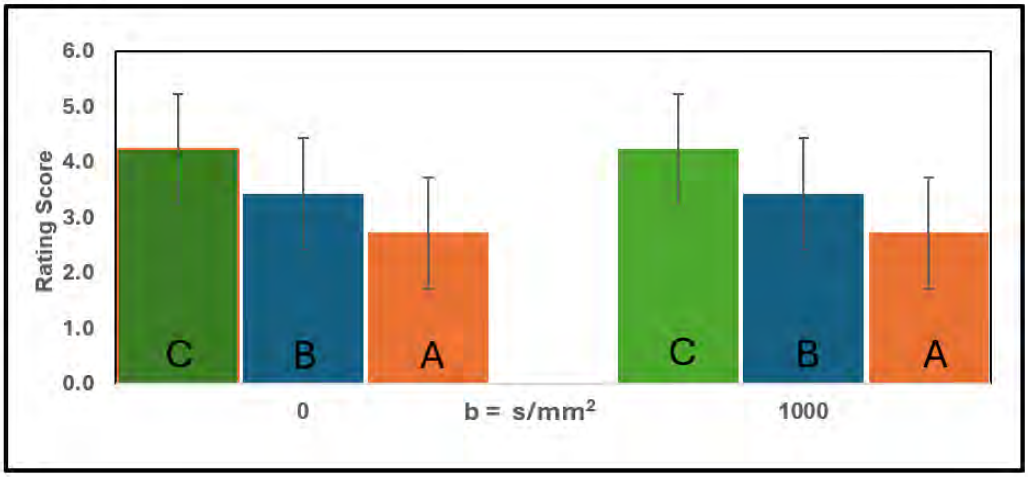

832 **A Systematic Review and Meta-analysis of Glymphatic Flow Impairment in Mild Cognitive Impairment Using Diffusion Tensor Imaging Along the Perivascular Space**

Sadegh Ghaderi PhD[1], Sana Mohammadi PhD[1], Ali Fathi Jouzdani MD[2], Amir Mahmoud Ahmadzadeh MD[3]

[1]Tehran University of Medical Sciences, Tehran, Tehran, Iran, Islamic Republic of. [2]Institute for Research in Fundamental Sciences, Tehran, Tehran, Iran, Islamic Republic of. [3]Mashhad University of Medical Sciences, Mashhad, Mashhad, Iran, Islamic Republic of

Purpose

The DTI-ALPS index is a non-invasive MRI biomarker used to assess glymphatic system function. Its utility in Mild Cognitive Impairment (MCI), a precursor to dementia, is emerging but requires consolidation. We aimed to systematically review and meta-analyze the literature to quantify the magnitude of glymphatic dysfunction (measured by the ALPS index) in MCI patients compared to healthy controls (HC).

Materials & Methods

A PRISMA-compliant search was conducted in four major databases (PubMed, Scopus, Embase, Web of Science) up to May 10, 2025. We included 18 studies that compared the DTI-ALPS index between MCI patients (n=1,133) and HCs (n=1,275). Data were pooled using a random-effects meta-analysis (Cohen's d). We performed sensitivity analyses, subgroup analyses (by age, diffusion directions), and comprehensive assessments of publication bias (Egger's test, Trim-and-fill) and study quality (NOS).

Results

The pooled meta-analysis of 18 studies (1,133 MCI patients, 1,275 HCs) revealed a significant, large reduction in the ALPS index in the MCI group (Cohen's d = −0.70; 95% CI: −1.10 to −0.29; p<0.001). This finding was robust in sensitivity analyses. High heterogeneity was present (I^2=95.3%). Subgroup analyses showed non-significant trends toward larger effect sizes in older patients (>68 years, d=−0.83) and studies using ≥64 diffusion directions (d=−0.99). Significant publication bias was detected (Egger's p=0.004).

Conclusion

Glymphatic dysfunction is a consistent feature of Mild Cognitive Impairment, detectable by a significantly reduced DTI-ALPS index. This meta-analysis supports the ALPS index as a non-invasive biomarker for early glymphatic impairment in the cognitive decline continuum.

References

1. Taoka T, Masutani Y, Kawai H, et al. Evaluation of glymphatic system activity with the diffusion MR technique: diffusion tensor image analysis along the perivascular space (DTI-ALPS) in Alzheimer's disease cases. Jpn J Radiol. 2017;35(4):172–8
2. Iliff JJ, Wang M, Liao Y, et al. A Paravascular Pathway Facilitates CSF Flow Through the Brain Parenchyma and the Clearance of Interstitial Solutes, Including Amyloid β. Sci Transl Med. 2012;4(147):147ra111
3. Bao C, Luo H, Wang J, et al. Poor glymphatic function is associated with mild cognitive impairment and its progression to Alzheimer's disease: A DTI-ALPS study. J Prev Alzheimers Dis. 2025:100156
4. Kamagata K, Andica C, Takabayashi K, et al. Association of MRI Indices of Glymphatic System With Amyloid Deposition and Cognition in Mild Cognitive Impairment and Alzheimer Disease. Neurology. 2022;99(24):e2648–60
5. Page MJ, McKenzie JE, Bossuyt PM, et al. The PRISMA 2020 statement: an updated guideline for reporting systematic reviews. BMJ. 2021;372:n71

Images/Tables

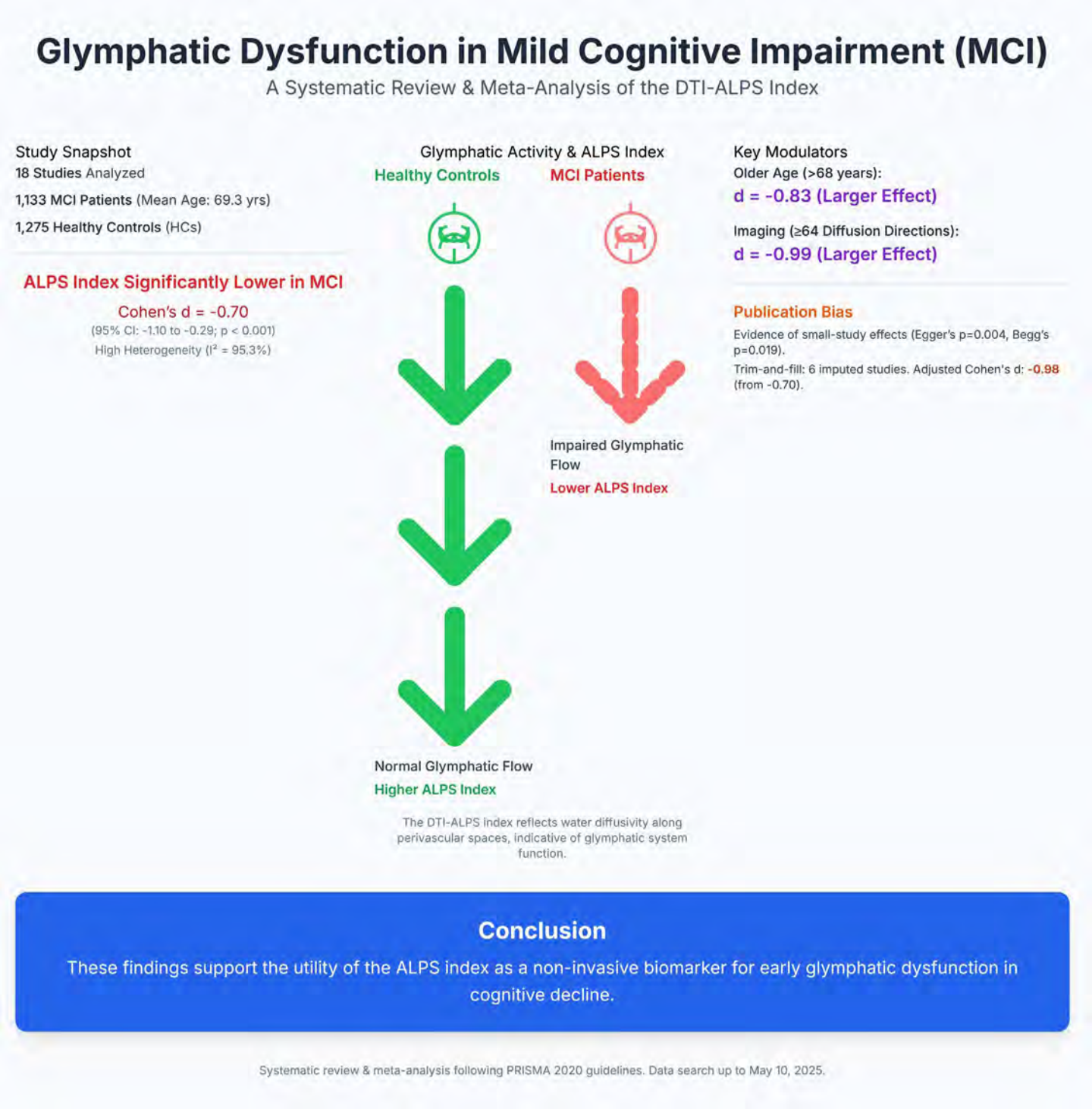

833 Experience with gadopiclenol in the detection of brain metastases: Single and double doses, comparison of standard and delayed imaging

Aaron Rulseh MD, PhD, Zuzana Ryznarova MD, PhD, Josef Vymazal MD, DSc
Na Homolce Hospital, Prague, NA, Czech Republic

Purpose

To demonstrate the role of gadopiclenol in MR imaging of brain metastases at standard (0.05 mmol/kg) and double doses (0.1 mmol/kg), including delayed examination (~15 minutes post-contrast).

Materials & Methods

One hundred sixty-two subjects with known brain metastases underwent MRI prior to radiosurgery (75 female, mean age 63.67 years ± 12.7 SD). A standard T1W 3D SPACE sequence was acquired post-contrast in all subjects (5 subjects at 1.5T, 157 at 3T), followed by a delayed acquisition. In roughly half of subjects (n=83), the delayed acquisition was preceded by additional contrast administration (cumulative double dose). After randomization, 3 blinded readers evaluated each subject in 2 sessions, minimally 4 weeks apart. A one-sided paired t-test was used to compare the number of lesions detected in the 2 groups: single dose (early versus delayed), and double dose (early versus delayed [double]).

Results

Agreement between all blinded readers was used for evaluation. The delayed single dose exam revealed 288 metastases compared to 279 metastases on the early exam. Delayed double-dose exam revealed 258 metastases compared to 221 metastases on the early single dose exam. In subjects that received a double dose, the number of lesions detected on the early versus delayed (double) dose exams differed significantly ($p=0.002$), while in subjects that received only a single dose no significant difference in the number of lesions detected on early versus delayed exams was detected ($p=0.24$).

Conclusion

Significantly more metastases were detected on delayed double dose imaging, while no difference was detected on early versus delayed single dose acquisitions. Our results suggest that a delayed, double dose gadopiclenol acquisition may improve the detection of metastases.

References

Maimouni I, Henoumont C, De Goltstein MC, Mayer JF, Dehimi A, Boubeguira Y, Kattenbeck C, Maas TJ, Decout N, Strzeminska I, Bazin G, Medina C, Factor C, Rousseaux O, Karst U, Laurent S, Catoen S. Gadopiclenol: A q = 2 Gadolinium-Based MRI Contrast Agent Combining High Stability and Efficacy. Invest Radiol. 2025 Mar 1;60(3):234-243. doi: 10.1097/RLI.0000000000001121. Epub 2024 Oct 9. PMID: 39724578; PMCID: PMC11801443.

835 Brain Aging is Not Static: A Deep Learning Analysis of Shifting Subcortical Predictors Across the Lifespan

Sana Mohammadi MD[1], Sadegh Ghaderi PhD[1], Minoo Sisakhti MSc[2], Seyed Amir Hossein Batouli PhD[1]
[1]Tehran University of Medical Sciences, Tehran, Tehran, Iran, Islamic Republic of. [2]Institute for Cognitive Sciences Studies, Tehran, Tehran, Iran, Islamic Republic of

Purpose

Accelerated brain aging is a significant risk factor for neurological disorders. This study aimed to use a deep learning approach to predict brain structure age (BSA) from subcortical volumes and to identify the dynamic, shifting influence of neuroanatomical, demographic (age, sex), and lifestyle (BMI, education) factors on the brain age gap across the adult lifespan.

Materials & Methods

This cross-sectional study analyzed high-resolution T1-weighted MRI data from 245 healthy individuals (20-60+ years) from the Iranian Brain Imaging Database. BSA was predicted using a deep learning model (volBrain platform) based on eight subcortical volumes. We used a series of stepwise multiple regression analyses to determine the key predictors of BSA in the total cohort, stratified by sex, and stratified by age group (Young: 20-39, Middle-aged: 40-59, Older: ≥60).

Results

An initial model, including the pallidum, basal forebrain, BMI, and education, explained 46.9% of the BSA variance. Pallidum volume was the strongest negative predictor ($\beta = -0.550$). When the age group was added, it became the dominant predictor ($\beta = 0.798$), and the effects of BMI and education were mediated. Crucially, age-stratified models revealed shifting predictors. For Young Adults, BSA was predicted only by pallidum and thalamus volumes ($R^2 = 0.098$). For Middle-Aged Adults, predictors shifted to the accumbens and basal forebrain volumes ($R^2 = 0.230$). For Older Adults, the model was strongest ($R^2 = 0.526$) and predicted by basal forebrain, pallidum, and caudate volumes.

Conclusion

The neuroanatomical drivers of brain aging are not static but shift dynamically across the lifespan. The pallidum is a consistent predictor, but different subcortical networks become vulnerable during mid-life (accumbens) and later-life (caudate, basal forebrain). These findings highlight age-dependent vulnerabilities and suggest that strategies for monitoring or mitigating accelerated brain aging must be tailored to specific life stages.

References

1. Nguyen H, Clément M, Mansencal B, et al. Brain structure ages—A new biomarker for multi-disease classification. Hum Brain Mapp. 2024;45:e26558
2. Coupé P, Mansencal B, Clément M, et al. AssemblyNet: A large ensemble of CNNs for 3D whole brain MRI segmentation. Neuroimage. 2020;219:117026
3. Cole JH, Franke K. Predicting Age Using Neuroimaging: Innovative Brain Ageing Biomarkers. Trends Neurosci. 2017;40:681–690
4. Raz N, Ghisletta P, Rodrigue KM, et al. Trajectories of brain aging in middle-aged and older adults: Regional and individual differences. Neuroimage. 2010;51:501–511
5. Tullo S, De Blasi M, FravvG, et al. MR-based age-related effects on the striatum, globus pallidus, and thalamus in healthy individuals across the adult lifespan. Hum Brain Mapp. 2019;40:5269–5288

Images/Tables

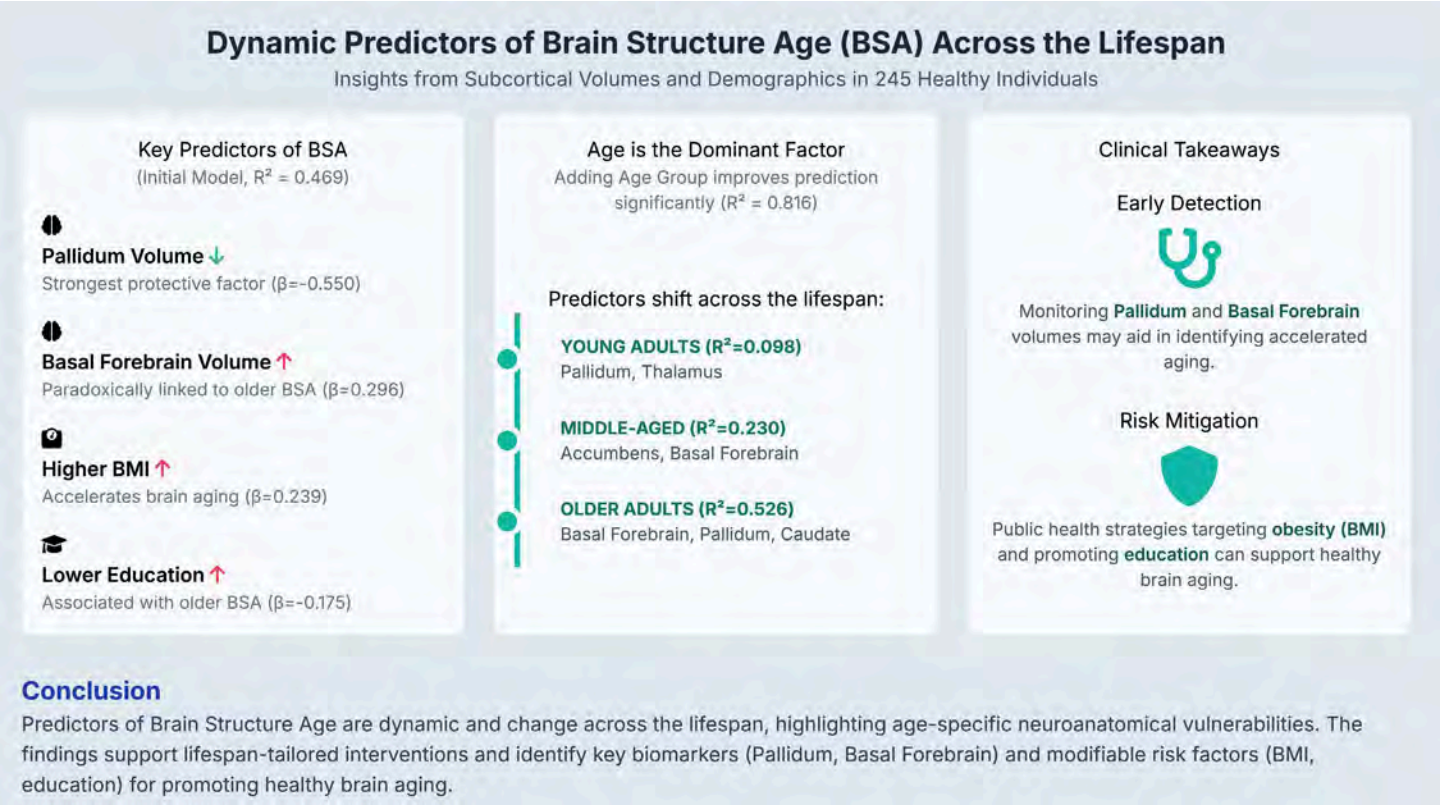

---

846 Clinical and Radiographic Determinants of Initial Post-Traumatic Intraparenchymal Hematoma Size: Implications for Early Risk Stratification

Mahla Radmard M.D.[1], Mona Gad M.D.[1], Ghazal Zandieh M.D.[1], Armin Tafazolimoghadam M.D.[2], Jay Kakadiya M.D.[1], David M. Yousem M.D., M.B.A.[1], Caline Azzi M.D.[1]

[1]Johns Hopkins University School of Medicine, Baltimore, Maryland, USA. [2]Tehran University of Medical Sciences, Tehran, Tehran, Iran, Islamic Republic of

Purpose

Initial size of a post-traumatic intraparenchymal hematoma (IPH) influences downstream management, follow-up imaging, and outcomes.. We sought to identify demographic, clinical, and radiographic factors associated with larger initial IPH on non-contrast CT (NCCT) after head trauma.

Materials & Methods

We retrospectively identified consecutive ED trauma NCCTs at two hospitals (July 2018–May 2024) in an academic health system. Acute IPH was confirmed by report review, with direct measurement when dimensions were not recorded. We recorded demographics, comorbidities, antithrombotic use, injury mechanism, patient management, and imaging features (location, midline shift, IVH, hydrocephalus, concomitant ICH). Group comparisons used Mann–Whitney/Kruskal–Wallis for continuous data and χ^2/Fisher for categorical data; correlations used Spearman's r. Significance: $p<0.05$.

Results

Among 239 patients (165 male), the mean age was 58.7 ± 21.9 years; 133 were < 65 years. The median initial IPH size was 13 mm (IQR 7–30). Larger baseline IPH was associated with age ≥ 65 (median 19.0 vs 10.0 mm, $p < 0.001$), history of hypertension ($p < 0.001$), and female sex (19.0 vs 12.0 mm, $p = 0.01$). Antithrombotic exposure tracked with increasing IPH size: dual antiplatelet/anticoagulant therapy had a median maximal diameter of 30.0 mm vs 11.0 mm without therapy ($p = 0.01$). Falls produced larger IPH than motor vehicle collisions (16.0 vs 9.0 mm, $p = 0.001$). Radiographically, larger size co-occurred with midline shift (43.0 vs 10.0 mm, $p < 0.001$), intraventricular hemorrhage (29.5 vs 11.0 mm, $p < 0.001$), and hydrocephalus (68.5 vs 12.0 mm, $p < 0.001$). Basal ganglia IPH had the largest median size (30.0 mm, $p = 0.01$) compared with other locations. Larger initial IPH aligned with lower GCS ($p = 0.005$), ICU admission ($p = 0.003$), in-hospital complications ($p = 0.06$, trend), and mortality (median 26.0 mm in deceased vs 12.0 mm in survivors; $p < 0.001$).

Conclusion

Baseline IPH size is influenced by age, sex, hypertension, antithrombotic exposure, and fall mechanism and strongly predicts mass-effect markers (midline shift, IVH, hydrocephalus) and worse clinical status. These readily available features at index CT can impact early triage—flagging patients for heightened neurocritical monitoring and neurosurgical readiness. Future analyses integrating volumetrics may further refine thresholds for level-of-care decisions.

References

1. **Rehman L, Afzal A, Aziz HF, Akbar S, Abbas A, Rizvi R.** Radiological parameters to predict hemorrhagic progression of traumatic contusional brain injury. *J Neurosci Rural Pract* 2019;10(2):212-217. doi:10.4103/jnrp.jnrp_335_18

2. **Khan AD, Elseth AJ, Brosius JA, Moskowitz E, Liebscher SC, Anstadt MJ, Dunn JA, McVicker JH, Schroeppel T, Gonzalez RP.** Multicenter assessment of the Brain Injury Guidelines and a proposal of guideline modifications. *Trauma Surg Acute Care Open* 2020;5(1):e000483. doi:10.1136/tsaco-2020-000483

3. **Stippler M, Keith S, Nelton EB, Parsons CS, Singleton J, Bilello LA, Tibbles CD, Davis RB, Edlow JA, Rosen CL.** Pathway-based reduction of repeat head computed tomography for patients with complicated mild traumatic brain injury: implementation and outcomes. *Neurosurgery* 2021;88(4):773-778. doi:10.1093/neuros/nyaa504

Images/Tables

Table. Association between study variables and initial IPH size

		N	Median (quartile1, quartile3)	P-value
Age group	<65	133	10.00 (5.50, 20.00)	<0.001
	≥65	106	19.00 (10.00,43.25)	
Age	quantitative	239	R=0.32	<0.001
Gender	Male	165	12.00 (6.00, 26.00)	0.01
	Female	74	19.00 (8.00, 42.25)	
Race	White	132	14.00 (7.00, 41.50)	0.11
	Black	82	12.00 (6.00, 25.75)	
	others	25	9.00 (5.00, 23.00)	
History of medication	None	160	11.00 (6.00, 22.00)	0.01
	Antiplatelet	49	15.00 (8.00, 46.50)	
	Anticoagulant	18	19.50 (10.75, 34.75)	
	Both	9	30.00 (13.00, 55.00)	
Elevated INR/PTT	Normal	166	11.00 (6.00, 28.00)	0.06
	Elevated	67	18.00 (10.00, 30.00)	
Thrombocytopenia	No	196	13.00 (6.00, 26.75)	0.21
	Yes	41	14.00 (8.00, 42.50)	
Mechanism	Fall	150	16.00 (7.75, 37.50)	0.001
	MVA	45	9.00 (5.00, 13.00)	
	Assault	24	12.00 (6.00, 24.25)	
	Others	16	20.00 (6.25, 33.50)	
Prior ICH	No	215	12.00 (6.00, 28.00)	0.14
	Yes	19	20.00 (8.00, 43.00)	
GCS	3-8	64	20.00 (7.25, 51.75)	0.005
	9-12	23	19.00 (8.00, 41.00)	
	13-15	143	11.00 (6.00, 21.00)	
HTN	No	119	10.00 (5.00, 21.00)	<0.001
	Yes	112	17.50 (8.50, 39.75)	
DM	No	189	13.00 (7.00, 28.00)	0.54
	Yes	42	14.00 (6.75, 31.00)	
CKD	No	207	13.00 (7.00, 29.00)	0.38
	Yes	23	19.00 (7.00, 40.00)	
Bleeding Diathesis	No	220	13.00 (7.00, 30.00)	0.52
	Yes	11	14.00 (3.00, 29.00)	
Surgical Tx at any time	No	212	12.00 (6.25, 28.00)	0.42
	Yes	26	20.00 (7.75, 30.00)	
Surgical Tx (surgical) (as initial tx)	No	213	12.00 (6.50, 28.00)	0.51
	Yes	25	20.00 (7.50, 30.00)	
Specific surgical TX	None	211	12.00 (7.00, 28.00)	0.71
	Craniotomy	19	20.00 (7.00, 35.00)	
	Burr hole	4	18.50 (12.25, 25.50)	
	Other	4	13.00 (4.50, 21.50)	
New surgical TX post follow-up	No	227	13.00 (7.00, 30.00)	0.39
	Yes	2	23.50 (20.00, NA)	
	None	227	13.00 (7.00, 30.00)	NA
Post follow-up surgical interventions	Craniotomy	1	-	
	Burr hole	1	-	
	Other	0	-	
Medical management (use of prophylaxis)	None	29	8.00 (5.00, 15.00)	<0.001
	mannitol	2	10.00 (6.00, NA)	
	keppra	141	10.00 (6.00, 21.50)	
	other	8	37.00 (15.25, 65.25)	
	Multiple medication	58	25.00 (14.50, 51.25)	
ICU	No	58	9.00 (5.75, 19.50)	0.003
	Yes	170	15.00 (7.75, 35.00)	
Complication	No	179	12.00 (7.00, 25.00)	0.06
	at least one	55	20.00 (8.00, 44.00)	
Length of hospitalization		238	R=0.10	0.13
Mortality	Deceased	44	26.00 (11.25, 58.75)	<0.001
	Alive	190	12.00 (6.00, 25.00)	
Rehospitalisation	No	211	13.00 (7.00, 30.00)	0.35
	Yes	21	20.00 (9.50, 26.50)	
Interventricular bleed	No	188	11.00 (6.00, 21.00)	<0.001
	Yes	48	29.50 (13.25, 62.75)	
Hydrocephalus at the time of presentation	No	226	12.00 (6.00, 25.25)	<0.001
	Yes	10	68.50 (58.75, 86.25)	
Number of IPH	1	152	27.50 (18.25, 43.50)	0.98
	2	38	12.00 (6.25, 28.75)	
	≥3	45	13.00 (6.00, 39.00)	
Location of IPH	Frontal	106	11.50 (6.00, 21.00)	0.01
	Temporal	27	14.00 (9.00, 25.00)	
	Parietal	27	11.00 (6.00, 37.00)	
	Occipital	5	6.00 (3.50, 14.00)	
	Multiple	63	20.00 (8.00, 48.00)	
	Basal ganglia	5	30.00 (20.00, 57.50)	
	Others	6	7.00 (4.75, 14.75)	
Epidural Hematoma	No	223	13.00 (7.00, 30.00)	0.04
	Yes	12	8.50 (4.25, 15.25)	
SDH	No	125	12.00 (7.00, 27.50)	0.98
	Yes	111	13.00 (6.00, 32.00)	
SAH	No	99	13.00 (7.00, 28.00)	0.70
	Yes	137	12.00 (6.50, 30.00)	
Midline shift	No	174	10.00 (6.00, 19.25)	<0.001
	Yes	62	43.00 (13.75, 63.50)	
Presence of fracture	No	145	13.00 (7.00, 33.50)	0.09
	Yes	91	12.00 (5.00, 22.00)	
CTA same admission	No	128	10.00 (6.00, 18.75)	<0.001
	Yes	111	20.00 (9.00, 47.00)	
IPH Enlargement	No	142	12.00 (6.00, 25.00)	0.046
	Yes	62	17.00 (8.00, 30.50)	
Total number of follow-up imaging procedures done		235	R=0.07	0.27

917 Vessel Suppression on Contrast Enhanced Brain MRI Reduces Signal Distraction and Improves Lesion Conspicuity.

Dayang Wang PhD[1], Srivathsa Pasumarthi[1], Ajit Shankaranarayanan PhD[1], Greg Zaharchuk PhD, MD[2]
[1]Subtle Medical, Menlo Park, CA, USA. [2]Stanford University, Stanford, CA, USA

Purpose

Contrast-enhanced (CE) MRI with gadolinium-based contrast agents (GBCAs) provides excellent lesion visualization but often suffers from prominent vascular enhancement, which can obscure or mimic true pathology. This issue is particularly pronounced in gradient-echo (GRE) sequences, where bright vascular signals can complicate the differentiation between small enhancing lesions (e.g., metastases) and nearby vessels. While AI-based vessel suppression has been explored in lung CT imaging [1,2], there are currently no known methods for vessel suppression as a post-processing algorithm in MRI. To address this gap, we propose the first deep learning–based approach for vessel suppression in CE-MRI, designed to preserve lesion contrast while reducing vascular hyperintensity.

Materials & Methods

Spin-echo (SE) sequences inherently suppress flowing blood and can reduce vessel–lesion confusion. However, SE images are typically lower in resolution and require additional scan time, limiting their clinical practicality. Drawing inspiration from recent advances in medical image synthesis [3], we developed a method that learns a transformation from GRE to SE images, where vessel signals are naturally suppressed.

To overcome the resolution disparity between GRE and SE scans, we performed a copy-paste preprocessing step: lesions manually segmented on GRE images were copied and inserted into the spatially corresponding locations in SE scans, after both were intensity-normalized. This ensured that the lesions in the processed SE retained the same spatial resolution as those in GRE.

A 2D Nested U-Net was then trained to learn the mapping from GRE to SE using 100 publicly available Stanford Mets studies (90 for training, 10 for validation). SE volumes were co-registered to GRE, intensity-normalized, and histogram-equalized to align gray–white matter contrast. The model was trained with L1, SSIM, perceptual, and adversarial losses to balance structural consistency and perceptual realism.

After training, the model generated synthetic SE images (SE-syn) from GRE inputs. A subtraction map (GRE − SE-syn) was then computed, and a threshold (e.g., >0) was applied to isolate vessel signals. This binary vessel mask was used to linearly attenuate vessel voxels in GRE image by a user-defined suppression factor, resulting in the final vessel-suppressed output (GRE_vsup).

Results

In our test dataset, ROI-based quantitative analysis showed that GRE_vsup effectively suppressed vascular signals while maintaining lesion intensity. For lesion ROIs, contrast-to-noise ratio (CNR) and contrast enhancement percentage (CEP) remained nearly unchanged (CNR: 13.9 → 13.0; CEP: 139% → 140%). For vessel ROIs, both measures decreased substantially (CNR: 8.2 → 2.8; CEP: 84.6% → 32.3%), confirming successful vascular signal attenuation.

To further evaluate downstream utility, we integrated the vessel suppression with an existing contrast enhancement algorithm, AiMIFY [4]. Results demonstrated that applying vessel suppression to AiMIFY-enhanced images relieves vascular hyperintensity while preserving lesion brightness, thus enhancing lesion conspicuity and overall diagnostic clarity.

Conclusion

The proposed vessel suppression method can be applied as a post-processing step to existing GRE exams. By reducing distracting vascular enhancement while preserving lesion signal, it improves lesion conspicuity and supports tasks such as metastasis detection and lesion counting. This work introduces a novel, generalizable framework for vessel suppression in CE-MRI, representing a meaningful step toward AI-driven image refinement and clinical workflow efficiency.

References

[1] Singh R, Kalra MK, Homayounieh F, et al. Artificial intelligence-based vessel suppression for detection of sub-solid nodules in lung cancer screening computed tomography. Quantitative imaging in medicine and surgery. 2021 Apr;11(4):1134.

[2] Gu X, Xie W, Fang Q, et al. The effect of pulmonary vessel suppression on computerized detection of nodules in chest CT scans. Medical physics. 2020 Oct;47(10):4917-27.

[3] Pasumarthi Venkata S, Campbell Arnold T, Colombo Serra S, et al. Deep-Learning Based Contrast Boosting Improves Lesion Visualization and Image Quality: A Multi-Center Multi-Reader Study on Clinical Performance with Standard Contrast Enhanced MRI of Brain Tumors. medRxiv. 2025 Jun 13:2025-06.

[4] Tanenbaum LN, Bash SC, Zaharchuk G, et al. Deep learning–generated synthetic MR imaging STIR spine images are superior in image quality and diagnostically equivalent to conventional stir: a multicenter, multireader trial. American Journal of Neuroradiology. 2023 Aug 1;44(8):987-93.

Images/Tables

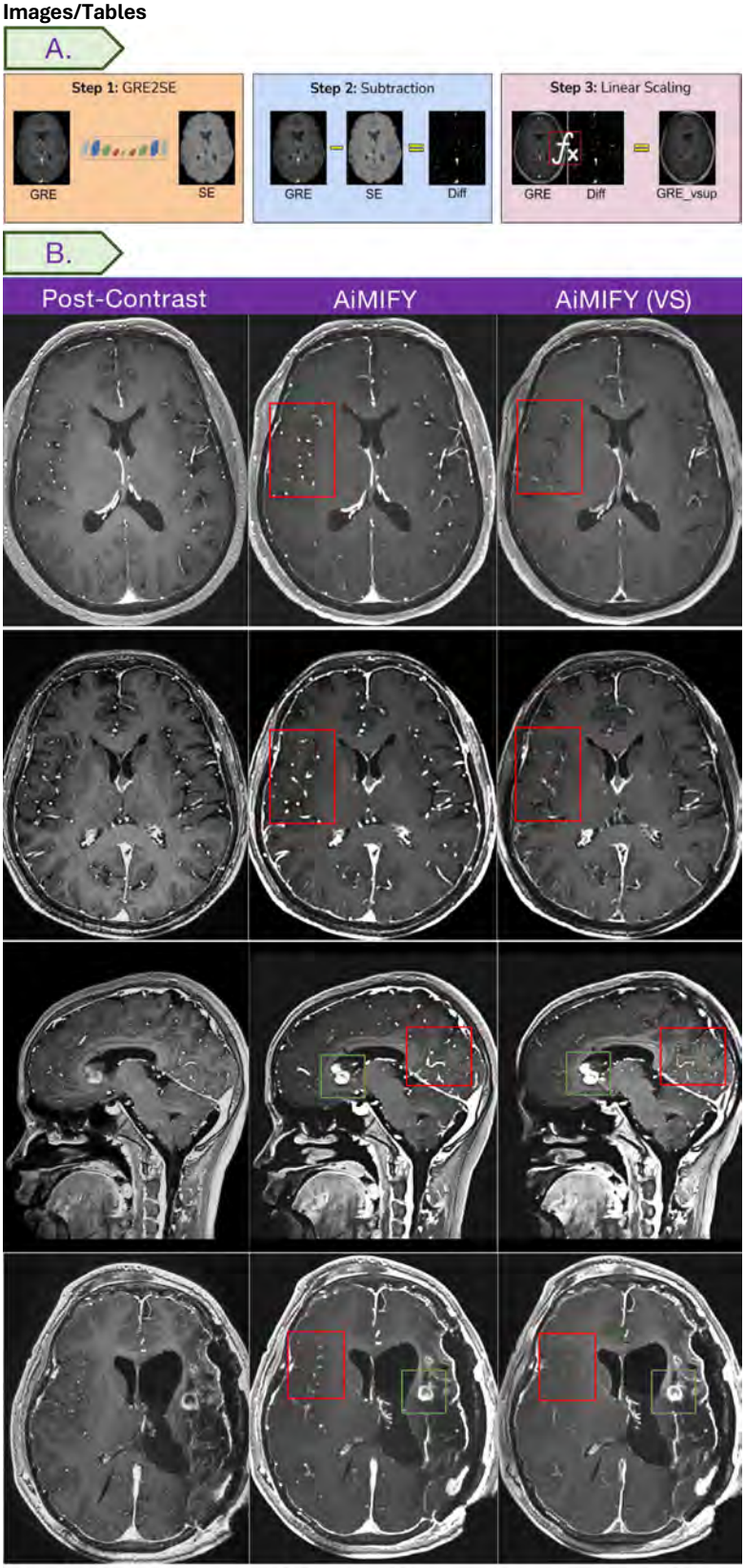

Fig. A. The three steps of the vessel suppresion algorithms: (1) GRE to SE sequence learning; (2) Subtraction from GRE to learnt SE to obtain the vessel signal; (3) The GRE post-contrast vessel attuation with the vessel map. B. Examples of vessel suppresion on a contrast enhancement Algorithm (AiMIFY [1]), results shows vessel suppresion with lesion signal preserved, which indicates reduced signal distraction and improved Lesion conspicuity.

957 VORTEX-Accelerated Pituitary MRI with Deep Learning Reconstruction: A Prospective Multi-Rater Comparison

Atefeh Zeinoddini MD[1], Thomas Dowling MD[1], Eugene Milshteyn[2], Ajeetkumar Gaddipati[3], Anand Venkatachari[4], Mary Thomas[5], Rory Cochran[1], Susie Huang MD-PHD[1], Ivan Jambor MD-PHD[1]

[1]Department of Radiology, Massachusetts General Hospital, Boston, Boston, MA, USA. [2]GE HealthCare, Boston, MA, USA. [3]GE HealthCare, Waukesha, WI, USA. [4]GE HealthCare, Rochester, MN, USA. [5]GE HealthCare, boston, ma, USA

Purpose

Improved accelerate acquisition methods combined with deep learning reconstruction hold a promise for significant reduction in MRI scan time. These new methods requires rigorous, clinically-oriented validation to evaluate their impact on diagnostic image quality. Aim of this study was to provide a comprehensive, multi-rater comparison of novel acquisition technique for fast-spin echo imaging (FSE), VORTEX (VERSE SAR reduction, Optimized RF waveform, Refocus flip angle modulation, Tuned Hyper Echoes, External volume suppression, X-factor spin efficiency) for MRI of the pituitary gland [1].

Materials & Methods

Twenty-one consecutive patients under pituitary MRI as a part of routine clinical workflow. All patients received pre-contrast coronal T2-weighted and pre-contrast sagittal T1-weighted sequences obtained using both a standard FSE (scan time: 45s for T2-weighted, 80s for sagittal T1-weighted) and VORTEX acquisition (scan time: 31 for T2-weighted, 45 for sagittal T1-weighted). In addition, 9 of these patients also had both a standard FSE and VORTEX acquisition for post-contrast sagittal T1 sequences. A commercially available DL reconstruction algorithm (AIRTM Recon DL, GE HealthCare, Waukesha, WI), which is based on a Convolutional Neural Network (CNN) trained to remove ringing, reduce noise, and increase sharpness, was applied to all acquisitions.

Three board-certified radiologists independently evaluated all sequences for five metrics (Diagnostic quality, Noise, Sharpness, Artifacts, and Visualization of Enhancement) on a 5-point scale, where 1=non-diagnostic, 2=poor, 3=good, 4=very good, and 5=excellent. Inter-rater reliability (IRR) was evaluated using the Intraclass Correlation Coefficient (ICC). Score differences were analyzed using Cumulative Link Mixed Models (CLMM) with crossed random effects for patient and rater.

Results

VORTEX reduced acquisition times by 31%, 44% and 44% for the coronal T2-weighted, pre-contrast and post-contrast sagittal T1-weighted sequences.

Inter-rater reliability was excellent for Image Quality (ICC=0.94) and Artifacts (ICC=0.92), good for Visualization of Enhancement (ICC=0.75), and moderate for Noise (ICC=0.59) and Sharpness (ICC=0.52).

Coronal T2 (Pre-contrast, 21 patients): VORTEX acquisition demonstrated significant improvements across all quality metrics. The very good/excellent ratings for VORTEX versus Standard were, respectively: 98.4% vs. 65.1% for image quality ($p<0.001$), 100% vs. 79.4% for artifacts, 92.1% vs. 65.1% for noise ($p<0.001$), and 98.4% vs. 82.5% for sharpness ($p=0.012$).

Sagittal T1 (Pre-contrast, 21 patients): The standard FSE demonstrated statistically significant superiority for lower Noise (90.5% vs. 74.6% very good/excellent, $p=0.011$). Other metrics, including diagnostic quality, showed no statistically significant differences between the standard and VORTEX acquisition ($p>0.05$).

Sagittal T1 (post-contrast, n=9 patients): The standard FSE and VORTEX acquisition demonstrated equivalent performance. No statistically significant differences were observed across any metric, including artifacts, image quality, noise, and sharpness (all $p>0.05$).

Conclusion

Our study demonstrates feasibility of an accelerated FSE-based imaging of pituitary gland using VORTEX which enabled substantial scan time reduction. VORTEX pre-contrast coronal T2 sequence was markedly superior across all metrics, while the VORTEX sagittal T1 sequences showed general equivalency. Larger sample follow-up studies are needed to further validate these specific findings. These results support further clinical evaluation of VORTEX protocols for pituitary imaging, offering reduced scan times, improved patient comfort, and enhanced diagnostic confidence.

References

1. Desai, A. D., Gunel, B., Ozturkler, B. M., Beg, H., Vasanawala, S., Hargreaves, B. A., ... & Chaudhari, A. S. (2021). VORTEX: Physics-Driven Data Augmentations Using Consistency Training for Robust Accelerated MRI Reconstruction. *arXiv preprint arXiv:2111.02549*.

Images/Tables

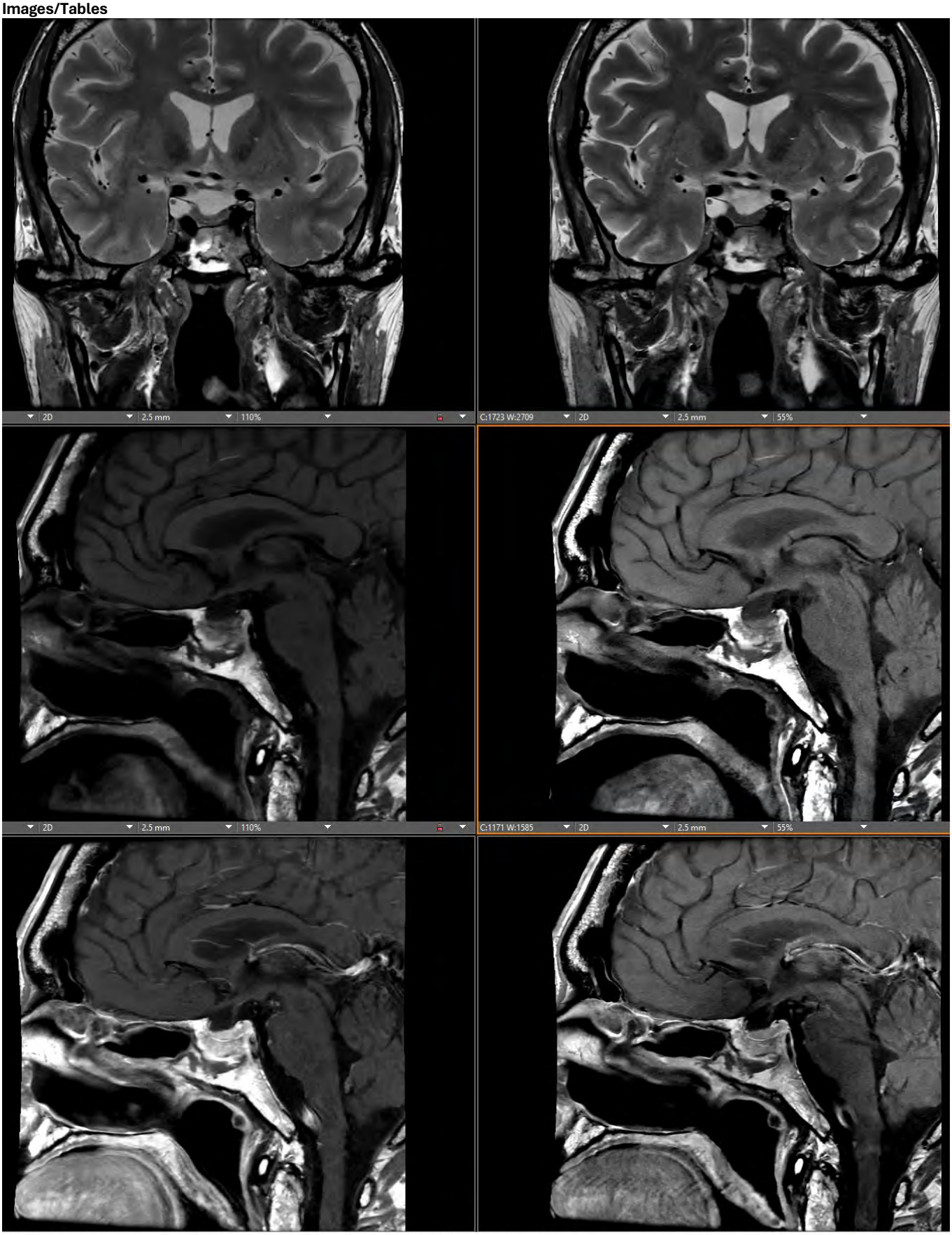

Figure 1. Comparison of standard and accelerated (Vortex) pituitary MRI. Representative images from the same patient demonstrating the standard acquisition versus the Vortex protocol. (A) Standard Coronal T2-weighted, (B) Vortex Coronal T2-weighted, (C) Standard Sagittal T1-weighted pre-contrast, (D) Vortex Sagittal T1-weighted pre-contrast, (E) Standard Sagittal T1-weighted post-contrast, (F) Vortex Sagittal T1-weighted post-contrast.

989 Vision Language Foundation Model for MRI Standarization Achieves High Accuracy in Modality and Anatomy Classification.

Dayang Wang PhD[1], Thomas C Arnold PhD[1], Ajit Shankaranarayanan PhD[1], Greg Zaharchuk PhD, MD[2]
[1]Subtle Medical, Menlo Park, CA, USA. [2]Stanford University, Stanford, CA, USA

Purpose

Magnetic Resonance Imaging (MRI) is widely used in both clinical and research settings. However, there is no standard system for naming or categorizing MRI sequences. This inconsistency is due to differences in imaging protocols, scanner vendors, and institutional practices. As a result, MRI sequences often vary in appearance, and DICOM metadata can be unreliable or conflicting. Clinician oversight is frequently required to verify the correct sequence type. This manual process is time-consuming and prone to error, especially when dealing with large datasets. The goal of this study is to create an efficient streamlined method to standarize the MRI sequences.

Materials & Methods

The challenges in MRI standarization is to identify the modality and anatomy types. In response to this challenges, we developed a vision-language foundation model to infer the Anatomy and Modality type from existing metadata and pixel information. Specifically, it combines BERT (for 36 selected metadata fields) and a 3D ResNet-18 (for 32 sampled image slices) to extract text and image features. These features are fed to six transformer layers with two separate classification heads for Modality and Anatomy.

The model is first pretrained on ~100k unlabeled studies using three complementary objectives: (1) BERT masking to infer missing tags, (2) CLIP-style alignment between metadata and pixel features, and (3) DINO for self-supervised visual representation learning. In the finetuning stage, we train on ~50k manually labeled cases to learn the Modality and Anatomy classifiers. Finally, an expert rule-based verifier checks metadata fields for sequence types better captured by rules (e.g., MRA, SSFP, ADC/DWI). This pipeline deliberately minimizes reliance on the often inconsistent Series Description tag. With the predicted anatomy and modality, we fuse with Orientation, Acquisition, and FatSat directly pulled from DICOM metadata to achieve standardized MRI naming convention.

The proposed model is evaluated on three datasets: (1) an internal brain validation data with 622 cases, (2) an external brain datasets with 310 cases, and (3) a multi-anatomy datasets with 1501 cases.

Results

Anatomies cover common neuro body parts, including Brain, Neck, C-Spine, T-Spine, and L-Spine. Modalities include T1, T1c, T2, T2-FLAIR, DWI, MRA, T2*, SWI, SSFP, ASL, ADC, CAL, and LOC, encompassing nearly all mainstream MRI sequence types.

On internal brain validation data, the model achieves 99.20% accuracy; on external brain validation, it achieves 99.03%. For multi-anatomy datasets, it achieves 98.78% modality accuracy and 94.64% anatomy accuracy on Neuro. Beyond Neuro, the model also performs strongly on MSK anatomies (Wrist, Hip, Elbow, Knee), reaching 98.6% modality and 99.3% anatomy accuracy. These results demonstrate high accuracy for both modality and anatomy classification and support high-level MRI standardization. Compared with existing models that target limited anatomy or modality scopes [1-3], this is, to our knowledge, the first foundation model to attain state-of-the-art performance across all major neuro and MSK anatomy–modality types.

Conclusion

The proposed method enables MRI metadata standardization, with high accuracy in MRI sequence and anatomy classification. This improves the reliability and efficiency of MRI data organization, retrieval, and downstream analysis.

References

[1] Stember JN, Shalu H. Deep neuroevolution squeezes more out of small neural networks and small training sets: Sample application to mri brain sequence classification. InInternational Symposium on Intelligent Informatics 2022 Aug 31 (pp. 153-167). Singapore: Springer Nature Singapore.
[2] Helm K, Mathai TS, Kim B, et al. Automated classification of body MRI sequence type using convolutional neural networks. InMedical Imaging 2024: Computer-Aided Diagnosis 2024 Apr 3 (Vol. 12927, pp. 119-123). SPIE.
[3] You S, Wiest R, Reyes M. SaRF: Saliency regularized feature learning improves MRI sequence classification. Computer methods and programs in biomedicine. 2024 Jan 1;243:107867.

Images/Tables

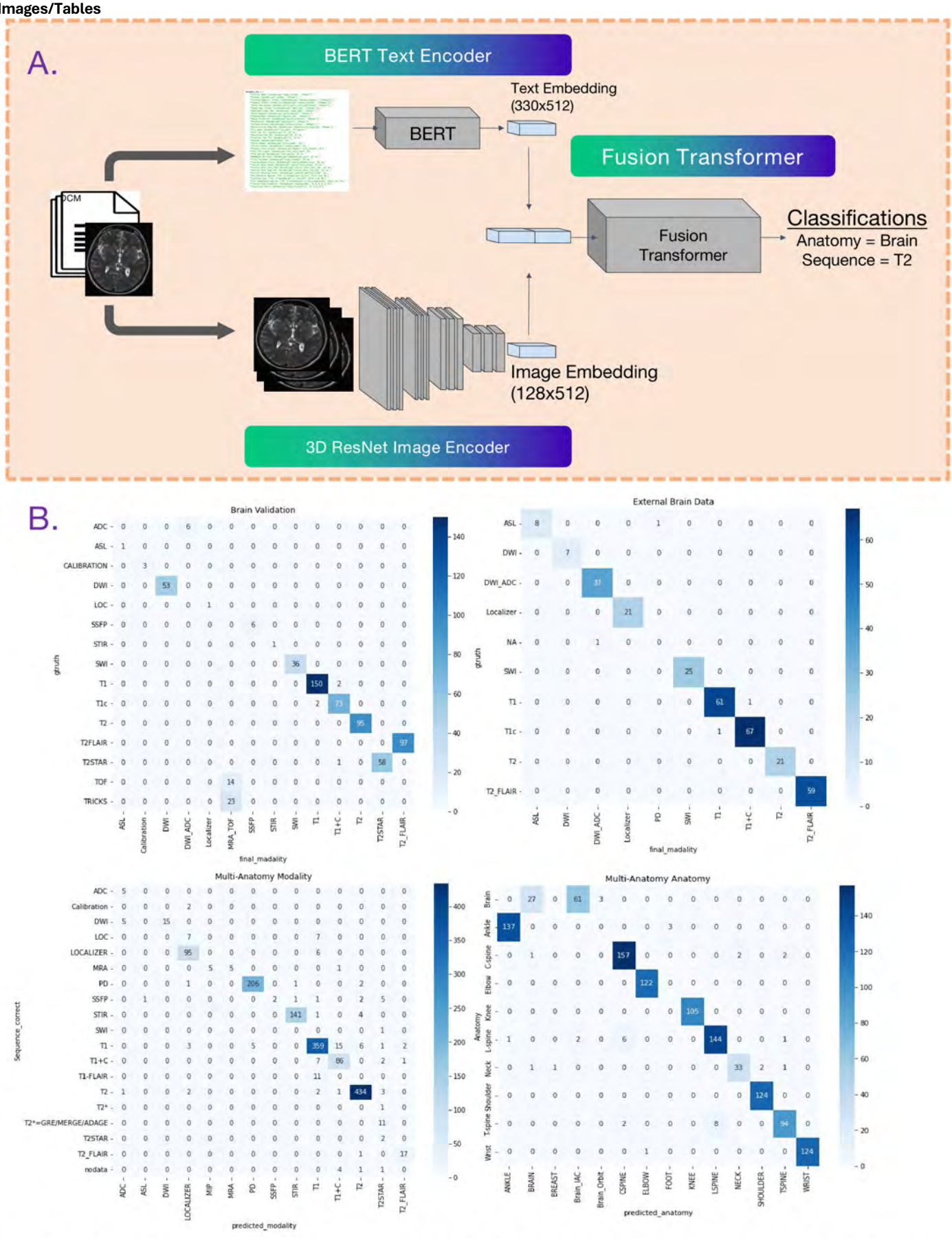

Fig. A. The architecture of the vision language model. B. The confusion matrix on the performance of the Brain Validation, external Brain data, and the multi-anatomy data (Moldaity and Anatomy).

996 In Vivo Characterization of the Redox Balance in IDH-Wildtype Glioblastomas using J-difference Edited MEGA-sLASER MRS at 3T

Seyma Alcicek[1], Andrei Manzhurtsev[1], Dennis C Thomas[1], Iris Divé[2], Katharina J Weber[3], Vincent Prinz[4], Daniel Jussen[4], Dinesh K Deelchand[5], Georg Oeltzschner[6], Michael W Ronellenfitsch[2], Joachim Steinbach[2], Elke Hattingen[1], Ulrich Pilatus[1], Katharina J Wenger[1]

[1]Goethe University Frankfurt, Institute of Neuroradiology and Cooperative Brain Imaging Center - CoBIC, Frankfurt, Hesse, Germany. [2]Dr. Senckenberg Institute of Neurooncology, University Hospital Frankfurt, Goethe University, Frankfurt, Hesse, Germany. [3]Institute of Neurology (Edinger-Institute), University Hospital Frankfurt, Goethe University, Frankfurt, Hesse, Germany. [4]Department of Neurosurgery, University Hospital Frankfurt, Goethe University, Frankfurt, Hesse, Germany. [5]Center for Magnetic Resonance Research, Department of Radiology, University of Minnesota, Minneapolis, Minnesota, Minneapolis, USA. [6]Russell H. Morgan Department of Radiology and Radiological Science, The Johns Hopkins University School of Medicine, Baltimore, MD, USA

Purpose

Isocitrate dehydrogenase-wildtype glioblastoma (IDHwt GBM) is the most common primary malignant brain tumor in adults, with a universally poor prognosis. For survival and growth under conditions of the tumor microenvironment, GBM cells require antioxidant glutathione (GSH) and its precursor cystathionine (Cth) to maintain redox balance[1,2]. This study aimed to measure the redox-cycle metabolites GSH and Cth using J-difference edited MR spectroscopy at 3T, evaluating their potential as in vivo biomarkers for redox-modulating therapies. After establishing the protocol's reliability and reproducibility in healthy volunteers[3], it was applied to IDHwt GBM patients to evaluate diagnostic performance while accounting for tumor subregions.

Materials & Methods

In this prospective study, 27 patients with MRI-suspected glioma were scanned on a 3T MR scanner. The protocol included 3D T1-weighted, 2D T2-weighted images, and a MEGA-sLASER sequence applying three editing conditions: GABA(gamma-aminobutyric acid)-Cth-on (1.9 ppm); GSH-on (4.56 ppm); edit-OFF (7.5 ppm). Other MEGA-sLASER parameters were TR/TE=2000/80 ms, editing-pulse duration=13 ms, voxel size=8–16 cm^3, number of transients=192, acquisition time=6.44 min. Water reference was acquired with the same parameters, but only 4 transients. All spectra were preprocessed with a modified version of Gannet[5] to create GABA-Cth-edited difference spectra (GABA-Cth-on – edit-OFF) and GSH-edited difference spectra (GSH-on – edit-OFF). Spectral fitting was performed using LCModel. Weighted images were used to generate water T1, T2, and proton density maps for metabolite quantification.BraTS Toolkit was used for automated segmentation of glioma subregions. Statistical analyses were performed in R(v4.4.1).

Results

To create a uniform GBM cohort, all patients with IDHwt GBM and high-quality spectra (n=15; mean age 59±11 years; 9 men) were included in the final analysis (**Table 1**, **Figure 1**). Tumor tissue exhibited significantly elevated Cth (1.17±1.30 mM vs 0.63±0.59 mM, p=0.03) and lower GABA+ (GABA and co-edited macromolecules at 3 ppm) levels (2.36±0.70 mM vs 3.04±0.89 mM, p=0.006) compared to contralateral tissue (**Figure 2).** Tumoral GSH concentrations correlated positively with Cth levels (p=0.00005) and enhancing-tumor fraction (p=0.0003), and negatively with TP53 accumulation (p=0.008) (**Figure 3**). No difference in GSH levels was observed with respect to MGMT status (p=0.66), whereas lower GSH concentrations were found in the mesenchymal subclass compared to RTK I/II (0.14±0.15 mM vs 0.65±0.49 mM, p=0.04).

Conclusion

The elevated Cth observed in tumor tissue is consistent with the role of cystathionine-γ-lyase as a key enzyme in the transsulfuration pathway. Increased Cth levels suggest pathway up-regulation, which enhances cysteine production for GSH synthesis and thereby augments the tumor's antioxidant capacity. The observed negative correlation between TP53 accumulation and GSH levels is consistent with the role of wild-type p53 in regulating cellular redox balance. The observed GSH difference between the mesenchymal and RTK I/II subclasses may indicate subclass-specific variation in redox balance within GBM. The lower GABA+ levels in GBM tissue relative to contralateral tissue may reflect increased metabolic use of GABA through the GABA shunt, feeding the tricarboxylic acid cycle and maintaining cellular redox homeostasis. Our findings highlight the need to assess tumor metabolism on an individual basis rather than relying on group-level-analyses.

References

1. Ruiz-Rodado V, Dowdy T, Lita A, et al. Cysteine is a limiting factor for glioma proliferation and survival. *Mol Oncol*. 2022;16(9):1777-1794. doi:10.1002/1878-0261.13148

2. Campos-Sandoval JA, Gómez-García MC, Santos-Jiménez J de los, Matés JM, Alonso FJ, Márquez J. Antioxidant responses related to temozolomide resistance in glioblastoma. *Neurochemistry International*. 2021;149:105136. doi:10.1016/j.neuint.2021.105136

3. Alcicek S, Manzhurtsev A, Ronellenfitsch MW, Deelchand D, Steinbach JP, Prinz, V. In vivo detection of GSH and GABA in high-grade glioma using MEGA-sLASER spectral editing at 3 T. In: *ISMRM 2024 Proceedings*. ; 2024:0361.

4. Edden RAE, Puts NAJ, Harris AD, Barker PB, Evans CJ. Gannet: A Batch-Processing Tool for the Quantitative Analysis of Gamma-Aminobutyric Acid–Edited MR Spectroscopy Spectra. *J Magn Reson Imaging*. 2014;40(6):1445-1452. doi:10.1002/jmri.24478

Images/Tables

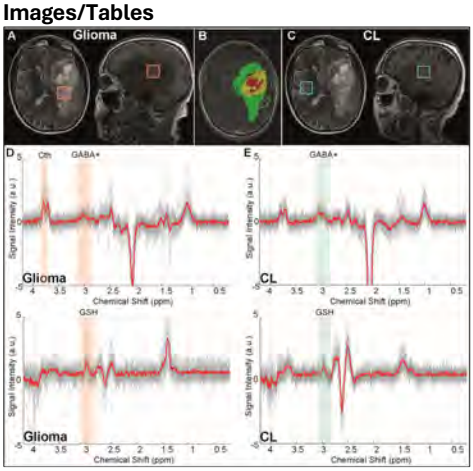

Figure 1. Example for MRS voxel placements in **(A)** tumor region and **(C)** CL tissue on T2W and T1W images, along with **(B)** tumor segmentation including ET (yellow), NETC (red), and SNFH (green). Overlapped edited **(D)** GABA-Cth and **(E)** GSH spectra acquired from GBM and CL regions. Mean spectra are displayed in red. The edited GABA+ and GSH peak spectral regions are highlighted with boxes. One of the prominent resonances from the edited Cth spectral pattern at ~3.85 ppm, partially overlapping with the glutamate-glutamine signal, is also highlighted.

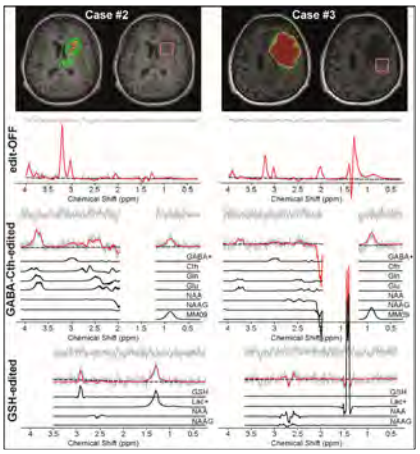

Figure 3. Two representative IDHwt GBM cases. MRS voxel placements and tumor segmentation are displayed in the upper panel, and MRS fitting of edit-OFF, GABA-Cth-edited, and GSH-edited difference spectra in the lower panel. In the tumor segmentation maps, yellow denotes enhancing tumor (ET), red non-enhancing tumor core (NETC), and green surrounding non-enhancing FLAIR hyperintensity (SNFH).

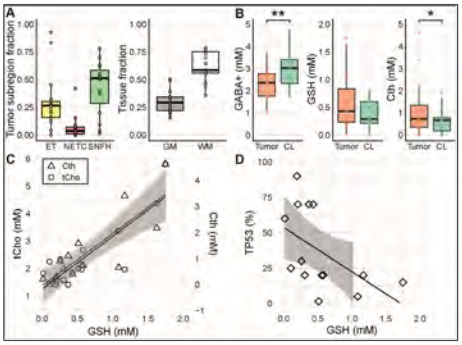

Figure 2. (A) Tumor subregion fraction in MRS tumor voxels and tissue fraction in CL voxels. **(B)** GABA+, GSH and Cth levels in the tumor and CL region. Results were considered significant at *p<0.05; **p<0.01. **(C)** Scatter plot of GSH concentration versus tCho (circles, first y-axis) and Cth (triangles, rescaled second y-axis), with a linear regression line and ±95% CI. **(D)** Scatter plot showing the relationship between GSH concentration and frequency TP53 immunoreactivity, with a linear regression line and ±95% CI.

Patient characteristics	IDH-wildtype glioblastoma (n = 15)
General	
Age, median (interquartile range)	59 (54 - 71)
Female	6
Integrated diagnosis, Molecular subclass	
Glioblastoma IDH-wildtype, grade 4, mesenchymal	3
Glioblastoma IDH-wildtype, grade 4, RTK I	3
Glioblastoma IDH-wildtype, grade 4, RTK II	8
Glioblastoma IDH-wildtype, grade 4, (unknown subclass)	1
MGMT promoter status	
Methylated	8
Unmethylated	6
Unknown	1
Prior treatment	
None	15

Table 1. Demographic characteristics of patients with IDH-wildtype glioblastoma.

1022 Post-Procedural Imaging Findings and Their Association with 90-Day Functional Outcomes After Mechanical Thrombectomy

Dan Cheng MD[1], Cristina Sanchez-Vizcaino MD[2], Ahmed Safwat MD[2], Mona Kharaji MD[2], Maoxue Wang MD[2], Gador Canton Ph.D[2], David L. Tirschwell MD[2], Thomas S. Hatsukami MD[2], Chun Yuan Ph.D[2], Niranjan Balu Ph.D[2], Mahmud Mossa-Basha MD[1]

[1]Univerisity of Alabama at Birmingham, Birmingham, Albama, USA. [2]Univerisity of Washintong, Seattle, Washington, USA

Purpose

Post-procedural imaging findings following mechanical thrombectomy (MT) in acute ischemic stroke patients, including iodine staining on dual energy CT and vessel wall enhancement (VWE) on vessel wall MRI (vwMRI), are frequently observed but their clinical significance remain poorly understood.[1–3] This study aims to identify the risk factors for iodine staining and MT VWE and their association with 90-day functional outcomes.

Materials & Methods

We retrospectively analyzed 120 consecutive patients who underwent MT for acute ischemic stroke from June 2022 to April 2024. All patients underwent post-procedural imaging evaluation including assessment of iodine staining presence on dual energy CT and VWE intensity (Level 1: less intensity than at the pituitary infundibulum, Level 2: higher intensity) on contrast-enhanced vwMRI. Patient demographics, clinical variables, stroke severity (admission NIHSS, NIHSS at 24 hours), imaging characteristics (infarct core volume, hypoperfusion intensity ratio (HIR)), treatment details (device used, number of passes, and TICI score), and 90-day modified Rankin Scale (mRS) scores were collected. Functional outcomes were dichotomized as poor (mRS 3-6) or good outcome (mRS 0-2).

Statistical analyses included group comparisons using Wilcoxon rank-sum test for non-normally distributed variables, t-test for normally distributed variables, chi-square and Fisher's exact test for categorical variables. Univariable and multivariable logistic regression analysis adjusted for confounders was performed. Multivariable models excluded initial NIHSS due to high correlation with NIHSS at 24 hours.

Results

Iodine staining was present in 64 patients (53.3%). VWE was Level 2 in 77 patients (65.3%).

Patients with poor outcomes had significantly higher admission NIHSS(mean 20.99 vs 14.62, P < 0.001), higher 24-hour NIHSS (18.41 vs 4.90, P < 0.001), larger infarct core volumes (96.09 cc vs 23.10 cc, P < 0.001), higher iodine staining rates (63.7% vs 32.5%, P = 0.002), and required more thrombectomy passes (2.00 vs 1.40, P = 0.014). Age (P = 0.024) and diabetes mellitus (P = 0.042) were also more prevalent in the poor outcome group. No significant difference was observed in VWE between groups (68.4% vs 60.0% Level 2, P = 0.483).

In univariable analysis, iodine staining was a significant predictor of poor 90-day functional outcome (3.65, 1.64-8.16, P=0.0016). Other significant univariable predictors included admission NIHSS (1.15, 1.07-1.23, P<0.001), 24-hour NIHSS (1.34, 1.21-1.48, P<0.001),infarct core volume (1.027, 1.01-1.04, P<0.001), number of passes (1.67, 1.08-2.57, P=0.021), age (1.031, 1.003-1.059, P=0.027), and diabetes mellitus (2.72, 1.11-6.67, P=0.028). In multivariable logistic regression, 24-hour NIHSS remained the only independent predictor of 90-day functional outcome (adjusted OR= 1.271, 1.146-1.449, P<0.001). (Table 1)

Conclusion

Iodine staining on dual energy CT was significantly associated with poor outcomes in univariable analysis, staining and VWE on vwMRI were not independently associated with outcomes in multivariable analysis. Further studies are needed to evaluate whether quantifying post-procedural imaging findings can provide stratified data to better predict prognosis.

References

1. Yan J, Xu X, Li H, et al. Prognostic significance of contrast staining following mechanical thrombectomy in acute ischaemic stroke. *Stroke Vasc Neurol* https://doi.org/10.1136/svn-2025-004113.

2. Abraham P, Scott Pannell J, Santiago-Dieppa DR, et al. Vessel wall signal enhancement on 3-T MRI in acute stroke patients after stent retriever thrombectomy. *Neurosurg Focus* 2017;42:E20.
3. Power S, Matouk C, Casaubon LK, et al. Vessel Wall Magnetic Resonance Imaging in Acute Ischemic Stroke: Effects of Embolism and Mechanical Thrombectomy on the Arterial Wall. *Stroke* 2014;45:2330–4.

Images/Tables

Table 1. Univariable and Multivariable Logistic Regression Analysis for 90-Day Functional Outcome

Variable	Univariable		Multivariable	
	OR (95% CI)	P-value	OR (95% CI)	P-value
24-hour NIHSS	1.34 (1.21-1.48)	<0.001	1.271 (1.146-1.449)	<0.001
Admission NIHSS	1.15 (1.07-1.23)	<0.001	-	-
Infarct core volume (per cc)	1.027 (1.01-1.04)	<0.001	1.001 (0.987-1.020)	0.949
Iodine staining (Yes vs No)	3.65 (1.64-8.16)	**0.002**	2.489 (0.741-8.916)	0.140
Age (per year)	1.031 (1.003-1.059)	0.027	1.040 (0.997-1.091)	0.066
Diabetes mellitus (Yes vs No)	2.72 (1.11-6.67)	0.028	3.050 (0.860-12.663)	0.085
Number of passes	1.67 (1.08-2.57)	0.021	1.136 (0.596-2.328)	0.711

1027 AI-based Differentiation of Oligodendriglioma from Astrocytoma

Hana Farzaneh MD[1], Sina Goodarzi MD[2], Sina Porkawosh MD[3], Parna Ghannadikhosh MD[4], Babak Ehsani Zonuz MD[5], Mohammad Reza Hosseini-Siyanaki MD[6], Shahriar Faghani MD[7], Arash Kamali MD[8]

[1]Mass General Hospital, Boston, MA, USA. [2]Lorestan University of Medical Sciences, Lorestan, Khoramabad, Iran, Islamic Republic of. [3]Urmia University of Medical Sciences, Urmia, Urmia, Iran, Islamic Republic of. [4]Tabriz University of Medical Sciences, Tabriz, Tabriz, Iran, Islamic Republic of. [5]Neuromusculoskeletal Research Center, Iran University of Medical Sciences, Tehran, Tehran, Iran, Islamic Republic of. [6]Department of Diagnostic and Interventional Radiology, University of Minnesota, Minneapolis, MN, USA. [7]Department of Radiology, University of Pennsylvania, philadelphia, pennsylvania, USA. [8]Department of Neuroradiology, University of Texas, Houston, Texas, USA

Purpose

Artificial intelligence (AI) has become increasingly relevant in neuro-oncology, particularly for tumor classification. This systematic review was undertaken to evaluate the performance of machine learning (ML) and deep learning (DL) methods in differentiating oligodendroglioma from astrocytoma on medical imaging.

Materials & Methods

The current systematic review was performed in accordance with the Preferred Reporting Items for Systematic Reviews and Meta-Analyses guidelines (1). A comprehensive search was conducted in PubMed, Scopus, Web of Science, Embase, and ProQuest databases using key terms related to Machine learning", "Deep learning", "Oligodendroglioma", and "Astrocytoma". Extracted data included 1st author, year of publication, data source, study design, inclusion/exclusion criteria, sample size, number of oligodendroglioma patients, number of astrocytoma patients, imaging sequences, AI approach, validation status, reported AUC, overall accuracy, overall sensitivity, overall specificity.

Results

Out of 395 identified articles, seven studies met inclusion criteria. The cumulative review involved 1170 patients with all subtypes of glioma, including 351 with oligodendroglioma and 333 with astrocytoma. Patients underwent imaging such as APTw CEST MRI, T1-weighted (T1w), T2-weighted (T2w), FLAIR, post-contrast T1-weighted (T1ce), and diffusion tensor imaging (DTI). Four studies utilized ML, and three studies used DL approaches. Data on four critical metrics were extracted, including Area Under the Curve (AUC), accuracy, sensitivity, and specificity. Reported AUC values ranged from 0.63 to 0.99. Accuracy, sensitivity, and specificity were reported in the ranges of 63_96%, 50_97%, and 89_95%, respectively. While AI shows promise, current evidence is limited by small sample sizes and methodological heterogeneity.

Conclusion

Although AI-based approaches demonstrate promising potential for differentiating oligodendroglioma from astrocytoma, diagnostic performance varied widely across studies. This variability highlights the importance of standardized imaging protocols, rigorous validation, and larger prospective investigations to achieve more reliable and clinically applicable outcomes.

References

1. Page MJ, McKenzie JE, Bossuyt PM, Boutron I, Hoffmann TC, Mulrow CD, et al. The PRISMA 2020 statement: An updated guideline for reporting systematic reviews. Int J Surg. 2021;88:105906.

Images/Tables

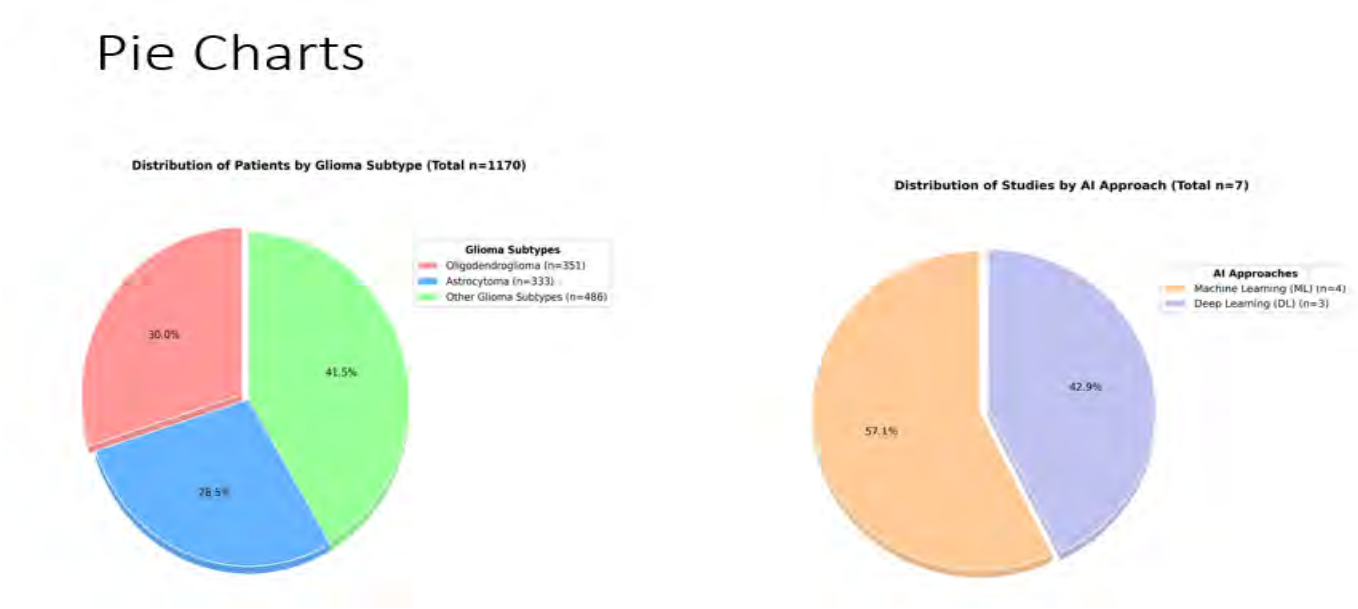

1063 Visualization of Recurrent Laryngeal Nerve in Cadavers on Sub-millimetric CISS MRI: A SPARC-REVA Study

Shruti Kumari MD, Mridhula Muthukumar MS, Ari Blitz MD
University Hospitals, Case Western Reserve University, Cleveland, Ohio, USA

Purpose

Recurrent laryngeal nerve (RLN) preservation is an essential component of thyroid and parathyroid surgeries. Permanent RLN injury can result in dysphonia, aspiration, and dyspnea with a significant impact on patient quality of life. Pre-operative imaging can determine both the location and trajectory relative to key cervical structures and guide surgical planning or be used with a navigation system during surgery to localize and preserve RLN in real-time. Despite its clinical importance, current clinical MRI does not routinely allow for visualization of the recurrent laryngeal nerve (RLN) as its imaging is fraught with several technical challenges, including small size and physiological motion in the neck. Routine clinical use of CISS to visualize the vagus nerve and its branches in patients is limited.

The purpose of this study is to evaluate the extent to which left and right RLN can be visualized on sub-millimetric 3-dimensional CISS MRI with isotropic resolution in human cadavers from its origin from CN X up to its entry into the larynx.

Materials & Methods

A prospective study of 54 cadavers with 3-dimensional isotropic 0.5-0.6 mm CISS on 3T MRI was conducted between February 2022 and June 2025. Two readers evaluated visualization of RLN using a qualitative scale from 0 to 3, with 3 being the best. The scale was defined as follows:

0-RLN not seen;

1-RLN followed up to the superior border of aortic arch on the left and right subclavian artery on the right;

2-RLN followed up to the thyroid isthmus (T2 vertebral level);

3-RLN followed up to the inferior cornu of thyroid cartilage before its entry into the larynx

A paired t-test was conducted to compare the mean scores between the left and right RLN. Inter-observer agreement on the Likert scales was tested using weighted κ analysis with quadratic weights.

Results

- 0.5mm-0.6mm CISS MRI allows for visualization of right and left RLN cadavers.
- The left RLN had an average visibility score of1.65 ± 0.84, while the right RLN had an average score of1.41 ± 1.05.
- We identified a non-recurrent RLN on the right side with findings confirmed on anatomic dissection.
- Overall, left RLN had a better visibility rating than the right.

Conclusion

In cadavers, the use of CISS MRI allows for excellent visualization of left and right RLN. Translation of this to living subjects with contrast administration and motion compensation techniques can be extremely valuable for pre-operative evaluation to prevent RLN injury, which is frequently encountered in procedures, especially thyroid and parathyroid surgeries.

References

- Randolph GW, editor. The recurrent and superior laryngeal nerves. New York, NY, USA:: Springer; 2016 May 27.
- Daniel A Herzka, Michael Markley, Noa B Nuzov, Goksel Sali, Shruti Kumari, Nicole A Pelot, Andrew J. Shoffstall, Chris Flask, Andrew R. Crofton, Ari Blitz 2025. REVA #3: Magnetic Resonance Imaging (MRI) of Embalmed Cadaver. **protocols.io** https://dx.doi.org/10.17504/protocols.io.6qpvrw9ezlmk/v1
- Wen J, Desai NS, Jeffery D, Aygun N, Blitz A. High-resolution isotropic three-dimensional MR imaging of the extraforaminal segments of the cranial nerves. Magnetic Resonance Imaging Clinics. 2018 Feb 1;26(1):101-19.

Images/Tables

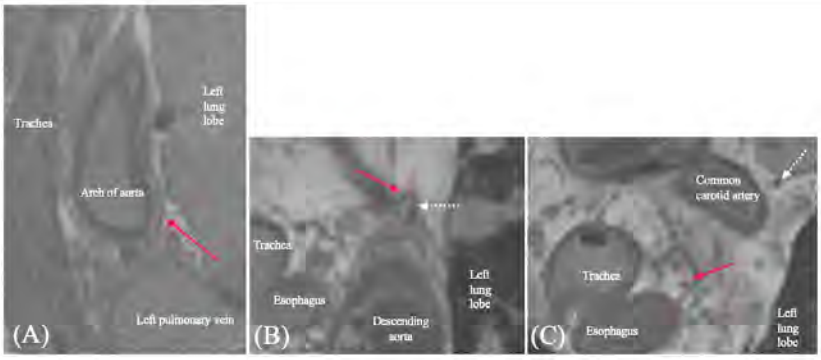

Fig.1 : (A) Curved MPR of CISS MRI in sagittal view showing left Recurrent laryngeal Nerve (RLN) (red arrow) going around the arch of aorta; (B) Axially reformatted CISS image of left RLN as it branches off the main trunk of CN X below the arch of aorta; (C) Axially reformatted CISS MRI of left RLN as it travels along the trachea-esophageal groove in the thorax going up to the larynx; main trunk of CN X (dotted white arrow);

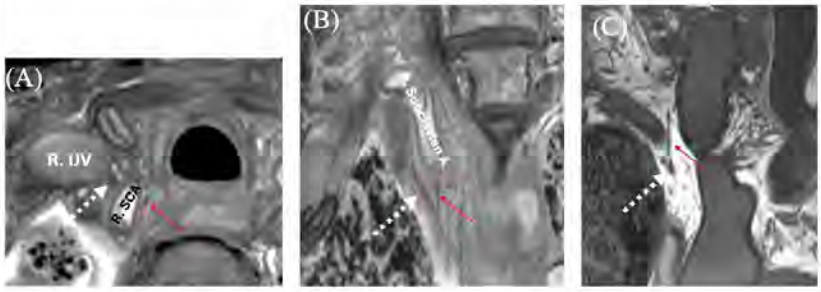

Fig.2 : (A) Axial MPR of CISS MRI showing right Recurrent laryngeal Nerve (RLN) (red arrow) going around the right subclavian artery; (B) Coronally reformatted CISS image of right RLN as it branches off the main trunk of CN X below the right subclavian artery; (C) Coronally reformatted CISS image of right RLN as it branches off the main trunk of CN X below the right subclavian artery; main trunk of CN X (dotted white arrow);

1071 Multimodal Analysis of CIC Mutation, Tumor Grade, and Survival in Oligodendroglioma: Clinical and MRI-Based Radiomics Insights

Mohammadreza Amjadzadeh MD[1], Nasim Batavani MD[1], Priyadarshini Mamindla MS[1], Vishal Peddagangireddy MS[1], Catherine Garcia MD[2], Mehtap Beker-Acay MD[1], Nazanin K. Majd MD[2], Rivka R. Colen MD[3]

[1]Hillman Cancer Center, University of Pittsburgh Medical Center, Pittsburgh, Pennsylvania, USA. [2]Department of Neuro-Oncology, The University of Texas, MD Anderson Cancer Center, Houston, TX, USA. [3]Hillman Cancer Center, University of Pittsburgh Medical Center, Pittsburgh, PA, USA

Purpose

To investigate clinical, demographic, and MRI-based radiomic texture features associated with survival outcomes, CIC mutation status, tumor grade, and disease status in patients with oligodendroglioma through descriptive statistical analyses, Kaplan–Meier survival analysis, and predictive radiomic modeling.

Materials & Methods

We retrospectively analyzed clinical and demographic variables included age, sex, tumor grade, disease status (newly diagnosed vs recurrent), and CIC mutation status. Overall survival (OS) and progression-free survival (PFS) were calculated using the Kaplan–Meier method. Group differences were assessed using the log-rank test. Associations between CIC mutation and disease status were assessed using Chi-square and Fisher's exact tests, followed by logistic regression adjusted for grade, age, and sex. Regions of interest (ROIs) including tumor, edema, necrosis, and hemorrhage were segmented on MRI scans using 3D-Slicer. Following intensity normalization, first-order (intensity-based) and second-order features (spatial relationships across four orientations derived from the Gray-Level Co-occurrence Matrix [GLCM]) were extracted from each ROI (1, 2). After quantization of each ROI at multiple gray levels, features were normalized to patient-specific white matter and ROI volume. A total of 400 features per ROI were computed. After removing highly correlated features (Pearson's correlation coefficient > 0.85), feature selection was performed using ElasticNet and Ridge regularization. Predictive models were developed using the XGBoost algorithm with hyperparameter tuning (*max_depth, gamma, learning_rate, n_estimators*) and three-fold cross-validation.

Results

50 patients (*CIC*-mutant: 29 [58%], wild-type: 21 [42%]; newly diagnosed: 28, recurrence: 22) entered the study. Median OS and PFS were 86.6 and 43.6 months, respectively (mean ± SD: OS, 108.6 ± 87.5 months; PFS, 62.1 ± 56.3 months). The 2-, 5-, 10-, 15-, and 20-year OS probabilities were 100%, 100%, 88.5%, 49.9%, and 41.6%, respectively, while PFS probabilities were 89.3%, 49.5%, 28.3%, 14.1%, and 0%. Kaplan–Meier analysis demonstrated significantly improved OS in CIC-mutant patients compared to wild-type (log-rank $p < 0.05$). PFS did not differ significantly across CIC mutation status, tumor grade, or disease status. Chi-square and Fisher's exact test showed no significant association between CIC mutation and disease status ($\chi^2 = 0.45$, $p = 0.50$; Fisher's exact OR = 0.57, 95% CI 0.14–2.35, $p = 0.39$). In the multivariate logistic regression model ($p = 0.037$; Pseudo $R^2 = 0.15$), age was independently associated with disease recurrence (OR = 0.92, $p = 0.018$), grade showed a borderline effect (OR = 3.41, $p = 0.073$), and CIC mutation was not significant (OR = 0.60, $p = 0.46$). For disease status prediction, the optimal model used five ElasticNet-selected texture features, achieving 86% accuracy, 90% sensitivity, 82% specificity, and 0.86 AUC. For tumor grade prediction, seven Ridge-selected features yielded 74% accuracy, 70% sensitivity, 78% specificity, and 0.69 AUC. For CIC mutation prediction, five ElasticNet-selected features achieved 84% accuracy, 83% sensitivity, 86% specificity, and 0.83 AUC.

Conclusion

CIC mutation status was a significant predictor of overall survival in oligodendroglioma. Additionally, MRI-based radiomics demonstrated strong potential for noninvasive prediction of CIC mutation, disease status, and tumor grade, underscoring its potential as a complementary imaging biomarker that could enhance molecular stratification and guide personalized management in oligodendroglioma.

References

1. Haralick RM, Shanmugam K, Dinstein I. Textural features for image classification. IEEE Trans Cybern 1973;Smc3(6):610–21.
2. Löfstedt T, Brynolfsson P, Asklund T, et al. Gray-level invariant Haralick texture features. PLoS One 2019;14(2):e0212110.

Images/Tables

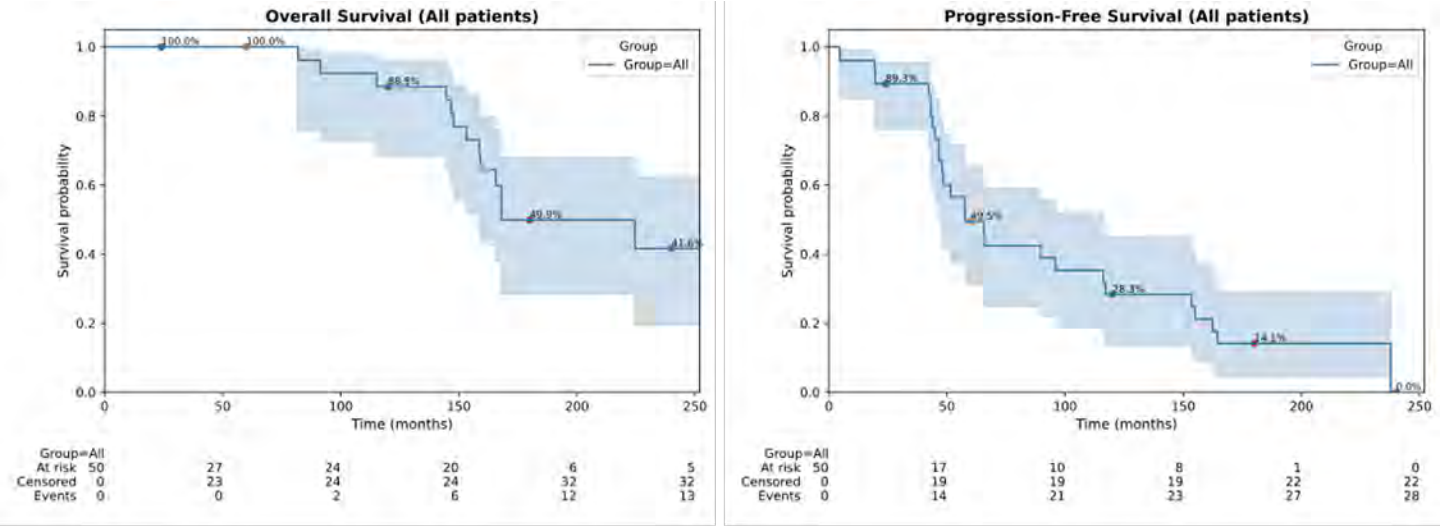

Figure1. Kaplan–Meier curve for overall survival (OS) and progression-free survival (PFS)

1079 Anatomy-Guided 3D Generative Framework for Missing MRI Sequence Synthesis

Moinak Bhattacharya BS[1], Angela Lignelli MD[2], Prateek Prasanna PhD[1], Gagandeep Singh MD[2]
[1]Stony Brook University, Stony Brook, NY, USA. [2]Columbia University, New York City, NY, USA

Purpose

In clinical neuroimaging, incomplete multi-contrast MRI protocols continue to be a significant limitation. Missing sequences like T2-FLAIR make it difficult to accurately characterize lesions, monitor treatment, and harmonize across sites. Current synthesis techniques that rely on 2D diffusion or GAN architectures frequently overlook 3D anatomical context, which results in anatomically unrealistic reconstructions and spatial discontinuities that impair clinical interpretability. In order to guarantee spatial and morphological consistency, this work creates a 3D anatomically guided diffusion framework that explicitly incorporates structural priors from anatomical masks. Our model improves data completeness, diagnostic fidelity, and downstream analytic reliability by ensuring anatomical correctness during synthesis and producing realistic, volumetrically coherent MRI sequences, such as predicting T2-FLAIR from T2-weighted scans.

Materials & Methods

The proposed framework utilizes a 3D SPADE (Spatially-Adaptive Normalization) based generative model that directly conditions MRI synthesis on anatomical structures. SPADE integrates tissue segmentation or parcellation masks into the generator, enabling anatomical regions to influence feature modulation and maintain spatial coherence during synthesis. This structural conditioning allows the model to preserve the geometric integrity of cortical and subcortical regions while effectively replicating modality-specific contrast features. The framework, trained on multi-sequence brain MRI from the BraTS-AG dataset (T2W, T2F, T1C) alongside anatomical masks generated using SynthSeg, exhibits superior cross-sequence generation and reconstruction capabilities, as assessed by PSNR and SSIM metrics.

Results

The proposed framework demonstrated high-fidelity synthesis of brain MRI sequences utilizing various conditioning strategies for 116 patients. For the Anatomy-to-Sequence experimental setting, the use of different anatomical priors yielded robust reconstructions, achieving mean PSNR/SSIM values of 26.18/0.84 for T1C, 27.90/0.84 for T2F, and 29.25/0.91 for T2W. For the Sequence-to-Sequence experimental setting, the method demonstrated moderate quality in cross-modal synthesis (e.g., T1C-to-T2W, T2F-to-T1C), with PSNR values between 23.8 and 26.1 dB and SSIM ranging from 0.78 to 0.82. This indicates difficulties in achieving both modality-specific contrast and anatomical coherence. The integration of anatomical control with sequence conditioning significantly enhanced image realism and structural consistency, resulting in PSNR/SSIM values of 29.76/0.93 for T2W-to-T2F and 28.95/0.91 for T2W-to-T1C synthesis. The findings indicate that explicit anatomical guidance improves multi-sequence translation, enhancing perceptual fidelity and structural alignment across modalities.

Conclusion

This study presents a 3D anatomy-guided generative framework for MRI sequence synthesis, which produces anatomically consistent and clinically realistic image contrasts. The integration of structural priors and contrast-aware modeling facilitates high-fidelity multi-modal MRI completion, thereby supporting downstream applications including automated segmentation, longitudinal analysis, and disease progression modeling in neuro-imaging.

References

Bhattacharya, M., Gupta, S., Singh, A., Chen, C., Singh, G., & Prasanna, P. (2025). BrainMRDiff: A Diffusion Model for Anatomically Consistent Brain MRI Synthesis. *arXiv preprint arXiv:2504.04532*.

Images/Tables

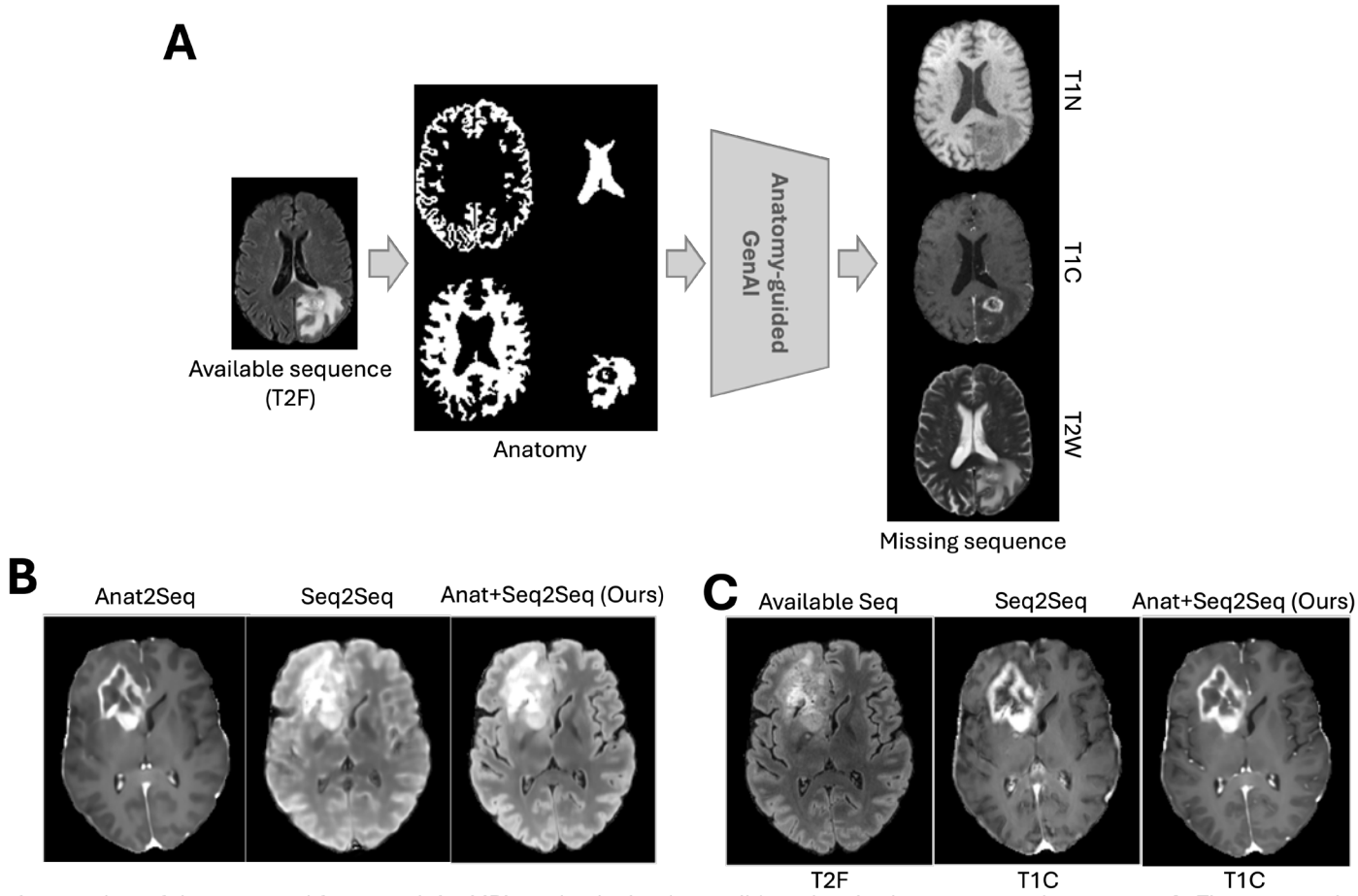

An overview of the proposed framework for MRI synthesis that is conditioned on both anatomy and sequence. **A.** The proposed pipeline: the multi-anatomy generative AI architecture uses available MRI sequences and matching anatomical masks as inputs to produce the missing target sequence. **B.** Samples of synthesized images from three different approaches: Anatomy-to-Sequence (Anat2Seq), Sequence-to-Sequence (Seq2Seq), and the proposed joint Anatomy + Sequence-to-Sequence (Anat + Seq2Seq) model, which combines available contrasts and anatomical priors for better synthesis. **C.** A comparison of the generated outputs and available input sequences from the Anat + Seq2Seq and Seq2Seq models, showing improved contrast fidelity and anatomical consistency in the suggested approach.

1089 Reduced antiplatelet therapy in the treatment of unruptured distal intracranial aneurysms arising from small caliber vessels with surface-modified flow diverter (P48 MW HPC): a multicenter comparison of single versus dual antiplatelet therapy

Ali Khanafer Dr., Hans Henkes Prof. Dr.
Klinikum Stuttgart, Stuttgart, Baden Wüttenberg, Germany

Purpose

To compare safety and efficacy of prasugrel-based single antiplatelet therapy (SAPT) versus dual antiplatelet therapy (DAPT) in patients with unruptured saccular aneurysms in small-caliber parent vessels treated with a hydrophilic polymer-coated (HPC) p48 flow diverter (FD).

Materials & Methods

Methods: We conducted a multicenter, retrospective cohort study of adults with unruptured saccular aneurysms in small-caliber (≤2 mm) parent vessels treated with the p48 HPC FD. The primary efficacy outcome was complete occlusion within the first 12 months. The primary safety outcome was MRI-detected silent ischemic lesions within 48 hours post-procedure and complications. Secondary outcomes were hemorrhagic complications, ischemic events, or mortality within 180 days post-treatment.

Results

Results: A total of 109 patients were treated (mean age 60.5 years; 68% female). SAPT and DAPT were used in 51 (47%) and 58 (53%) patients. Complete occlusion within the first 12 months was achieved in 80.4% and 66.7% (p = 0.089). Ischemic and hemorrhagic event rates did not differ significantly (3.9% vs. 6.9%, p = 0.219; 0% vs. 5.2%, p = 0.100, respectively). No significant difference in postprocedural silent emboli between the two groups was found. In multivariate analysis, the antiplatelet regimen was not an independent predictor of complete occlusion (SAPT: OR 0.55, 95% CI 0.19–1.63; p = 0.279), whereas diabetes mellitus was a negative predictor (OR 0.26, 95% CI 0.07–0.96; p = 0.043)

Conclusion

Conclusions: In this multicenter cohort of small-vessel flow diversion with a surface-modified device, prasugrel-based SAPT achieved safety and efficacy comparable to DAPT, with a favorable, though non-significant, hemorrhage profile.

References

Khanafer A, Lobsien D, Sirakov A, Almohammad M, Schüngel MS, Pielenz D, Borgmann T, Hajiyev K, Bäzner H, Ganslandt O, Hennersdorf F, Cohen JE, Felber S, Schob S, Kemmling A, Sirakov S, Forsting M, Klisch J, Henkes H. Flow diversion with hydrophilic polymer coating with prasugrel as single

antiplatelet therapy in the treatment of acutely ruptured intracranial aneurysms: a multicenter case series, complication and occlusion rates. **J Neurointerv Surg.** 2025;17:870–877.
Khanafer A, Henkes H, Cohen J, Albiña-Palmarola P, Gomori JM, Forsting M, von Gottberg P. Endovascular treatment of distal anterior cerebral artery aneurysms using flow modulation devices: mid- and long-term results from a two-center study. **Front Neurol.** 2024;15:1368612.

1093 Diagnostic Utility of Arterial Spin Labeling MRI in Patients with Seizures: A Comparative Analysis with FLAIR Sequence and EEG

Mona Gad, Derek Tsang, Andrew Cho, Vivek Yedavalli
Department of Radiology and Radiological Science, Johns Hopkins University School of Medicine, Baltimore, MD, USA

Purpose

The primary goal of this study is to investigate the usefulness of ASL-perfusion imaging in determining the epileptogenic focus in patients with seizures and compare it with structural MRI sequences, particularly FLAIR, as well as electroencephalography (EEG) as the gold standard diagnostic tool in the setting of epilepsy.

Materials & Methods

We searched our medical records for patients who were presented to the brain attack team (BAT) with stroke-like symptoms and were diagnosed with seizures between July 2018 and October 2025. Data including age, sex, race, and premorbid mRS were collected. ASL abnormalities were classified as hyper- or hypoperfusion, based on visual assessment. Location of the abnormality was determined according to the involved brain lobe, cerebral hemisphere, thalamus, and cerebellum. ASL focality in a non-territorial distribution was categorized as either focal, multifocal, or hemispheric. Furthermore, ROI was used to quantitatively measure the cerebral blood flow in the abnormality (including the grey matter) and compared to the corresponding area on the contralateral hemisphere. Structural MRI images were evaluated to determine the etiology of epilepsy. FLAIR abnormalities were categorized according to the location. Both ASL and FLAIR abnormalities were compared with each other and with the seizure focus determined by clinical information and EEG.

Results

Of our total 81 patients, 58 had complete data for statistical analysis. Several variables demonstrated complete separation (i.e., were 100% predictive of EEG abnormality), including hemispheric ASL focality, premorbid mRS scores 1, 2, and 4, and ASL localization in the frontal lobe, holohemispheric, cerebellum, and thalamus. To create a stable model, these categories were collapsed. In our final multivariable logistic regression (Table 1), ASL focality was the strongest predictor of EEG abnormality. Compared to patients with no ASL abnormality, those with focal ASL had 44.6 times the odds (95% CI 2.93–3471, p=0.023) and those with multifocal/hemispheric ASL had 214 times the odds (95% CI 7.68–39652, p=0.009) of an abnormal EEG. No other covariates were statistically significant. A separate model of the remaining ASL localizations (temporal, parietal, and occipital) showed no significant association.

Conclusion

ASL-MRI perfusion has the potential to demonstrate the cerebral blood flow alterations in the setting of seizure, which represents a major stroke mimic. Furthermore, it can accurately predict and delineate the epileptogenic focus with high diagnostic accuracy and concordance to EEG. Hence, it can be used as a reliable imaging marker for detection and localization of the epileptogenic zone, which has significant implications on the patient's outcome.

References

1. Zeng JY, Hu XQ, Xu JF, Zhu WJ, Wu HY, Dong FJ. Diagnostic Accuracy of Arterial Spin-Labeling MR Imaging in Detecting the Epileptogenic Zone: Systematic Review and Meta-analysis. AJNR Am J Neuroradiol. 2021 Jun;42(6):1052-1060. doi: 10.3174/ajnr. PMID: 33766822
2. Kim TJ, Choi JW, Han M, Kim BG, Park SA, Huh K, Choi JY. Usefulness of arterial spin labeling perfusion as an initial evaluation of status epilepticus. Sci Rep. 2021 Dec 20;11(1):24218. doi: 10.1038/s41598-021-03698-7. PMID: 34930959
3. Lee SM, Kwon S, Lee YJ. Diagnostic usefulness of arterial spin labeling in MR negative children with new onset seizures. Seizure. 2019 Feb;65:151-158. doi: 10.1016/j.seizure.2019.01.024. Epub 2019 Jan 27. PMID: 30718217

Images/Tables

Table 1. Adjusted Odds Ratios for Predicting EEG Abnormality (N=58)

Predictor	Odds Ratio (OR)	95% Confidence Interval	p-value
ASL Focality (vs. None)			
Focal (Category 1)	**44.6**	**2.93 – 3471**	**0.023**
Multifocal/Hemispheric (Category 2+)	**214**	**7.68 – 39652**	**0.009**
Age (per year)	1.03	0.98 – 1.09	0.304
Sex (Male v.s. Female)	0.46	0.04 – 3.73	0.492
Race (vs. Black)			
White (Category 1)	0.31	0.03 – 3.06	0.311
Asian/Other (Category 2+)	0.55	0.02 – 20.7	0.717
Premorbid mRS (Disabled v.s. None)	3.54	0.19 – 405	0.494
FLAIR (Abnormal vs. None)	0.37	0.02 – 4.08	0.440

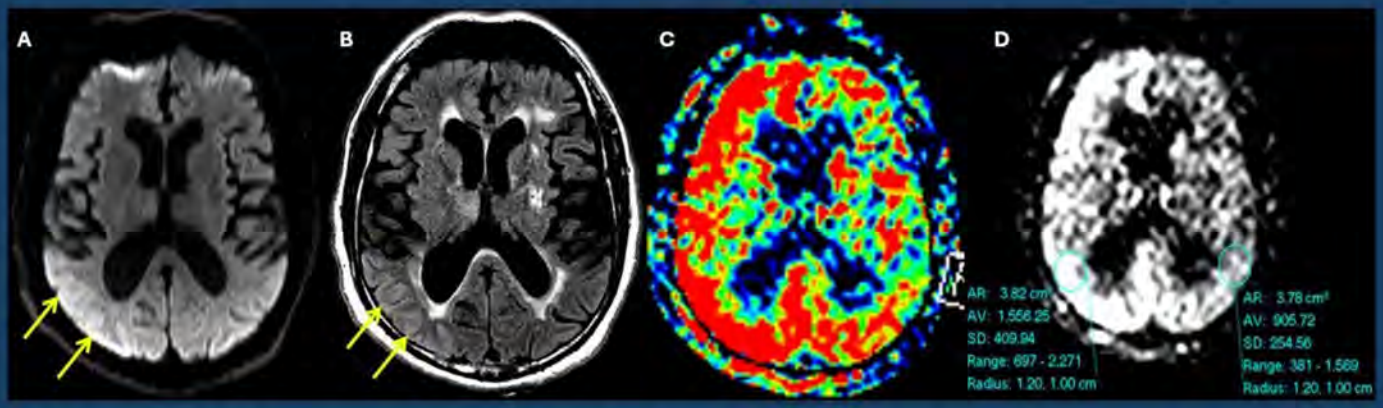

Fig.1 A 64yo male patient presented with status epilepticus. Axial DWI (A) and FLAIR (B) images show right parieto-occipital cortical restricted diffusion with corresponding FLAIR hyperintensity. Axial colored ASL map (C) shows diffuse increased perfusion over the right cerebral hemisphere. ASL-rCBF map (D) reveals hyperemia of the right cerebral hemisphere compared to the left one, evidenced by both qualitative and quantitative evaluation. EEG revealed severe cerebral disturbance over the right cerebral hemisphere, consistent with the perfusion abnormality detected on ASL.

1098 Topographic Profiles of Radio-pathomic Maps of Cellularity Near Contrast Enhancement Predict Overall Survival in Glioblastoma

Benjamin Chao, Samuel Bobholz PhD, Savannah Duenweg PhD, Aleksandra Winiarz, Allison Lowman, Daniel Kim, Hope Reecher, Mrina Mtenga, Adam Lahrache, Fitzgerald Kyereme, Elaine Tanhehco MD, Jennifer Connelly MD, Max Krucoff MD, E. Kelly Mrachek MD, Rupen Desai MD, Jennifer Tuscher PhD, Peter LaViolette

Medical College of Wisconsin, Milwaukee, WI, USA

Purpose

The bulk of a Glioblastoma (GBM) brain tumors enhance on T1-weighted MRI with the injection of Gd contrast agents, though infiltrative tumor cells invade well past this margin[1]. In this work, we explore radio-pathomic maps of cell density, shown to accurately predict cell density from commonly acquired clinical MR images, to explore the contrast enhancing margin[2, 3]. We hypothesized that image-derived cell density patterns near the contrast enhancing rim could predict overall survival.

Materials & Methods

The publicly available UPENN-GBM dataset[4] and UCSF-PDGM v2 datasets[5] contain presurgical clinical images, with radiologist-drawn annotations of contrast enhancement (CE) and associated survival data. For each patient, radio-pathomic maps of cell density were created using standard clinical imaging, and masks of brain tissue were extracted using HD-BET. Brain tissue voxels were assigned a distance from the CE border at increments of ±0.5 mm. Cell density values were averaged within each of these bins. Profiles from the UPENN dataset were averaged to determine a reference cell density vs distance from CE lesion border graph. The UCSF patients' cell density profiles were compared to this reference line. Two regions of interest were defined: 1) 0-2 mm from the edge within the CE ROI and 2) 0 to 5 mm outside the CE ROI. Patients were split into four groups depending on their

average cell density deviation from the UPENN-derived reference line: 1) above-within/above-outside CE, 2) above-within/below-outside CE, 3) below-within/above-outside CE, and 4) below-within/below-outside CE.

Results

In the UPENN cohort, we see a distinct trend of cellularity near the CE border: high cell density just inside the border, rapidly decreasing at the border, and leveling out around 2 mm. UCSF cohort patients with less hypercellularity within their inner CE tumor border compared to the UPENN reference, and with higher hypercellularity outside the CE tumor border (inner-below/outer-above) had a statistically significant survival advantage over each of the other 3 groups. The inner-below/outer-above had a median survival 73 days longer (p=0.01) than the inner-above/outer-above. The inner-below/outer-above had a median survival 23 days longer (p=0.04) compared to the inner-above/outer-below. Finally, the inner-below/outer-above had a median survival 37 days longer (p=0.04) than the inner-below/outer-below group.

Conclusion

In this work, we found higher cellularity inside the CE margin is associated with shorter overall survival, while higher cellularity outside the CE margin seems to have a positive impact on overall survival prior to treatment. Biologically, higher cellularity inside the CE margin may represent a more aggressive tumor subtype, leading to poorer survival. Higher cellularity outside the tumor margin may represent a strong cellular immunological response to the tumor, contributing to the patient's prolonged survival. This work raises new questions about the tumor microenvironment near the contrast enhancing margins.

References

1. Lasocki A, Gaillard F. Non-Contrast-Enhancing Tumor: A New Frontier in Glioblastoma Research. AJNR Am J Neuroradiol. 2019;40(5):758-765. doi:10.3174/ajnr.A6025

2. Bobholz SA, Lowman AK, Connelly JM, et al. Noninvasive Autopsy-Validated Tumor Probability Maps Identify Glioma Invasion Beyond Contrast Enhancement. Neurosurgery. 2024;95(3):537-547. doi:10.1227/neu.0000000000002898

3. Bobholz SA, Lowman AK, Brehler M, et al. Radio-Pathomic Maps of Cell Density Identify Brain Tumor Invasion beyond Traditional MRI-Defined Margins. AJNR Am J Neuroradiol. 2022;43(5):682-688. doi:10.3174/ajnr.A7477

4. Bakas S, Sako C, Akbari H, et al. The University of Pennsylvania glioblastoma (UPenn-GBM) cohort: advanced MRI, clinical, genomics, & radiomics. Sci Data. 2022;9(1):453. doi:10.1038/s41597-022-01560-7

5. Calabrese E, Villanueva-Meyer J, Rudie J, et al. The University of California San Francisco Preoperative Diffuse Glioma MRI (UCSF-PDGM). Published online April 7, 2023. doi:10.7937/TCIA.BDGF-8V37

Images/Tables

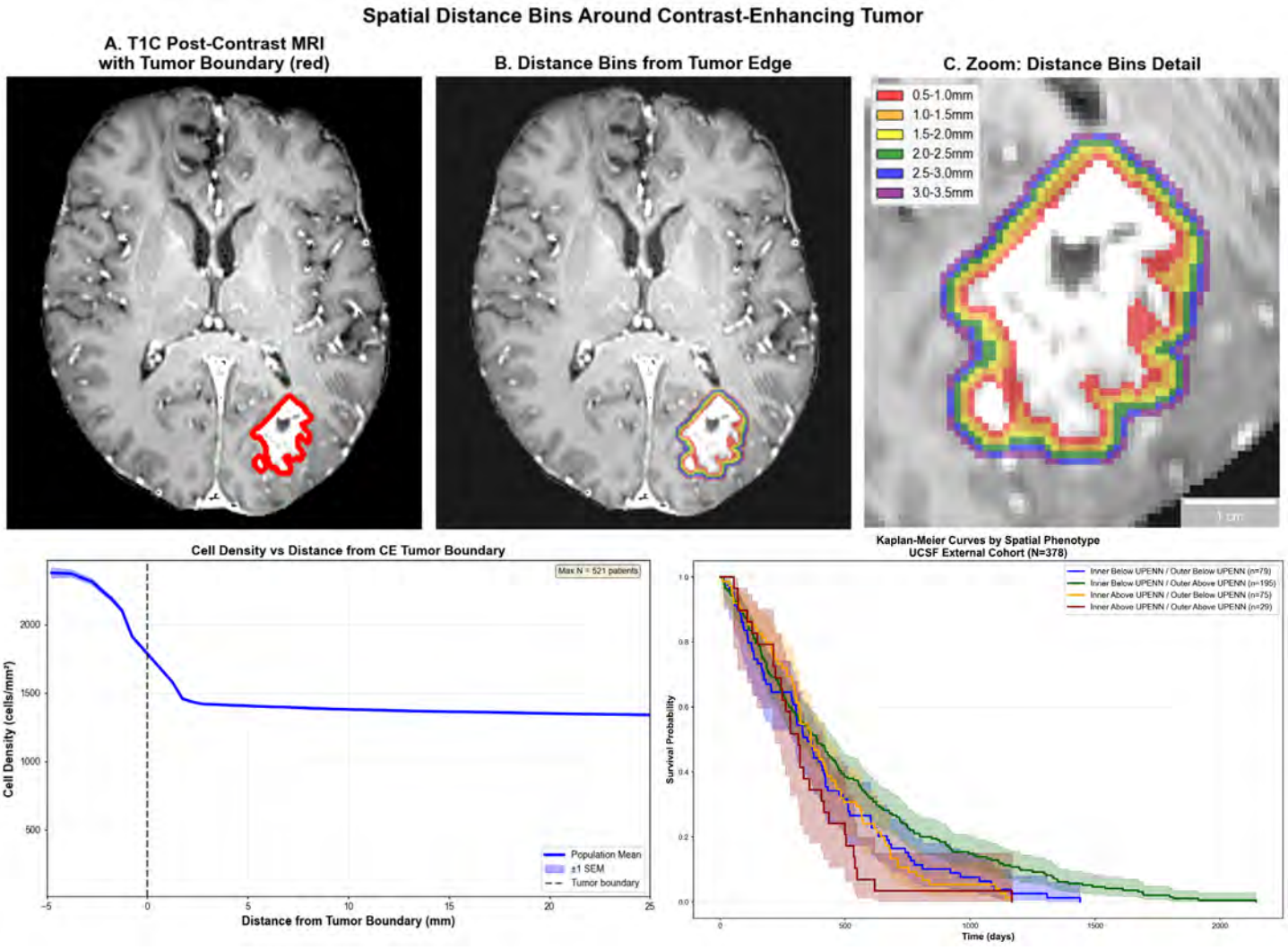

1105 Reduced Interpretation Time, Improved Detection of High-Grade Stenosis and Occlusions using Lumina3D: A Multi-Reader, Multi-Case Study

Justin Addicks MD, Dhairya A Lakhani MD
West Virginia University, Morgantown, WV, USA

Purpose

Timely detection of vessel occlusion and high-grade stenosis is crucial in stroke care. While CT angiography (CTA) source images are standard, interpretation can be time-consuming. 3D reconstructions improve anatomical clarity, but manual processing may take over 30 minutes. Lumina 3D by RapidAI automates this process, producing 3D head and neck reconstructions and curved planar reformats (CPRs) in minutes. This study evaluated Lumina 3D's impact on diagnostic accuracy and interpretation time.

Materials & Methods

Five radiologists (3 general, 2 neuro) reviewed 20 head and neck CTA cases using a randomized crossover design. Cases included large vessel occlusions (8), distal medium vessel occlusions (16), and/or high-grade stenoses (12), defined as >75% luminal narrowing. Reference diagnoses were established by consensus of 3 expert neuroradiologists with full clinical access. Each reader reviewed all 20 cases twice—once with and once without Lumina 3D —separated by a one-month washout. The review order was randomized. Readers identified vessels with occlusions or stenoses, simulating clinical conditions. Mixed models assessed accuracy (percent agreement with reference), accounting for reader and scan variability.

Results

The 20 cases included 24 occlusions and 11 stenoses across various vessels. With Lumina 3D, accuracy was 85.6% (95% CI: 73–98.5%) vs. 76.1% (95% CI: 63–89%) without it—an overall 9% improvement (p = 0.0004). Accuracy gains were independent of pathology type but varied by specialty: general radiologists improved 12%, neuroradiologists 6%. Stenosis detection was 7% more accurate than occlusion detection. Interpretation time decreased by 34 seconds per case (from 4.5 to 3.9 minutes; p = 0.027). General radiologists showed the greatest time savings (>1 minute).

Conclusion

Automated 3D reconstructions via Lumina 3D improved diagnostic accuracy and reduced interpretation time, particularly for general radiologists. These findings suggest Lumina 3D may enhance stroke workflows and support faster, more accurate treatment decisions.

References

1. Pula M, Kucharczyk E, Piersiak M, Ziomek M, Zdanowicz-Ratajczyk A, Guzinski M. Improved CTA imaging for stroke evaluation - deep learning and iterative reconstruction comparative study. Neuroradiology. 2025 Sep;67(9):2437-2445. doi: 10.1007/s00234-025-03733-8. Epub 2025 Aug 12. PMID: 40794135.

2. Yang Y, Huan X, Guo D, Wang X, Niu S, Li K. Performance of deep learning-based autodetection of arterial stenosis on head and neck CT angiography: an independent external validation study. Radiol Med. 2023 Sep;128(9):1103-1115. doi: 10.1007/s11547-023-01683-w. Epub 2023 Jul 18. PMID: 37464200.

Images/Tables

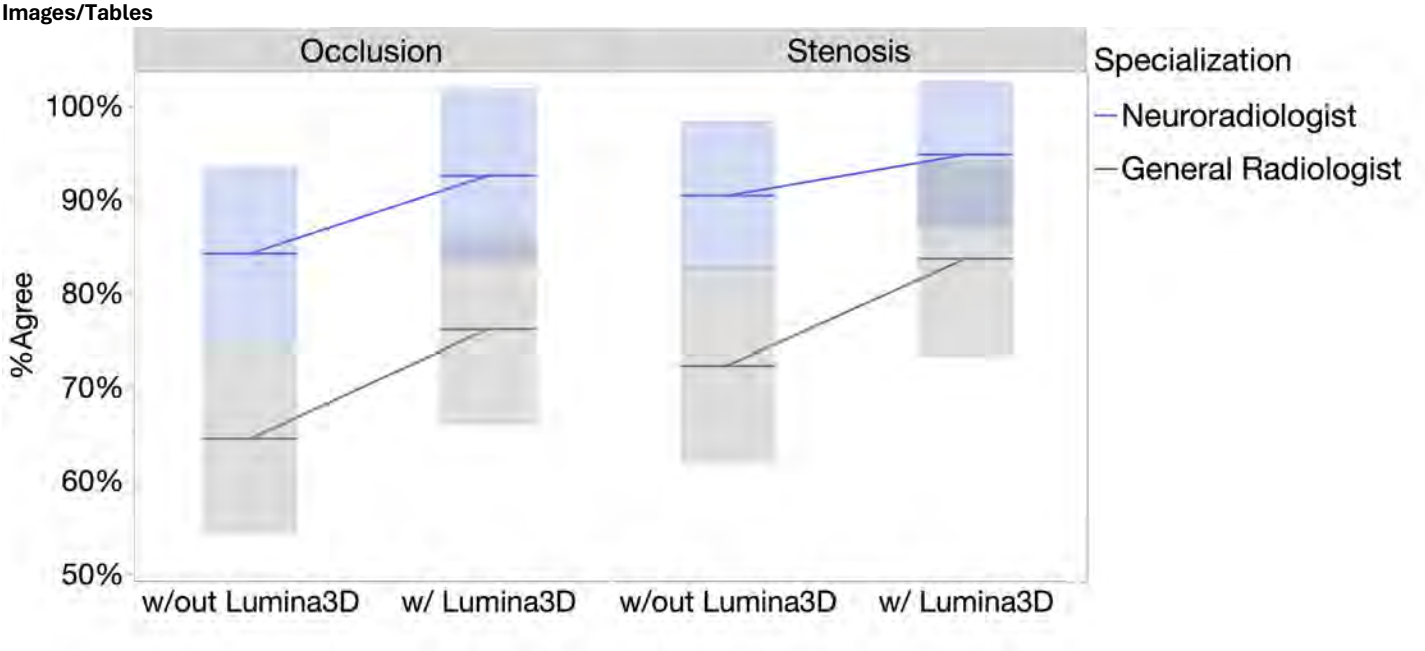

1125 Assessment of Factors Contributing to The Presence of Plaques and Intraplaque Hemorrhage in One or Multiple Vascular Beds of Patients with Stroke-Like Symptoms.

Hisham Alfarra M.D[1], Gador Canton[2], Cristina Sanchez-Vizcaino[2], Ahmed Safwat[2], Mona Kharaji[2], Maoxue Wang[2], Charles Watt[2], Dan Cheng[1], David Tirschwell[2], Thomas Hatsukami[2], Chun Yuan[2], Niranjan Balu[2], Mahmud Mossa-Basha[1]
[1]University of Alabama in Birmingham, Birmingham, Alabama, USA. [2]University of Washington, Seattle, Washington, USA

Purpose

To investigate the demographic and vascular risk factors contributing to the presence of atherosclerotic plaques and intraplaque hemorrhage (IPH) in both intracranial and extracranial vascular beds, and their co-occurrence across beds, in patients who underwent vessel wall MRI (vwMRI) with stroke-like symptoms.

Materials & Methods

We retrospectively reviewed patients evaluated for stroke-like symptoms between June 2022 and April 2024 who had undergone head and neck CTA and vwMRI as part of their diagnostic work-up. Patients with evidence of atherosclerosis in either the extracranial carotid or intracranial vascular beds

were included. We recorded the presence of IPH defined as a region of signal intensity intensity >150% of the adjacent sternocleidomastoid muscle in cases with carotid plaques, or the temporal muscle in cases with intracranial plaques [1], Demographic and clinical variables were also collected. We considered three different groups for each analysis: plaque/IPH only in the carotid, only intracranially, or in both.
Fisher's exact test and one-way ANOVA were used to assess differences in clinical and demographic variables across vascular beds, separately for (1) plaque and (2) IPH locations.

Results

Plaques were identified in 712 patients (mean age 68 +/- 13.4 years; 57% males). Patients with intracranial plaques only (n=58, 8%) were significantly younger (55.7 +/- 14.4 years; p<0.001) than those with only carotid plaques (n=200, 28%; 63.9 +/- 12.4 years) and those with plaques in both vascular beds (n=454, 64%; 71.7 +/- 12.1 years). Vascular risk factors, such as dyslipidemia and hypertension, were less common among patients with intracranial plaques only compared with the other groups (p=0.002, and p=0.004, respectively). Atrial fibrillation was absent among patients with exclusively intracranial plaques but was present in 22% of those with carotid plaques only and in 25% of those with plaques in both vascular territories (p=0.003). Plaque and IPH distribution across races differed significantly (p=0.032 and p=0.029 respectively).
IPH was detected in 201 patients (28.2%). Parallel to the plaque cohort, patients with intracranial IPH only (n=30, 15%) were significantly younger (69.3 +/- 13.1; p<0.001), and the Asian population was more represented in this group compared to the group with IPH only in carotid plaques, or in both beds. IPH was more prevalent among males independent of its location.

Conclusion

Our findings show that while atherosclerosis is a systemic condition, isolated intracranial atherosclerosis and associated high-risk features such as IPH occurred at a younger age compared to extracranial and multiple vascular bed disease. In addition, the distribution of racial groups among patients with isolated intracranial disease differed from those with extracranial and multiple vascular bed atherosclerosis [2-3]. Ongoing analyses aim to determine potentially modifiable factors that may further characterize this subgroup that may benefit from earlier targeted risk assessment and potentially tailored treatment approaches.

References

[1] Altaf N, MacSweeney ST, Gladman J, Auer DP. Carotid intraplaque hemorrhage predicts recurrent symptoms in patients with high-grade carotid stenosis. Stroke. 2007 May;38(5):1633-5. doi: 10.1161/STROKEAHA.106.473066. Epub 2007 Mar 22. PMID: 17379827.
[2] Watase H, Shen M, Sui B, Gao P, Zhang D, Sun J, Balu N, Hippe DS, Jarvik GP, Zhao X, Li R, Chen S, Yuan C, Hatsukami TS. Differences in atheroma between Caucasian and Asian subjects with anterior stroke: A vessel wall MRI study. Stroke Vasc Neurol. 2021 Mar;6(1):25-32. doi: 10.1136/svn-2020-000370. Epub 2020 Aug 13. PMID: 32792458; PMCID: PMC8005910.
[3] Suri MF, Johnston SC. Epidemiology of intracranial stenosis. J Neuroimaging. 2009 Oct;19 Suppl 1:11S-6S. doi: 10.1111/j.1552-6569.2009.00415.x. PMID: 19807851.

1132 Impact of the COVID-19 pandemic on outcomes of acute ischemic stroke patients treated with endovascular therapy: A multicenter Canadian study

Shenghua Zhu MD FRCPC[1], Ammar Alam BSc[2], Rebecca Thornhill PhD[1], Richard Aviv PhD[3], Vered Tsehmaister-Abitbul MD FRCPC[1], Grant Stotts MD FRCPC[1], Hailey Pettem RN[3], Ronit Agid MD FRCPC MSc[4], Aleksandra Pikula MD FRCPC[4], Jai J.S. Shankar MD FRCPC[5], Genevieve Milot MD FRCSC[6], Brian Van Adel MD FRCPC[7], Samuel Yip MD FRCPC[8], Robert Fahed MD MSc[1], Manraj Heran MD FRCPC[8], Fabio Settecase MD FRCPC[8], Marlise P dos Santos MD FRCPC MSc MPH[1]
[1]University of Ottawa, Ottawa, ON, Canada. [2]OHRI, Ottawa, ON, Canada. [3]The Ottawa Hospital, Ottawa, ON, Canada. [4]University of Toronto, Toronto, ON, Canada. [5]University of Manitoba, Winnipeg, MB, Canada. [6]Université Laval, Quebec, QC, Canada. [7]McMaster University, Hamilton, ON, Canada. [8]University of British Columbia, Vancouver, BC, Canada

Purpose

To determine the effect of COVID infection control protocols on the functional outcomes and angiographic time metrics of large vessel occlusion (LVO) acute ischemic stroke (AIS) patients treated with endovascular therapy (EVT).

Materials & Methods

Data were obtained from prospectively collected quality improvement stroke databases at six Canadian comprehensive stroke centres from March 11, 2020, to March 11, 2021. This patient cohort was compared to pre-pandemic patients consecutively treated with EVT from March 11, 2019, to March 10, 2020. The primary outcome is a 90-day modified Rankin Score (mRS). The secondary outcomes are angiographic time metrics.

Results

A total of 1329 EVT patients (pre-pandemic n = 666) were included. The initial NIHSS was statistically significantly lower in the pandemic cohort. Other baseline patient characteristics were comparable between the two periods. Median (interquartile range, IQR) time from last seen normal (LSN) to emergency department (ED) (172 (68–316) vs 210 (97–382) min; p = 0.0001), LSN to puncture (235 (160–378) vs 280 (184–475); p < 0.0001), computed tomography (CT) to angiographic table (68 (44–108) vs 84 (57–125) min; p = 0.002), ED to angiographic table (65 (37–96) vs 80 (50–112) min; p = 0.001), CT to recanalization (117 (84–156) vs 130 (89–173) min; p = 0.038) and LSN to recanalization (279 (198–453) vs 327 (219–561) min; p = 0.002) were longer in the pandemic period as compared to the pre-pandemic. There were no significant differences in median time from angiographic table to arterial puncture (13 (8–19) vs 12 (9–16) min; p = 0.70) or arterial puncture to first pass (21 (14–31) vs 20 (14–30) min; p = 0.50). Patients were more likely to have favourable outcomes (mRS at 90 days score of ≤ 2) post-EVT pre-pandemic than pandemic (53% vs 44%; p = 0.02). Furthermore, analysis of the time interval from “LSN to arterial puncture” in relation to functional outcomes showed that the percentage of unfavourable outcomes increased among patients who underwent EVT within 240 minutes. Specifically, the rate of unfavourable outcomes rose from 32.9% to 42.9% (p = 0.37 for intervals under 150 minutes) and from 41.6% to 52.3% (p = 0.15 for intervals between 151 and 240 minutes) when comparing pre-pandemic to pandemic periods. However, the detrimental effect associated with the pandemic was diminished in patients who received EVT beyond 240 mins (p = 1.0).

Conclusion

In this multicenter study involving six Canadian stroke centers, patients exhibited a higher probability of unfavourable long-term functional outcomes following EVT during the pandemic period compared to those in the pre-pandemic cohort, particularly during the first year of the pandemic.

References
1. Fraser JF, Arthur AS, Chen M, et al. Society of NeuroInterventional Surgery recommendations for the care of emergent neurointerventional patients in the setting of COVID-19. J Neurointerv Surg. 2020 Jun;12(6):539-541. doi: 10.1136/neurintsurg-2020-016098.
2. Soltany A, Hamouda M, Ghzawi A, et al. A scoping review of the impact of COVID-19 pandemic on surgical practice. Ann Med Surg (Lond). 2020 Jul 9;57:24-36. doi: 10.1016/j.amsu.2020.07.003. Erratum in: Ann Med Surg (Lond). 2023 Sep 29;85(10):5304. doi: 10.1097/MS9.0000000000001324.
Images/Tables

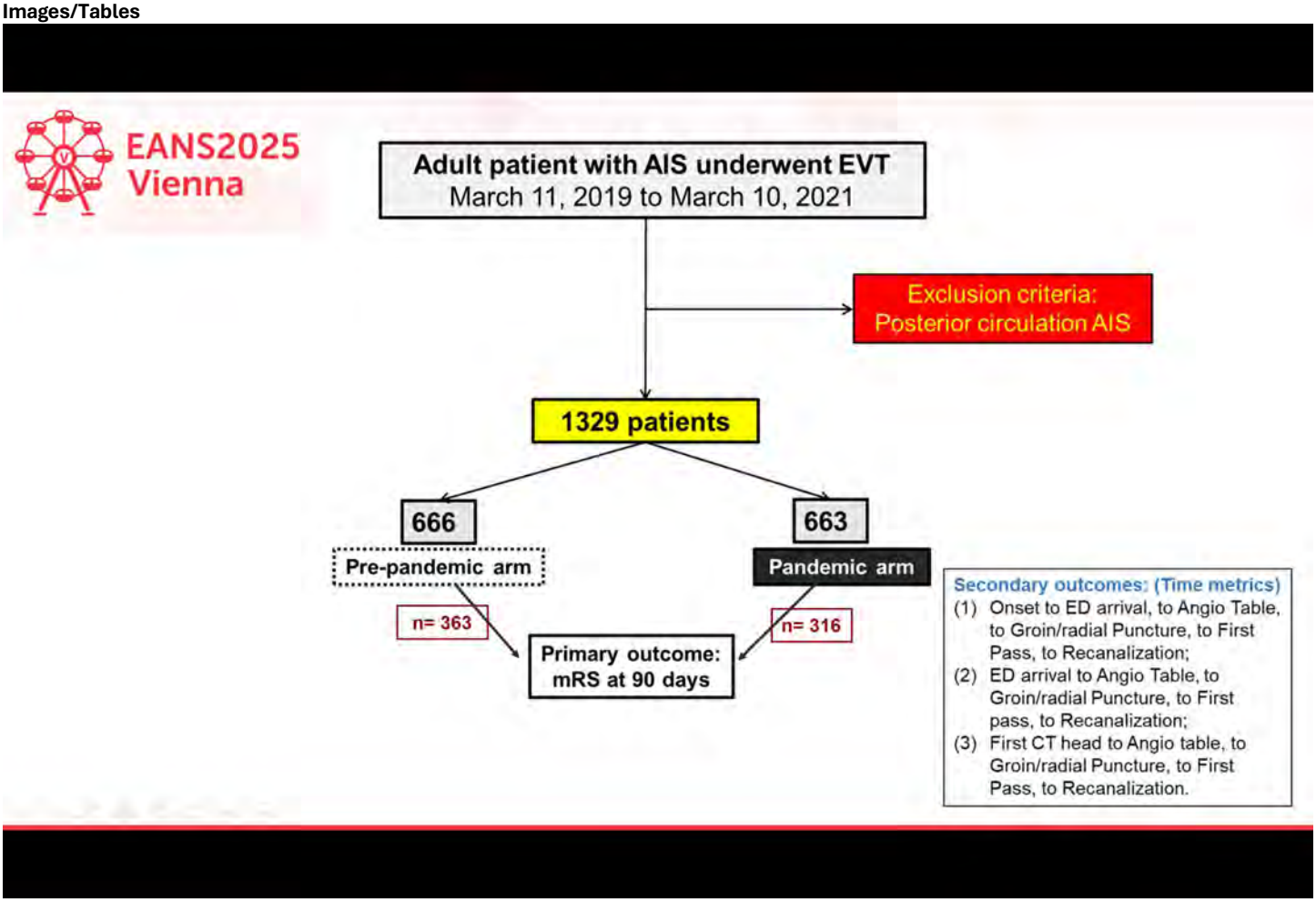

1138 Deep Learning Reconstruction Enables 3D Post-contrast T1-weighted Cube Sequence with Higher Acceleration for Brain Metastasis Detection

Sahar Alizada, Rami Eldaya, Amit Agarwal, Ziyi Li, Max Wintermark, Ho-Ling Anthony Liu
MD Anderson Cancer Center, Houston, Texas, USA

Purpose

Deep learning-based image reconstruction (DLBIR) techniques have the potential to enable higher acceleration for MRI acquisition while preserving image quality. In this study, we compared the image quality of a post-contrast T1-weighted Cube sequence with DLBIR and higher acceleration (3D-T1C+ $_{DLBIR}$) with a baseline post-contrast T1-weighted Cube sequence without DLBIR (3D- T1C+$_{SOC}$) for brain metastasis detection and evaluation.

Materials & Methods

Our retrospective study included 50 patients who underwent both T1-weighted Cube sequences following administration of a standard dose of Gadolinium-based contrast agent during the same study session. The order of the two sequences was balanced among the patients. 22 patients were scanned on a 1.5T Artist scanner (GE Healthcare, Milwaukee, WI) and 28 patients were scanned on a 3T Premier scanner (GE Healthcare, Milwaukee, WI). Higher parallel imaging factors were applied for 3D-T1C+ $_{DLBIR}$ with an acquisition time reduction of 24% (4:19 vs 5:42 min) at 1.5T and 27% (3:10 vs 4:19 min) at 3T. Two board-certified neuroradiologists assessed overall tissue contrast, overall signal-to-noise ratio (SNR), sharpness, extent of artifacts, and lesion conspicuity, if applicable, using 5-point Likert-like scales. Lesion conspicuity was graded separately for lesions <3 mm and >3 mm.

Results

3D-T1C+ $_{DLBIR}$ received higher ratings for overall tissue contrast (Hodges–Lehmann $\Delta \approx +0.50$ Likert points for 3D-T1C+ $_{DLBIR}$; $p < .001$), overall SNR ($\Delta \approx +0.50$; $p < .001$), and sharpness ($\Delta \approx +0.75$; $p < .001$). Artifact scores were similar (HL $\Delta \approx 0.00$; $p = 0.22$). All four image-quality endpoints met non-inferiority when compared to 3D- T1C+$_{SOC}$ at $\delta = 0.5$ (one-sided $p < 0.001$ for each), with superiority for SNR and sharpness. For lesion conspicuity, 3D-T1C+ $_{DLBIR}$was higher for lesions ≥3 mm (HL $\Delta \approx +0.75$ toward 3D-T1C+ $_{DLBIR}$; $p = 0.012$, $n = 18$), and similar for lesions <3 mm (HL $\Delta \approx 0.00$; $p = 0.9$, $n = 19$). No lesions were missed on either sequence (3D-T1C+ $_{DLBIR}$ or 3D- T1C+$_{SOC}$).

Conclusion

DLBIR allows higher accelerations for the post-contrast T1-weighted Cube sequence while maintaining or improving image quality for the detection and evaluation of brain metastasis, supporting its potential integration into standard imaging protocols.

References

1. Rai P, Mark IT, Soni N, Diehn F, Messina SA, Benson JC, Madhavan A, Agarwal A, Bathla G. Deep Learning-Based Acceleration in MRI: Current Landscape and Clinical Applications in Neuroradiology. AJNR Am J Neuroradiol. 2025 Jul 28:ajnr.A8943. doi: 10.3174/ajnr.A8943. Epub ahead of print. PMID: 40721279.

2. Kiryu S, Akai H, Yasaka K, Tajima T, Kunimatsu A, Yoshioka N, Akahane M, Abe O, Ohtomo K. Clinical Impact of Deep Learning Reconstruction in MRI. Radiographics. 2023 Jun;43(6):e220133. doi: 10.1148/rg.220133. PMID: 37200221.

3. Lebel, RM. Performance characterization of a novel deep learning-based MR image reconstruction pipeline. 2020 August. http://arxiv.org/abs/2008.06559

Images/Tables

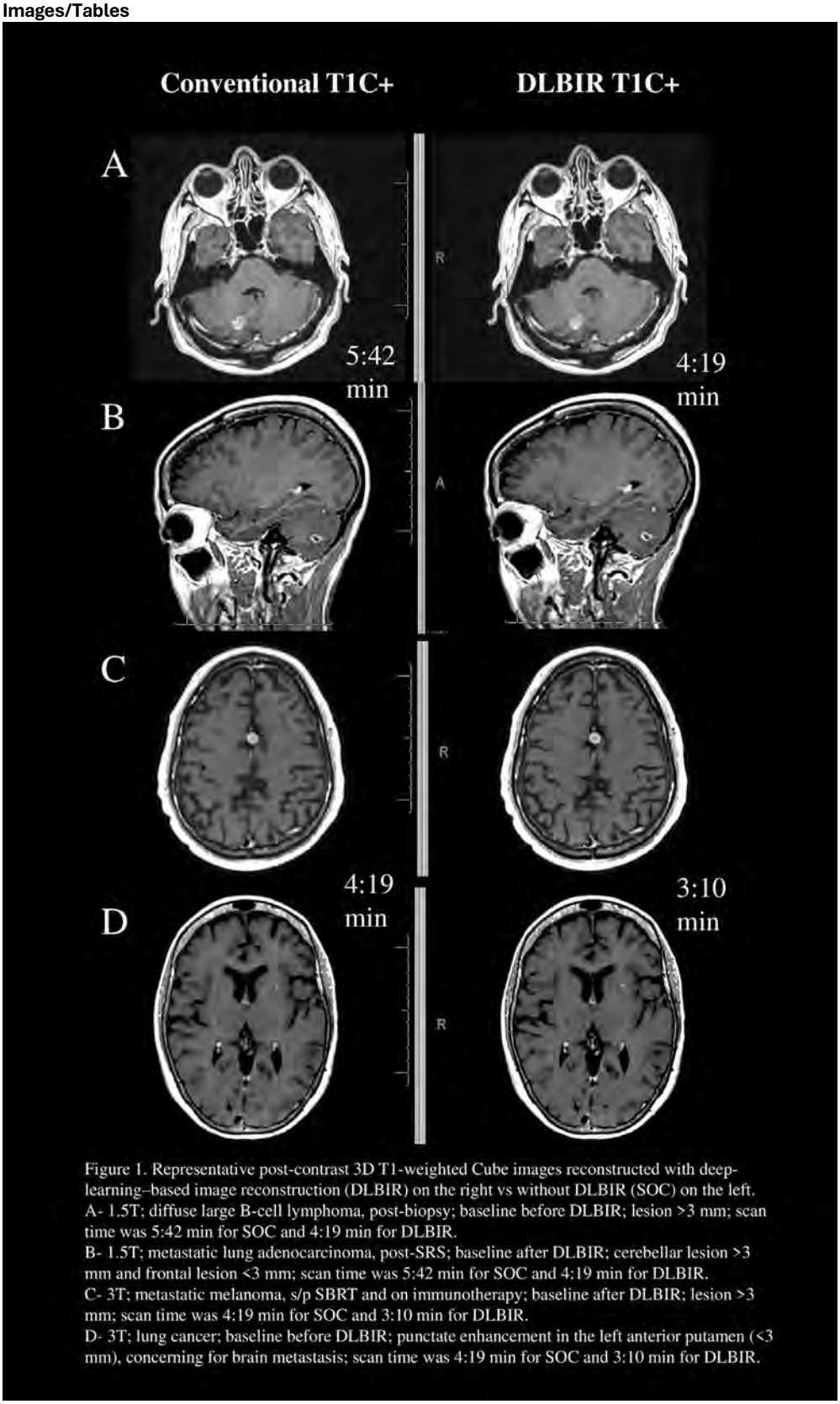

Figure 1. Representative post-contrast 3D T1-weighted Cube images reconstructed with deep-learning–based image reconstruction (DLBIR) on the right vs without DLBIR (SOC) on the left.
A- 1.5T; diffuse large B-cell lymphoma, post-biopsy; baseline before DLBIR; lesion >3 mm; scan time was 5:42 min for SOC and 4:19 min for DLBIR.
B- 1.5T; metastatic lung adenocarcinoma, post-SRS; baseline after DLBIR; cerebellar lesion >3 mm and frontal lesion <3 mm; scan time was 5:42 min for SOC and 4:19 min for DLBIR.
C- 3T; metastatic melanoma, s/p SBRT and on immunotherapy; baseline after DLBIR; lesion >3 mm; scan time was 4:19 min for SOC and 3:10 min for DLBIR.
D- 3T; lung cancer; baseline before DLBIR; punctate enhancement in the left anterior putamen (<3 mm), concerning for brain metastasis; scan time was 4:19 min for SOC and 3:10 min for DLBIR.

1144 Large Language Model-Based IDH Genotyping in Diffuse Gliomas from Expert Radiology Findings

James M Holcomb BS, Khushi Hiremath BME, Elizabeth M Davenport PhD, Florence L Chiang MD, PhD, Fabricio S Feltrin MD, Phd
UT Southwestern, Dallas, TX, USA

Purpose

Diffuse gliomas are aggressive primary malignancies associated with poor clinical outcomes. However, a mutation in the isocitrate dehydrogenase (IDH) enzyme confers significantly improved prognosis. While prior approaches using radiomics[1] and deep learning with convolutional neural networks[2] have demonstrated high accuracy in predicting IDH mutations, these methods rely on large datasets. Large language models (LLMs) represent a novel class of machine learning algorithms that demonstrate strong reasoning capabilities. This study investigates the use of LLM-generated embeddings derived from radiologist findings to predict IDH mutations in a small *n* dataset.

Materials & Methods

For this study, sample size was intentionally kept small. A total of 99 diffuse glioma cases were obtained from the UCSF-PDGM dataset.[3] One blinded board-certified neuroradiologist with over ten years of experience provided written findings for each case based on T1, T2, T2-FLAIR, T1 post contrast, and arterial spin labeling images. Findings focused on tumor location, T2/FLAIR mismatch sign, presence of enhancement or necrosis, and perfusion characteristics. These notes were compiled into a prompt for each case. The associated text embeddings from each prompt were then extracted from OpenAI's embedding-ada-002 model. A random forest model was trained on these embeddings along with Pyradiomics[4] features from each of the five image contrasts. Model performance was evaluated on an independent test set of 40 cases from the UCSF-PDGM dataset (20 IDH mutated, 20 wild-type). Findings for the test dataset were reported by a second blinded board-certified neuroradiologist with over 10 years of clinical experience.

Results

Direct classification by submitting prompts to ChatGPT yielded a poor accuracy of 52.5% on the held out test set. Similarly, just using Pyradiomics features yielded a poor 52.7% accuracy on the held out test set. In contrast, the random forest model trained on ChatGPT embeddings and Pyradiomics features achieved 92.5% accuracy on the held-out test set.

Conclusion

This study demonstrates that IDH mutation accuracy can be improved by using LLM-derived embeddings, even on a limited sample dataset. These findings underscore the potential of combining LLM reasoning capabilities with domain-expert annotation to develop efficient, non-invasive diagnostic tools.

References

1. Truong NC, Bangalore Yogananda CG, Wagner BC*, et al*. Two-stage training framework using multicontrast MRI radiomics for IDH mutation status prediction in glioma. *Radiology: Artificial Intelligence*. 2024;6(4):e230218.

2. Bangalore Yogananda CG, Wagner BC, Truong NC*, et al*. MRI-based deep learning method for classification of IDH mutation status. *Bioengineering*. 2023;10(9):1045.

3. Calabrese E, Villanueva-Meyer JE, Rudie JD*, et al*. The University of California San Francisco preoperative diffuse glioma MRI dataset. *Radiology: Artificial Intelligence*. 2022;4(6):e220058.

4. Aerts, Hugo JWL, et al. "Decoding tumour phenotype by noninvasive imaging using a quantitative radiomics approach." *Nature communications* 5.1 (2014): 4006.

Images/Tables

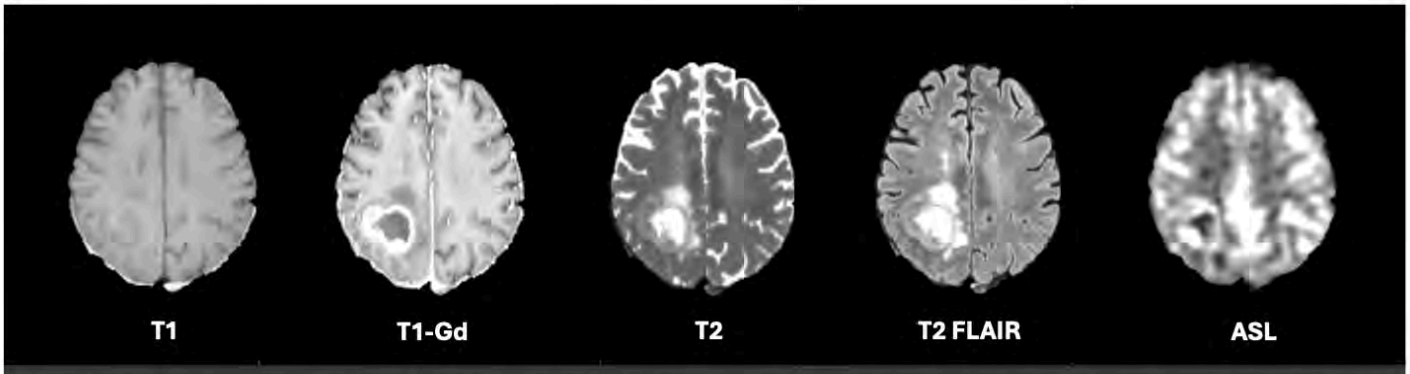

'Radiology review shows that a patient has a diffuse glioma. The following is the patient's radiology report: Mass centered in the right parietal lobe with a necrotic core and areas of thin and areas of thick contrast enhancement. Halo of FLAIR hyperintensity involving the adjacent parietal lobe extending to the corpus callosum. The enhancing component exhibits increased perfusion. Mild mass effect with effacement of regional sulci and right lateral ventricle. There is no T2/FLAIR mismatch. The age of the patient is ##. The sex of the patient is M/F. Please determine whether the tumor is IDH mutated or IDH wildtype in a single word response.'

Fig 1. Example Text Prompt Sent to ChatGPT

Fig 2. Word Cloud Displaying Words Most Important to Correctly Classify Wildtype Cases

Fig 3. Word Cloud Displaying Words Most Important to Correctly Classify Mutated Cases

---

1162 Imaging Characterization of Primary Hyperparathyroidism with Syndromic Mutations

Elham Beheshtian MD, Amrutha Ramachandran MD, Xin Cynthia Wu MD, Christine M Glastonbury MD
UCSF, San Francisco, CA, USA

Purpose

To evaluate the imaging features, demographics and differentiating characteristics of patients imaged with 4D CT for parathyroid adenoma with or without a known predisposing genetic mutation.

Materials & Methods

We retrospectively reviewed the imaging and medical records of patients younger than age 50, who were imaged for primary hyperparathyroidism (PHPT) with a 4D neck CT scan at our institution between January 2022 and September 2025. Demographics, location and number of parathyroid lesions, PTH and Calcium levels, genetic testing results, history of prior surgery/recurrence and history of other malignancies were recorded.

Results

The number of patients and genetic tests are reported in diagram 1.

From a total of 115 patients with diagnosis of PHPT who underwent 4D CT, 64 patients underwent genetic testing prior to or after the 4D CT, from which 21 (32.8%) had at least one positive genetic mutation, including MEN 1 (7), MEN 2 A (2), MEN 4 (1), CDC73 mutation for Hyperparathyroidism-Jaw Tumor Syndrome (HPT-JT) (1), familial isolated primary hyperparathyroidism (FIHP) (3), Familial Hypocalciuric Hypercalcemia (FHH) (1), hypophosphatemic hypercalciuric rickets (1), autosomal dominant hypophosphatemia (1) and nonspecific mutations of BRCA 1 and 2 (2) and two patients had mutation of uncertain significance including EGLN1 heterozygous Uncertain Significance and CFTR which is seen in cystic fibrosis.

In the positive mutation group the average patient age is 34.1 years (Ranges 11-48 years old), with female sex predominance of 66% (14), with average PTH 118.8, and Calcium 10.9. The average number and size of lesions are 2.3 and 10.9 ± 4.2 mm ($p \approx 0.012$).

In the negative mutation group the average patient age is 37 years (Ranges 15-48 years old), 60% (26) female, with average PTH 135.4, and Calcium 10.8. The average number and size of lesions are 1.46 and 16.1 ± 15.0 mm.

Conclusion

Multiglandular primary hyperparathyroidism is more likely to be associated with hereditary genetic mutations (2.3 vs 1.46 lesions). Patients with these mutations often have younger ages with higher number but smaller parathyroid adenomas.

32.8% of patients with primary hyperparathyroidism who are younger than 50 years of age have at least one genetic mutation with syndromic association that could place them at risk for other types of malignancies. Early detection of these mutations could save patient lives and potentially those of other family members with the same mutations. Neuroradiologists should be cautious while reporting 4D neck CTs. If a patient is known to have a predisposing genetic syndrome, be aware that they are more likely to have multiple lesions of smaller size. Conversely, if multiple lesions are identified in a younger patient, consider recommending genetic testing to evaluate for relevant syndromes.

References

1. Jha S, Simonds WF. Molecular and Clinical Spectrum of Primary Hyperparathyroidism. Endocr Rev. 2023 Sep 15;44(5):779-818. doi: 10.1210/endrev/bnad009. PMID: 36961765; PMCID: PMC10502601.

2. Včelák J, Šerková Z, Zajíčková K. Molecular Genetic Aspects of Sporadic Multiglandular Primary Hyperparathyroidism. Physiol Res. 2023 Dec 17;72(S4):S357-S363. doi: 10.33549/physiolres.935253. PMID: 38116772; PMCID: PMC10830163.

3. Krol JP, Joosten FBM, de Boer H, Bernsen MLE, Slump CH, Oyen WJG. Four-dimensional computed tomography as first-line imaging in primary hyperparathyroidism, a retrospective comparison to conventional imaging in a predominantly single adenoma population. EJNMMI Rep. 2024 May 1;8(1):11. doi: 10.1186/s41824-024-00198-5. PMID: 38748330; PMCID: PMC11061064.

Images/Tables

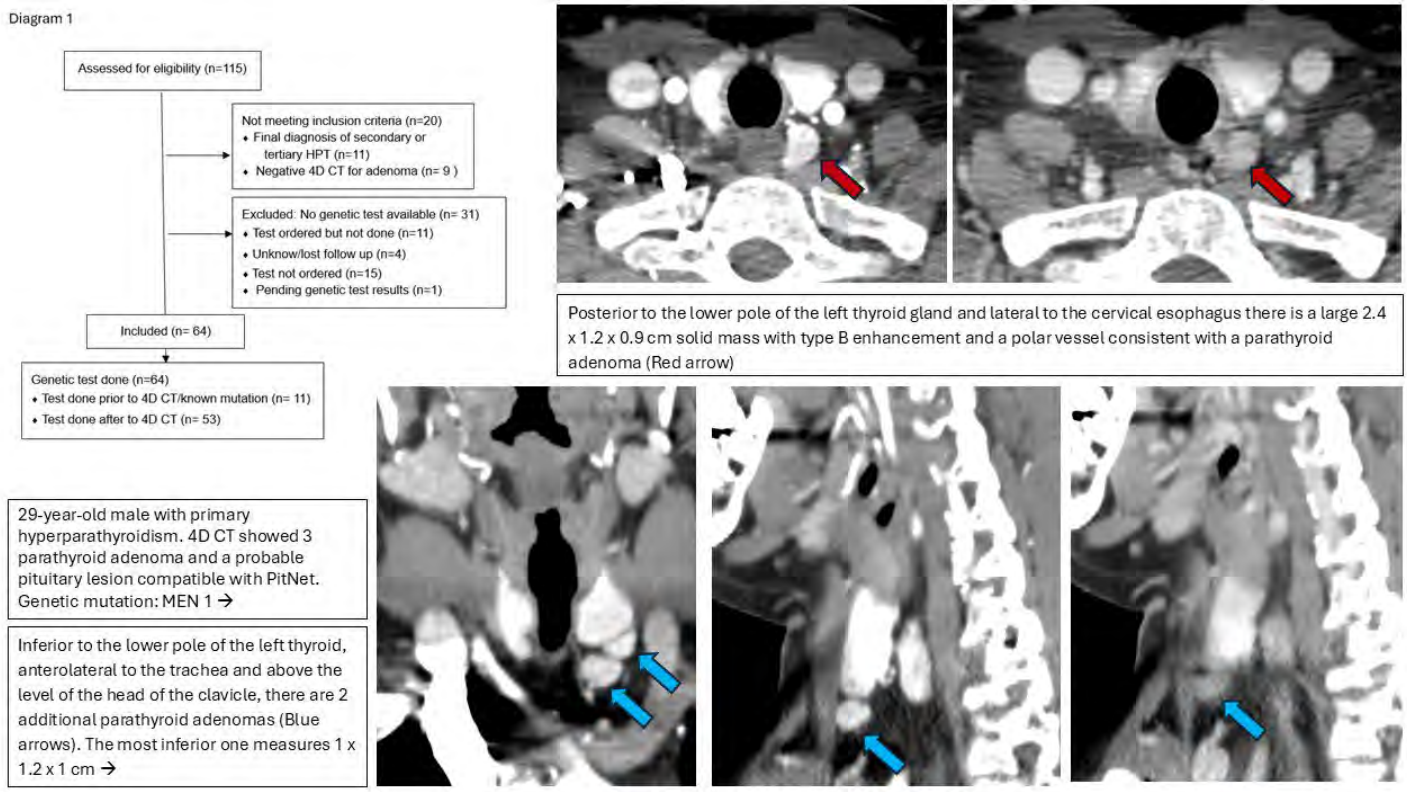

1166 The Extent of Cortical Involvement in Spinal Metastases Predicts the Presence and Character of Back Pain

Zahra Soltani PhD, Ron Alkalay PhD, David Hackney MD

Beth Israel Deaconess Medical Center, Boston, MA, USA

Purpose

Vertebral metastases are often associated with severe back pain. A particular nature of the pain, made worse by motion, is considered mechanical-mechanical pain (MP), as distinguished from other potential causes of pain in these patients. This is also an indicator of higher risk for pathologic fractures. Accurately assessing the mechanical abnormalities will guide therapy.

Materials & Methods

We developed a database of CT and MR imaging in a set of patients being treated with radiotherapy for spinal metastases. We studied the relationship between MR evidence of cortical involvement by the lesion and spine pain. We used the Spinal Instability Neoplastic Score (SINS), a standardized method for evaluating the clinical prognosis of spine metastases, to classify vertebrae as free of pain (SINS 0), painful but without mechanical pain (SINS 1) and mechanical pain (SINS 3). There is no SINS score of 2. The vertebral body MR images were segmented into involved or non-involved components using 3D Slicer. We estimated vertebral body cortical involvement using the same techniques.

Results

Non-mechanical pain and mechanical pain vertebrae had greater cortical involvement, a mean (SD) of 65.9 (29.22)% and 60.0 (24.6)%, respectively, than vertebrae free of pain, 48.4 (21.8)%. We found a statistically significant association ($p\chi 2 = 0.001$) between SINS pain score and lesion cortex involvement on MRI.

Conclusion

The presence and character of pain in the setting of metastases is highly related to the extent of overall vertebral body tumor content and to the extent of cortical involvement. These results imply that vertebral body cortical involvement and potential deformity may underlie pain and specifically mechanical pain in this setting

References

Alkalay RN, Harrigan T. Mechanical assessment of the effects of metastatic lytic defect on the structural response of human thoracolumbar spine. Journal of Orthopedic Research. 2016;34(10):1808-19. PubMed PMID: 26748564.

Soltani Z, Xu M, Radovitzky R, Stadelmann MA, Hackney D, Alkalay RN. CT-based finite element simulating spatial bone damage accumulation predicts metastatic human vertebrae strength and stiffness. Front Bioeng Biotechnol. 2024;12:1424553. Epub 20240723. PubMed PMID: 39108596; PMCID: PMC11300227.

Alkalay RN. Effect of the metastatic defect on the structural response and failure process of human vertebrae: An experimental study. Journal of Clinical Biomechanics. 2015;30(2):121-8. PubMed PMID: 25586264; PMCID: PMC9190195.

Doyle PF, Caplan S, Klinger N, Shin K-Y, Groff M, Dillon-Martin M, et al. Spinal Instability Neoplastic Score as a predictor of vertebral fracture risk in patients undergoing radiation therapy to spinal metastases: A prospective single-institution study. JCO Oncology Practice 2025;10(7):101803; PMCID: PMC12180991.

1179 Care-Setting Determinants and Clinical Appropriateness of Head and Neck CTA: A National Multi-Payer Analysis

Nagaraja S Moily MBBS, PhD, MBA, MAM[1], Keervani Kandala MS[1], Max Wintermark MD, MS, MBA[2], Ajay Malhotra MD, MMM[1]

[1]Department of Radiology and Biomedical Imaging, Yale School of Medicine, New Haven, CT, USA. [2]Chair, Department of Neuroradiology, The University of Texas MD Anderson Cancer Center, Houston, TX, USA

Purpose

Head and neck computed tomography angiography (CTA) is essential for evaluating acute cerebrovascular and traumatic conditions, yet variation in its deployment across care settings remains poorly defined. We developed and applied a reproducible informatics framework to characterize care-setting determinants and clinical appropriateness of CTA utilization across U.S. commercial and employer-linked Medicare populations. Prior institutional and national studies have reported increasing CTA use and declining diagnostic yield, underscoring the need for scalable, validated analytic frameworks to assess real-world imaging appropriateness (1-4).

Materials & Methods

We developed a claims-based informatics framework to analyze 1,991,194 head and neck CTA procedures (2016–2024) from the IBM MarketScan® Commercial and Medicare Supplemental databases (> 40 million covered lives annually). The framework harmonized inpatient, outpatient, and facility claim tables into encounter-level records using deterministic record linkage and multi-key de-duplication (< 10 % redundancy). A validated multi-indicator emergency-department (ED) classifier combined revenue, place-of-service, and emergency E/M codes to improve fidelity in identifying acute versus elective imaging encounters (> 95 % accuracy). Clinical indications were hierarchically mapped through ICD-9/10 prefix-based groupings stratified by urgency (cerebrovascular, trauma, vascular anomaly, neoplasm, neurologic symptoms). CPT code validation used the PROCTYP field and procedural cross-auditing (> 97 % specificity). Encounter-level analytics compared imaging intensity, same-day head–neck combinations, and utilization concentration across settings using nonparametric and distributional statistics.

Results

The cohort comprised 833,128 encounters representing 701,815 unique patients (mean age, 55.8 ± 17.8 years; 57 % female). ED encounters accounted for 22.7 % of procedures (annual rates under validation). Median utilization was two CTAs (IQR, 1–4); high utilizers (≥ 5 CTAs) represented 6.9 % of patients but produced 17.6 % of all procedures (Gini = 0.43). Care setting strongly influenced imaging scope: same-encounter head + neck coverage occurred in 53.8 % overall but was markedly higher in non-ED (78.7 %) than ED settings (61.5 %, $p < 0.001$), suggesting protocol-driven comprehensiveness in elective contexts versus targeted imaging in acute presentations. Clinical-indication profiles reflected setting-based appropriateness: cerebrovascular emergencies and trauma predominated in ED encounters, whereas non-ED imaging more often addressed chronic or indeterminate neurologic symptoms. Regional variation was modest, paralleling MarketScan population distributions (South 38.2 %, Midwest 30.6 %).

Conclusion

By integrating multi-source claims harmonization, a validated multi-indicator ED classifier, and hierarchical ICD mapping, this study establishes a novel informatics framework for large-scale, reproducible assessment of neurovascular imaging appropriateness. Head and neck CTA utilization demonstrates substantial cross-setting variability: ED imaging remains concentrated on acute cerebrovascular and trauma indications, while non-ED contexts show higher imaging intensity and frequent head–neck combinations reflecting structural and workflow standardization. The framework's validated architecture enables future AI-enabled appropriateness modeling, benchmarking of protocol efficiency, and data-driven quality improvement in neurovascular imaging practice.

References

1. Tu LH, Krupinski EA, Heilbrun ME, et al. Head and neck CT angiography utilization: analysis of ordering frequency and nonroutine results communication. *AJR Am J Roentgenol.* 2022;218(3):544-551. doi:10.2214/AJR.21.26543
2. Rigney GH, Romano AM, Carhuapoma JR, et al. Trends in nonfocal neurological chief complaints and CT angiography utilization among adults in the emergency department. *Intern Emerg Med.* 2024;19(4):785-793. doi:10.1007/s11739-024-03569-9
3. Ginde AA, Shanbhag P, Cabrera D, et al. Variation in advanced neuroimaging utilization across emergency departments in the United States. *Radiology.* 2020;297(2):357-365. doi:10.1148/radiol.2020191731
4. Edlow JA, Panagos PD, Godwin SA, et al. Appropriate use of CT angiography for suspected stroke and TIA in emergency care. *Acad Emerg Med.* 2017;24(8):988-996. doi:10.1111/acem.13201

1209 Demographic and MRI Predictors of Metastasis in Spinal Chordoma: A Case–Control Evaluation

Sahar Alizada, Heba Al Qudah, Ahmed Abdelgawad, Chloe Barakat, Hamza Salim, Ahmed Msherghi, Samir Dagher, Max Wintermark, Rami Eldaya
MD Anderson Cancer Center, Houston, Texas, USA

Purpose

Chordoma is a rare bone cancer originating from the remnants of the notochord, a mesoderm-derived structure essential for normal embryonic development. Tumors most commonly localize to the skull base, sacrum and vertebral column, in order of descending prevalence. In this study, we aimed to determine whether baseline demographic and pre-resection imaging features of primary spinal chordoma can identify tumors that will metastasize.

Materials & Methods

We retrospectively searched our institutional records (January 2000–October 2025) and identified 21 patients with metastatic spinal chordoma who had pre-resection imaging of the primary lesion. We randomly selected 21 patients with non-metastatic spinal chordoma as controls. We compared patient demographics and the imaging features such as quantitative T2 signal characteristics, apparent diffusion coefficient (ADC), anatomic location (cervical, thoracic, lumbar, junctional), number of involved vertebral bodies, posterior-element involvement, presence/size of prevertebral component, epidural disease, and degree of cord compression between these groups. Group comparisons used Welch t tests or Fisher's exact tests as appropriate. A prespecified multivariable logistic framework was planned to evaluate independent associations, with attention to sample-size constraints. Overall survival (OS) was explored as a secondary analysis.

Results

Demographics were comparable between groups (mean age 57±15 vs 51±21 years; sex distribution similar). Anatomic region differed: metastatic cases were enriched for thoracic primaries whereas non-metastatic controls more often involved the lumbar spine (p=0.04). Among the 21 metastatic cases, the median time from diagnosis to first detected metastasis was 21.7 months (range ~0–156 months). Osseous/axial sites were the most common metastasis locations (9/21, 43%), followed by lung (7/21, 33%), pleura/chest wall (5/21, 24%), and other soft-tissue sites such as psoas, abdominal wall, submandibular, and perinodal fat (5/21, 24%). Multifocal metastatic involvement (≥2 sites) was present in 8/21 cases (38%). In the exploratory survival analysis, overall survival did not differ significantly between groups (log-rank p=0.49).

Conclusion

In this size-matched, retrospective cohort, baseline anatomic location emerged as a differentiating feature, with thoracic tumors more frequently observed among patients who later developed metastases.

References

1. Berg AR, Hanna G, Mendiratta D, Para A, Michel M, Beebe K, Vives MJ. Risk factors for metastatic disease at presentation with chordoma and its prognostic value. N Am Spine Soc J. 2024 Nov 6;21:100566. doi: 10.1016/j.xnsj.2024.100566. PMID: 39834500; PMCID: PMC11743829.
2. Saint-Germain MA, Kramer P, Weber-Levine C, Jiang K, Al-Mistarehi AH, Redmond KJ, Lee SH, Bettegowda C, Theodore N, Lubelski D. Characterizing the presentation, management, and clinical outcomes of patients with intradural spinal chordomas: a systematic review. Neurosurg Focus. 2024 May;56(5):E14. doi: 10.3171/2024.2.FOCUS2419. PMID: 38691865.

Images/Tables

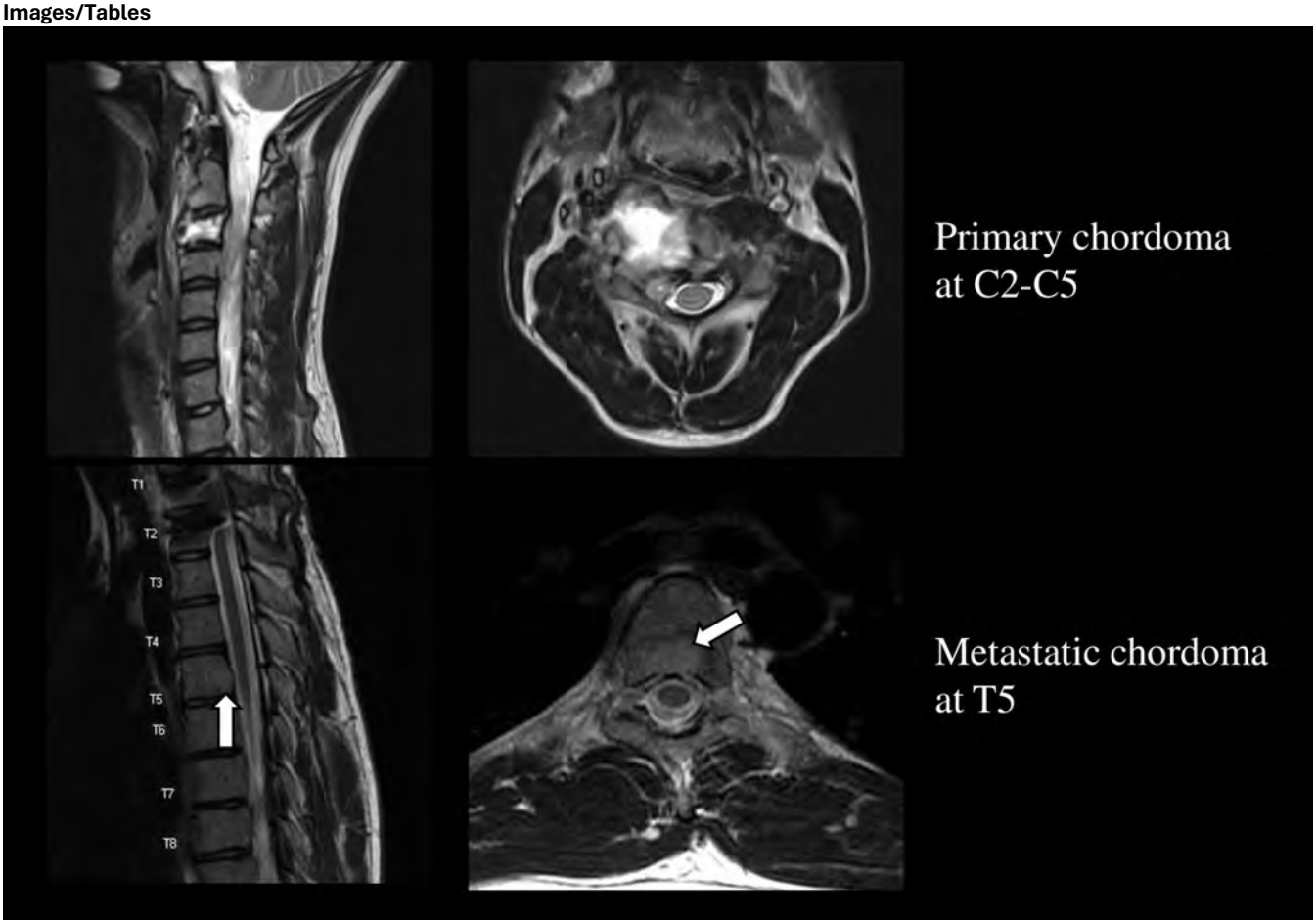

1213 Deep Learning Post-Processing Enhances Brain Metastases on MRI: An Assessment of Subject and Quantitative Metrics

Tanvir Agnihotri MD, Bryan bryan.pacheco@mountsinai.org MD, Mark Finkelstein MD, Amish Doshi MD
Icahn School of Medicine at Mount Sinai, NYC, NY, USA

Purpose

To evaluate the clinical performance of an FDA-cleared deep learning-based (DLB) post-processing algorithm designed to enhance MRI images by improving lesion conspicuity and overall visualization of anatomical structures. This study examines the subjective and objective impact of DLB on the reader experience, and lesion conspicuity, respectively.

Materials & Methods

All MRI brain examinations (n=60) with contrast performed on two 3 Tesla scanners between September 26, 2025 and November 3, 2025 were included, and assessed for the following subjective features: contrast enhancement (CE), border delineation (BD), internal morphology (IM), overall image quality (OIQ), artifacts, and vessel conspicuity (VCI). Two unblinded readers rated each metric using a Likert scale (1 = poor, 2 = fair, 3 = good, 4 = very good, 5 = excellent). 35 metastatic lesions were identified from the included 60 studies. Quantitative analysis was performed on these cases, measuring signal intensity (SI) of lesions, normal brain tissue, and the standard deviation (SD) of both regular post-processed and DLB post-processed series. Contrast-to-noise ratio (CNR) was calculated as the difference between lesion and normal brain SI divided by the SD of brain tissue, as a proxy for lesion conspicuity relative to background variability. Lesion-to-brain ratio (LBR) was defined as the ratio of lesion SI to normal brain SI, reflecting relative lesion brightness. Paired t-tests compared standard and Aimify-processed images ($p < 0.05$ considered significant). Inter-reader agreement was assessed using Cohen's kappa coefficient.

Results

Deep learning-based processing performed better amongst most subjective metrics. Significant enhancements were observed in CE ($p = 0.0075$), BD ($p = 0.0024$), IM ($p = 0.0096$), OIQ ($p = 0.0167$), and VCI ($p = 9.3 \times 10^{-7}$). Artifact scores were not significantly altered ($p = 0.1023$), indicating that Aimify does not introduce detectable confounding changes. Quantitative metrics demonstrated significant increases in CNR ($p = 1.12 \times 10^{-4}$) and LBR ($p = 3.33 \times 10^{-6}$), while lesion SI remained stable ($p = 0.9295$) and normal brain SI decreased ($p = 7.76 \times 10^{-16}$), reflecting selective enhancement of lesions relative to surrounding tissue. Cohen's kappa analysis showed excellent agreement for CE (κappa = 0.935) and very good agreement for IM (κappa = 0.866) and OIQ (κappa = 0.880). Artifact scoring showed good agreement (κappa = 0.740), while BD and VCI demonstrated poor or no agreement (κappa = 0.164 and −0.094, respectively). These findings confirm that deep learning-based post-processing improves lesion conspicuity while maintaining robust inter-reader consistency for key metrics.

Conclusion

DLB augments MRI images, enhancing both subjective and quantitative features while supporting consistent interpretation across readers. Improvements in CNR and LBR demonstrate its utility in making metastatic lesions more conspicuous without increasing artifacts. DLB may enable reductions in contrast dosing while preserving lesion detectability, positioning it as a valuable adjunct for clinical interpretation and workflow efficiency. Future studies will validate its performance in reduced-contrast protocols and across diverse lesion types, reinforcing its role in enhancing MRI for metastatic disease evaluation.

References

Ozkara BB, Chen MM, Federau C, Karabacak M, Briere TM, Li J, Wintermark M. Deep Learning for Detecting Brain Metastases on MRI: A Systematic Review and Meta-Analysis. Cancers (Basel). 2023 Jan 4;15(2):334. doi: 10.3390/cancers15020334. PMID: 36672286; PMCID: PMC9857123.
Park JE. Artificial Intelligence in Neuro-Oncologic Imaging: A Brief Review for Clinical Use Cases and Future Perspectives. Brain Tumor Res Treat. 2022 Apr;10(2):69-75. doi: 10.14791/btrt.2021.0031.

Images/Tables

Table 1: Subjective and Quantitative MRI Metrics – Standard vs. DLB

Metric	Standard Avg	DLB Avg	Standard SD	DLB SD	P-value
Subjective Image Quality (n = 60)					
Contrast Enhancement	4.21	4.43	0.71	0.50	0.01*
Border Delineation	4.28	4.50	0.57	0.50	0.00*
Internal Morphology	4.22	4.43	0.70	0.50	0.01*
Overall Image Quality	4.21	4.40	0.69	0.49	0.02*
Artifacts	4.19	4.32	0.71	0.47	0.10
Vessel Conspicuity / Impact	4.19	4.57	0.54	0.58	9.30×10^{-7}*
Quantitative Metrics (n = 35)					
SI Lesion	365.41	365.12	95.36	95.17	0.93
SI Normal Brain	174.09	116.31	8.81	1.89	7.76×10^{-16}*
CNR	27.99	151.80	25.98	73.78	1.12×10^{-4}*
LBR	2.17	3.23	0.71	0.99	3.33×10^{-6}*

Note. Subjective metrics were rated on a 5-point Likert scale: 1 = very poor, 2 = poor, 3 = fair, 4 = good, 5 = excellent. CNR = contrast-to-noise ratio; LBR = lesion-to-brain ratio; SI = signal intensity.

112 Elevated Oxygen Extraction Fraction in Type 2 Diabetes Mellitus: Evidence for Early Cerebral Metabolic Changes in Cognitive-Associated Regions

Dhruv Bhagat[1], Sri Sai Akkineni[1], Lea Bergeot[2], Fahad Salman[3], Ferdinand Schweser Ph.D.[3], Junghun Cho Ph.D.[4], Rafeeque Bhadelia M.D.[5], Katherine L Tucker Ph.D.[6], Salil Soman M.D.[7]

[1]Medical College of Georigia, Athens, GA, USA. [2]Northeastern University, Boston, MA, USA. [3]University of Buffalo, Buffalo, NY, USA. [4]The George Washington University, Washington, D.C, USA. [5]Beth Israel Deaconess, Boston, MA, USA. [6]University of Massachusetts Lowell, Lowell, MA, USA. [7]University of San Francisco, San Francisco, California, USA

Purpose

Type 2 Diabetes Mellitus (T2DM) is linked to accelerated cognitive aging and neurovascular dysfunction. Cerebral oxygen extraction fraction (OEF), measured by susceptibility-weighted MRI, serves as a noninvasive marker of brain oxygen metabolism. We hypothesized that individuals with T2DM (defined by HOMA-IR ≥ 3.0) show elevated OEF in cognition- and memory-related brain regions, even without clinical cognitive decline.

Materials & Methods

We analyzed cross-sectional data from the Boston Puerto Rican Health Study, including 130 T2DM and 116 non-T2DM participants. Regional OEF was derived from susceptibility MRI. T2DM status was determined by HOMA-IR over multiple timepoints. Multivariable linear regression assessed the association between T2DM and OEF, adjusting for age and sex, with FDR correction for multiple comparisons. For OEF comparisons between cognitive subgroups (executive, memory, global decline), Mann-Whitney U tests were used due to non-normal data and small subgroup sizes. Participants were stratified by presence or absence of cognitive decline to examine metabolic correlations.

Results

T2DM participants had significantly higher OEF in bilateral hippocampi, thalamus, superior frontal, parietal, and temporal cortices (all FDR-adjusted $p < 0.05$). Age was modestly negatively associated with OEF; sex was not significant. Mann-Whitney U tests found no significant OEF differences between those with and without cognitive decline in either group. Sample sizes for “any decline” were T2DM with decline (n=30), without decline (n=100), non-T2DM with decline (n=33), and without decline (n=83). Lack of significance may reflect limited power.

Conclusion

T2DM is associated with elevated OEF in cognition-related brain regions prior to measurable cognitive decline, suggesting cerebral metabolic dysfunction may precede clinical impairment. OEF shows promise as an early imaging biomarker of diabetes-related neurodegeneration, meriting further longitudinal study. Further longitudinal studies with larger cohorts are warranted to determine if OEF elevations precede measurable cognitive impairment and to establish OEF as a predictive imaging biomarker in diabetic populations.

---

115 Prenatal Marijuana Exposure and Its Association with White Matter and Cortical Development in Late Childhood

Hector Acosta Rodriguez

Yale School of Medicine, New Haven, CT, USA

Purpose

To investigate the association between prenatal marijuana exposure and neuroimaging metrics of brain health at late childhood.

Materials & Methods

For our study, we gathered all neuroimaging, clinical, and prenatal drug exposure data from the Adolescent Brain Cognitive Development (ABCD) database, which originally contained 11,868 subjects. All subjects with incomplete clinical information, any history of traumatic brain injury, or those who failed MRI quality control were excluded from this study. Mixed linear models, controlling for age and education and applying the False Discovery Rate to correct for multiple comparisons, were used to establish the association between prenatal marijuana exposure and neuroimaging metrics of brain health. These metrics included fractional anisotropy, neurite density, mean diffusivity, and radial diffusivity of white matter (WM) tracts, as well as cortical surface area.

Results

We analyzed the information of 1085 children, 418 which were prenatally exposed to marijuana and 667 matched controls subjects who were not prenatally exposed, with a mean age ± (standard deviation) of 9.9 ± (0.6) years for both groups. We found that prenatal exposure to marijuana is associated with diffuse brain alterations. Specifically, those children who were prenatally exposed to marijuana showed negative alterations in white matter microstructure and cortical regions essential for goal directed behaviors, including motivation, cognitive skills for achieving specific objectives, and emotional processing. This was evidenced by our findings of decreased WM microstructure, where we found that prenatally exposed children had decreased fractional anisotropy and neurite density, and increased mean and radial diffusivity mainly in the superior corticostriate tract and corticostriate projections via the external capsule to the superior parietal and frontal cortices. In addition, those children who were prenatally exposed to marijuana had reduced cortical surface area on the left hemisphere parahippocampal and right hemisphere postcentral gyrus.

Conclusion

Overall, our findings suggest that prenatal exposure to marijuana may have long lasting alterations in children brain neurodevelopment. These alterations may impair critical skills needed as children grow into adolescence, such as proper behavioral functioning and emotional regulation. These results underscore the potential long-term neurodevelopmental impact of prenatal marijuana exposure and support the need for clearer public health messaging and early developmental monitoring in affected children.

Images/Tables

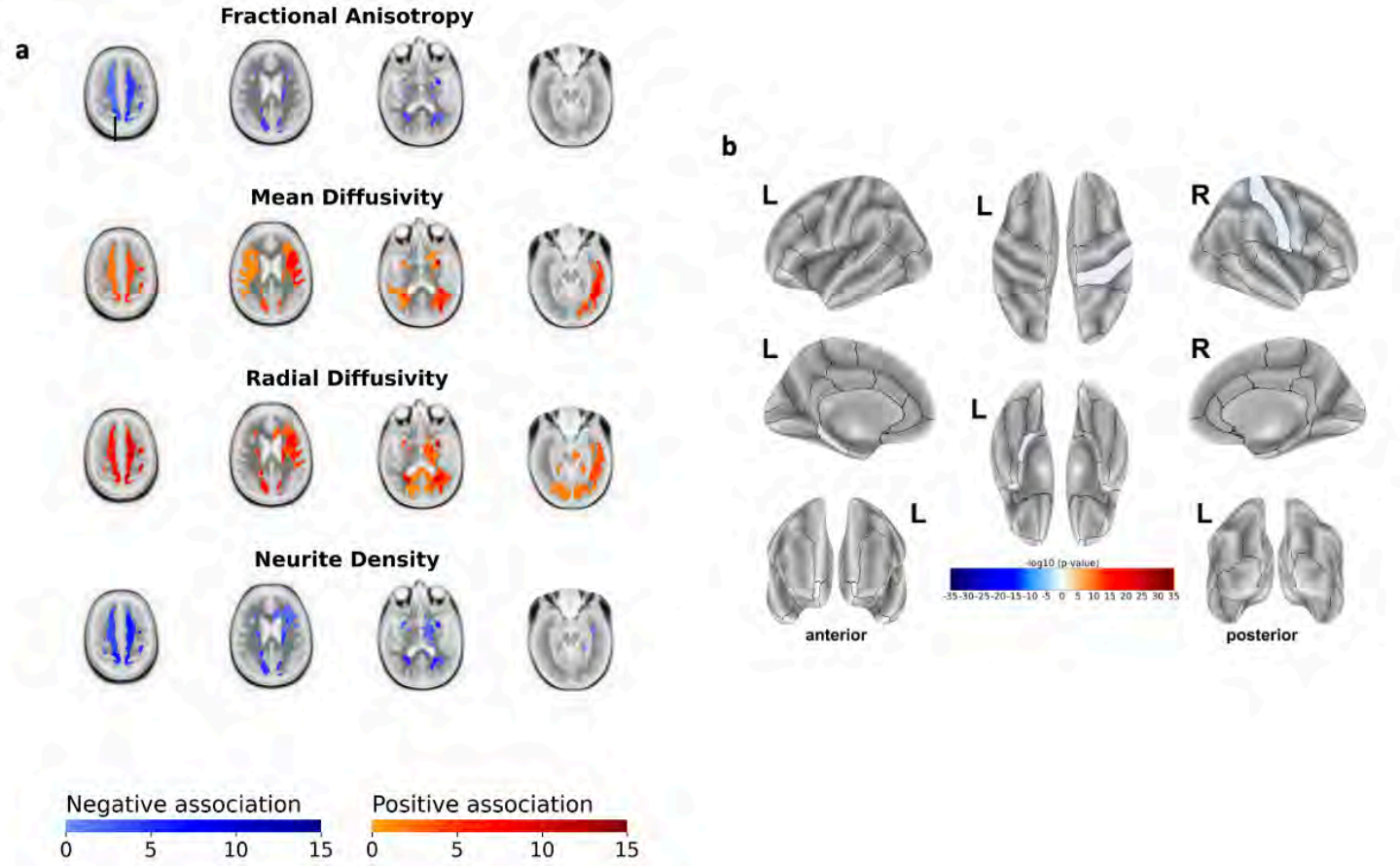

Figure 1. Mixed linear model analyses of the association of prenatal marijuana exposure with **(a)** diffusion tensor imaging metrics and **(b)** cortical surface area. Values shown were corrected for subjects' age at time of imaging, sex, BMI z-score at time of imaging, handedness, race, and cranial volume at time of imaging as covariates and adjusting for the highest parental level of education and combined parental income level as random effects. Blue areas depict regions of significant negative association while red areas depict regions of significant positive association (both with false discovery rate corrected p-value<0.05).

---

140 Clinical and VASARI Features to Predict CDKN2AB Homozygous Deletion in IDH-Mutant Astrocytomas A Multicenter Study

Zhengyang Zhu MD, PhD[1], Huiquan Yang MD[2]

[1]Mayo Clinic, Rochester, Minnesota, Armenia. [2]Nanjing Drum Tower Hospital, Nanjing, China, China

Purpose

Preoperative MRI images of 122 astrocytoma patients (101 without CDKN2A/B homozygous deletion, and 21 with CDKN2A/B homozygous deletion) were retrospectively collected as training set. Eighteen patients with astrocytomas from another center (14 without CDKN2A/B homozygous deletion, and 4 with CDKN2A/B homozygous deletion) were enrolled as external test set. VASARI features in MRI images of astrocytoma patients were evaluated by radiologists. Prediction models for identifying CDKN2A/B homozygous deletion status based on clinical and VASARI features were constructed using logistic regression.

Materials & Methods

Preoperative MRI images of 122 astrocytoma patients (101 without CDKN2A/B homozygous deletion, and 21 with CDKN2A/B homozygous deletion) were retrospectively collected as training set. Eighteen patients with astrocytomas from another center (14 without CDKN2A/B homozygous deletion, and 4 with CDKN2A/B homozygous deletion) were enrolled as external test set. VASARI features in MRI images of astrocytoma patients were evaluated by radiologists. Prediction models for identifying CDKN2A/B homozygous deletion status based on clinical and VASARI features were constructed using logistic regression.

Results

Multivariate regression analysis showed that age (OR: 1.057, p = 0.038) and definition of enhancing margin (OR: 15.672, p = 0.001) were independent predictors of CDKN2A/B homozygous deletion in IDH-mutant astrocytomas. The prediction model in the training set exhibited an AUC of 0.84 (95% CI: 0.73-0.95), 89.3% accuracy, 52.4% sensitivity, and 97.0% specificity. The prediction model in the external test set showed an AUC of 0.86 (95% CI: 0.63-1.00), 83.3% accuracy, 50.0% sensitivity, and 92.9% specificity.

Conclusion

The prediction model based on the VASARI MRI features was useful for preoperative identification of CDKN2A/B homozygous deletion status in IDH-mutant astrocytomas.

Clinical Relevance/Application: This research may help radiologists identify CDKN2A/B homozygous deletion status of astrocytomas in the reading room.

Images/Tables

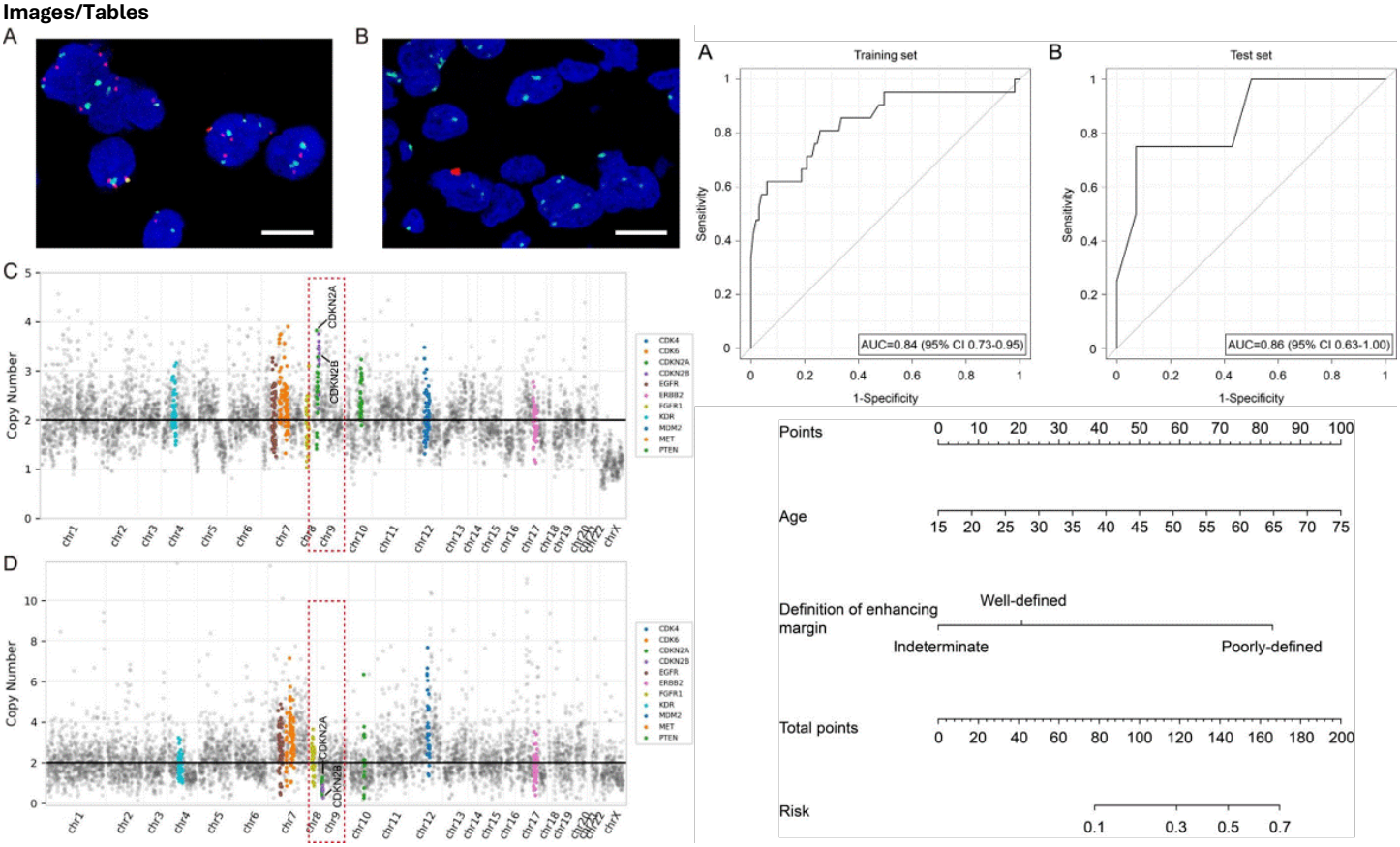

159 Evaluation of Conventional Deep Learning and Slice-Aware Models For High Sensitivity Intracranial Hemorrhage Coverage

Souradeep Bhattacharya MS[1], Jason Handwerker MD[2], Steve Fung MD[3]

[1]Texas A&M University, School of Engineering Medicine, Houston, Tx, USA. [2]UCSD Health Center, San Diego, CA, USA. [3]Houston Methodist Hospital, Houston, Tx, USA

Purpose

Radiologists need reliable tools that can safely identify head CTs with no hemorrhage and reduce review workload without missing true bleeds. While receiver-operating-characteristic (ROC) analysis and area-under-the-curve (AUC) scores summarize overall accuracy, they do not answer the operational question: How many studies can an algorithm mark as low risk while maintaining near-perfect sensitivity?

We compared two neural network models for intracranial hemorrhage (ICH) detection: a conventional 2D model that analyzes each slice individually, and a sequential "slice-aware" model that also considers relationships between slices in a scan. We then tested whether these models could maintain 97%/99% sensitivity when applied to both internal and external datasets. "Coverage" was defined as the percentage of head CT exams that could be confidently identified as low risk at a given sensitivity threshold.

Materials & Methods

Models were trained on the RSNA 2019 ICH dataset [1] (Conventional: ResNet; Sequential: SE-ResNeXt + BiGRU). Probabilities were temperature-calibrated [2]. Thresholds guaranteeing 97% or 99% sensitivity were chosen on a held-out set using a split-conformal approach [3] and then applied to the internal RSNA test set and the external CQ500 cohort [4] without retuning. Heat maps were generated for visual review [5].

Results

On the internal RSNA test set, AUCs were 0.9648 (conventional) and 0.9727 (sequential). Although this AUC gap is small, the practical difference at a fixed sensitivity is larger:

- Sensitivity 99%: the sequential model marked 33.5% of exams as low-risk vs 26.8% for the conventional model, and produced fewer false positives among flagged studies (44.9% vs 55.8%).
- Sensitivity 97%: coverage rose to 52.9% (sequential) vs 50.0% (conventional), with lower false-positive rates (14.1% vs 18.8%).

External testing revealed distribution shift. With RSNA-tuned thresholds applied unchanged to CQ500:

- Sensitivity 99%: the conventional model's sensitivity fell to 63.4% at 46.9% coverage. The sequential model maintained 98.9% sensitivity at 6.6% coverage and generated significant false positives (86.3%).
- Sensitivity 97%: the sequential achieved 88.1% sensitivity at 23.0% coverage (false-positive 62.4%); the conventional model reached 57.5% sensitivity at 53.5% coverage (false-positive 32.2%).

Calibration effects: Threshold tuning improved the model's Expected Calibration Error (ECE), meaning the predicted probabilities better matched actual outcomes. However, this calibration did not improve external coverage. When thresholds were refit to preserve 97% and 99% sensitivity, coverage decreased even further. This finding suggests that calibration alone cannot overcome distribution shift between datasets. Most missed cases involved very small, low-contrast hemorrhages. Lesion size labels were unavailable, which we note as a limitation. Heat maps correctly highlighted hemorrhage regions when present.

Conclusion

Both conventional and sequential models achieved high AUC scores, but they resulted in poor coverage especially when applied to an external dataset. Calibration improved sensitivity but did not restore coverage when applied to the external dataset.

In practical terms, a high AUC does not guarantee coverage across institutions. Calibration and threshold tuning are not enough; local validation is strongly advised before deployment in a particular clinical workflow.

Images/Tables

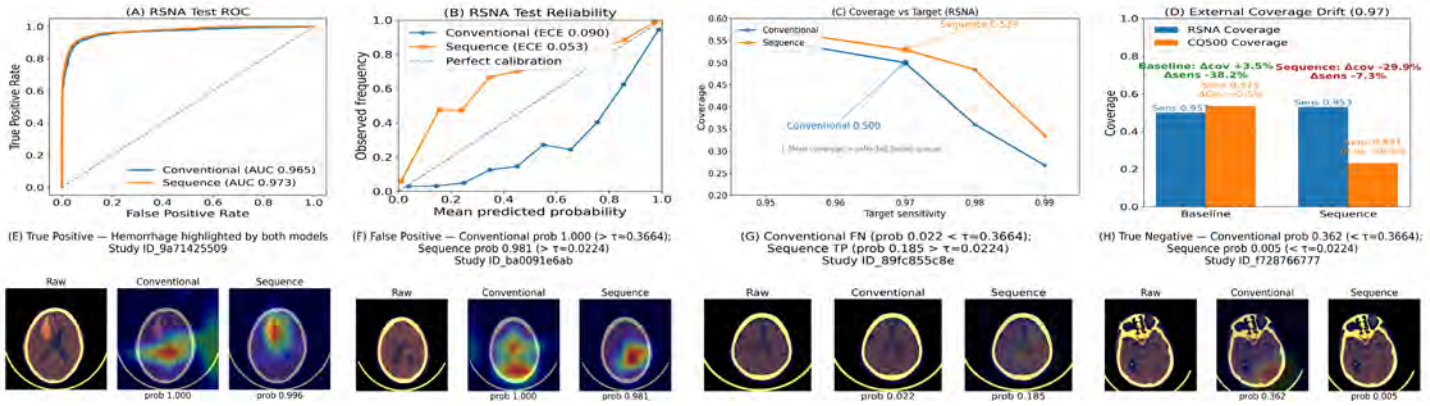

180 Identifying Risk Factors for Microgravity-induced Jugular Vein Thrombosis

Larry A. Kramer MD[1], Dorsa Dayani MD[1], Edwin Mulder PhD[2], Stefan Moestl PhD[2], Justin L. Brown PhD[1], Paul E. Schulz MD[1], Darius Gerlach PhD[2], Anja Bach MTR[2], Katrina J. Carter PhD[3], Matthew J. Poczatek B.S.[4], Sophie Simon MTR[2], Bryan J. Caldwell PhD[3], Brandon R. Macias PhD[5]

[1]UTHealth, Houston, TX, USA. [2]German Aerospace Center, Cologne, North Rhine-Westphalia, Germany. [3]KBR Wyle, Houston, TX, USA. [4]JES Tech, Houston, TX, USA. [5]NASA, Houston, TX, USA

Purpose

A case report of an asymptomatic left internal jugular vein (LIJV) thrombosis occurring during spaceflight was published in 2020 (1). Although treated without complication, the association of venous thrombosis with spaceflight raised new safety concerns for long-duration microgravity exposure. The purpose of this study was to use MRI quantitative flow and anatomical measurements to identify inherent risk factors that could potentially promote thrombosis of the head and neck venous system.

Materials & Methods

A head down tilt bedrest (HDTBR) study was conducted at the German Aerospace Medicine Research Facility to simulate headward venous fluid volume shift associated with microgravity exposure. Measurements were all obtained at baseline at 6 degrees of downward head tilt using 3T MRI. Cine phase-contrast angiography at the C2/C3 disk space level was used to measure IJV peak flow rate. 3D MPRAGE was used to measure cross-sectional area (CSA) of the IJV at the skull base. A 3D VIBE was used to measure aortic arch position and the narrowest axial-plane diameter of the brachiocephalic veins (BCV) relative to the mid-sternoclavicular level. BCV diameter and IJV peak flow rate were obtained in arms down and up positions.

Results

Twelve participants (8 women; mean [SD] age, 32 [5.2] years; BMI 22.6 [3.0] kg/m2) had a larger mean RIJV CSA than the LIJV (76.1 [28.6] versus 43.9 [18.5] mm2, P=.017). Arms down or up, RIJV mean peak flow rate was larger compared to the LIJV (DOWN: 11.1 [5.5] versus 6.2 [3.2] ml/s, (P=.04); UP: 10.6 [5.8] versus 5.7 [3.4] ml/s, (P=.05)). With arms up, left BCV mean diameter decreased from 6.6 [2.1] to 5.3 [2.0] mm2, (P=.008). With arms up, right BCV showed a trend towards a decrease in mean diameter (14.3 [2.3] versus 13.1 [1.3] mm2 (P=.075)). Aortic arch thoracic position was negatively correlated with left BCV diameter with arms up (r = -0.87, Pearson correlation, P<.001). Arms up positioning in the subject with the highest aortic arch position was associated with the narrowest diameter of the left BCV (1.0 mm) dampening peak flow rate (Figure 1).

Conclusion

Known risk factors associated with venous thrombosis are endothelial injury, hypercoagulability and blood flow stasis (Virchow's triad). Here we demonstrate that smaller LIJV CSA is associated with lower peak flow rates. A high aortic arch position increases the likelihood of aortosternal venous compression during arms up positioning accentuating LIJV outflow resistance and further suppressing peak flow rate. Aortosternal venous compression is known to be associated with LIJV flow reversal (2). Therefore, with the natural tendency for arms to float headward in microgravity, individuals with a high aortic arch position may be prone to LIJV flow reversal. These combined observations could increase the probability of developing the LIJV stagnant flow pattern identified by ultrasound during spaceflight (3). Repetitive severe compression of the left BCV could also potentially result in endothelial injury resulting in another thrombosis risk factor. Future 4D flow MRI studies may delineate spatially variable abnormalities in vortical flow and wall shear stress along the entire LIJV, providing insights beyond single-slice 2D phase-contrast angiography.

Images/Tables

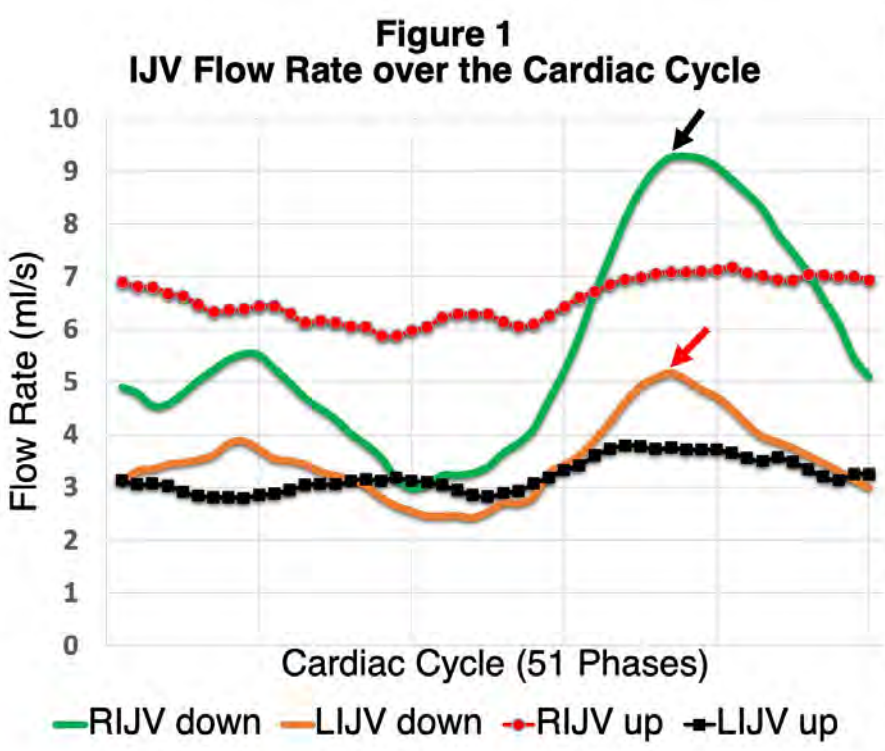

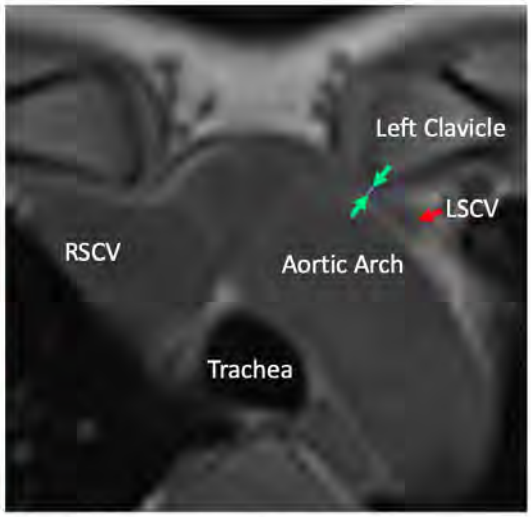

In the arms up position, the left subclavian vein (LSCV, red arrow) is severely compressed between the aortic arch and left clavicle (green arrows, diameter line in purple). In the arms down position, peak IJV flow rates shown by black and red arrows are suppressed when the arms are placed in the up position. Note lower peak flow rate of the LIJV compared the RIJV. RSCV = right subclavian vein.

---

182 **Impact of Deep Learning Reconstruction on Vascular and Collateral Visualization in Moyamoya Disease: A Comparison Across Magnetic Field Strengths**

Ayako Omori MD, Hiroyuki Tatekawa MD, PhD, Tatsushi Oura MD, Natsuko Atsukawa MD, Shu Matsushita MD, Daisuke Horiuchi MD, PhD, Hirotaka Takita MD, PhD, Taro Shimono MD, PhD, Tsutomu Ichinose MD, PhD, Yukio Miki MD, PhD, Daiju Ueda MD, PhD
Osaka Metropolita University, Osaka, Osaka, Japan

Purpose

Deep learning reconstruction (DLR) techniques have advanced remarkably and are increasingly applied to clinical magnetic resonance angiography (MRA). While previous studies have shown that DLR can reduce noise and enhance vessel delineation, the effect of magnetic field strength on DLR-enhanced MRA remains unclear, particularly in moyamoya disease. This study aimed to determine whether DLR can improve vascular visualization and staging assessment of moyamoya disease across different field strengths using SwiftMR, a commercially available DICOM-based post-processing tool.

Materials & Methods

This retrospective study included 32 patients (mean age, 40 years; male/females, 9/23) with suspected or confirmed moyamoya disease between 2015 and 2024. All patients underwent time-of-flight (TOF) MRA at both 1.5T and 3T scanners within a 400-day interval, with exclusion of cases involving interval surgery or clinical deterioration. TOF MRA datasets were reconstructed both with and without DLR, yielding four acquisition types per patient (1.5T original, 1.5T DLR-enhanced, 3T original, and 3T DLR-enhanced). Maximum intensity projection (MIP) images were generated after intensity harmonization, and three blinded radiologists independently evaluated them.

Primary endpoints were within-subject rankings of overall image quality, major artery depiction, and moyamoya vessel (MMV) visualization across the four datasets. Secondary endpoints included Houkin's classification score for arterial stenosis and a 3-point MMV visibility score. Statistical analysis employed Friedman tests and Wilcoxon signed-rank tests with Holm correction. Inter-rater agreement was assessed with Kendall's W and quadratic-weighted κ statistics.

Results

Across all readers, both overall image quality and visualization of MMVs were consistently ranked higher for DLR-enhanced MRA than for original MRA (all $p<0.001$). Notably, 1.5T DLR-enhanced MRA achieved significantly higher rankings than 3T original MRA ($p<0.048$). For depiction of major cerebral arteries, DLR images were also consistently superior, although one reader found no significant difference between 1.5T DLR and 3T original.

Ordinal scoring confirmed these findings: mean Houkin's scores were lower (indicating less severe stenosis) for DLR-enhanced MRA compared with original images at the same field strength ($p<0.005$). This effect reflected improved visualization of arterial continuity rather than true disease regression. MMV visibility scores tended to increase with DLR; while 3T DLR was significantly superior to 1.5T original for two readers, other comparisons did not reach statistical significance.

Inter-rater agreement was substantial, with Kendall's W of 0.70 for image quality, 0.61 for major artery visualization, and 0.60 for MMVs. The mean quadratic-weighted κ among three readers was 0.77 for Houkin's classification and 0.32 for MMV visibility.

Conclusion

DLR significantly improved image quality and vascular visualization in moyamoya disease, with 1.5T DLR-enhanced MRA outperforming 3T original MRA in overall quality and MMV depiction. By reducing noise and restoring vascular continuity, DLR yielded lower Houkin's classification scores, reflecting clearer vessel depiction rather than clinical improvement. These findings demonstrate that DLR can provide high-quality cerebrovascular

evaluation even on 1.5T systems, offering particular value for patients unable to undergo 3T MRI and for facilities limited to 1.5T scanners. However, when interpreting MRA in moyamoya disease, not only differences in scanner and magnetic field strength but also the presence or absence of DLR should be carefully considered.

Images/Tables

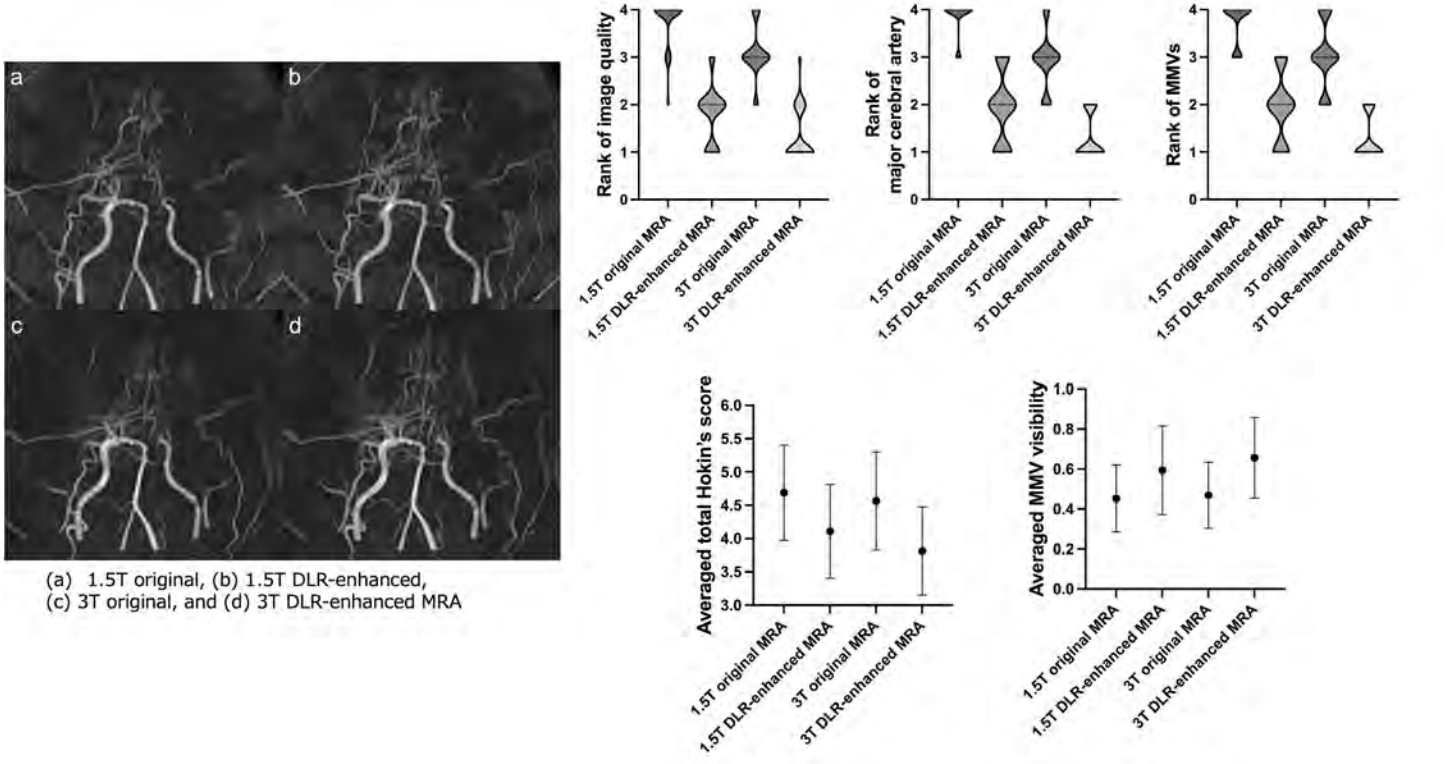

(a) 1.5T original, (b) 1.5T DLR-enhanced, (c) 3T original, and (d) 3T DLR-enhanced MRA

---

184 Agentic Artificial Intelligence in Neuroradiology: Technical Promise Without Clinical Evidence

Sara Salehi MD, Bradley Erickson M.D., Ph.D., Yash Singh Ph.D., Parnian Habibi MD, Wei Yujia MD, Amirali Khosravi MD, varekan keishing Ph.D., Jaidip Jagtap Ph.D.

Mayo Clinic, Rochester, MN, USA

Purpose

Agentic artificial intelligence (AI) refers to systems designed to reason through problems step-by-step, make decisions autonomously, or collaborate with other specialized models. These systems have been proposed to address the well-known limitations of large language models (LLMs) in medical imaging. Although the concept has attracted growing attention, it is unclear how often such systems have been developed, validated, or evaluated in neuroradiology. This review summarizes published work to clarify the current evidence, strengths, and gaps in this emerging field.

Materials & Methods

A systematic literature search was conducted through PubMed, Web of Science, and Scopus for studies published between January 2022 and August 2025, following PRISMA 2020 reporting guidelines. The search strategy combined terms related to agentic AI, multi-agent systems, autonomous reasoning, and neuroradiology. After removing duplicates, titles and abstracts were screened using a large language model–assisted workflow (LLaMA 3.3–70B), which automatically extracted study aims, data types, and AI architecture descriptions. The model flagged candidate papers that met predefined inclusion criteria for human review.

Six independent reviewers (three Medical Doctors and three AI specialists) then performed manual verification and full-text assessment. Studies were included if they demonstrated (i) iterative reasoning combined with either (ii) autonomous tool use or (iii) multi-agent collaboration (distinct coordinated agents with defined roles). Systems limited to single-pass LLM inference, information retrieval, or static text generation were excluded. Study quality was evaluated using an adapted QUADAS-AI framework, assessing five domains: (1) data representativeness and patient selection bias, (2) clarity of AI system design and autonomy description, (3) adequacy of reference standards, (4) validation type and reproducibility, and (5) reporting transparency, including access to reasoning logs and performance metrics. Disagreements were resolved through discussion with a senior neuroradiologist reviewer.

Results

From 230 unique records, nine studies (3.9%) met inclusion criteria. Of these, five (55%) described genuine multi-agent or tool-using systems, while four (45%) relied on single LLMs labeled as agentic despite lacking autonomous behavior. All nine were single-center studies, and none included external or multi-center validation. Sample sizes were small (median = 142 cases; range 16–302).

The only randomized controlled trial, INSPIRE (Gorenshtein et al., 2025), reported 92.2 % accuracy, AIGERS improvement from 0.45 to 0.83 ($p < 0.001$), and a 67 % reduction in reporting time, but no measurable clinical benefit when radiologists used AI assistance compared with independent reporting. None of the studies conducted systematic safety evaluations or assessed hallucination rates.

Most research originated from Asia (44 %), followed by Europe (22 %), the United States (22 %), and Israel (11 %). The majority were retrospective (67 %) and relied on internal datasets only.

Conclusion
Agentic AI in neuroradiology remains at an early research stage. While several systems demonstrated strong technical performance in controlled settings, none provided convincing evidence of clinical benefit. The literature is limited by small single-center samples, absence of safety testing, and inconsistent use of the term "agentic." Future progress will depend on multi-center prospective trials, transparent validation methods, and patient-centered outcome measures to determine whether these complex AI frameworks can meaningfully improve neuroradiologic care.
Images/Tables

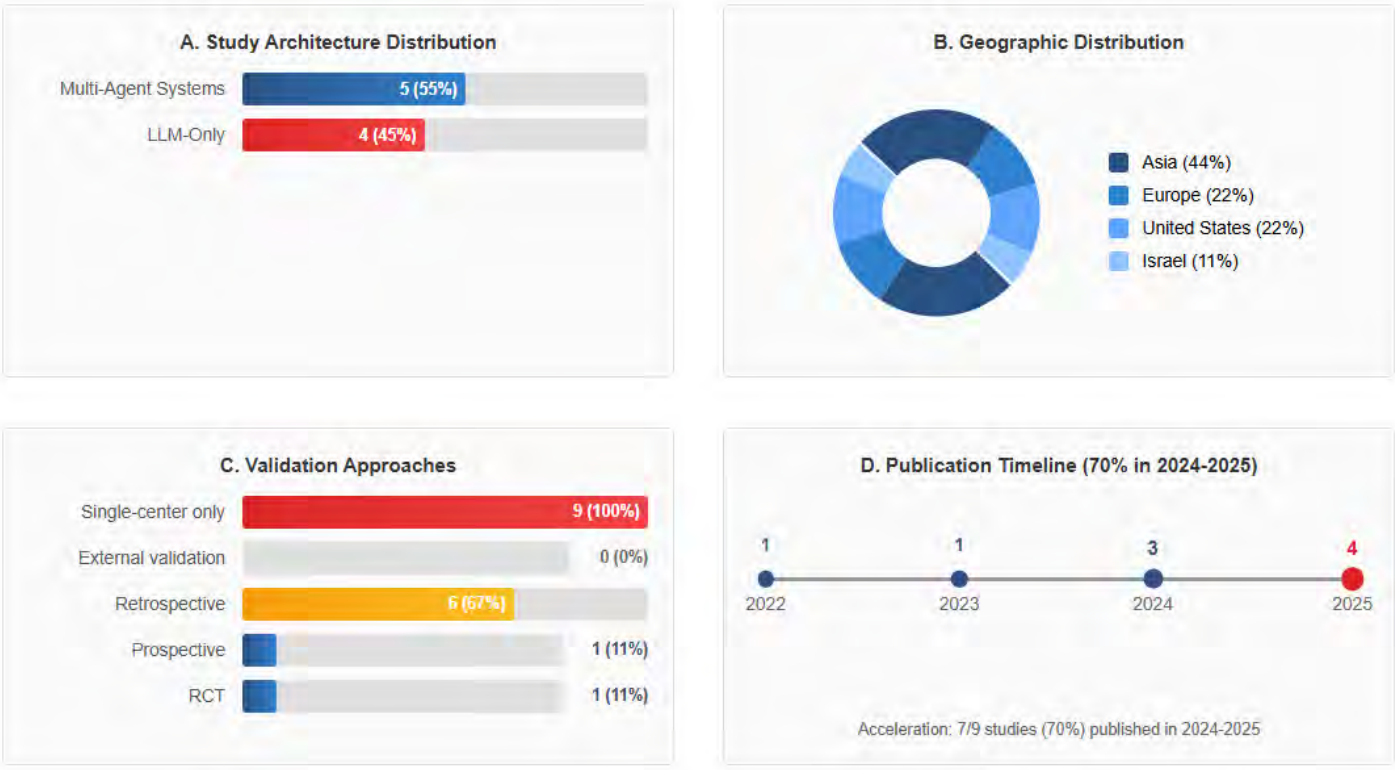

---

220 **Anatomically Constrained Tractography of the Fetal Brain**
Matheus Dorigatti Soldatelli MD, PhD[1], Camilo Calixto MD[1], Simon Warfield PhD[2], Ali Gholipour PhD[2], Camilo Jaimes MD[1], Davood Karimi[2]
[1]Mass General Brigham, Boston, MA, USA. [2]Boston Children's Hospital, Boston, MA, USA
Purpose
Diffusion-weighted Magnetic Resonance Imaging (dMRI) is increasingly used to study the fetal brain in utero, enabling tractography for white matter tract-specific analysis and structural connectivity assessment. However, the low quality of fetal dMRI data and the inherent challenges of tractography often result in highly inaccurate outcomes. This study addresses these limitations by introducing an anatomically constrained tractography method that accurately segments fetal brain tissue directly within dMRI.
Materials & Methods
We develop a deep learning method to compute the segmentation within dMRI automatically. It involves:

- Acquiring fetal MRI scans and preprocessing with motion correction and resampling.
- Estimating local fiber orientations using a diffusion tensor model, enhanced with a sharpening technique for improved accuracy.
- Development of a deep learning model for brain tissue segmentation in the dMRI, using diffusion tensor information modulated by fractional anisotropy.
- Converting the segmentations into five-tissue-type maps for anatomically constrained tractography.
- Performing streamline tracing with the iFOD2 algorithm, using anatomical constraints to launch and terminate streamlines at appropriate boundaries.

The method was validated against established tractography techniques and demonstrated improved accuracy, robustness, and success in reconstructing various tracts, as confirmed by expert radiologist ratings.
Results
In validation using 94 fetal brain MRIs, the method achieved an average Dice similarity coefficient (DSC) of 0.898 for white matter and 0.841 for cortical gray matter, outperforming Attention U-Net by 4.9% and 2.9%, respectively.
The tractography method demonstrated a 99.9% success rate in reconstructing 11 major tracts, compared to 72.2% with iFOD2, 55.6% with FACT, and 52.2% with rk2.
It consistently achieved high-quality ratings, averaging 4.27 out of 5, versus around 1.80 for the other methods, highlighting its potential to enhance fetal brain development and structural connectivity studies.
Conclusion
The study demonstrates that anatomically constrained tractography significantly improves the accuracy of fetal brain imaging.
This method enhances dMRI-based assessments of brain connectivity, offering valuable insights for both scientific and clinical applications in early brain development.

Images/Tables

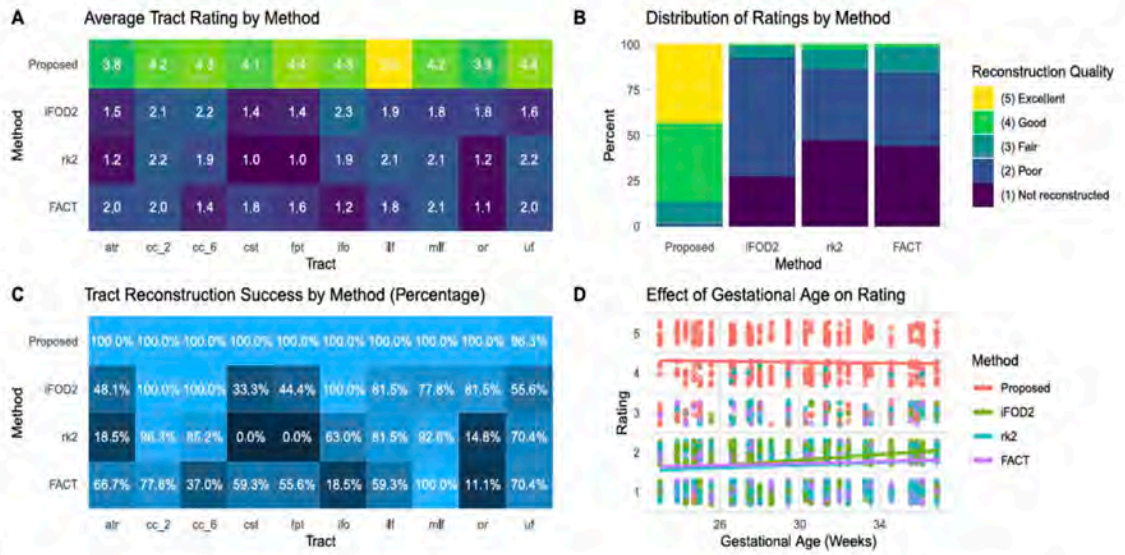

Comparison of the tractography methods. (A) Heatmap displaying the average ratings for each tractography method across different tracts. Each cell is annotated with the average rating value. (B) Bar plot showing the percentage distribution of reconstruction quality ratings for each tractography method. (A) and (B) share the same legend of ratings categorized from "(1) Not reconstructed'' to "(5) Excellent''. (C) Heatmap quantifying the percentage of successful tract reconstructions by each method. Percentages are shown on the plot, increasing brightness with higher success rates. (D) Scatter plot with fitted lines illustrating how ratings vary with gestational age for each tractography method. Points are jittered to prevent overplotting, and lines indicate trends, providing insights into how method effectiveness might change over the gestational period.

---

230 Application of the MR Bone Imaging to Carotid Plaque Imaging

Kazuhiro Tsuchiya, Miho Gomyo, Kenichi Yokoyama
Kyorin University, Mitaka, Tokyo, Japan

Purpose

MR bone imaging is a recently developed technique of imaging bony structures, acquiring signals of tissues with a short T2 value, which is difficult to depict with conventional MR imaging. Obtaining signals from cortical/trabecular bones can show bones and calcification, like CT. As vessels present as areas of a signal void like other sequences, we hypothesized that MR bone imaging could be applied to carotid vessel wall imaging (VWI) that can demonstrate calcified plaques, and conducted this preliminary study to assess its feasibility.

Materials & Methods

We performed MR bone imaging on 24 consecutive patients (23 males and 1 female, age range: 53 to 86 years; average: 68 years) referred for carotid plaque MR imaging and assessed their images. MR imaging was performed on a 1.5-T imager (Avanto fit, Siemens Healthineers). In addition to 3D time-of-flight MR angiography, conventional T1- and T2-weighted VWI was performed using a T1-weighted SPACE and a fat-suppressed turbo spin-echo T2-weighted sequence, respectively. Additionally, MR bone imaging was performed by a 3D multi-echo gradient-echo sequence. We visually evaluated the four kinds of images regarding stenosis and, in patients with stenosis, plaque characteristics. Furthermore, we compared MR bone images with CT angiograms when available.

Results

Proximal internal carotid artery stenosis of any degree was present in 23 sides of a total of 48 sides of the 24 patients. Among the 23 sides, an unstable plaque was found on 13 sides and not found on the remaining 10 sides. On MR bone imaging, calcification was detected on 19 sides and not on 10 sides. Among the 19 sides, calcification was noted within an unstable plaque on 11 sides, while just an unstable part was revealed on 2 sides. Plaques were mostly calcified on 8 sides. In 3 patients whose CT angiography for comparison was available, CT angiography and MR bone imaging corresponded regarding calcification.

Although the number of patients whose CT angiography was directly compared with MR bone imaging was limited, our results suggest that MR bone imaging is likely to be effective in demonstrating calcification in the carotid plaques. It is noteworthy that partial calcification is a frequent finding even in unstable plaques. This could be important information in establishing the therapeutic strategy.

Conclusion

MR bone imaging could be an effective technique when added to conventional carotid VWI, possibly obviating CT angiography.

Images/Tables

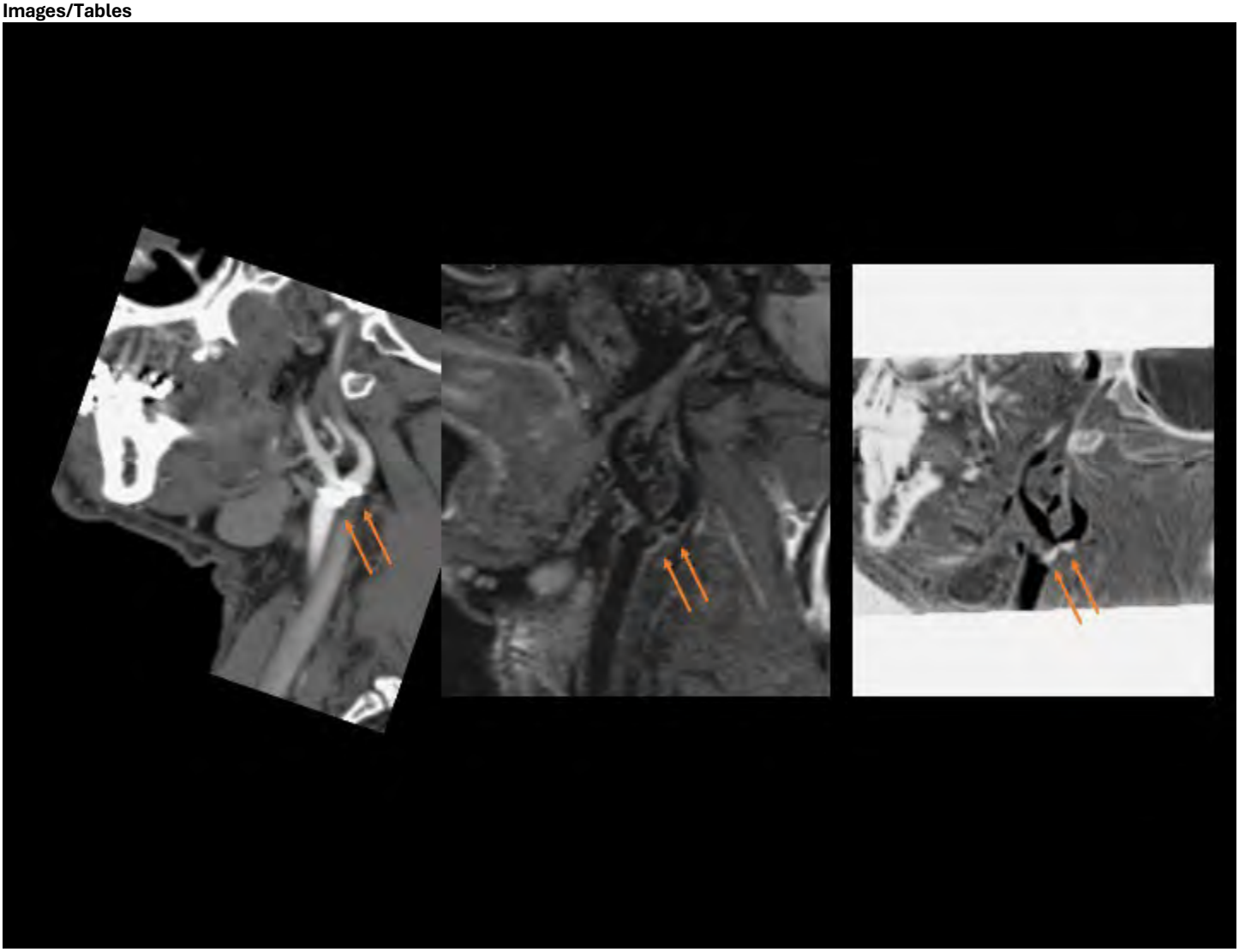

233 **Identifying Concomitant Alzheimer Pathology in Idiopathic Normal-Pressure Hydrocephalus Using CSF AT(N) and p-tau/Aβ42 Ratio**

Eugene Moon MD[1], Justin Hoskin MD[2], Jacob Knittel MD[3], Peter A Chiarelli MD[4], Kevin King MD[2], Raza Mushtaq MD[2]

[1]Creighton University, Pheonix, AZ, USA. [2]Barrow Neurological Institute, Phoenix, AZ, USA. [3]Dignity Health East Valley, Pheonix, AZ, USA. [4]Phoenix Children's Hospital, Phoenix, AZ, USA

Purpose

Idiopathic normal-pressure hydrocephalus (iNPH) can arise concurrently with Alzheimer's disease (AD). Distinguishing iNPH-only from iNPH with concomitant AD (AD+iNPH) is clinically important because concomitant AD may contribute to suboptimal cognitive treatment/shunting response. This study estimated the prevalence of biological Aβ42 positive (A+)/p-tau positive (T+) AD through high-volume lumbar puncture (LP) CSF sampling within an iNPH cohort, and evaluated p-tau/Aβ42 ratio as a screening tool that could be applied at the NPH lumbar puncture test to triage patients for confirmatory testing and inform shunt candidacy.

Materials & Methods

Patients with clinically diagnosed iNPH and CSF biomarkers from a prospective series (n=30) and a retrospective series (n=93) were combined (n=123). Prespecified thresholds for Aβ42 and tau protein positivity were applied: A+ if Aβ42 ≤ 834 pg/mL; T+ if p-tau181 > 21.6 pg/mL; N+ if total tau > 238 pg/mL. Biological AD was defined per NIA-AA framework as A+T+ (N+ optional). The p-tau/Aβ42 ratio was analyzed continuously and at two a priori screening cut points utilized in clinical workflow: >0.028 (sensitive, rule-out) and >0.035 (more specific, rule-in). Outcomes included the prevalence of A+T+ with Wilson 95% CIs; discrimination by ROC AUC with bootstrap 95% CIs (2,000 resamples); operating characteristics at each threshold (sensitivity, specificity with Wilson CIs; PPV; NPV); and between-group ratio differences by Mann–Whitney U.

Results

Among 123 iNPH patients, A+T+ AD was present in 11 (8.9%; 95% CI, 4.8–15.3). The p-tau/Aβ42 ratio showed statistically significant ability to discriminate A+T+ AD (AUC, 0.96; 95% CI, 0.91–1.00). Ratio values were substantially higher in A+T+ AD than in non-A+T+ patients (median, 0.056 vs 0.015; $p=4.5\times10^{-7}$). Testing of the more sensitive screening threshold (ratio>0.028) identified 25/123 patients and yielded sensitivity=0.91 and specificity=0.87 (PPV=0.40; NPV=0.990), and captured 10 of 11 A+T+ cases. The more specific screening criteria (ratio>0.035) identified 14/123 patients with sensitivity=0.82 and specificity=0.96 (PPV=0.64; NPV=0.982), suitable for preselection when false positives must be limited. Among ratio-positive but non-A+T+ cases, most were A+T− (amyloid-only), consistent with "Alzheimer pathologic change" rather than biological AD.

Conclusion

A clinically important sub-group of patients evaluated for iNPH demonstrate concomitant biological AD by CSF analysis. LP to assess symptomatic improvement is already a part of the clinical NPH diagnostic workflow, and analyzing p-tau/Aβ42 ratios from this LP represents a pragmatic approach to differentiate AD+iNPH from iNPH-only. The >0.028 threshold functions as a sensitive rule-out screen for AD, whereas >0.035 prioritizes specificity for rule-in. A simple two-step workflow is proposed—screen by ratio, then confirm A and T—, which is immediately implementable and can help clinical teams contextualize cognitive findings, interpret imaging in a biologic framework, and guide counseling regarding expectations for NPH treatment.

Images/Tables

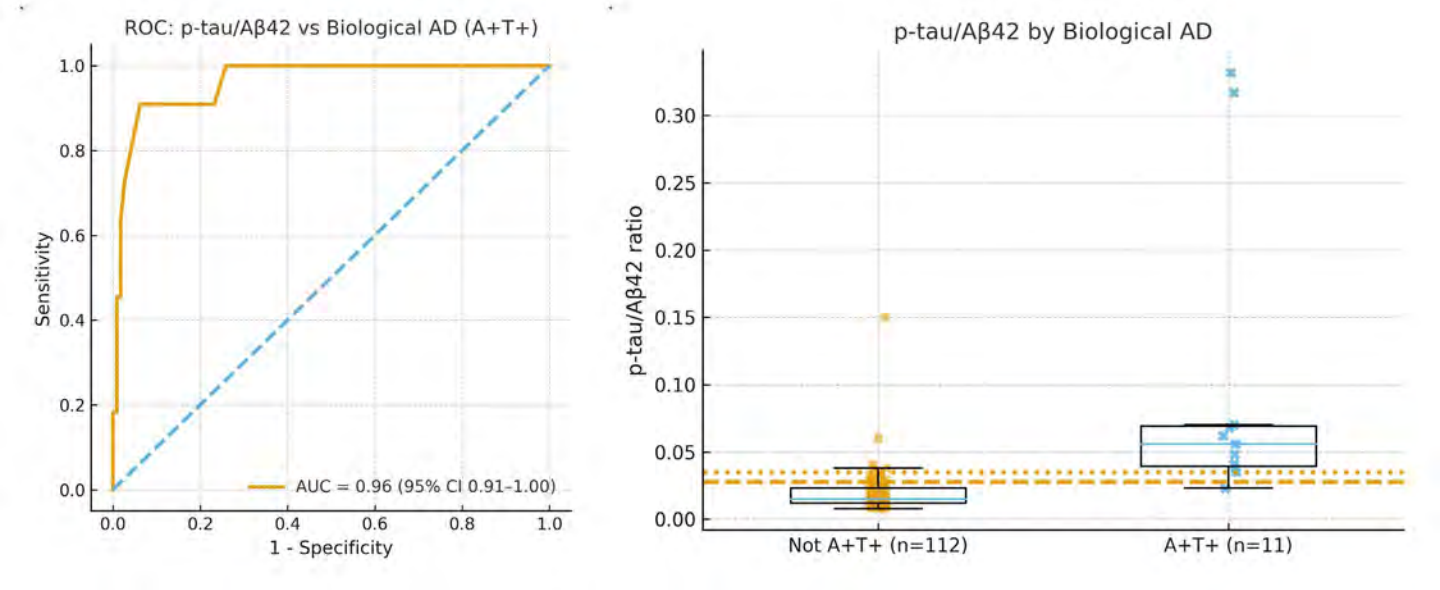

---

262 Phineas Gage Syndromes in the MRI Era: Orbitofrontal Lesions and Behavioral Dyscontrol Across Diverse Etiologies

Beatriz De Faria Sousa BS, Ana Ruas BS, Juan Espinosa MD
FIU HWCOM, Miami, FL, USA

Purpose

The orbitofrontal cortex (OFC) plays a pivotal role in regulating inhibition, decision-making and social behavior. Lesions in this region, regardless of etiology, produce profound personality and behavioral changes reminiscent of the historic Phineas Gage case. Despite characteristic neurobehavioral patterns, these syndromes remain underrecognized on MRI, leading to frequent misclassification as primary psychiatric illness. This study reviews structural and functional imaging findings of orbitofrontal lesions across several major etiologies, highlighting reproducible patterns of behavioral dyscontrol.

Materials & Methods

Case reports and series published since 2000 were identified through PubMed using combinations of key search terms, including *orbitofrontal cortex*, *lesion*, *disinhibition*, *impulsivity* and *behavior*. Studies were included if MRI and/or other functional imaging modalities localized pathology to the OFC and provided clinical behavioral descriptions. Twenty-four reports met criteria and were grouped by etiology: trauma, tumor, stroke and neurodegeneration. Data extracted for our analysis included hemispheric laterality of the lesion, the OFC subregion affected, behavioral phenotype, neural network involvement and patient outcome.

Results

Across etiologies, OFC disruption produced a shared behavioral signature – disinhibition, impulsivity and/or emotional lability – with preserved general cognition.

- Trauma: Bilateral or right OFC contusions caused chronic disinhibition and poor judgment despite normal IQ. Lesions were often undetectable on standard MRI but apparent on high-resolution 3T imaging.
- Tumor: Orbitofrontal or ventromedial compression from meningiomas produced hypersexuality, euphoria or aggression, frequently reversible after surgical resection.
- Stroke: Left medial OFC infarcts yielded compulsive checking behaviors; right or subcortical (thalamic, striatocapsular) lesions with secondary OFC hypoperfusion produced hypersexuality or inappropriate humor.
- Neurodegeneration: In behavioral-variant frontotemporal dementia (bvFTD) and Parkinson disease, right and ventromedial OFC atrophy correlated with impulsivity, binge eating and loss of inhibitory control. bvFTD exhibited the most severe disinhibition, compared to other neurodegenerative diseases.

Across all groups, right or bilateral OFC injury correlated with behavioral release, while left medial OFC lesions produced compulsivity and perseveration. Recovery varied by etiology – reversible in tumor compression, partial in vascular lesions, and persistent in trauma and neurodegenerative conditions.

Conclusion

Independent of etiology, orbitofrontal network disruption yields a reproducible syndrome of disinhibition and impaired social judgment. Multimodal imaging, particularly high-resolution MRI, PET and/or SPECT, enables recognition of these “Phineas Gage syndromes,” improving diagnostic accuracy and reducing psychiatric misdiagnosis. Radiologists should regularly examine the basal frontal surfaces when assessing unexplained behavioral changes for reversible orbitofrontal pathology.

Images/Tables

Trauma: 54-Year-Old Man Hit by Passing Vehicle

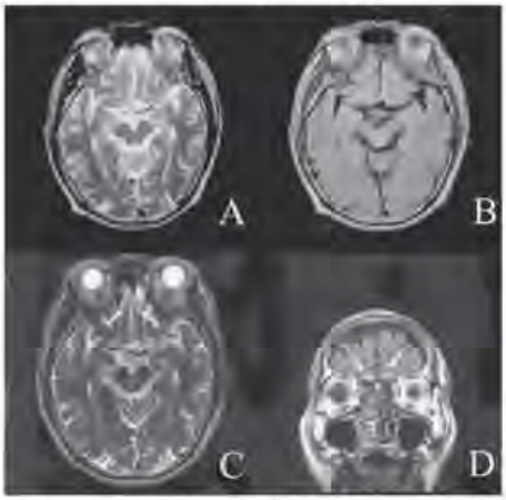

Figure 1: Panels A and B (1.5T MRI T2-weighted and FLAIR [slice number = 20; slice thickness = 5 mm] images, respectively) highlight unclear high-intensity signals in the orbitofrontal cortex (OFC). Panels C and D (3T MRI T2-weighted and FLAIR [slice number = 32; slice thickness = 3.5 mm] images, respectively) provide a more clear depiction of the high intensity signals (arrows) in the bilateral OFC.

Image obtained from: Namiki C, Yamada M, Yoshida H, Hanakawa T, Fukuyama H, Murai T. Small orbitofrontal traumatic lesions detected by high resolution MRI in a patient with major behavioural changes. *Neurocase*. 2008;14(6):474-479. doi:10.1080/13554790802459494.

Tumor: 40-Year-Old Male with a Hemangiopericytoma

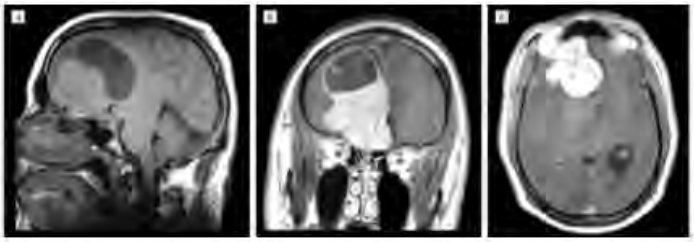

Figure 2: MRI findings at the time of initial neurologic examination:

a) T1 sagittal view
b) Contrast-enhanced coronal view
c) Contrast-enhanced axial view

Panels a) and b) highlight the tumor mass extending superiorly to displace the right OFC and distorting the dorsolateral prefrontal cortex.

Image obtained from: Burns JM, Swerdlow RH. Right orbitofrontal tumor with pedophilia symptom and constructional apraxia sign. *Arch Neurol*. 2003;60(3):437-440. doi:10.1001/archneur.60.3.437.

Stroke: 88-Year-Old Female Post-Caudate Stroke

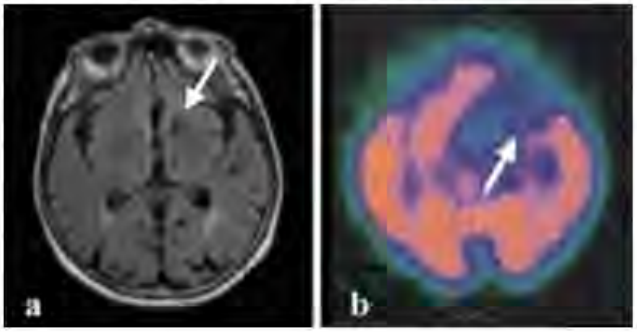

Figure 3:

a) Stroke of the ventral head of the left caudate nucleus (arrow) as visualized by MRI; hippocampal volume preserved.
b) Disconnected regions with hypoperfusion of the left orbitofrontal cortex seen on SPECT (arrow).

Image obtained from: Lanna ME, Alves CE, Sudo FK, et al. Cognitive disconnective syndrome by single strategic strokes in Vascular dementia. *Journal of the Neurological Sciences*. 2012;322(1-2):176-183. doi:10.1016/j.jns.2012.08.004.

Neurodegeneration: Behavioral Variant FTD vs. Alzheimer's disease

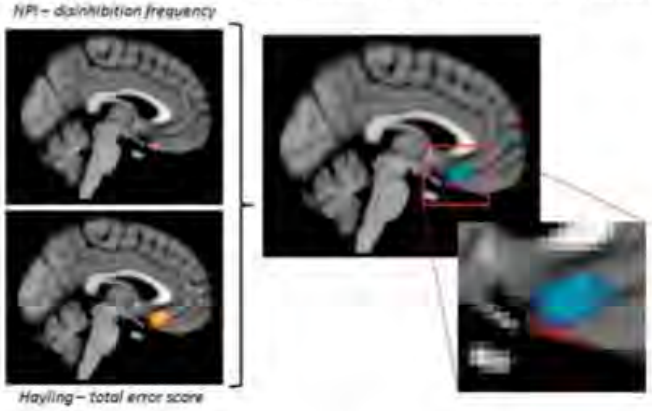

Figure 4: Overlap of disinhibition frequency with grey matter atrophy in patients with behavioral variant FTD and Alzheimer's disease. Colored voxels highlight significant regions (e.g. the OFC) in the analysis.

Image obtained from: Hornberger M, Geng J, Hodges JR. Convergent grey and white matter evidence of orbitofrontal cortex changes related to disinhibition in behavioural variant frontotemporal dementia. *Brain*. 2011;134(Pt 9):2502-2512. doi:10.1093/brain/awr173.

---

275 COMPARISON OF AMINO-ACID IMAGING METHODS - AN MR PET STUDY USING APT AND FET-PET IN TREATED GLIOMAS

Sandhya Mangalore MBBS,MD,DM, Venkatesh Murthy
NIMHANS, Bengaluru, Karnataka, India

Purpose

The study involves treated glioma cases where tumour and non-tumour components overlap on imaging features such as contrast enhancement and edema. Routine MRI (T1/T2/FLAIR) and advanced MRI (SWI/DWI/DCE/MRS/CEMRI) are standard, with equivocal cases referred to PET/MR for FET-PET. FET-PET, using O-(2-[18F]fluoroethyl)-L-tyrosine ([18F]FET), is the gold standard due to its high sensitivity/specificity and selective uptake in glioma cells via LAT2 transporter. However, FET-PET requires a cyclotron, radiopharmaceutical injection, and is costly. APT imaging detects amide

protons in mobile proteins/peptides, driven by intracellular amide macromolecules and alkaline pH in tumours, increasing APT signal. Our tertiary neuro-oncology center with in-house FET-PET aims to validate APT as a potential alternative to FET-PET.

Materials & Methods

Imaging was conducted on a Siemens Biograph mMR 3T simultaneous PET/MR scanner. After intravenous injection of 4.44 mCi F-18 FET, whole-brain PET images were collected in 3D list mode for 23 minutes following a 20-minute uptake. The APT protocol, supplied by Prof. Morris Weiss, was adapted on the 3T Biograph mMR, optimizing parameters to match FET's SNR. Both scans used 5 mm slice thickness, and APT acquisition used a 96x96x14 matrix. Manual B_0 shimming (FWHM ≤ 25 Hz) preceded CEST acquisition. A Gaussian-shaped RF saturation pulse train (2μT, 40 pulses) was applied with NSA=4 and total acquisition time 13 minutes. Frequency offsets from −6 to +6 ppm covered the amide proton resonance at +3.5 ppm (3 repeats). Multi-slice 2D acquisition improved saturation uniformity. Post-acquisition, a B_0 map was reacquired (TA=2 min) for voxel-wise field correction. APT-weighted maps were generated via in-house code using the MTRasymm formula: [M(3.5)−M(−3.5)]/M0. APT images underwent QC including curve-fit quality, artifact removal, and B_0 homogeneity screening, then color-coded to match PET uptake patterns.

Results

Nine patients were studied. APT imaging matched FET-PET in all cases (100%) better than basic and advanced MRI. Lesions identified as recurrence on FET-PET showed increased APT signals, while necrotic lesions showed no significant APT effect. Heterogeneous lesions revealed necrotic components with low FET uptake and low APT signal, showing both modalities capture tumour heterogeneity. Cystic proteinaceous components, which did not invert on FLAIR, demonstrated higher APT signals alongside tumour recurrence foci.

Conclusion

APT imaging demonstrated good concordance with FET-PET in evaluating treated gliomas. By providing molecular information without the need for radiotracers, APT represents a promising non-radioactive, MRI-based alternative to amino-acid PET. With continued technical refinement and validation in larger multicenter studies, APT could evolve into a viable substitute for FET-PET.

---

291 Ticagrelor vs Clopidogrel for Carotid Artery Stenting: Is There a Difference in Safety and Efficacy? A Multicenter Analysis

Jay Kakadiya MD[1], Huanwen Chen MD, MHSc[2], Hamza A Salim MD[3], Muhammed Amir Essibayi MD, MSc[4], Pranjal Rai MD[5], Amelia Adcock MD[6], Ahmed Y Azzam MD[7], Arsh Patankar MD[8], Vivek S Yedavalli MD[1], Adam A Dmytriw MD, MPH[9], Marco Colasurdo MD[10], Ajay Malhotra MD[11], Dheeraj Gandhi MD[12], Dhairya A Lakhani MD[13]

[1]Division of Neuroradiology, Department of Radiology and Radiological Sciences, Johns Hopkins University, Baltimore, MD, USA. [2]Department of Neurology, University of Maryland Medical Center, Baltimore, MD, USA. [3]Department of Neuroradiology, MD Anderson Cancer Center, Houston, TX, Houston, TX, USA. [4]Department of Neurological Surgery, Montefiore Medical Center, the University Hospital for Albert Einstein College of Medicine, New York, NY, USA. [5]Department of Radiology, Mayo Clinic, Rochester, Rochester, MN, USA. [6]Department of Neurology, Rockefeller Neuroscience Institute, West Virginia University, Morgantown, WV, USA. [7]Department of Neurological Surgery and Montefiore-Einstein Cerebrovascular Research Lab, Montefiore Medical Center, Albert Einstein College of Medicine, Bronx, NY, USA. [8]Faculty of Clinical Medicine, University of Oxford, Oxford, Oxford, United Kingdom. [9]Neuroendovascular Program, Massachusetts General Hospital & Brigham and Women's Hospital, Harvard Medical School, Boston, MA, USA. [10]Department of Interventional Radiology, Oregon Health and Science University, Portland, OR, USA. [11]Department of Radiology, Yale New Haven hospital, New Haven, CT, USA. [12]Department of Neurosurgery, University of Maryland Medical Center, Baltimore, MD, USA. [13]Department of Neuroradiology, Rockefeller Neuroscience Institute, West Virginia University, Morgantown, WV, USA

Purpose

Carotid artery stenting (CAS) generally requires dual antiplatelet therapy (DAPT) to reduce periprocedural stroke risk. While clopidogrel is widely used, its therapeutic onset and reliability may be limited by pharmacokinetics and genetic polymorphism. Recently, ticagrelor has gained popularity as a more potent alternative to clopidogrel; however, whether ticagrelor confers an advantage over clopidogrel in the setting of CAS is largely unknown.

Materials & Methods

We conducted a retrospective cohort study using the TriNetX database, identifying patients with carotid artery stenosis undergoing CAS between 2015–2023 who received ticagrelor or clopidogrel. Propensity score matching (PSM) was performed to balance baseline characteristics. The primary outcomes were stroke, major hemorrhage, intracranial hemorrhage, and all-cause mortality at 180 days. Secondary outcomes included subarachnoid and intraparenchymal hemorrhage, emergency room visits, and hospital readmissions. Kaplan–Meier survival analysis and Cox regression were used to compare outcomes.

Results

A total of 6,996 patients were included (378 ticagrelor; 6,618 clopidogrel), and after PSM, 377 remained within each group. Compared to those who received clopidogrel, patients treated with ticagrelor had comparable rates of stroke (HR 0.56 [95%CI 0.25–1.27]), major hemorrhage (HR 0.61 [95%CI 0.29–1.30]), intracranial hemorrhage (HR 0.61 [95%CI 0.14–2.53]), or all-cause mortality (HR 1.64 [95%CI 0.68–3.97]). (Table 1)

Conclusion

Ticagrelor was not associated with different rates of stroke, intracranial hemorrhage or higher risk of all-cause mortality compared to clopidogrel for patients undergoing CAS.

Images/Tables

Table 1: Study outcomes within 180 days among PSM cohorts

	PSM cohorts			
Outcomes^	Ticagrelor N = 377	Clopidogrel N = 377	p-value	HR [95%CI]
Stroke	2.7% (<11)	4.2% (16)	0.159	0.56 [0.25-1.27]
Major hemorrhage	2.9% (11)	4.8% (18)	0.197	0.61 [0.29-1.30]
Subarachnoid hemorrhage	2.7% (<11)	2.7% (<11)	0.989	-
Intraparenchymal hemorrhage	2.7% (<11)	2.7% (<11)	0.651	0.50 [0.09-2.75]
Any ICH	2.7% (<11)	2.7% (<11)	0.488	0.61 [0.14-2.53]
Emergency room visit	14.3% (54)	14.6% (55)	0.895	0.97 [0.67-1.42]
Hospital readmission	15.9% (60)	19.1% (72)	0.223	0.81 [0.57-1.14]
All-cause mortality	3.4% (13)	2.7% (<11)	0.263	1.64 [0.68-3.97]

^Outcomes were reported as event probability at 180 days per Kaplan Meier analysis and event counts, p-values were derived from log-rank tests of Kaplan Meier curves, and hazard ratios (HR) represent risk associated with ticagrelor versus clopidogrel calculated using Cox proportional hazards models. Outcomes with less than 11 events were reported as such per data use agreement with ANONYMIZED DATABASE; having counts <11 did not impact the exact calculation of true event probabilities, p-values, or hazards ratios.

---

292 **Optimizing post-contrast MRI for melanoma brain metastases: Comparative Value of 3D T1 GRE and 3D T1 TSE Black Blood Sequences**

Zhao Hui Chen Zhou, Elena Salvador Álvarez, Amaya Hilario, Agustín Cárdenas, Juan Romero, Carmen Lechuga, Ana Martínez de Aragón, Ana Ramos
Hospital Universitario 12 de Octubre, Madrid, Madrid, Spain

Purpose

Brain metastases are the most common type of malignant brain tumor (10–40% of cancer patients). Post-contrast 3D T1 TSE black blood sequences are superior to traditional 3D T1 GRE in detecting brain metastases. Consequently, there has been a gradual shift towards using post-contrast 3D-TSE instead of 3D-GRE. However, melanoma-related brain metastases are different because they may contain melanin, which exhibits intrinsic T1 hyperintensity. Our objective is to compare the ability of post-contrast 3D T1 TSE black blood sequences and post-contrast 3D T1 GRE sequences to detect melanoma brain metastases based on melanocytic content.

Materials & Methods

A retrospective observational study of cranial MRIs in patients suspected of melanoma brain metastases was conducted over a 12-month period (March 2024 - March 202). Two neuroradiologists (8 and 15 years of experience), independently reviewed the images. Each brain metastasis was categorized as melanocytic, non-melanocytic or hemorrhagic based on the signal on 3D T1 sequences without contrast and susceptibility weighted imaging. A subjective visual comparison was performed using a 5-point scale: 1 – only identified in black blood; 2 – better visualization on black blood ; 3 – visualization is the same in both sequences; 4 – better visualization on the 3D T1 GRE sequence; and 5 – only identified in the 3D T1 GRE sequence. The contrast-to-noise ratio (CNR) was measured for each metastasis in both sequences, and the difference between them was calculated as ΔCNR = CNR_GRE − CNR_SN, with positive values indicating higher contrast on GRE. Statistical analysis included paired t-tests and Wilcoxon signed-rank tests for comparing paired CNR values, chi-square tests for analyzing subjective scores across metastasis types. A p value < 0.05 was considered statistically significant.

Results

We have included 120 brain metastases in 23 patients (mean age: 59.9 ± 12.8 years; 52% male) with melanoma. Subjective visualization was strongly influenced by the type of metastasis (χ^2 = 88.9, p < 0.001). Melanin metastases were predominantly rated as better or only visible on GRE (82% of lesions, scores 4–5), whereas non-melanin and hemorrhagic metastases were mostly rated 2–3, indicating equal or better visualization on black blood. Objective measurements showed consistent results. For melanin metastases, the mean ΔCNR was +10.7 ± 10.3 (p < 0.001), confirming significantly higher contrast in GRE. For non-melanin and hemorrhagic lesions, mean ΔCNR values were −10.2 ± 14.8 and −8.8 ± 10.1, respectively (both p < 0.001), indicating higher contrast in SN. Median ΔCNR values followed the same trend.

Conclusion

The detection of brain metastases from melanoma using post-contrast 3D T1 GRE/black blood sequences depends on the subtype of metastasis (melanin versus non-melanin). Melanocytic metastases are better identified in post-contrast 3D T1 GRE sequences, whereas non-melanocytic

metastases are better identified in 3D T1 TSE black blood sequences. However, it is not possible to determine which is which until the cranial MRI scan has been performed. Therefore, when it comes to melanoma brain metastases, using both post-contrast sequences may maximize sensitivity, optimize image interpretation and increase radiologist confidence in detecting melanoma brain metastases.

Images/Tables

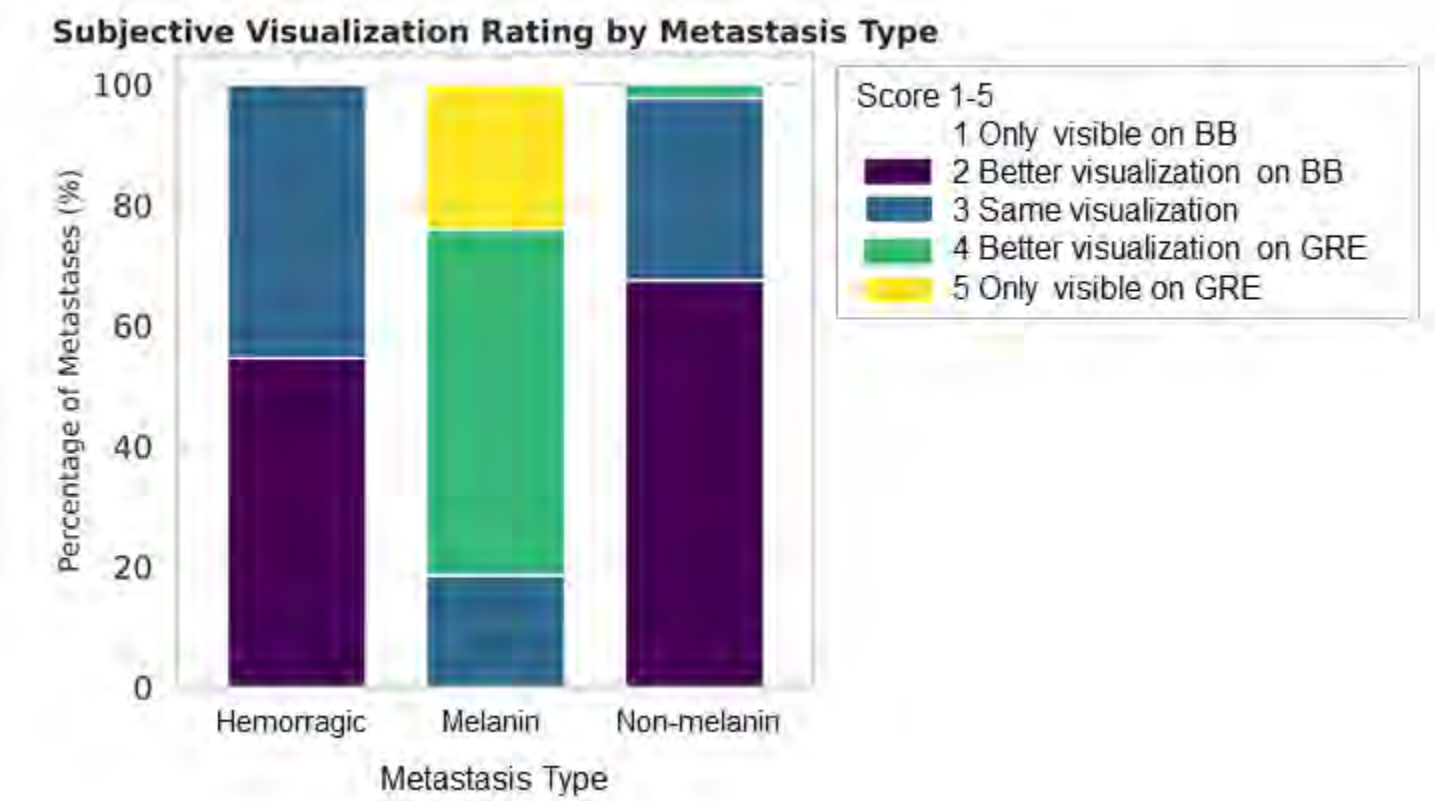

322 Early and Late Mortality Prognostication in Acute Ischemic Stroke

Bianca Savant, Paolo Panales
University of North Dakota School of Medicine and Health Sciences, Fargo, North Dakota, USA

Purpose

Accurate prognostication after acute ischemic stroke (AIS) aids in long-term management. We previously assessed ASTRAL, DRAGON, and THRIVE in predicting good vs. poor outcomes at 90-days and found they do not reliably predict poor function (mRS >3). In this study, we evaluate their ability to predict early and late mortality post-AIS, testing whether distinguishing survival vs. mortality improves accuracy. We also examined several clinical factors for an association with mortality post-AIS to enhance prognostication and identify strong predictors for developing a superior stroke scale in the future.

Materials & Methods

A retrospective analysis of 233 ischemic stroke cases from 2014-2023 at Sanford Medical Center was conducted. Prognostic scores were calculated at 7 and 90 days. ROC curve analysis was used to assess discriminative ability. We also compared late, 90-day mortality with pre-stroke mRS, Trial of ORG 10172 in Acute Stroke Treatment (TOAST) stroke etiologies, altered mental status on admission, and ipsilateral extracranial artery stenosis on neck computed tomography angiography (CTA neck). This analysis was generated using GraphPad Prism version 10.0 (GraphPad Software, Inc., San Diego, CA).

Results

ASTRAL showed excellent predictive ability for 7-day mortality (AUROC 0.92) and considerable accuracy at 90 days (AUROC 0.83). DRAGON and THRIVE performed considerable and fair, respectively. Pre-stroke mRS, cardioembolic etiology, and altered mental status were strongly associated with 90-day mortality ($p < 0.0001$). Ipsilateral extracranial stenosis was not predictive.

Conclusion

Among the three scoring tools, ASTRAL exhibited the strongest ability to predict early mortality, but its accuracy decreased for late mortality. The discrepancy in ASTRAL, THRIVE, and DRAGON's performance may be attributed to the different variables each tool utilizes for scoring. Certain clinical factors may hold greater prognostic value than others. Our preliminary analysis suggests pre-stroke mRS, TOAST stroke etiology, and altered mental status at presentation may have good prognostic value.

Images/Tables

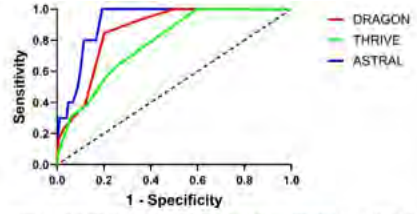

Figure 1: Receiver operating characteristic (ROC) curves generated for 7-day mortality

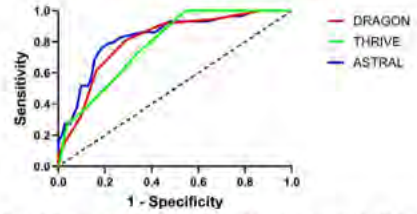

Figure 2: Receiver operating characteristic (ROC) curves generated for 90-day mortality

	7-day mortality	90-day mortality
	AUROC (95% CI)	AUROC (95% CI)
ASTRAL	0.92 (0.87 - 0.97)	0.83 (0.76 - 0.91)
DRAGON	0.86 (0.79 - 0.93)	0.81 (0.74 - 0.88)
THRIVE	0.78 (0.68 - 0.89)	0.78 (0.72 - 0.85)

Table 1: Area under receiver operating characteristic curve (AUROC) for 7-day and 90-day mortality

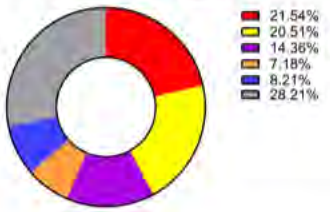

Figure 3: Distribution of TOAST stroke subtype in patients alive at 90-days post-AIS

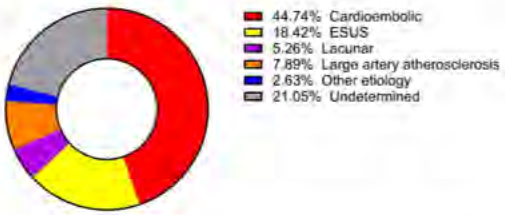

Figure 4: Distribution of TOAST stroke subtype in patients deceased at 90-days post-AIS

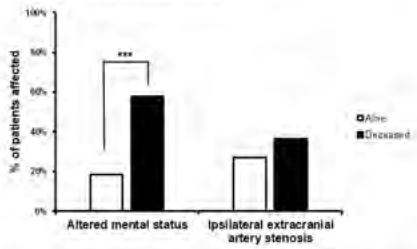

Figure 5: Proportion of alive vs. deceased patients with altered mental status or ipsilateral extracranial artery stenosis
***, p ≤ 0.0001 calculated by Chi-square test

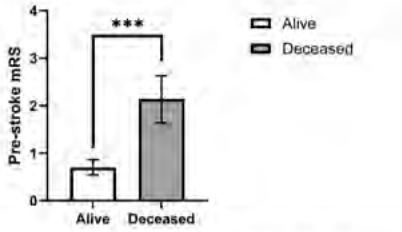

Figure 6: Average pre-stroke mRS of alive vs. deceased 90 days after acute ischemic stroke
***, p < 0.0001 calculated by the Mann-Whitney test; Effect size: Cohen's d = 1.2

323 Real World Performance of VIZ AI Detection of Intracranial Hemorrhage and Subdural Hematoma.

Farooq Hassan DO, Mark Gedrich DO, D'Shaun Adams MD, Kristian Quevada MD, Khuram Kazmi MD
Cooper University Hospital, Camden, NJ, USA

Purpose

To assess the institutional efficacy of VIZ artificial intelligence models in detecting intracranial hemorrhage (ICH) and subdural hematomas (SDH).

Materials & Methods

A retrospective analysis was performed on over 400 brain computed tomography (CT) cases which were processed by the proprietary VIZ AI software for ICH and SDH. The VIZ AI analysis was compared to the reference standard of the final attending radiology report. Concordance and discordance were determined for each case, with reasons for discordance subsequently identified. Performance was quantified using accuracy, specificity, sensitivity, negative predictive value (NPV), positive predictive value (PPV) and F1 scores for both ICH and SDH algorithms.

Results

The study cohort of 422 cases (August 2023 – March 2024) revealed 45 ICH and 40 SDH cases, as per the final attending radiologist read. The ICH model had an accuracy of 94%, sensitivity of 64.4% and a specificity of 97.4%. The NPV was 97.4%, PPV was 74.6%, and F1 score was 0.69. The SDH model exhibited an accuracy of 95%, sensitivity of 74.6% and a specificity of 97.6% The NPV was 97.1%, PPV was 76%, and F1 score was 0.74.

Conclusion

The widely used VIZ AI software for ICH and SDH detection demonstrated mixed results when reviewing its real-world performance at our institution. Specifically, it showed stronger capability for excluding hemorrhage when truly absent but was weaker in detecting hemorrhage when present. Physicians should consider these potential limitations when utilizing the software in their practice.

Images/Tables

Figure 1: VIZ AI ICH	**Positive ICH**	**Negative ICH**	
Positive Test	29	10	PPV: 74.6%
Negative Test	16	367	NPV: 97.4%
	Sensitivity: 64.4%	Specificity: 97.4%	F1: 0.69

Figure 1: VIZ AI intracranial hemorrhage algorithm performance.

Figure 2: VIZ AI SDH	**Positive SDH**	**Negative SDH**	
Positive Test	29	9	PPV: 76%
Negative Test	11	373	NPV: 97.1%
	Sensitivity: 74.6%	Specificity: 97.6%	F1: 0.74

Figure 2: VIZ AI subdural hematoma algorithm performance.

---

331 The Rising Cost of Code Stroke Imaging and Treatment: A Six-year Experience at a Primary Stroke Center

Nisharg Parikh MD[1], Yosef Glick MD[1], Alyson Bryson BSN, RN[2], Deonna Williams-Square BS[2], Stanley Lu MD[2]

[1]Rutgers Robert Wood Johnson Medical School, Department of Radiology, New Brunswick, NJ, USA. [2]Department of Radiology, Monmouth Medical Center, Long Branch, NJ, USA

Purpose

The increasing cost of acute stroke evaluation has been well documented, primarily driven by increased utilization of advanced neuroimaging (CTA, CTP, MRI) and costs associated with intravenous thrombolysis (IVT) or endovascular thrombectomy (EVT).[1,2] Given the expanded use of IVT and EVT in published guidelines[3], we hypothesized that increasing costs of neuroimaging over the years would correspond to higher rates of definitive stroke therapy.

Materials & Methods

A retrospective analysis of all code stroke activations at our institution between January 1, 2020 and September 30, 2025 was conducted for patients aged >18 years. For each code stroke, initial neuroimaging modality (non-contrast head CT [CTH], CT angiography [CTA] of the head and neck, and non-contrast MRI of the brain) and subsequent treatment with IVT and/or EVT were recorded.

The primary outcome measured was the total annual imaging cost, calculated using the historic average New Jersey Medicare reimbursement for each imaging modality in a given year. Given the observed trend of increasing image utilization, a secondary outcome of interest was the cumulative radiation exposure per year. This was calculated as the product of the dose-length product (DLP) and number of CT examinations performed for each modality (CTH, CTA), using institutional average observed DLP values in line with published benchmarks.4-5

Analysis focused on identifying trends in total imaging cost, number of code stroke activations per year, and the average imaging cost per "positive" code stroke, defined as a case resulting in IVT or EVT treatment.

Results

From 2020 to 2025, annual code stroke activations increased from 120 to over 300, with imaging costs rising from $90,000 to $266,000. From 2021 to 2024, annual imaging costs nearly tripled, most notably due to an exponential increase in CTA head and neck utilization. In 2020, CT angiography contributed approximately $20,000 to total cost share and increased nearly seven-fold to $140,000 in 2025. In comparison, CTH and MRI brain costs showed more modest growth from $25,000-30,000 to $45,000-$60,000. Analysis of cumulative radiation dose exposure demonstrated a similar upward trend, with total annual DLP increasing from 140,000 mGy-cm in 2020 to over 500,000 mGy-cm in 2025.

Despite the increasing number of code stroke activations, the number of patients receiving IVT or EVT remained stable (between 10-20 treatments per year). Consequently, the proportion of positive code strokes resulting in definite therapy decreased over time, with the average cost per treated patient increasing nearly 3-fold ($6,000 to $17,000) from 2020 to 2024-25.

Conclusion

Our findings demonstrate a disproportionate rise in imaging utilization, consequent radiation exposure, and cost relative to the number of treatment rates. In contrast to our initial hypothesis, increasing costs of neuroimaging at our institution had no significant correlation with rates of EVT or IVT. This further emphasizes the growing economic burden of code stroke activations among a greater number of patients who are ultimately ineligible for definitive stroke therapy and suggests that code stroke imaging pathways can be further optimized.

Images/Tables

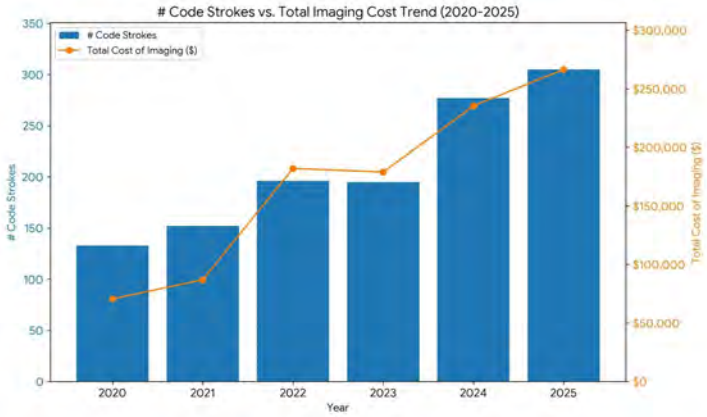

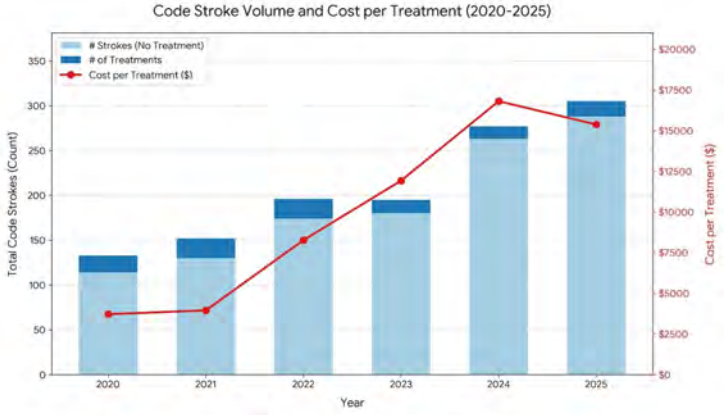

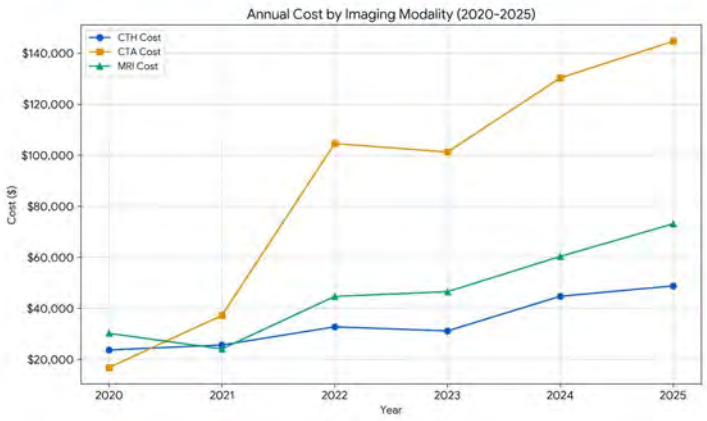

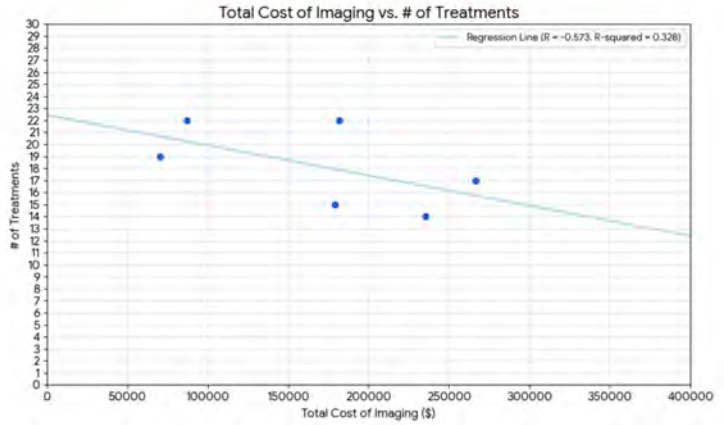

---

418 Longitudinal Neuroimaging and Machine Learning Approaches for Distinguishing Stages of Cognitive Decline

Marufjon Salokhiddinov PhD[1], Dharmesh Singh PhD[2], Dileep Kumar PhD[2]

[1]Kimyo International University, Tashkent, Tashkent, Uzbekistan. [2]Global Research and Collaboration Institute, Shanghai, Shanghai, China

Purpose

The aim of the study is to improve the accuracy of differentiation between stages of cognitive decline—normal cognitive status (NC), mild cognitive impairment (MCI), and Alzheimer's disease (AD)—based on longitudinal neuroimaging biomarkers and machine learning methods. Early patient stratification is key for predicting progression and optimizing therapy, but traditional cross-sectional studies are limited in assessing single-stage changes.

Materials & Methods

The study included 75 subjects (NC n=25, MCI n=25, AD n=25). Brain region volumes were calculated using a cascaded weakly supervised CINet (Confidence Integration Network), which ensures highly accurate segmentation. Linear mixed models (Volume ~ Diagnosis × Time + (1|Subject)) were used to assess the influence of diagnosis, time, and their interaction. Correction for multiple comparisons was performed using the Benjamini–Hochberg method. An ensemble ANOVA-ranking + L1-regularized logistic regression was used to select significant features. The resulting features were used to train two classifiers, XGBoost and SVM, evaluated using stratified cross-validation.

Results

The analysis revealed an annual decline in gray matter volume: NC ~0.5–1%, MCI ~2–3%, AD ~4–5%. The most significant predictors were the basal volume and rate of decline of the hippocampus, as well as the volume of the entorhinal cortex for the early distinction between NC and MCI. The parahippocampal gyrus and amygdala distinguished MCI from AD, while features from the posterior cingulate cortex and precuneus strengthened the distinction between NC and cognitively impaired groups. The XGBoost classifier showed the best results (accuracy ~78%, AUC = 0.82), outperforming SVM (accuracy ~75%), especially in differentiating MCI from AD.

Conclusion

Longitudinal analysis of volumetric biomarkers combined with machine learning algorithms provides high diagnostic efficiency in the early staging of cognitive impairment. The XGBoost model demonstrated the highest accuracy and robustness to longitudinal variations, highlighting the potential of integrating dynamic neuroimaging features into clinical diagnosis and prediction of Alzheimer's disease progression.

---

421 Deep Learning-Based Volumetry for Early Detection of Prodromal Parkinson's Disease

Marufjon Salokhiddinov PhD[1], Dharmesh Singh PhD[2], Dileep Kumar PhD[2]

[1]Kimyo International University, Tashkent, Tashkent, Uzbekistan. [2]Global Research and Collaboration Institute, Shanghai, Shanghai, China

Purpose

Early detection of neuroanatomical changes in the prodromal stage of Parkinson's disease (PD) is crucial for timely diagnosis and intervention. Traditional volumetric analysis methods are often limited in sensitivity and reproducibility, hindering the detection of subtle preclinical structural changes. The aim of this study was to apply volumetric analysis based on deep learning methods to identify small-scale regional brain changes and evaluate its effectiveness in differentiating prodromal PD patients from healthy controls.

Materials & Methods

The study included brain MRI scans of 25 patients with prodromal Parkinson's disease and 25 age-matched healthy controls. Brain region volumes were calculated using a weakly supervised Confidence-Integrated Deep Learning Network (CIDN) and normalized by intracranial volume. Comparisons between groups were performed across 109 cortical and subcortical regions using Welch's t-test and Benjamini-Hochberg multiple comparison correction (FDR). Principal component analysis (PCA) was used to reduce data dimensionality, and random forest and L1-regularized logistic regression (L1-LR) algorithms were used for classification. Model performance was assessed using five-fold stratified cross-validation, ensuring the stability and reproducibility of the results.

Results

Significant volumetric differences were found in the choroid plexus, nucleus accumbens, subnuclear structures of the amygdala, temporal pole, and third ventricle ($q < 0.05$). PCA showed that the first ten principal components explained approximately 75% of the total variance, reflecting characteristic patterns of atrophy in prodromal patients. The Random Forest classifier achieved 85% accuracy (AUC = 0.90), and the L1-regularized logistic model achieved 90% accuracy (AUC = 0.92), demonstrating high discrimination between groups. Feature significance analysis revealed that the most informative regions were the choroid plexus, nucleus accumbens, paracentral lobule, thalamic pulvinar, and optic chiasm, reflecting early patterns of degeneration.

Conclusion

A volumetric analysis based on deep learning and supplemented by machine classification enables reliable early detection of the prodromal stage of Parkinson's disease using structural MRI data. The method identifies specific patterns of atrophy that precede the onset of motor symptoms, particularly in limbic, subcortical, and ventricular structures. This approach has the potential to become a quantitative neuroimaging biomarker for risk assessment and progression monitoring, as well as the basis for precision strategies for the prevention of neurodegenerative diseases.

---

431 Defining Normal Optic Nerve Sheath Enhancement on MRI

Ashraf Abdulhalim M.D., Emma Bentley D.O., Benjamin Ludwig M.D., Amit Desai M.D., Alok Bhatt M.D.
Mayo Clinic, Jacksonville, Fl, USA

Purpose

The optic nerve sheath is a continuation of the meninges surrounding the optic nerve. The central retinal artery runs within the dural sheath inferior to the optic nerve, providing small branches to the optic nerve and pia mater. Therefore, we hypothesize optic nerve sheath enhancement is a normal finding on post-contrast, fat-saturated T1-weighted images on both 1.5T and 3T scanners.

Materials & Methods

Fifty patients without clinical symptoms localizing to the optic nerve undergoing MRI by using the orbit protocol were identified at our institution, 25 cases on a 1.5T scanner and 25 cases on a 3T scanner; a total of 100 optic nerve sheaths. Presence or absence of enhancement of the optic nerve sheath on post-contrast, fat-saturated T1-weighted images were independently evaluated by 2 neuroradiologists.

Results

On 1.5T, of 50 optic nerve sheaths evaluated, 92% of sheaths enhanced. On 3T, of 50 optic nerve sheaths, 100% of sheaths enhanced. Out of all enhancing sheaths, 100% had left-right symmetry. There was a statistically significant difference in enhancement between 1.5 and 3T scanners ($p = 0.041$). All cases had a nodular enhancement pattern on coronal images.

Conclusion

Enhancement of the optic nerve sheath is a normal finding on post-contrast, fat-saturated T1-weighted images on both 1.5T and 3T scanners. Careful attention to clinical history, asymmetry, and presence of adjacent fat stranding should be considered before calling abnormality of the optic nerve sheath.

Images/Tables

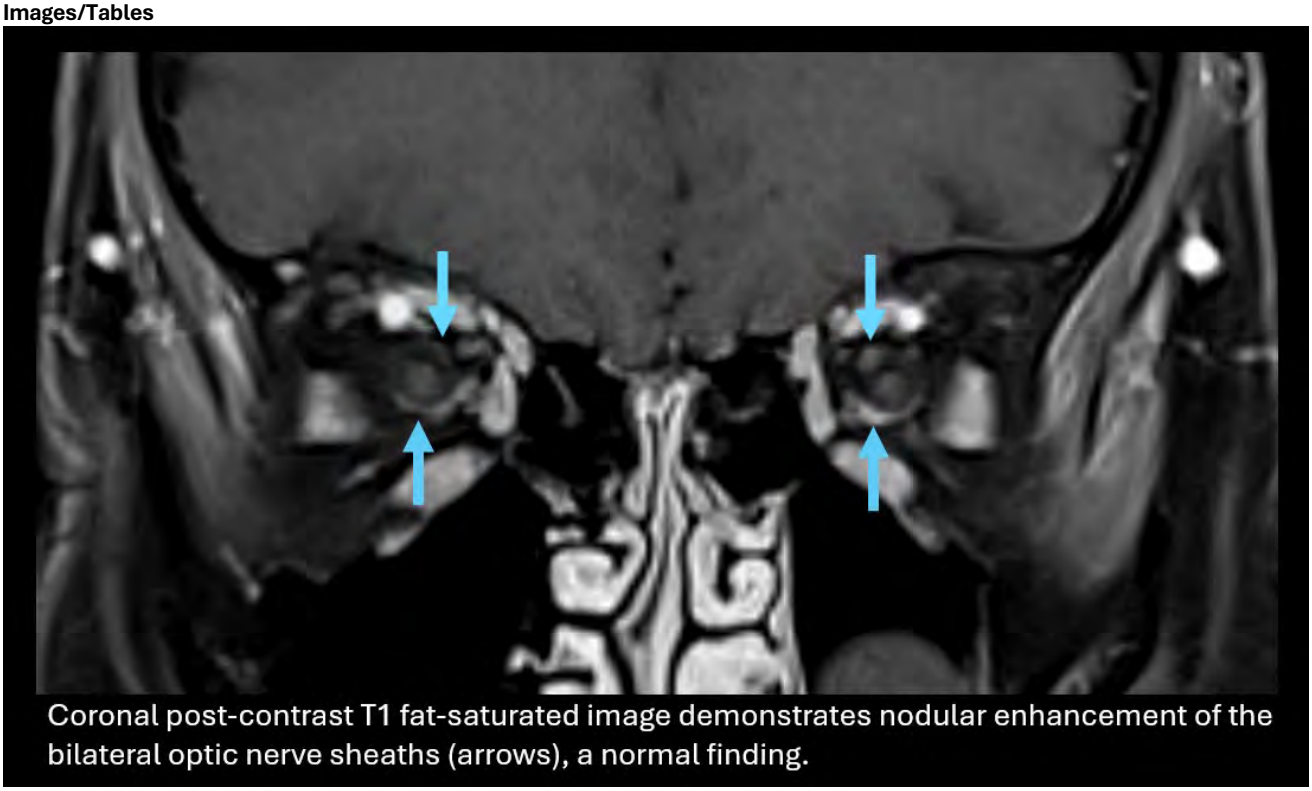

Coronal post-contrast T1 fat-saturated image demonstrates nodular enhancement of the bilateral optic nerve sheaths (arrows), a normal finding.

461 Preliminary Meta-Analysis of Cerebral Venous Sinus Thrombosis in Traumatic Brain Injury: Associations with Mortality and Recanalization

Samir Shinnawi MD, Goni Merhav MD, Anat Yahav-Dovrat MD
Rambam Health Care Campus, Haifa, Northern District, Israel

Purpose

To provide preliminary pooled estimates and explore effect modifiers of cerebral venous sinus thrombosis (CVST) in traumatic brain injury (TBI), assessing associations with (1) mortality and (2) venous recanalization rates under anticoagulation therapy.

Materials & Methods

CVST is an underrecognized complication of TBI with skull fractures. Its impact on mortality, long-term outcomes, and the role of anticoagulation remain incompletely understood.

We conducted a systematic search of PubMed, Embase, and the Cochrane Library for studies reporting patients with post-traumatic CVST. We pooled prevalences for mortality and recanalization in a random-effects model. The arcsine transformation was applied to account for extreme values. Meta-regressions were conducted as an exploratory analysis to examine the influence of age, sex, follow-up duration, and treatment strategy. A test for subgroup difference was performed. Statistical analyses were performed in R (v4.4.1).

Results

Twenty-two studies (n = 1267 patients) met the inclusion criteria.

The pooled recanalization rate was 75.94% (95% CI 58.24 to 87.72), and the pooled mortality rate was 11.41% (95% CI 5.43 to 22.44). For both outcomes, respectively, no significant difference was found between follow-ups of less than 60 days and those of more than 60 days (p = 0.55; p=0.97). For the recanalization rate, no difference was found between adults and children (p =0.79). Meta-regressions did not show significant iteration for anticoagulation (p = 0.74), conservative management (p = 0.64), antiplatelet therapy (p = 0.31), age (p = 0.35), follow-up time (p = 0.29), and male gender (p = 0.79) in patients with traumatic CVST.

Conclusion

Preliminary evidence suggests that effect modifiers, such as anticoagulation and conservative management, may not independently predict recanalization in post-traumatic CVST. Larger, prospective studies are needed to clarify treatment-related effects and optimize management pathways.

Images/Tables

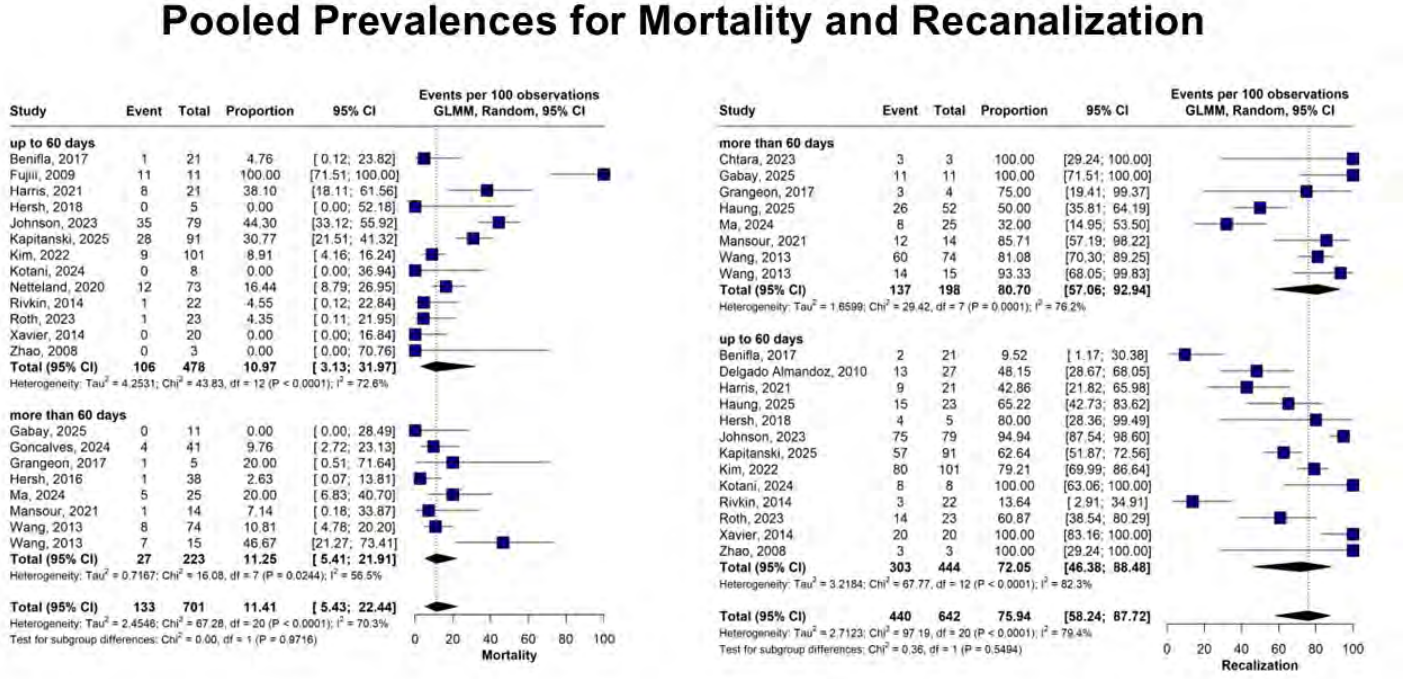

490 Feasibility of Shortened [68Ga] DOTATATE PET/MRI Acquisition for Meningioma: Comparison of 50-Minute and 20-Minute Uptake Intervals.

Alex Valenzuela MD, Arman Sharbatdaran MD, Nelson Duran, Bernard Ho, Sadek Nehmeh PhD, Andrew Kuhn MD, Jana Ivanidze MD, PhD
New York Presbyterian Weill Cornell Medical Center, New York, New York, USA

Purpose

[68Ga]DOTATATE PET provides valuable molecular information for meningioma detection and characterization. However, long acquisition times in hybrid PET/MRI can limit scanner throughput and patient comfort [1,2]. This study compared maximum absolute standardized uptake values (SUV) derived from the full 50-minute dynamic dataset (SUV_{50}) with those from the final 20 minutes (SUV_{20}) along with SUV ratio referencing the superior sagittal sinus ($SUVRsss_{50}$ and $SUVRsss_{20}$, respectively) in patients with meningioma, to evaluate whether a shortened acquisition yields quantitatively and clinically equivalent results.

Materials & Methods

This ongoing retrospective study included consecutive adult patients who underwent Ga-68 DOTATATE PET/MRI in the past six months for evaluation of path-proven or presumed meningioma. Qualitative visual analysis was performed by a dual-board-certified neuroradiologist and nuclear medicine physician. For each lesion, maximum absolute SUV (SUVmax) and lesion-to-superior-sagittal-sinus relative SUV were extracted from two reconstructions

1. Full 50-minute dataset (SUV_{50})
2. Final 20 minutes of acquisition (SUV_{20})

Respective greement between SUV_{50} and SUV_{20}, and $SUVRsss_{50}$ and $SUVRsss_{20}$, was assessed using Bland–Altman analysis.

Results

A total of 18 consecutive patients (12 women and 6 men; ages 29 – 85 years, 11 WHO Grade 1, 30 WHO Grade 2, 2 WHO Grade 3, 6 presumed based on MRI and PET findings) with 55 MRI- and PET-ascertained meningiomas were analyzed. Visual assessment demonstrated no significant qualitative difference between SUV_{50} and SUV_{20} PET/MRI datasets. SUV_{20} values were consistently higher than SUV_{50} across all lesion grades. Absolute SUV analysis demonstrated a mean bias = 3.44 SUV units; 95 % limits of agreement (−3.73 to 10.61 SUV). SUVRsss analysis demonstrated a mean bias = 3.34 SUV units; 95 % limits of agreement (−4.54 to 11.22 SUV). Bland–Altman plots demonstrated strong agreement at lower SUV, with divergence at higher SUV consistent with mild proportional bias.

Conclusion

Quantitative and qualitative agreement between 20-minute and 50-minute reconstructions supports the feasibility of abbreviated Ga-68 DOTATATE PET/MRI protocols for meningioma evaluation. While SUVs from shortened acquisitions slightly overestimate uptake at higher values, the differences are not clinically significant. Implementing a 20-minute protocol could improve scanner efficiency and patient comfort without compromising diagnostic reliability.

Previous studies from out group demonstrated high diagnostic accuracy using SUV_{50}-based thresholds for differentiating meningioma from post-treatment change. The present work establishes a framework for validating whether similar diagnostic performance can be achieved with SUV_{20}-derived parameters. Future prospective studies will be essential to confirm that the excellent diagnostic accuracy previously reported with SUV_{50} generalizes to shortened acquisitions, and to determine effect of lesion size, WHO grade and molecular profile, ensuring both efficiency and clinical robustness in quantitative meningioma imaging. This study thus provides a critical foundation for continued brain Ga-68 DOTATATE PET/MRI protocol optimization in patients with meningiomas.(3, 4).

Images/Tables

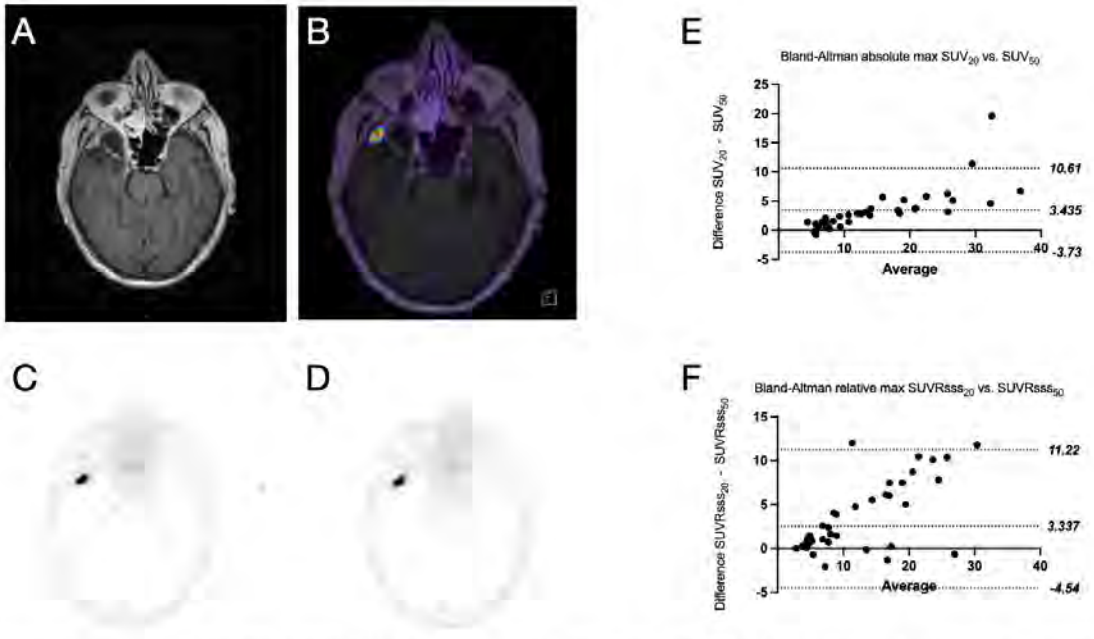

Figure 1: (A) Axial T1 post post-gadolinium enhancement MR image. **B)** Fused PET/MR T1-weighted post–gadolinium enhancement image. **(C,D)** Axial 68Ga-DOTATATE PET images acquired over the entire 50-minute period (C) and over the last 20 minutes of acquisition (D) in a woman with a WHO grade 2 meningioma status post-resection, obtained to evaluate residual somatostatin receptor–positive tumor. Respective Bland–Altman plots comparing absolute and relative SUV_{ax} and SUV_{ax} values **(E,F)**. Relative SUV calculated as SUV/SUVsagital sinus. Most SUV20−SUV50 differences being positive and lying within the plotted 95% CIs. SUV20 = SUV extracted from the last 20 minutes of acquisition, SUV50 =SUV extracted from the entire 50 minutes of acquisition. DOTATATE = tetraazacyclododecane tetraacetic acid octreotate, 68Ga = gallium 68.

---

534 Characterizing Cerebral Venous System Using Advanced Imaging

Niloufar Valizadeh MD, Alborz Feizi MD, Ava Mohseny MD, Shahram Majidi MD
Mount Sinai Hospital, New York, New York, USA

Purpose

Endovascular brain–computer interfaces (BCIs) are emerging as minimally invasive tools for recording and modulating cortical activity. While the superior sagittal sinus (SSS) is currently the primary target for endovascular BCI implantation, extending access to the superficial cortical veins could further enhance motor control and sensory feedback, given their closer proximity to the primary motor cortex and other functionally relevant cortical regions. Therefore, a detailed characterization of the size, configuration, and anatomical relationships of these cortical veins is essential to inform device design, patient selection, and procedural planning.

This study aims to map the anatomy of the cerebral venous system using neuroimaging data. We are characterizing cerebral venous networks in relation to key cortical structures to build a detailed anatomical model that could guide the placement of future BCI and other endovascular devices.

Materials & Methods

A total of 34 brain imaging data collected at the Mount Sinai Health System between January 1, 2024, and January 1, 2025, were retrospectively analyzed. Eligible participants were adults (≥18 years) who underwent high-quality MRI and MRV. Patients with venous thrombosis, abnormal vasculature, or special status were excluded.

Images were retrieved through a PACS query, processed and segmented to reconstruct 3D models of the cerebral venous system and assess its relationship to major brain landmarks.

Primary motor cortex is identified using FreeSurfer opensource segmentation model based on a T1 sequence. Venous segmentations were done using 3Dslicer based on MRV with contrast. Subsequently, the distance between cortical veins above 2mm and precentral cortex was measured using Python.

Results

Our preliminary results show that 100% of the 34 brains analyzed had a vein with ≥ 2mm diameter within a 2 cm radius of the central point of the left or right precentral cortex. Furthermore, 25 brains had a vein of ≥ 2 mm diameter within a 1cm radius of the central point of the left precentral cortex, while 22 brains had at least one vein of similar size within a 1cm radius of the corresponding point in the right hemisphere.

Conclusion

The precentral cortex, which contains the primary motor cortex, controls voluntary movements and coordinates muscle contractions. For this reason, it is a common target for minimally invasive BCIs aimed at assisting individuals with motor impairments. Our study demonstrates that venous structures of the brain can provide access to within 1-3 cm of the precentral cortex, offering promising approach for BCI implantation and suggesting the potential for additional veins in future applications.

Images/Tables

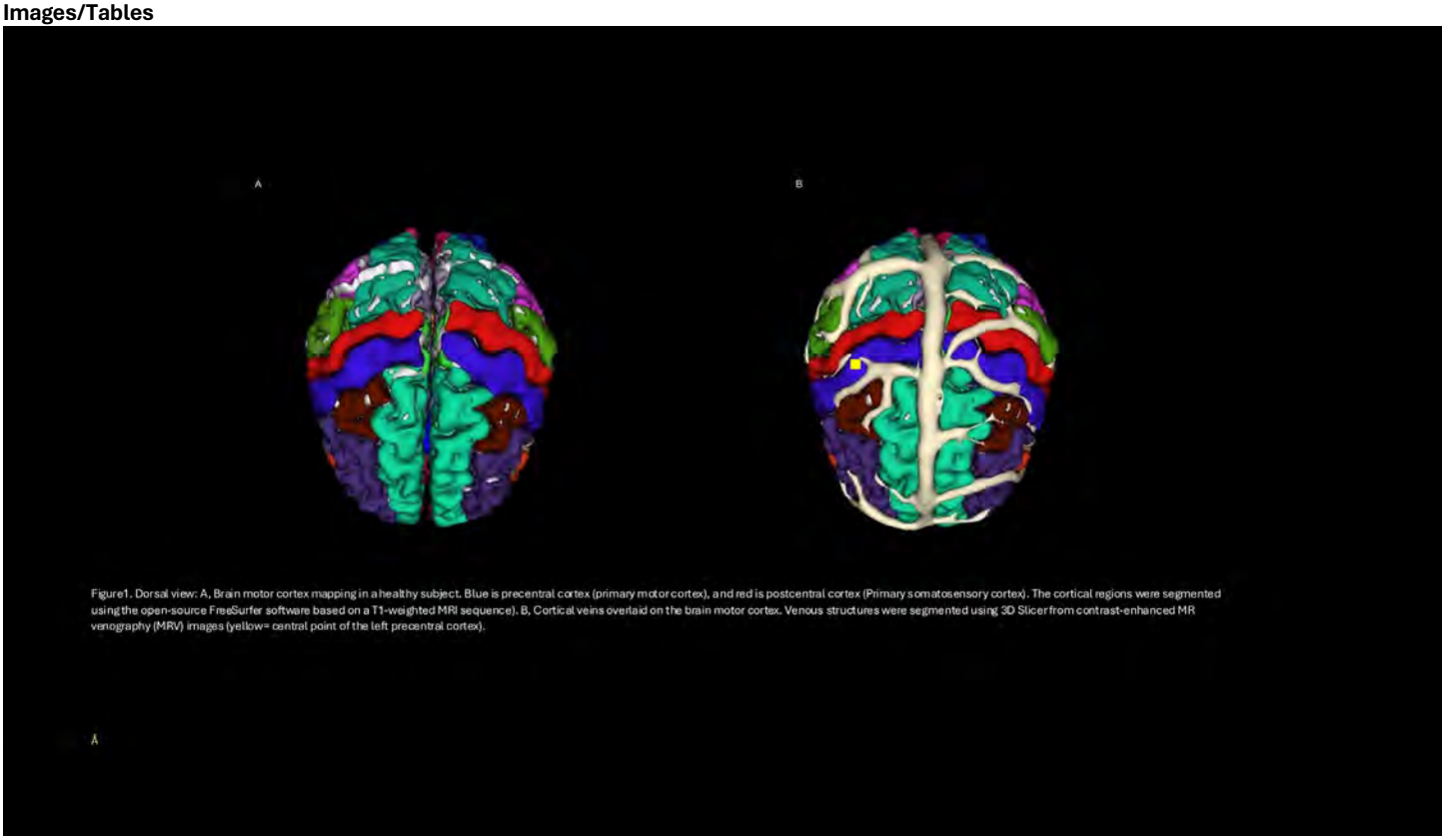

---

545 Dual-Energy CT-Based Thrombus Characterization for Etiology Distinction in Middle Cerebral Artery Acute Ischemic Stroke Undergoing Endovascular Thrombectomy

Shiu-Yuan Huang, Hung-Chieh Chen, Wen-Hsien Chen

Department of Radiology, Taichung Veterans General Hospital, Taichung, Taiwan, Taiwan

Purpose

Endovascular thrombectomy (EVT) is the standard of care for selected patients with large vascular occlusion (LVO) acute ischemic stroke (AIS). Because EVT strategies may differ between intracranial atherosclerotic disease (ICAD)-related and embolic LVO, the objective of our study is to explore whether dual-energy CT (DECT) iodine-map metrics can help differentiate these etiologies.

Materials & Methods

We retrospectively analyzed patients with segment one of middle cerebral artery (M1) LVO AIS who underwent EVT and had DECT both before EVT and within 24 h after EVT. Patients with posterior circulation stroke, concurrent of ICA or ACA stroke were excluded from the study. Etiology (ICAD vs embolic) was adjudicated by intra-procedural digital subtraction angiography. Iodine concentration (mg/mL) was quantified at the pre-EVT thrombus site and the post-EVT residual-thrombus site. Clinical variables included baseline NIHSS, LDL, total cholesterol; imaging/clinical outcomes included 24-h NIHSS improvement, follow-up DECT-ASPECTS, hemorrhagic transformation, and 90-day favorable functional outcome were recorded.

Results
Among the 25 patients, those with ICAD had significantly lower post-EVT residual-site iodine concentration (ICAD vs embolism, 0.2 vs 0.4 mg/ml, p=0.025) and a greater reduction from pre-EVT sites to post-EVT sites (-0.1 vs 0.1 mg/ml, p=0.006) than those with embolic LVO. Clinically, the ICAD group had lower baseline NIHSS (p=0.048), poorer 24-h NIHSS improvement (p=0.023), higher LDL (p=0.005), and total cholesterol (p=0.005). Ninety-day favorable functional outcome, follow-up DECT-ASPECTS, and hemorrhagic transformation did not differ between groups.
Conclusion
In M1 AIS undergoing EVT, DECT iodine-map metrics differentiated ICAD from embolic LVO and may inform etiology-specific EVT strategies. Prospective external validation is warranted.
Images/Tables

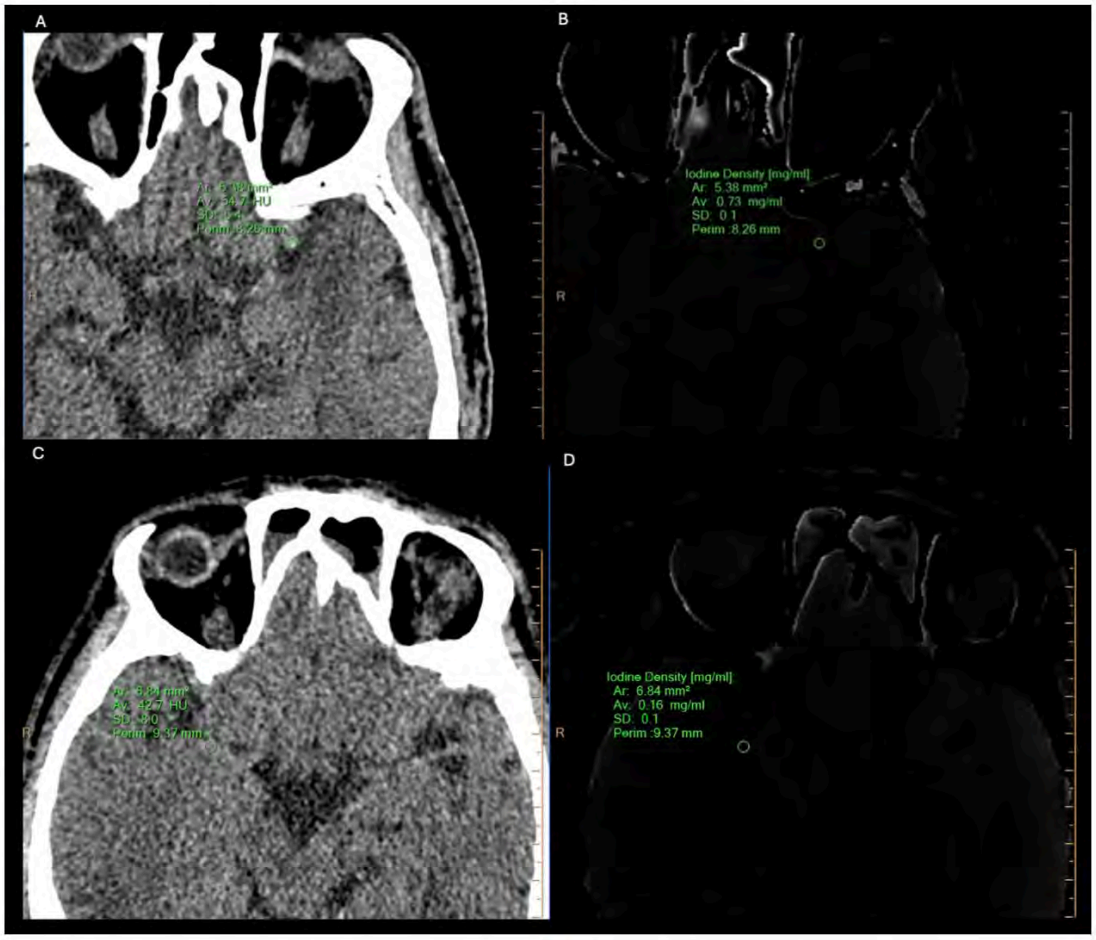

Figure (A,B) Embolic type, post-EVT residual thrombus site attenuation and iodine concentration. A 51 y/o male with left M1 occlusion with successful recanalization (mTICI 3), pre-EVT thrombus iodine concentration was 0.25 mg/ml, and post-EVT thrombus residual site iodine concentration was 0.73 mg/ml, showing 24-h NIHSS improvement from 15 to 7. Figure (C,D) ICAD type, post-EVT residual thrombus site attenuation and iodine concentration. A 69 y/o male with right M1 occlusion with successful recanalization (mTICI 2B), pre-EVT thrombus iodine concentration was 0.3 mg/ml, and post-EVT thrombus residual site iodine concentration was 0.16 mg/ml, showing 24-h NIHSS progression from 12 to 16.

---

556 Dynamic Contrast Enhanced MRI to Evaluate Radiation Treatment Response in Hyper- and Hypo- Vascular Spinal Metastases
Matthew Arthur BA, Kyung Peck PhD, Onur Yildirim MD, Andrei Holodny MD, Atin Saha MD
Memorial Sloan Kettering Cancer Center, New York, New York, USA
Purpose
Dynamic contrast-enhanced MRI (DCE-MRI) is a non-invasive imaging technique which is used to characterize the perfusion of spine metastases using derived values of plasma volume (Vp) and time intensity curves (TICs). Spinal metastases frequently demonstrate a reduction in Vp as well as a shift in the TIC pattern after radiation treatment (RT).
The objective is to use DCE-MRI to investigate whether there is a (1) significant reduction in Vp post-RT within the hyper- and hypo- vascular spinal metastases groups, (2) significant difference in % reduction between the groups post-RT, and (3) difference in TIC curve post-RT.
Materials & Methods
Retrospective study of 60 lesions in 42 patients that underwent DCE-MRI before and after RT to a treatment-naïve spinal metastasis. Spinal lesions were categorized based on pathology as hypervascular (renal, thyroid) or hypovascular (colorectal, prostate).

NordicICE was used to determine the fractional plasma volume (Vp); and mean and maximum Vp for each lesion.
Mann Whitney U tests were conducted at a significance level of P < 0.05 to assess the difference in the % change in Vp between the groups post-RT.
Wilcoxon signed-rank tests were conducted at a significance level of P < 0.05 to assess post-RT changes in Vp within the groups.

Results

There was a significant reduction in mean and maximum Vp within the hyper- and hypo- vascular groups post-RT, but no significant difference in % reduction.
In the hypervascular group, the averaged mean Vp before RT was 3.901 and 1.676 after RT (P=3.15*10^-7). The averaged max Vp before RT was 8.04 and 5.5 after RT (P=2.56*10^-4). The average TIC curve resembled a type D pattern pre-RT and type C pattern post-RT.
In the hypovascular group, the averaged mean Vp was 2.206 prior to RT, and 1.023 after RT (P=2.79*10^-7). The averaged max Vp prior to RT was 3.93 and 2.51 after RT (P=0.00134). The average TIC curve resembled a type D pattern pre-RT and type E pattern post-RT.
The averaged % reduction in mean Vp in the hypervascular group was -53.85% and -55.99% in the hypovascular group (p=0.657); the averaged % reduction in max Vp in the hypervascular group was -45.44% and -35.49% in the hypovascular group (p=0.409).

Conclusion

DCE-MRI reveals significant reductions in Vp (mean, maximum) for both hyper- and hypo- vascular spinal metastases post-RT. Morphological changes in the averaged TIC curve were observed in each group post-RT. Both groups had type D patterns prior to RT, which is associated with a high positive predictive value for spinal metastases; the hypervascular group shifted to a type C pattern, and the hypovascular group exhibited a shift to a type E pattern. The type C pattern is non-specific and seen in both malignancy and healthy tissue, while the type E pattern is consistent with post-inflammatory changes and is not common in active malignancy. The slower rising slope observed in the hypovascular group post-RT (type E), which represents a slower wash-in of contrast, suggests that the radiation-induced alterations to the tumor microvasculature may be more prominent in this group compared to in the hypervascular group.

Images/Tables

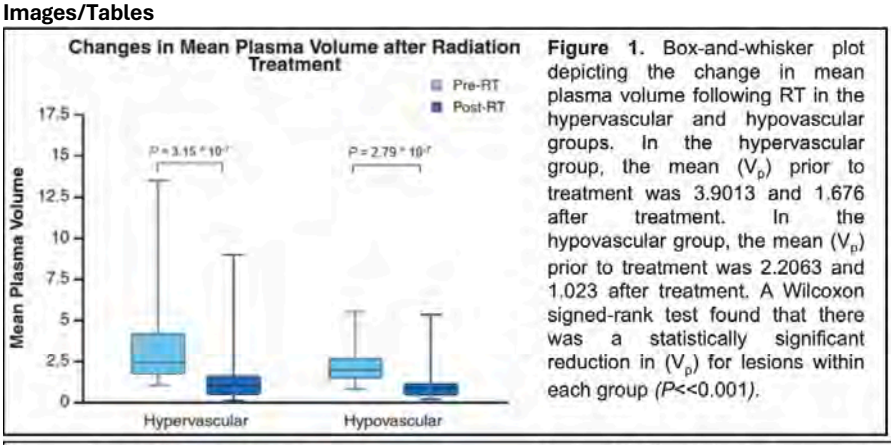

Figure 1. Box-and-whisker plot depicting the change in mean plasma volume following RT in the hypervascular and hypovascular groups. In the hypervascular group, the mean (V_p) prior to treatment was 3.9013 and 1.676 after treatment. In the hypovascular group, the mean (V_p) prior to treatment was 2.2063 and 1.023 after treatment. A Wilcoxon signed-rank test found that there was a statistically significant reduction in (V_p) for lesions within each group (*P*<<0.001).

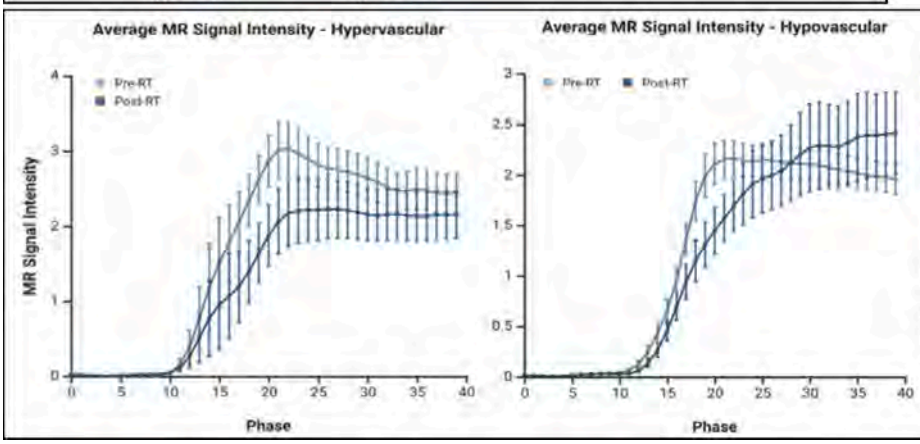

Figure 2. Graph depicting the averaged MR time intensity curve (TIC) and standard error for lesions within the hypervascular and hypovascular spinal metastases groups. In both groups, the pre-RT curves resemble a type D SI curve, which is highly predictive of malignant vertebral lesions. After RT, there is a morphological shift in both SI curves, noting a shift to Type C for hypervascular and Type E for hypovascular. Type C curves are non-specific and are seen in both healthy and malignant vertebral tissue. Type E curves are associated with an inflammatory response. This shift is likely associated with radiation-induced changes to the tumor microvasculature. In both groups post-RT, there is also a slower wash-in of contrast, suggesting poor blood flow into the lesion, potentially due to poor integrity of the microvasculature.

609 A Two-stage Deep Learning Pipeline for Intracranial Aneurysm Screening with Segmentation and Lesion Localization

Lindsey Katelyn Greenlund MD, James Clark MD, Tej Mehta MD
Johns Hopkins, Baltimore, MD, USA

Purpose

Intracranial aneurysms affect 3-5% of the population and artificial intelligence algorithms have shown promise in aiding radiologists in aneurysm detection[1,2]. The purpose of our project was to develop and evaluate a two-stage pipeline for intracranial aneurysm screening on CTA/MRA that first performs whole-brain cerebrovascular segmentation and then detects/localizes aneurysms. The system builds on a modified nnU-Net and uses the RSNA 2025 AI Challenge composite endpoint—the mean of case-level presence AUC and macro location AUC—as the primary metric.

Materials & Methods

We used the RSNA 2025 AI Challenge dataset of 4,348 unique instances, split 70/15/15 into train/validation/test at the patient level.
Stage 1 (vessel segmentation): A nnU-Net–style 3D U-Net was trained on RSNA provided vessel masks and then used to generate pseudo-labels for remaining studies, yielding full vascular masks across the training set.
Stage 2 (aneurysm detection/localization): Volumes were masked by Stage 1 vessels. Candidate patches were sampled along vessel centerlines; labels captured aneurysm presence and anatomical territory. The detector used AdamW with cosine decay/warmup, mixed precision, 3D spatial and

intensity augmentations, and patient-wise 5-fold cross-validation on the training split. Inference used sliding-window tiling with test-time augmentation. Post-processing applied connected-component clustering within the vessel mask to consolidate voxel-level probabilities into lesion candidates and to assign territories. Implementation was optimized for dual high-end GPUs via gradient checkpointing, cached preprocessing, and early stopping.

Results

On the held-out 15% test set, the two-stage model achieved a combined AUC-ROC of 0.81 for the joint task of presence and localization. Constraining detection to vessel masks reduced false positives from bone and parenchyma and improved territorial stability across anterior and posterior circulations. Post-processing further decreased spurious detections and improved exam-level consistency.

Conclusion

A modified nnU-Net configured as a two-stage pipeline with global vessel segmentation followed by vessel-constrained aneurysm detection/localization achieved a combined AUC-ROC of 0.81 on the RSNA 2025 AI Challenge. Vessel-mask constraints materially improve specificity and territorial assignment while maintaining practical inference speed. Future work could evaluate centerline-aware proposal generation, uncertainty-weighted fold ensembling, and domain-robust normalization.

Images/Tables

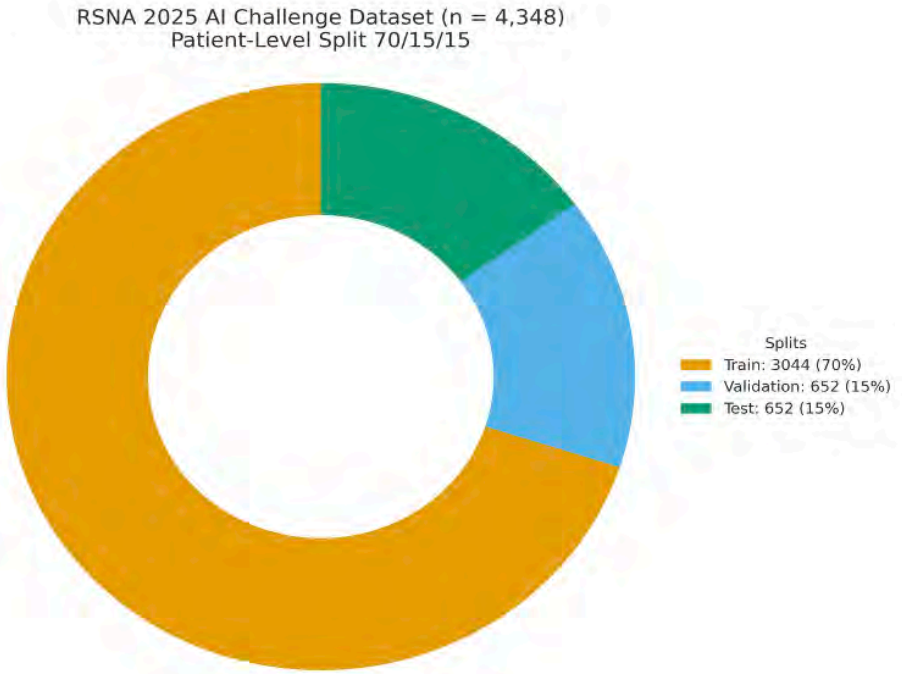

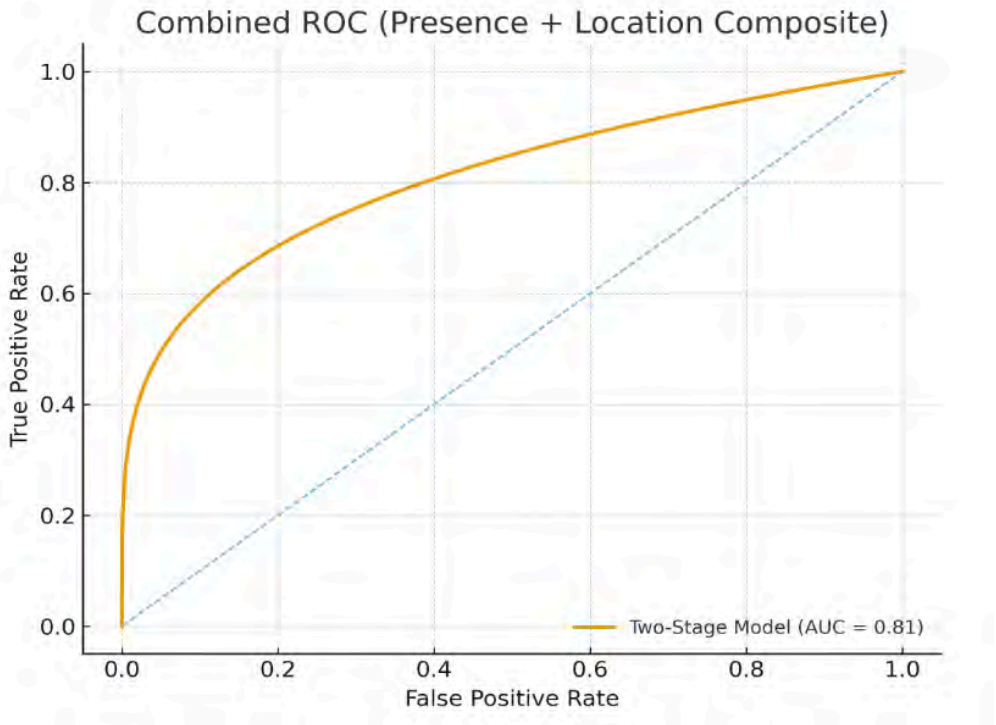

626 3D EPI versus 3D SWAN: A Preliminary Comparison of Susceptibility Imaging at 1.5T

Ian Langenfeld[1], Dan Rettmann[1], Brice Fernandez[2], Suchandrima Banerjee[3], Tim Sprenger[4], Steven Messina[5], Yunhong Shu[5], Petrice Cogswell[5]
[1]GE Healthcare, Rochester, MN, USA. [2]GE Healthcare, Buc, Yvelines, France. [3]GE Healthcare, Berkeley, CA, USA. [4]GE Healthcare, Munich, Bavaria, Germany. [5]Mayo Clinic, Rochester, MN, USA

Purpose

Susceptibility-weighted MR imaging is essential for detecting blood products and mineralization associated with a range of neurologic pathologies, including microhemorrhage and hemosiderin deposition.(1–3) SWAN (T2*-weighted angiography) is a widely used 3D multi-echo gradient-echo sequence developed by GE HealthCare to enhance lesion conspicuity.(4) A recently developed, investigational 3D Echo Planar Imaging (EPI) sequence has been optimized to provide similar susceptibility contrast with shorter acquisition time. This study aimed to compare 3D EPI and 3D SWAN at 1.5T in terms of lesion visualization, spatial resolution, and scan efficiency relevant to routine clinical neuroimaging

Materials & Methods

Participants: This study included 13 patients scanned over one week at Mayo Clinic for a variety of clinical indications.

Imaging: Patients were scanned using a 19-channel head coil on Optima MR450Ws and Signa Artist, GE HealthCare 1.5T MRI systems. Both 3D EPI and 3D SWAN sequences were acquired in the axial plane as part of the same clinical brain MRI exam. The scan time for 3D EPI was approximately 2 minutes and 31 seconds, and 4 minutes and 39 seconds for 3D SWAN. The voxel size for 3D EPI was 0.7 × 0.7 × 1.5 mm and for SWAN was 0.9 × 1.1 × 3.0 mm. (Figure 1)

Analysis: A board-certified neuroradiologist independently reviewed both sequences for the presence of susceptibility findings, including microhemorrhage, superficial siderosis, hemosiderin deposition.

Results

Of the 13 patients included, 7 demonstrated microhemorrhages and 3 demonstrated hemosiderin deposits, with 2 of those associated with infarction. The remaining 3 patients showed no susceptibility abnormalities. The microhemorrhages and hemosiderin deposition were similarly well visualized on both 3D EPI and 3D SWAN sequences. The SWAN sequence demonstrated greater susceptibility effects of microhemorrhages relative to vessels, improving conspicuity of the microhemorrhages. An advantage of the 3D EPI sequence is the higher spatial resolution and thinner slices, which provided better distinction of microhemorrhages from closely adjacent vessels. Representative examples are shown in Figures 2–5.

Conclusion

3D EPI demonstrated feasibility for clinical susceptibility imaging at 1.5T, providing lesion conspicuity comparable to 3D SWAN in less than half the acquisition time. These results suggest that 3D EPI may serve as a time-efficient alternative or complement to SWAN for evaluating blood products and hemosiderin deposition. Further studies with larger cohorts and quantitative analysis are warranted to confirm diagnostic equivalence.

Images/Tables

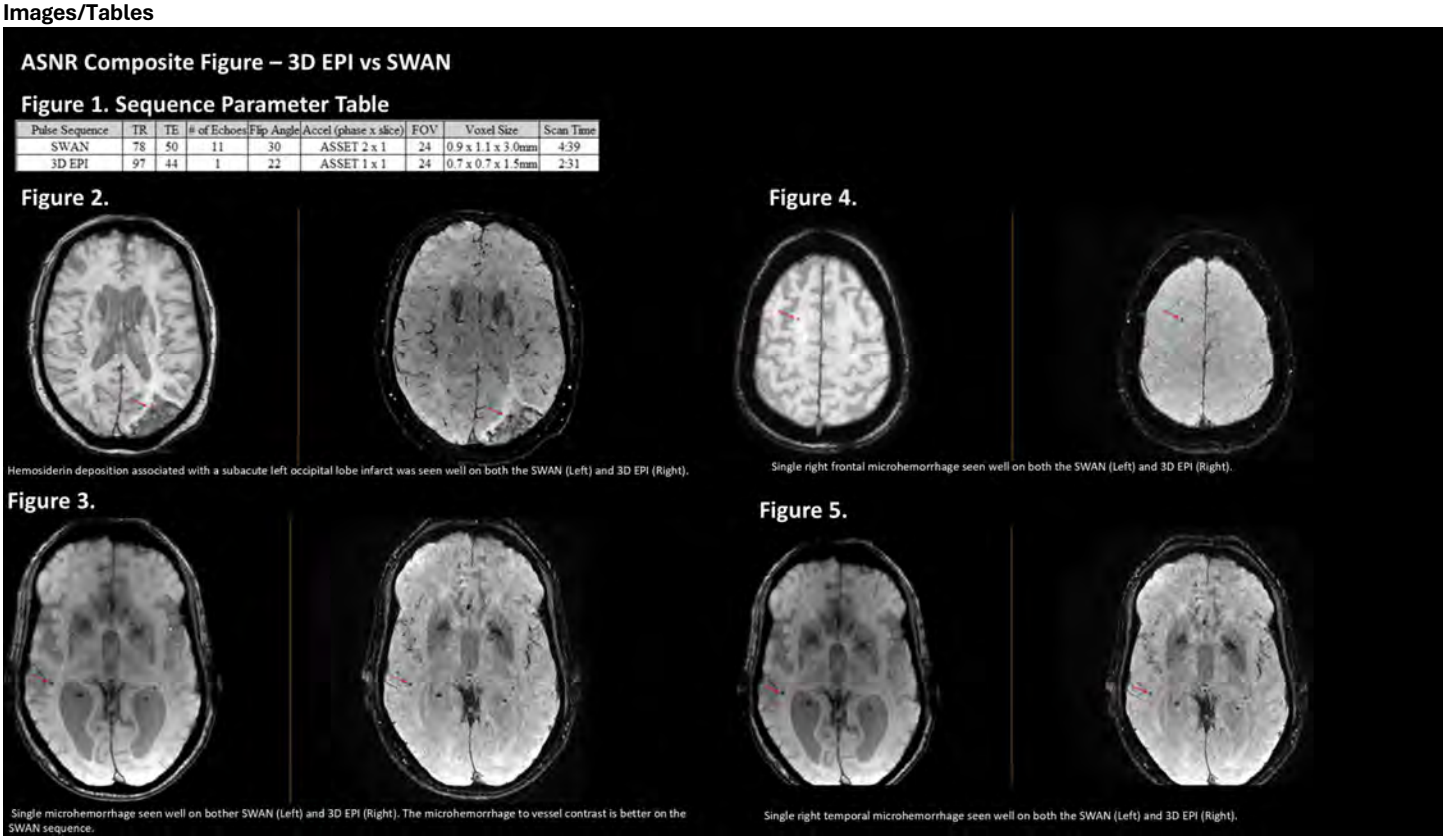

Pulse Sequence	TR	TE	# of Echoes	Flip Angle	Accel (phase x slice)	FOV	Voxel Size	Scan Time
SWAN	78	50	11	30	ASSET 2 x 1	24	0.9 x 1.1 x 3.0mm	4:39
3D EPI	97	44	1	22	ASSET 1 x 1	24	0.7 x 0.7 x 1.5mm	2:31

634 Multimodal Pretreatment Radiomics and Genomics Predict Early Survival in Glioblastoma Patients Initiating Anti-PD-1 Therapy: A Pilot Study

Kevin Pierre MD[1], Kyle McGrath MD[2], Kyle See PhD[1], Md Mahfuz Al Hasan PhD[1], Grace Hey BS[1], Chloe DeYoung BS[1], Vincent Archibald MD[3], Megan Still MD[1], Rachel Moor MD[1], Maryam Rahman MD[1], Ashley Ghiaseddin MD[1]
[1]University of Florida, Gainesville, FL, USA. [2]Washington University in St. Louis, St. Louis, Missouri, USA. [3]Duke University, Durham, North Carolina, USA

Purpose
Immune checkpoint inhibitors (ICIs) such as anti–PD-1 therapy have shown limited but heterogeneous efficacy in recurrent glioblastoma (GBM). Identifying patients most likely to benefit remains a major challenge. Radiomics and artificial intelligence (AI) can extract imaging biomarkers that may non-invasively reflect tumor biology. We aimed to evaluate whether pre-anti-PD-1 MRI radiomics, alone and in combination with genomic data, predict survival outcomes in recurrent GBM.
Materials & Methods
We retrospectively identified 26 patients with recurrent GBM from our prospectively maintained database who underwent surgical resection, received standard chemoradiation, and subsequently initiated anti-PD-1 therapy. Exclusion criteria were prior immunotherapy, prior multiple recurrences, laser interstitial thermal therapy, bevacizumab treatment, or repeat resection during immunotherapy. Pre-immunotherapy T1 post-contrast and post-contrast T2-FLAIR images were manually segmented (ITK-SNAP) to delineate enhancing tumor, central necrosis, and peritumoral abnormality. PyRadiomics extracted 107 features across seven categories (shape, first-order, GLCM, GLDM, GLRLM, GLSZM, NGTDM) from each region of interest. Genetic markers included MGMT methylation and ATRX mutation status. Feature selection (t-test, recursive feature elimination [RFE], principal component analysis [PCA]) limited final models to 2–3 features to avoid overfitting. Analysis included Cox proportional hazards modeling for overall survival (OS) from PD-1 initiation and binary classification (survival <1 year vs ≥1 year) using logistic regression, random forest, and k-nearest neighbors with leave-one-out and 5-fold cross-validation.
Results
Mean overall survival (OS) was 891 days (range, 198–2382; SD, 559). In Cox analysis using radiomics alone, enhancing-region shape flatness independently predicted longer OS (HR 0.43, $p<0.005$, concordance = 0.71). When combining radiomics with genetics, necrosis surface-to-volume ratio predicted poorer survival (HR 13.07, $p=0.04$, concordance = 0.90). Regression models achieved cross-validated RMSE ≈ 250–350 days. For binary classification, multimodal (radiomics + genomics) models outperformed radiomics alone; accuracy improved from 0.718 → 0.808 for the enhancing mask (t-test features, no outliers) and 0.744 → 0.782 for the FLAIR mask (RFE).
Conclusion
Pretreatment MRI radiomics combined with tumor genetics demonstrated encouraging predictive performance for survival in patients with recurrent GBM initiating anti–PD-1 therapy, particularly for classification of early versus late survival. The variability in prediction accuracy is consistent with the known heterogeneity of GBM outcomes and the limited sample size of this pilot cohort. These preliminary findings may serve as a foundation for developing integrated imaging–genomic biomarkers to guide patient stratification and for future multi-institutional validation to establish clinical utility and generalizability.

---

642 **A Hybrid Deep Learning Framework for Assessing Intracranial Aneurysm Rupture Risk Using High-Dimensional Morphological Features**
Amirhossein Zare MD[1], Ibrahim Mohammadzadeh MD[2], Saeed Mohammadzadeh MD[1], Alireza Soltani Khaboushan MD[1], Ali Mortezaei MD[3], SeyedAbolfazl Rahimi PhD[4], Parya Valizadeh MD[1], Amirhessam Zare MD[1], Lawrence Tatiqaj MD[5], Adam Andrew Dmytriw MD, MPH, MSc[6], Leo Anthony Celi MD, MPH, MSc[7]
[1]Tehran University of Medical Sciences, Tehran, Tehran, Iran, Islamic Republic of. [2]Shahid Beheshti University of Medical Sciences, Tehran, Tehran, Iran, Islamic Republic of. [3]Gonabad University of Medical Sciences, Gonabad, East Khorasan, Iran, Islamic Republic of. [4]Yale University, New Haven, Connecticut, USA. [5]Medical Sciences Division, University of Oxford, Oxford, United Kingdom, United Kingdom. [6]Harvard Medical School, Boston, Massachusetts, USA. [7]Massachusetts Institute of Technology, Cambridge, Massachusetts, USA
Purpose
The prediction of intracranial aneurysm rupture risk is a critical clinical challenge. Traditional risk stratification tools have limitations, leading to a need for more comprehensive, data-driven assessments. This study aimed to develop and validate a novel hybrid deep learning model, the Wide & Deep Neural Network (WDNN), for classifying aneurysm rupture status using a comprehensive set of morphological features.
Materials & Methods
We utilized a multicenter dataset of 735 intracranial aneurysms (261 ruptured, 474 unruptured). Features included demographic data, geometric indices, and high-dimensional Zernike Moment Invariants (ZMIs). A key methodological contribution was the use of a Variational Autoencoder (VAE) to distill the 141 high-dimensional ZMI features into a meaningful 40-dimensional latent representation. We developed a hybrid Wide & Deep Neural Network (WDNN) model, integrating a "wide" linear path for feature memorization and a "deep" neural path for pattern generalization. The model's performance was rigorously assessed using a 20-repeated 5-fold cross-validation protocol and benchmarked against six traditional machine learning models (MLP, SVM, LR, k-NN, RF, XGBoost).
Results
The proposed WDNN model demonstrated strong and robust performance, achieving a mean Area Under the Receiver Operating Characteristic Curve (ROC AUC) of 0.810 (95% CI: 0.804–0.818), an accuracy of 0.752 (95% CI: 0.746–0.759), a precision of 0.678 (95% CI: 0.667–0.689), and a recall of 0.583 (95% CI: 0.564–0.601). The WDNN outperformed all six baseline models across key metrics, including ROC AUC and Brier score. Permutation feature importance analysis revealed that the VAE-derived ZMI features were highly predictive, contributing more to the model's performance than traditional risk factors, including aneurysm size.
Conclusion
The hybrid WDNN architecture provides an effective and robust framework for classifying intracranial aneurysm rupture status. Our findings underscore the significant predictive power of advanced morphological descriptors, demonstrating that high-dimensional Zernike Moment Invariants (ZMIs), when harnessed via a Variational Autoencoder (VAE), are more discriminative than traditional risk factors like aneurysm size. This framework provides a promising, data-driven tool to help inform more precise and individualized treatment decisions.

Images/Tables

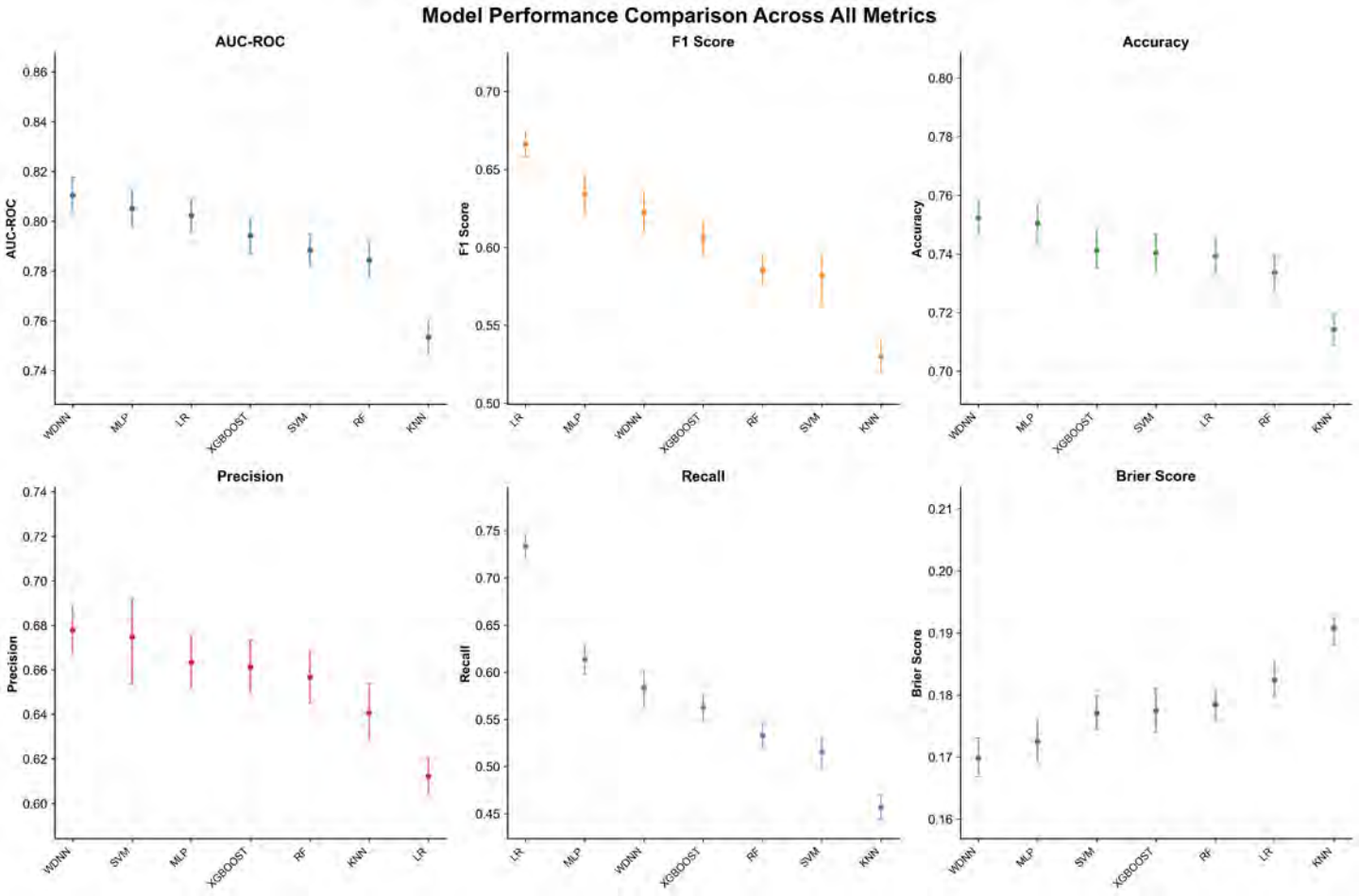

655 Respiration-Associated Characteristics Within Gray Matter and Foramen Magnum in Functional MRI BOLD Signal

Daniel C Kim, David N Jacobson, Marin E Nycklemoe, Daehun Kang PhD, Seokbeen Lim PhD, Paul H Min PhD
Mayo Clinic, Rochester, MN, USA

Purpose

The cerebrospinal fluid (CSF) and glymphatic system together form the waste clearance pathway of the central nervous system[1]. Dysfunction in these systems has been associated with neurodegenerative conditions, including Alzheimer's disease (AD)[2]. One suggested marker of glymphatic function in vivo involves measuring the coupling between CSF signals near the foramen magnum (FM) and cortical gray matter (GM) BOLD fluctuations in resting-state fMRI, termed CSF-BOLD coupling[3]. Reduced CSF-BOLD coupling has been reported in AD and may predict cognitive decline[3,4]. Physiological processes such as cardiac pulsation and respiration affect fMRI signals[5], yet it remains unclear how specific respiratory features influence signal characteristics in relevant ROIs. In this study, we compared individuals trained in controlled breathing with untrained controls to examine how respiration affects fMRI signals.

Materials & Methods

32 participants were recruited: 15 with ≥1 year of breathing training and 17 untrained controls. Each underwent 2 fMRI sessions in random order: regular and deep breathing (85 volumes each). Imaging was performed on a Philips Ingenia Elition X 3T scanner using gradient-echo echo-planner imaging (EPI) (TR = 1.5 s, TE = 30 ms, FA = 80°, voxel size = 1.5 × 1.5 × 3 mm^3). High-resolution T1-weighted images were segmented with FastSurfer and registered to EPI space to extract cortical GM labels. FM CSF was manually segmented on the bottommost EPI slice. Physiological signals were monitored using photoplethysmography and a respiration belt sampled at 496 Hz.

Results

Both raw CSF and raw cortical GM ROIs showed spectral peaks aligning with respiratory frequency bands, with mean coherence at 0.1 Hz of 0.576 in CSF and 0.310 in GM (Figure 1a). Two-way ANOVA showed that, within the CSF ROI, coherence was influenced by both training ($p<0.001$) and breathing condition ($p=0.002$), while in GM these effects were weaker (training: $p=0.022$; condition: $p=0.176$). Coherence in both ROIs was negatively associated with respiratory frequency.

Linear regression between the raw fMRI and respiratory signals using peak lag within a 10-second lag window revealed that the maximum coefficient of determination (R^2) was affected by both training (FM: $p<0.001$; GM: $p=0.585$) and breathing condition (FM: $p<0.001$; GM: $p=0.001$). R^2 values were also negatively associated with respiratory frequency (Figure 1b).

Visual inspection of fMRI and physiological traces showed temporally aligned peaks and troughs—especially within FM CSF (Figure 1c). Interestingly, standard preprocessing for CSF-BOLD analysis (slice-timing and motion correction, linear detrending, 0.01–0.1 Hz bandpass filtering, and temporal z-normalization) did not consistently remove respiratory signals; in some cases, these steps enhanced apparent respiratory-related variance in FM CSF, reducing cross-correlations between GM and FM ROIs (Figure 1c).

Conclusion

Respiration exerts a strong influence on fMRI signals, explaining up to 77% of the variance in CSF and 74% in cortical GM. This influence diminishes at higher respiratory rates and varies with breathing training and condition. In some cases, particularly with deep breathing, respiration-linked signal may still be strong in processed fMRI signals particularly in the CSF, potentially confounding CSF-BOLD signals without concurrent physiological data.

Images/Tables

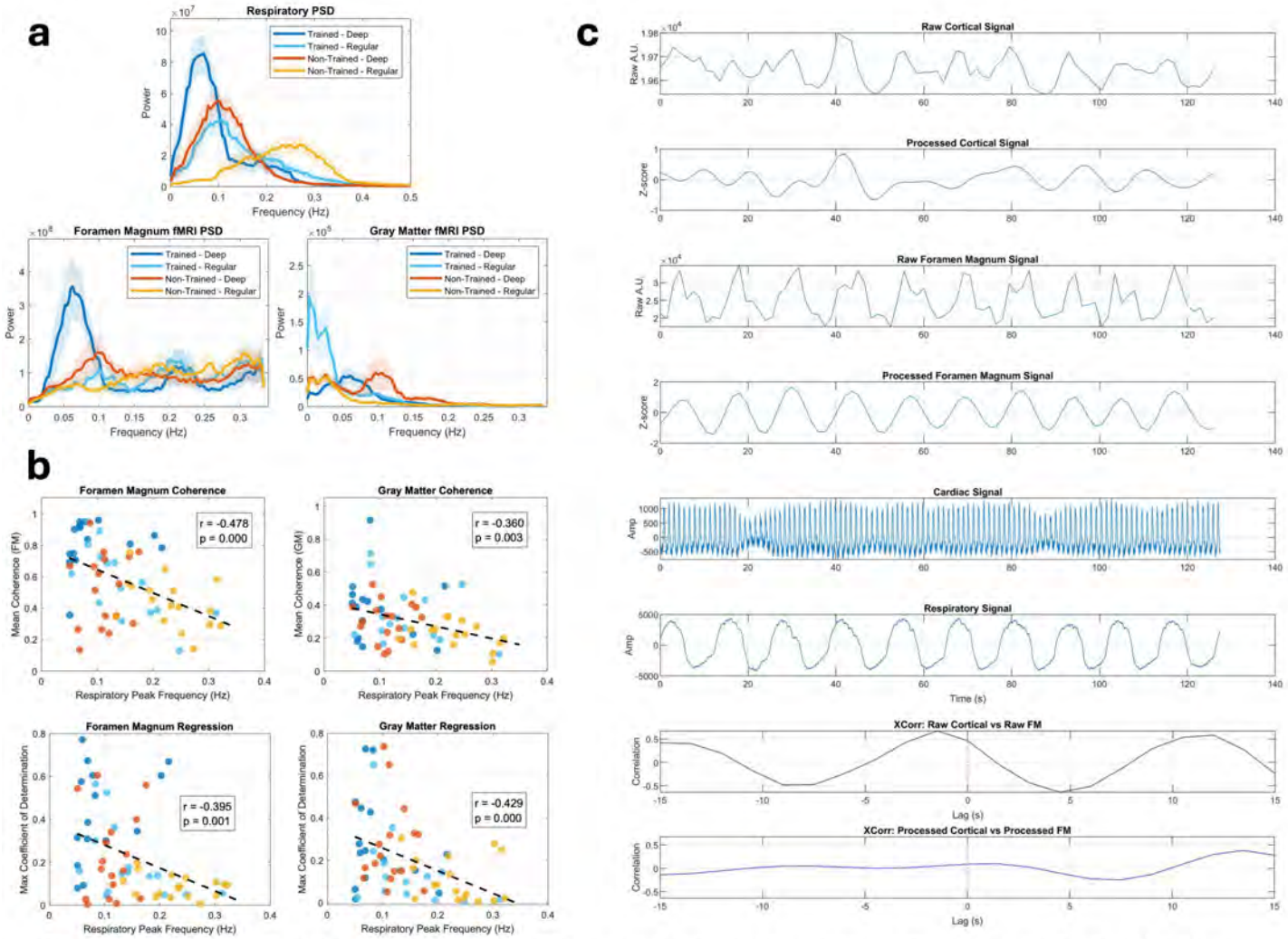

Figure 1. a) Plots demonstrating cohort power spectral density (PSD) curves calculated using the multitaper method for the respiration signal, foramen magnum CSF fMRI signal, and gray matter fMRI signal. Shaded regions indicate the standard error of the mean. **b)** Scatter plots demonstrating mean fMRI power-weighted coherence calculated within a 0.1 hz band centered around the peak respiratory frequency as well as scatter plots demonstrating maximum univariate linear regression coefficient of determination between fMRI and respiration signals. **c)** Traces from a single participant's deep breathing condition demonstrating raw FM and GM fMRI signals as well as processed signals in addition to physiological signals (PPG and respiration belt) and cross correlations between raw FM and GM signals and processed FM and GM signals.

---

676 **Effect of Coronal Scan Location on MRI Visualization of the Lateral Rectus–Superior Rectus Band**

Rishi D Patel MD[1], Nicolas A Tomaras BS[2], Nathalie Azar MD[3], Mehmet C Mocan MD, MPH[3], Burce Ozgen MD[1]

[1]UIC Department of Radiology, Chicago, IL, USA. [2]University of Illinois in Chicago Medical School, Chicago, IL, USA. [3]UIC Department of Ophthalmology, Chicago, IL, USA

Purpose

The lateral rectus–superior rectus (LR–SR) band is an intermuscular connective tissue structure that stabilizes extraocular muscle positioning. Age-related degeneration of this band has been implicated in the pathogenesis of sagging eye syndrome (SES). Although previous MRI studies have described its appearance on coronal images, the optimal slice location relative to the globe–optic nerve junction for evaluating the LR–SR band remains uncertain. This study aimed to analyze the imaging characteristics of the LR–SR band across different orbital scan locations to inform standardization of orbital MRI protocols for SES assessment.

Materials & Methods

High-resolution orbital MRI studies obtained for non-strabismus-related indications were retrospectively reviewed. Two independent readers assessed the LR–SR band at three pre-defined coronal locations: 2.5 mm anterior to (Zone I), at (Zone II), and 2.5 mm posterior to (Zone III) the globe–optic nerve junction. Each zone was evaluated for (1) visibility, (2) continuity, and (3) superotemporal bowing of the LR–SR band in a binary manner.

Results

Forty-eight orbits from 26 patients (age range: 58–86 years) were analyzed. LR–SR band visualization was significantly higher in Zone I (89.6%) compared with Zone II (79.2%, p=0.025) and Zone III (47.9%, p<0.001). When visible, the band demonstrated greater continuity in Zone I (94.7%) than in Zone II (68.4%, p=0.002) or Zone III (52.2%, p<0.001). Conversely, superotemporal bowing was more frequently observed posteriorly, increasing

from 21.1% in Zone I to 47.4% in Zone II (p=0.002) and 56.5% in Zone III (p<0.001). Interobserver agreement was highest for LR–SR band visibility and continuity in anterior scan zones.

Conclusion

The LR–SR band is best visualized on coronal MRI acquired anterior to the globe–optic nerve junction, whereas posterior sections more commonly demonstrate degenerative changes. These findings suggest that anterior imaging planes are optimal for assessing LR–SR band integrity in SES.

Images/Tables

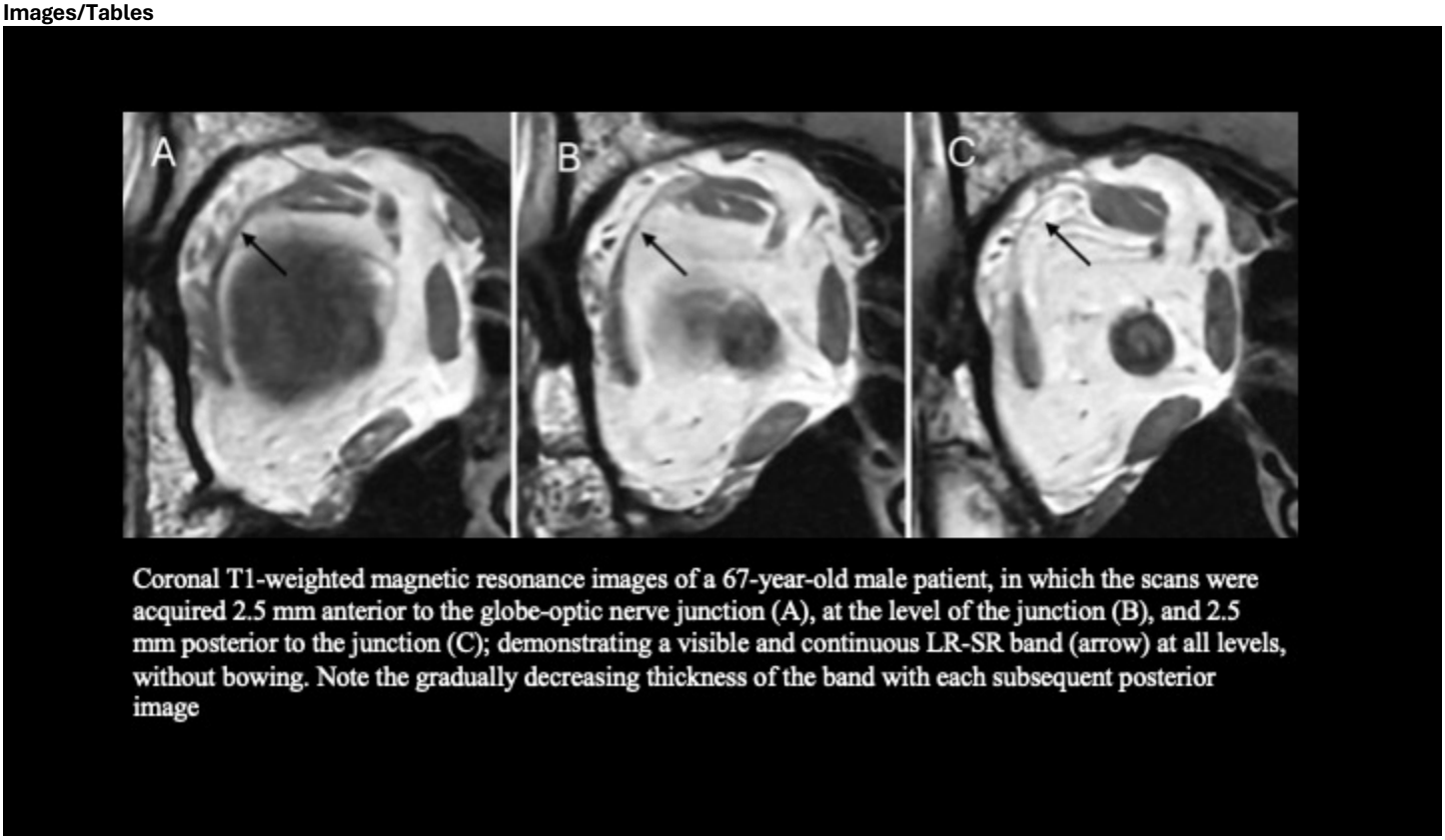

Coronal T1-weighted magnetic resonance images of a 67-year-old male patient, in which the scans were acquired 2.5 mm anterior to the globe-optic nerve junction (A), at the level of the junction (B), and 2.5 mm posterior to the junction (C); demonstrating a visible and continuous LR-SR band (arrow) at all levels, without bowing. Note the gradually decreasing thickness of the band with each subsequent posterior image

---

686 Neurological manifestations of HIV: a systematic review and case-based experience from a tertiary center

Mariana Duarte Gomes MD[1], Cátia Araújo MD[2], Raquel Pontes Figueiredo MD[1], Bruno Cunha MD[1], Miguel Quintas-Neves PhD[1]

[1]Unidade Local de Saúde de Braga, Braga, Braga, Portugal. [2]SESARAM, Madeira, Madeira, Portugal

Purpose

This study aimed to systematically review the literature on neurological manifestations in adult patients with HIV, focusing on opportunistic infections, primary central nervous system (CNS) neoplasms, and HIV-associated neurocognitive complications, identifying clinical, imaging, and laboratory findings most suggestive of each condition, and their outcomes. In addition, we sought to contextualize these findings with local experience from a tertiary care center and to propose a diagnostic algorithm to guide clinical reasoning and imaging interpretation.

Materials & Methods

We conducted a systematic review of the literature following PRISMA guidelines. PubMed and ScienceDirect were searched for original studies published between 2000 and 2024. Eligible studies included adult HIV patients with CNS manifestations. Data were extracted regarding the study population, type of manifestation, diagnostic methods, and outcomes. From an initial pool of 814 studies, 67 were included in the final analysis.

Results

The most frequently reported neurological manifestations in adults with HIV were cerebral toxoplasmosis, cryptococcal meningitis, progressive multifocal leukoencephalopathy (PML), primary central nervous system (CNS) lymphoma, and HIV-associated neurocognitive disorders (HAND). Imaging findings with high diagnostic specificity included the eccentric and concentric target signs for toxoplasmosis, soap-bubble cysts and alpha-trehalose peaks in cryptococcosis, restricted diffusion and subependymal involvement in CNS lymphoma, and asymmetric periventricular white matter lesions in PML. HAND was associated with diffuse cerebral atrophy and symmetrical periventricular hyperintensities sparing U-fibers.

Local case-based data from a tertiary center (n=7) mirrored literature trends, with delayed HIV diagnosis being a frequent factor. Clinical–radiological correlation enabled early recognition of atypical presentations and differentiation from mimickers.

Based on the synthesis of clinical, imaging, and laboratory findings, a diagnostic algorithm was outlined to support the systematic approach to neurological syndromes in HIV patients, emphasizing integration of neuroimaging features to streamline diagnosis and management.

Conclusion

Neurological manifestations of HIV remain clinically relevant and should be systematically considered in the differential diagnosis of atypical or subacute neurological syndromes. Recognition of specific patterns can guide early suspicion, while timely multidisciplinary management is essential to improve outcomes.

Images/Tables

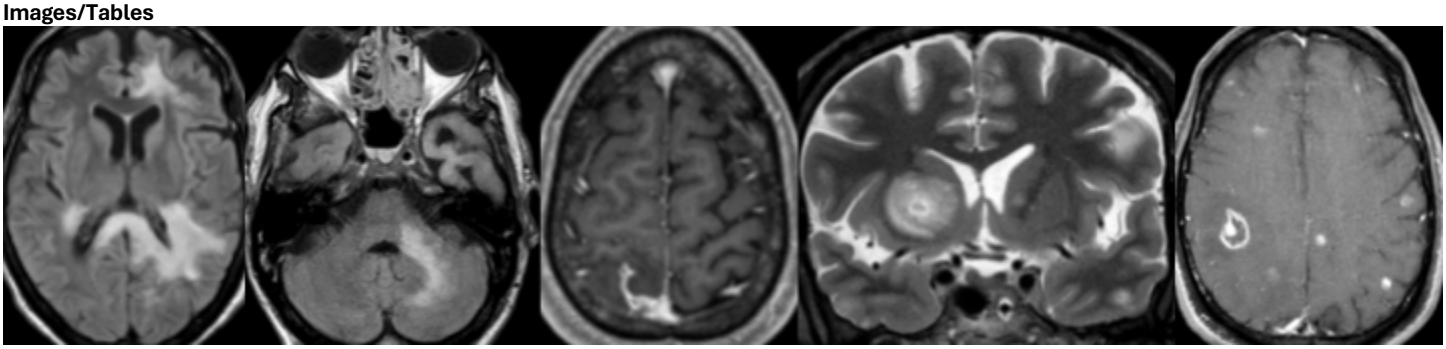

690 **Radiological features in MRI for the prediction of high-grade intracranial meningiomas**

Mariana Duarte Gomes MD[1], Henrique Cardoso Medical Student[2], Rita Coutinho MD[1], Miguel Quintas-Neves PhD[1]
[1]Unidade local de Saúde de Braga, Braga, Braga, Portugal. [2]Life and Health Sciences Research Institute (ICVS), School of Medicine, University of Minho, Braga, Braga, Portugal

Purpose

To evaluate whether preoperative MRI features can accurately predict WHO grade 2/3 meningiomas using routinely available imaging parameters.

Materials & Methods

This retrospective single-center study included 282 patients (mean age 58.4 ± 13.4 years; 176 women) who underwent surgery for histologically confirmed meningiomas between 2010 and 2024. Preoperative MRI was assessed for tumor volume, peritumoral edema, heterogeneous enhancement, cystic components, midline shift, and normalized apparent diffusion coefficient (NADC). Univariable and multivariable logistic regression analyses identified independent predictors of high-grade meningiomas (WHO grade 2/3). Model performance was evaluated with ROC curve analysis.

Results

Among 282 meningiomas, 78% were WHO grade 1 and 22% were grade 2 or 3. High-grade tumors were significantly associated with tumor volume ≥ 45 cc (p = 0.016), presence of cystic components (p = 0.005), midline shift ≥ 3 mm (p = 0.024), and NADC < 1.07 (p = 0.028). These features remained independently associated with higher grade in the multivariable model. The resulting model achieved an AUC of 0.768 (95% CI: 0.689–0.847), with 75.5% sensitivity and 62.8% specificity at the optimal threshold.

Conclusion

A multivariable MRI-based model combining morphologic and diffusion features enables preoperative risk stratification of meningiomas, supporting surgical decision-making. Further validation in prospective, multicenter cohorts is warranted.

723 **Characterizing Turbulent Flow in the Carotid Bulb on Time-of-Flight Magnetic Resonance Angiography**

Sachin D Shah DO[1], Katrin Vetter DO[2], Stanley Lu MD[2]
[1]Rutgers Health - Robert Wood Johnson Medical School, New Brunswick, NJ, USA. [2]Rutgers Health - Monmouth Medical Center, Long Branch, NJ, USA

Purpose

Under normal conditions, blood travels via laminar flow, characterized by a profile of parallel flow lines with a parabolic velocity profile; maximum velocity occurs at the center, and no flow occurs at the outer blood-wall interface (Figure A). Abnormalities in hemodynamics occur when properties like flow velocity, vessel diameter, vessel wall integrity, and flow direction change [1]. The carotid bulb is a common location for turbulent flow due to its increased vessel diameter which predisposes it to recirculating and vortex flow. Turbulent flow may undergo spin dephasing and shortening of the T2 relaxation time, resulting in signal loss which can appear as an artifact or pseudostenosis [2]. These flow artifacts can mimic more serious conditions such as high-grade stenosis, intramural hematoma, or carotid dissection in an otherwise healthy individual [3]. The purpose of this study is to analyze flow artifacts on Time-of-Flight (TOF) Magnetic Resonance Angiography (MRA) in healthy individuals and correlate these artifacts with normal variant anatomy rather than underlying disease.

Materials & Methods

A retrospective chart review was performed on patients who underwent TOF MRA of the head and neck. Inclusion criteria were patients aged 18-95 who underwent MRA studies that showed no clinically significant stenosis as the final imaging diagnosis. Patients with a known dissection or high-grade stenosis were excluded from this study. Measurements that were obtained include artifact diameter, ipsilateral carotid bulb diameter, and ipsilateral distal internal carotid artery (ICA) diameter (Figure B). The ratio of bulb to distal ICA size was calculated to assess its correlation with artifact size.

Results

A total of 51 TOF MRAs were reviewed (mean patient age, 61 years). A statistically significant correlation ($r = 0.48$, $p < 0.05$) was observed between the ratio of carotid bulb to distal ICA diameter and the measured artifact size (Figure C).

Conclusion

On average, a larger carotid bulb to distal ICA ratio is associated with a larger artifact size. This suggests, with increasing diameter of the carotid bulb there is increased turbulent flow. This abnormal flow may predispose patients to vascular disease by promoting endothelial injury and atherosclerotic calcification. Future work will evaluate whether patients with higher bulb to distal ICA ratio are predisposed to increased atherosclerotic plaque burden at the carotid bulb.

Images/Tables

Title: Characterizing Hemodynamic Flow through the Internal Carotid Artery on Time-of-Flight Magnetic Resonance Angiography

Diagrams

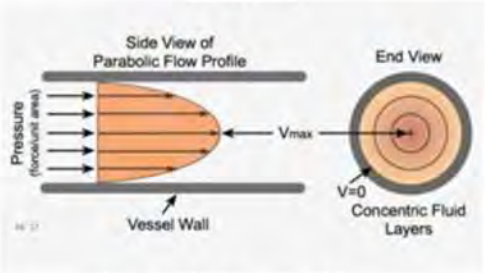

Figure A: Laminar Flow

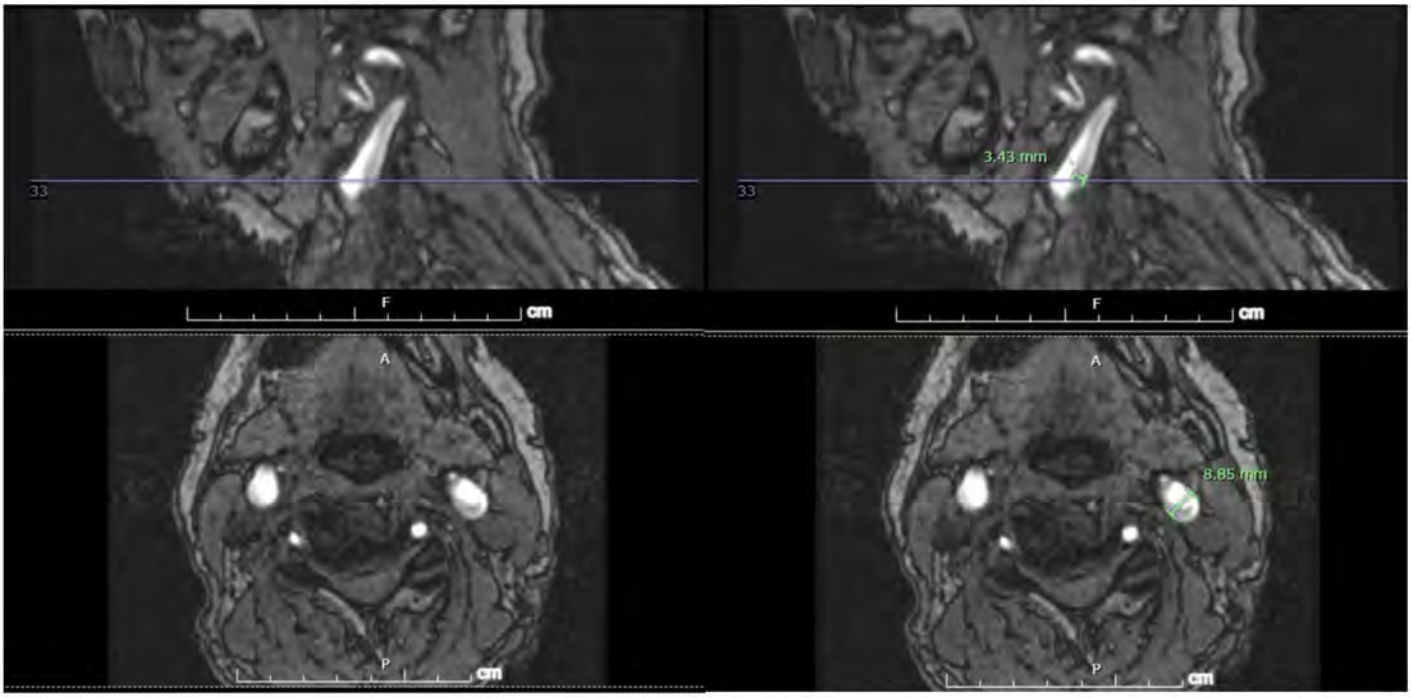

Figure B: Sagittal View (Top) and Axial View (Bottom) of a MRA Head and Neck Without Contrast Demonstrating Artifact (Top Right) and Carotid Bulb (Bottom Right) Measurements

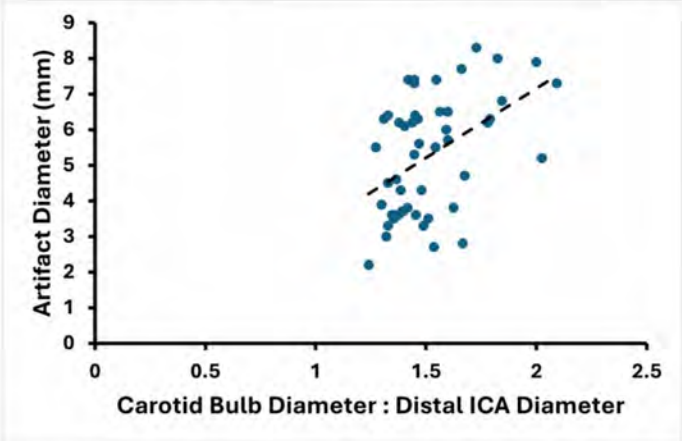

Figure C: Relationship of Carotid Bulb Dilatation to Artifact Size

737 Rapid Voxel-Based Cortical Thickness Estimation: A Comparable Performance Alternative to FreeSurfer for Clinical Applications

Min-Woo Lee Master, Jundong Hwang Master, Da Hyun Kim Bachelor, Sunghwan Park Bachelor, Mijung Park Bachelor, HaJin Kim Master, Hyungyou Park Ph.D, Regina E.Y. Kim Ph.D, DongHyeon Kim Ph.D, Min-ho Lee Ph.D
Research Institute, Neurophet Inc., Seoul, Korea, Republic of

Purpose

This study aims to develop and validate a rapid, automated, voxel-based method for estimating the cortical thickness of the brain. We compared its diagnostic performance in differentiating Alzheimer's disease (AD) from normal controls (NC) against the established FreeSurfer pipeline.

Materials & Methods

In this study, we obtained 440 normal subjects and 439 AD subjects from the ADNI (Alzheimer's Disease Neuroimaging Initiative) database to perform a comparative analysis of cortical thickness estimation results using FreeSurfer and our methods. FreeSurfer is known to adopt a mesh-based cortical thickness estimation approach [1,2]; however, it requires a relatively long processing time of approximately one hour. In contrast, our method is designed to perform the estimation at the voxel level. The core workflow of our methods is as follows: (1) T1-weighted MRI images are input into Neurophet AQUA (Version 3.2, Neurophet Inc., Seoul, Republic of Korea) to perform brain segmentation; (2) GM (gray matter), WM (white matter), and other regions are obtained from the segmentation results. At this stage, WM is merged with ventricle information to ensure a filling effect; (3) inner boundaries (GM/WM) and outer boundaries (others/GM) are extracted in the 2.5D directions by computing boundaries separately from the axial, sagittal, and coronal views, and then generating the final inner and outer boundaries as the intersections of these results. (4) Using the FMM (Fast Marching Method) algorithm, a WMD is calculated as the shortest distance from the WM towards the other regions, and a CSFD is calculated as the shortest distance from the other regions towards the WM. (5) A projection algorithm is applied to correct for overestimation inherent in simple distance summation, with an additional correction for partial volume effects. Regional cortical thickness values were compared between groups using multiple tests with False Discovery Rate (FDR) correction.

Results

Table 1 shows no significant age or sex differences between NC and AD groups. Table 2 compares cortical thickness across ROIs after multiple test correction. In FreeSurfer, no significant differences were found in the left (p=0.935) and right caudal anterior cingulate cortex (p=0.201) and right rostral anterior cingulate cortex (p=0.062). Our method showed a nonsignificant result only in the right caudal anterior cingulate cortex (p=0.069). Moreover, it required about 70 seconds per sample. These results indicate that our method is sufficient for detecting AD-related brain atrophy.

Conclusion

Our method matched FreeSurfer's performance in distinguishing NC and AD within two minutes. Integration into clinical tools and an in-house normative database could enable rapid, personalized cortical atrophy estimation, enhancing diagnostic and therapeutic decision-making.

Images/Tables

Table 1. Demographic characteristics of study subjects

Characteristics	Normal (n= 440)	AD (n= 439)	p-value
Age, mean (std)	75.74 (7.57)	76.26 (7.81)	0.32
Sex, Female ratio (N)	0.47 (207)	0.43 (188)	0.23

Statistical analyses were performed using two-sample t-test for age and chi-square test for sex.

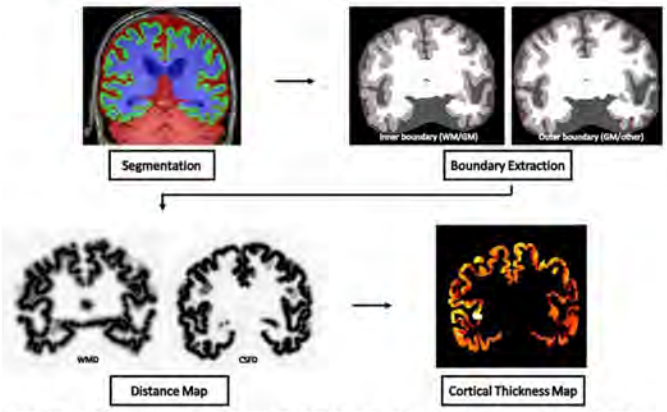

Figure 1. Our method's cortical thickness estimation workflow. WM; white matter, GM; gray matter, WMD; the shortest distance from the WM to the other regions, CSFD; the shortest distance from the other regions to WM.

Table 2. Statistical comparison of ROIs cortical thickness between normal and AD groups with multiple test correction.

ROI_name	FreeSurfer	Our methods	ROI_name	FreeSurfer	Our methods
ctx_lh_bankssts	< 0.001	< 0.001	ctx_rh_bankssts	< 0.001	< 0.001
ctx_lh_caudal_anterior_cingulate	0.935	< 0.001	ctx_rh_caudal_anterior_cingulate	0.201	0.069
ctx_lh_caudal_middle_frontal	< 0.001	< 0.001	ctx_rh_caudal_middle_frontal	< 0.001	< 0.001
ctx_lh_cuneus	< 0.001	< 0.001	ctx_rh_cuneus	< 0.001	< 0.001
ctx_lh_entorhinal	< 0.001	< 0.001	ctx_rh_entorhinal	< 0.001	< 0.001
ctx_lh_fusiform_gyrus	< 0.001	< 0.001	ctx_rh_fusiform_gyrus	< 0.001	< 0.001
ctx_lh_inferior_parietal	< 0.001	< 0.001	ctx_rh_inferior_parietal	< 0.001	< 0.001
ctx_lh_inferior_temporal_gyrus	< 0.001	< 0.001	ctx_rh_inferior_temporal_gyrus	< 0.001	< 0.001
ctx_lh_isthmus_cingulate	< 0.001	< 0.001	ctx_rh_isthmus_cingulate	< 0.001	< 0.001
ctx_lh_lateral_occipital	< 0.001	< 0.001	ctx_rh_lateral_occipital	< 0.001	< 0.001
ctx_lh_lateral_orbitofrontal	< 0.001	< 0.001	ctx_rh_lateral_orbitofrontal	< 0.001	< 0.001
ctx_lh_lingual_gyrus	< 0.001	< 0.001	ctx_rh_lingual_gyrus	< 0.001	< 0.001
ctx_lh_medial_orbitofrontal	< 0.001	< 0.001	ctx_rh_medial_orbitofrontal	< 0.001	< 0.001
ctx_lh_middle_temporal_gyrus	< 0.001	< 0.001	ctx_rh_middle_temporal_gyrus	< 0.001	< 0.001
ctx_lh_parahippocampal_gyrus	< 0.001	< 0.001	ctx_rh_parahippocampal_gyrus	< 0.001	< 0.001
ctx_lh_paracentral	< 0.001	0.011	ctx_rh_paracentral	< 0.001	< 0.001
ctx_lh_pars_opercularis	< 0.001	< 0.001	ctx_rh_pars_opercularis	< 0.001	< 0.001
ctx_lh_pars_orbitalis	< 0.001	< 0.001	ctx_rh_pars_orbitalis	< 0.001	< 0.001
ctx_lh_pars_triangularis	< 0.001	< 0.001	ctx_rh_pars_triangularis	< 0.001	< 0.001
ctx_lh_pericalcarine	< 0.001	< 0.001	ctx_rh_pericalcarine	< 0.001	< 0.001
ctx_lh_postcentral_gyrus	< 0.001	< 0.001	ctx_rh_postcentral_gyrus	< 0.001	< 0.001
ctx_lh_posterior_cingulate	< 0.001	< 0.001	ctx_rh_posterior_cingulate	< 0.001	< 0.001
ctx_lh_precentral_gyrus	< 0.001	< 0.001	ctx_rh_precentral_gyrus	< 0.001	< 0.001
ctx_lh_precuneus	< 0.001	< 0.001	ctx_rh_precuneus	< 0.001	< 0.001
ctx_lh_rostral_anterior_cingulate	< 0.001	< 0.001	ctx_rh_rostral_anterior_cingulate	0.062	< 0.001
ctx_lh_rostral_middle_frontal	< 0.001	< 0.001	ctx_rh_rostral_middle_frontal	< 0.001	< 0.001
ctx_lh_superior_frontal_gyrus	< 0.001	< 0.001	ctx_rh_superior_frontal_gyrus	< 0.001	< 0.001
ctx_lh_superior_parietal	< 0.001	< 0.001	ctx_rh_superior_parietal	< 0.001	< 0.001
ctx_lh_superior_temporal_gyrus	< 0.001	< 0.001	ctx_rh_superior_temporal_gyrus	< 0.001	< 0.001
ctx_lh_supramarginal_gyrus	< 0.001	< 0.001	ctx_rh_supramarginal_gyrus	< 0.001	< 0.001
ctx_lh_frontal_pole	< 0.001	< 0.001	ctx_rh_frontal_pole	0.006	0.002
ctx_lh_temporal_pole	< 0.001	< 0.001	ctx_rh_temporal_pole	< 0.001	< 0.001
ctx_lh_transverse_temporal_gyrus	< 0.001	< 0.001	ctx_rh_transverse_temporal_gyrus	< 0.001	< 0.001
ctx_lh_insula	< 0.001	< 0.001	ctx_rh_insula	< 0.001	< 0.001

Note. p-values were adjusted using false discovery rate (FDR) correction. Values with FDR-corrected $p < 0.05$ are indicated in bold.

771 Longitudinal MRI-based Radiomic Analysis of Meningioma Growth and Heterogeneity

Ahmad Pour-Rashidi M.D., Laetitia Perronne M.D., James P. Chandler MD, Yuri S Velichko PhD
Northwestern University, Feinberg School of Medicine, Chicago, IL, USA

Purpose

Meningiomas, the most common primary brain tumors in adults, exhibit diverse and unpredictable growth patterns. This longitudinal MRI-based radiomics study analyzes meningioma volumetric growth rate and the rate of change in tumor-image heterogeneity.

Materials & Methods

This retrospective study enrolled 199 patients with histologically confirmed meningioma, categorized as grade I (63%), and grade II (30%), regardless of their specific subtypes. Patient age, gender, tumor location, pathology grade, and MIB-1 labeling index were collected. In cases with two differing pathology reports, the highest grade was used for analysis. All patients underwent high-resolution (1 mm^3) MRI, including post-contrast T1-weighted

and T2-weighted sequences. Tumors were manually segmented, and 231 MRI-based radiomic features were extracted. To analyze longitudinal changes, a linear mixed-effects model was constructed. Tumor volume, radiomic features, and meningioma grade were considered fixed factors, while patient ID was treated as a random factor. The model was used to estimate the volumetric growth rate and the rate of change in tumor-image heterogeneity, assessed as the slope of the relationship between tumor volume or the radiomic feature and days since diagnosis. Independent samples t-tests were used to compare the mean values of the radiomic features across different categories, such as meningioma grade, to identify statistically significant differences.

Results

The volumetric growth rate and the rate of change in tumor heterogeneity varied widely within each grade, making differentiation challenging. For example, the median (IQR) volumetric growth rates were 0.0015 ml/day (0.0006, 0.003) for Grade 1 and 0.001 ml/day (0.0005, 0.006) for Grade 2 (mean values: 8.3e-03 and 4.6e-03 ml/day, respectively; p=0.54). On the contrary, several radiomic features demonstrated better discriminatory power. For example, the rate of change in the Gray Level Co-occurrence Matrix (GLCM) Angular Second Moment, a measure of gray-level uniformity, showed a clear distinction between grades: -5.5E-5 (IQR: -2.2E-4, 3.3E-4) for Grade 1 and +2.2E-4 (IQR: -0.6E-4, +7.6E-4) for Grade 2 (mean values: -1.35e-03 and 3.3e-03, respectively; p<0.02).

Conclusion

This longitudinal study demonstrates that while volumetric growth rate alone is insufficient to differentiate between Grade 1 and Grade 2 meningiomas, rate of changes in MRI-based radiomic features show promise as potential discriminators. These results highlight the added value of longitudinal radiomic analysis in characterizing meningioma growth patterns beyond simple volumetric assessment.

Images/Tables

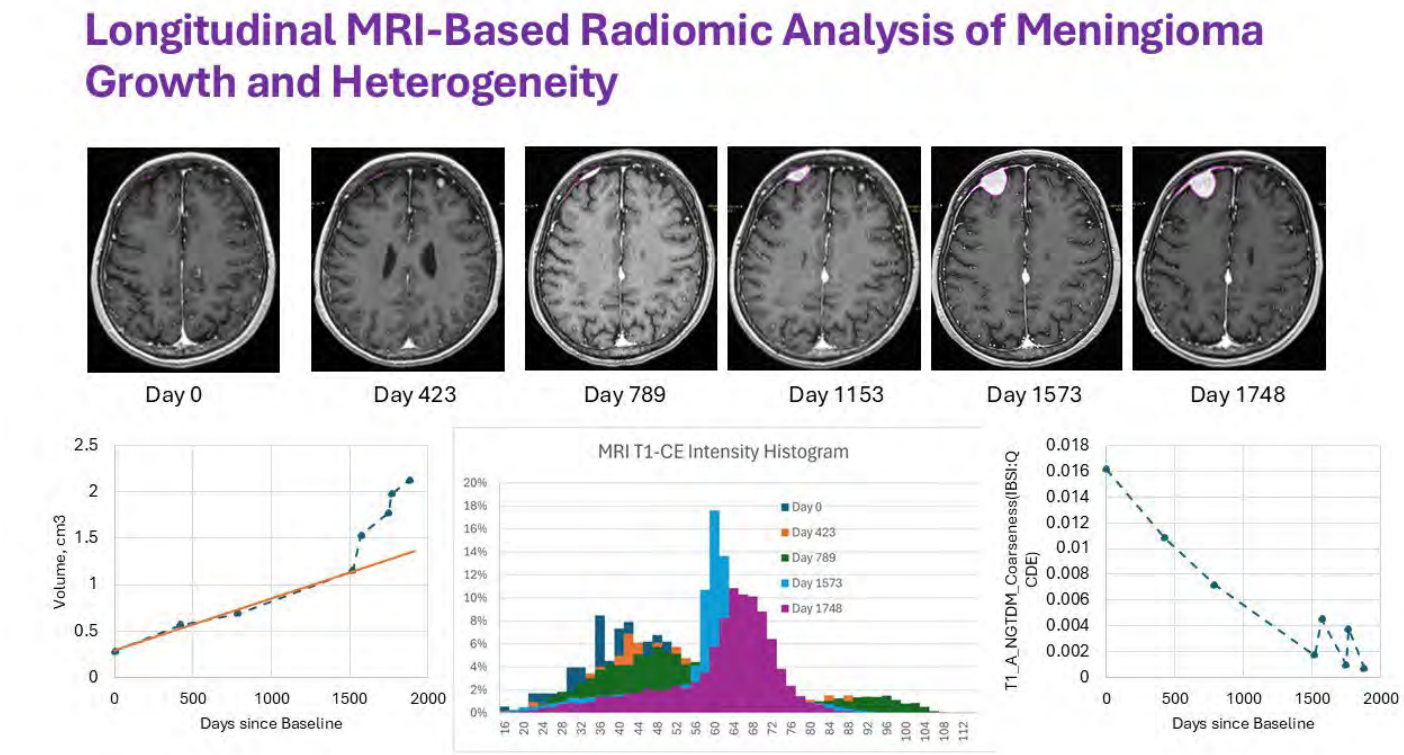

---

792 Comparative Evaluation of Ferumoxytol MRI and Conventional Imaging Modalities for Detection of Brain Arteriovenous Malformations in Patients with Hereditary Hemorrhagic Telangiectasia

Alex Gill BA, Jing Liu PhD, Yoo Jin Lee MD, Miles Conrad MD, MPH, Michael Ohliger MD, PhD, Daniel Langston NP, MSN, Jonas Schollenberger PhD, Kambiz Nael MD, Javier Villanueva-Meyer MD, Sartaaj Walia MD, Steven Hetts MD, David Saloner PhD
University of California San Francisco, San Francisco, CA, USA

Purpose

Small arteriovenous malformations (AVMs) are often challenging to detect and characterize with non-invasive imaging. These lesions can present in patients with Hereditary Hemorrhagic Telangiectasia (HHT) who have a high likelihood (10-20%) of developing brain AVMs that present a risk of hemorrhage. Conventional MR imaging approaches are not always able to identify these small lesions. Ferumoxytol is an ultrasmall paramagnetic agent that provides a strong and consistent intravascular magnetization strength enabling high CNR images at very high resolution. In this study we investigated the use of Ferumoxytol-enhanced MRI at 3T for identifying HHT lesions in comparison to catheter angiography and conventional MRI.

Materials & Methods

Patients with HHT were enrolled in this study. Following informed consent, 3mg/kg Ferumoxytol was administered by intravenous infusion over 15 minutes. Subjects were then scanned with whole brain 3D VIBE imaging. Scans were acquired at 3 resolutions: (1) 1.0 mm isotropic (TE 1.3 ms, TR 2.9 ms, acquisition time 1 minute), (2) 0.8 mm isotropic (TE 1.6 ms, TR 3.3 ms, acquisition time 2 minutes), and (3) 0.5 mm isotropic (TE 1.9 ms, TR 4.3 ms, acquisition time 4 minutes). The MRI data was reformatted on multiple planes and with multiple maximal intensity projection (MIP) slab thicknesses. Three experienced neuroradiologists compared the FeMR study to DSA and conventional MRI studies obtained for clinical purposes independently of the research project.

Results

40 subjects with HHT were enrolled. Among these, there were 18 known HHT brain lesions. All AVMs found on catheter angiography were detected on 3T Ferumoxytol-enhanced VIBE MRA. A number of lesions found on both catheter angiography and on Ferumoxytol-enhanced MRI were difficult to detect on conventional clinical MRI scanning. Figure 1 shows an AVM in the left inferior paramedian pons supplied by a left AICA branch that is much clearer and more readily identified on the Ferumoxytol scan. Figure 2 shows an AVM centered in the left hippocampal head with arterial supply from a temporal branch of the left posterior cerebral artery and deep venous drainage clearly shown on high-resolution Ferumoxytol images.

Conclusion

Ferumoxytol has an intravascular half-life of 15 hours providing substantially shortened T1 values throughout the MR imaging session. Sequences with very short TR values can then be used, provided ultrashort echo times are used to mitigate T2* effects. This combination is provided by the VIBE sequence which yields whole brain coverage with very high and isotropic spatial resolution. The very short TR also allows relatively short acquisition times. The resultant Ferumoxytol-enhanced MRI images acquired at 3T strongly suppress stationary background signal and that angiographic effect facilitates the identification of all AVMs previously seen on DSA and to better advantage than is seen on conventional clinical MRI. Quantitative MR techniques may also be less subject to inter-operator-dependency, providing a more objective means for tracking over time. These imaging approaches may be generalized to any patients needing high-resolution vascular imaging. Further studies are needed to determine if high-risk features (e.g., feeding artery aneurysms, nidus aneurysms, venous outflow stenoses) of such AVMs can be reliably identified as compared to DSA.

Images/Tables

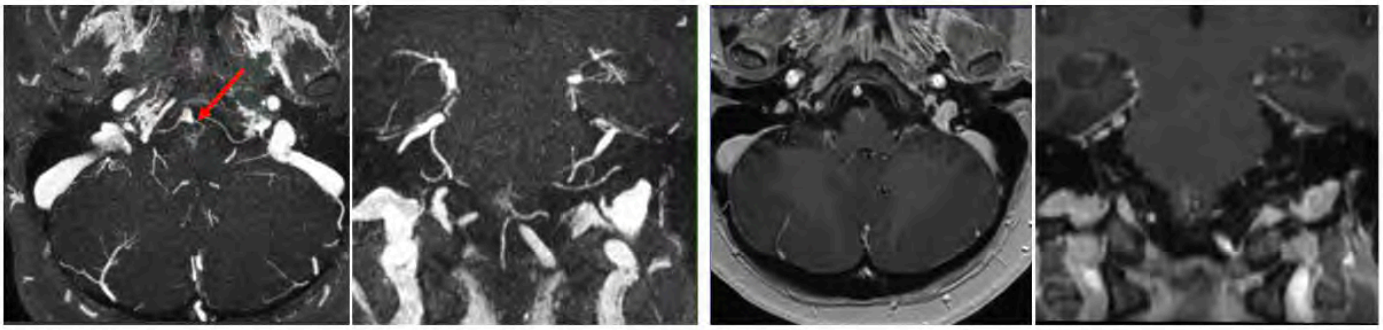

Figure 1
An arteriovenous malformation in the left inferior paramedian pons supplied by a left AICA branch much clearly and readily identified by Ferumoxytol scan.

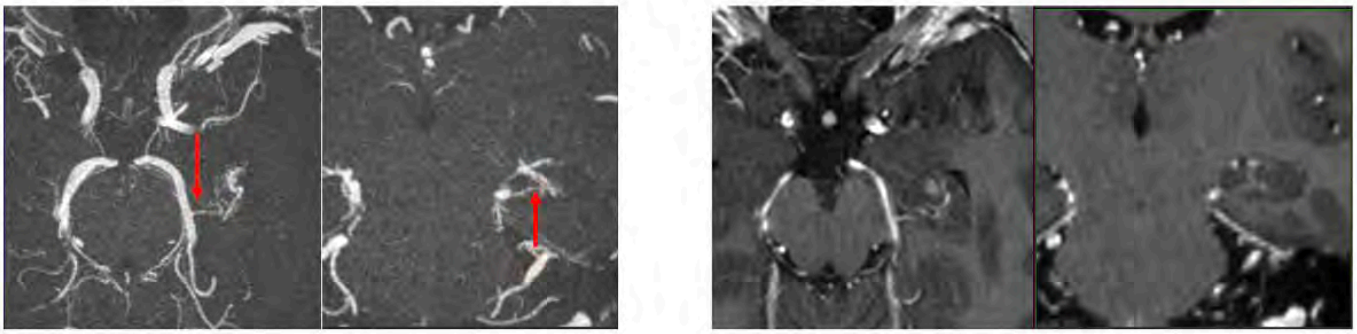

Figure 2
An arteriovenous malformation centered in the left hippocampal head. Arterial supply from a temporal branch of the left posterior cerebral artery and deep venous drainage are clearly shown on high resolution Ferumoxytol images (arrows).

---

801 Proton Beam Therapy-Associated Radiation Changes in the Subependymal Periventricular Region - a Mimicker of Recurrent Tumor?

Rajeev N Herekar DO, Kirby E Quinn MD, Russ A Kuker MD, Natalya Nagornaya MD, Gaurav M Saigal MD
University of Miami/Jackson Health Systems, Miami, FL, USA

Purpose

Proton beam radiation treatment (PBT) is a relatively recent form of therapy for brain cancers. PBT, like other forms of radiation therapies, can result in post radiation changes that are visible on imaging. PET/CT or MR Perfusion are the imaging tests of choice to help differentiate between post radiation changes and recurrent tumor. In this study, we demonstrate a relatively unknown effect of proton therapy predominantly seen in the periventricular regions of the brain, resulting in false positive MR Perfusion and/or PET/CT findings.

Materials & Methods

Sixty-one patients with resected high grade oligodendroglioma or astrocytoma who received PBT and had follow-up MRI Perfusion and/or PET/CTs were evaluated.

Results

Of the evaluated patients, thirty-one demonstrated nodular enhancement in and around the surgical bed on follow-up MR studies. Of these, 13 patients demonstrated positive correlates on MR Perfusion and/or PET/CT studies suggesting recurrence and subsequently underwent biopsy. Of these, 8cases were true positives for tumor whereas the other 5 were false positives (negative for tumor recurrence). Four additional patients who did not undergo biopsy of the suspected recurrence were deemed to be false positives due to decrease/resolution of enhancement on follow-up imaging. Of note, the enhancement seen in all of the 9 false positive cases was periventricular/subependymal in location. Of the 8 true positive cases, none showed enhancement in the periventricular region ($p<0.05$).

Conclusion

Non-tumor periventricular enhancement can be seen on follow-up imaging in patients who have undergone PBT following glioma resection and can be falsely positive on MR perfusion and/or PETCT. The cause is not entirely clear but might be related to the higher sensitivity of the subependymal region to PBT resulting in an intense inflammatory reaction. Such a finding should be treated with caution and followed up with short interval imaging rather than surgery. Further studies are needed to investigate the mechanistic differences between PBT and other radiation therapies, regarding their propensity to affect the periventricular region. When seen, periventricular enhancement following PBT therapy in the post operative setting for glioma patients should be further evaluated with short interval follow up imaging as opposed to surgery.

Images/Tables

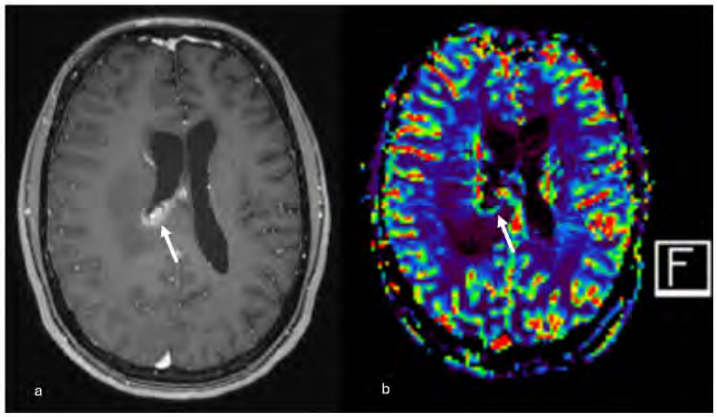

Figures a (Axial T1W post contrast) and b (Axial Perfusion MR). 22-year-old male with biopsy proven WHO grade III oligodendroglioma, status post resection. Follow up imaging nine months post proton beam therapy completion demonstrating periventricular enhancement and increased CBV (arrows). Recurrent biopsy demonstrated reactive gliosis, inflammatory infiltrate, and dystrophic calcifications consistent with therapy-induced changes.

---

811 Intracranial Atherosclerosis and Thrombectomy: Modifiable Risks and Outcomes in Large Vessel Occlusion Stroke

Sacha C Baldeosingh MD[1], Deep K Pujara MBBS[2], Amrou Sarraj MD[2], Clark W Sitton MD[1]

[1]UT Health Houston, Houston, TX, USA. [2]University Hospitals Neurological Institute, Clevaland, OH, USA

Purpose

Intracranial atherosclerotic disease (ICAD) is a common comorbidity in LVO, especially amongst the black and Asian population. Recent single center studies [3-4] showed worse outcomes in ICAD patients with successful MT. Our analysis of 117 patients with TICI3 reperfusion from the SELECT trial[1] demonstrated significant negative impact of ICAD on functional outcomes. We expanded this study to include TICI 2b/c patients and TICI 3 patients from additional centers. To our knowledge this is the largest multi-center cohort to evaluate the effect of ICAD on IAT outcomes.

Materials & Methods

We retrospectively analyzed digital subtraction angiograms of 233 MT patients with TICI3, TICI 2b, and TICI 2c recanalization from 9 institutions (SELECT)[1] for evidence of ICAD. Catheter, stent, and wire positions were noted. We defined ICAD as convincing evidence of atherosclerotic irregularity distal to the carotid siphon, outside the region of recanalization, and not morphologically likely to represent spasm or dissection.[5] ICAD was evaluated in the contralateral and posterior circulation where available (n=42). All angiograms were evaluated by both a neuroradiology fellow and a neuroradiology attending with 23 years of experience.

ICAD patients were compared to similar patients without ICAD, and outcomes were analyzed using the metrics of mRS shift, mortality, symptomatic intracranial hemorrhage, neurological worsening, final infarct volume (on DWI or CT), and growth in infarct size from baseline. All p-values were calculated using multivariable logistic regression models, which were adjusted for age, NIHSS score, tPA administration, time to procedure, ASPECT score, and CT perfusion core volume (prior to intervention).

Results

We found 32/233 cases with evidence of ICAD. ICAD patients had a significantly increased incidence of hypertension ($p=0.043$), diabetes ($p=0.016$), and elevated serum glucose ($p=0.013$). There was no significant association with coronary artery disease, congestive heart failure, or atrial fibrillation. (Significant values ($p<0.05$)

In our cohort (n=233) there was a significant negative effect of ICAD on mRS shift ($p=0.45$) but after adjusting for hypertension and diabetes this effect was no longer significant ($p=0.156$). There was no significant effect on functional outcome, mortality, symptomatic hemorrhage, or final infarct

volume. Analyzing the TICI 2b/c subgroup by itself with adjustments for HTN and DM, there was a significant effect on mRS shift (p=0.17) but not in other outcomes.
Limitations included: limitations of cerebral angiography to detect non-caliber-changing ICAD, 4-vessel angiogram not available on all patients, and insufficient power to correlate ICAD with dissection/ spasm.

Conclusion

In our cohort of randomized MT, ICAD was strongly associated with hypertension and diabetes. Although there was a trend, there was no significant difference in functional outcomes between patients with and without ICAD when adjusted for HTN and DM. No significant association of ICAD with coronary artery disease, congestive heart failure, or atrial fibrillation. In the future, we can expand analysis to include additional patients in the SELECT2 database to increase study power. When we added additional centers, our previous results were diluted. We need to re-analyze the data to try to assess the effect of individual centers on outcomes.

Images/Tables

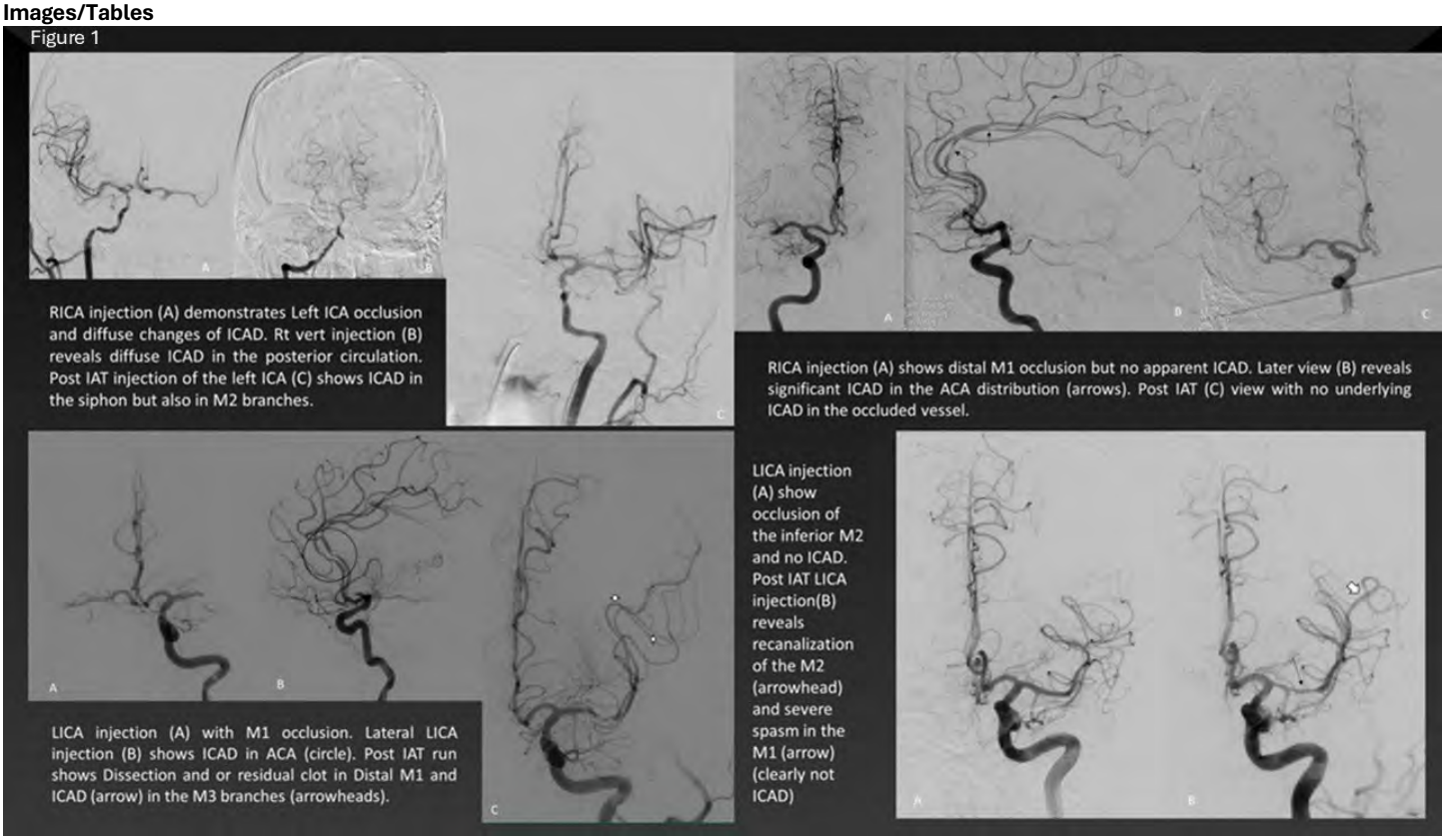

816 Automated AI-Approach for Detecting Lesions and Enlarged Lymph Nodes in Head and Neck Squamous Cell Carcinoma using CT

Rikhil D Makwana BA[1], Fahmida Haque PhD[1], Stephanie A Harmon PhD[1], Nathan Lay PhD[1], Haoyue Zhang PhD[1], Charalampos S Floudas MD[2], Ismail B Turkbey MD[1]
[1]National Cancer Institute, Artificial Intelligence Resource, Bethesda, MD, USA. [2]National Cancer Institute, Center for Cancer Research, Center for Immuno-Oncology, Bethesda, MD, USA

Purpose

Head and neck cancer squamous cell carcinoma (HNSCC) is an aggressive tumor arising from the nasal sinuses and inferiorly to the larynx, and is commonly detected in the later stages (III-IV)[1] of the disease. Contrast-enhanced CT (CECT) is used for diagnosis and treatment planning for HNSCC. There have been limited efforts to utilize artificial intelligence (AI) in diagnosis on CT, with lack of multi-center validation in existing models being one of the most prominent limitations in current practice[2]. In this study, we aimed to develop an AI model for the detection of primary lesions and enlarged lymph nodes in the head and neck CT imaging.

Materials & Methods

In this study, CECT images from two populations were used. The first was from "The Cancer Genome Atlas Head-Neck Squamous Cell Carcinoma Collection"[3] (TCGA-HNSC) collection, a multi-center open-access dataset, and the second was from an independently provided cohort of patients with Stage-IV HNSCC participating in a clinical (NCT: IRB001564) trial at our institution. A radiologist with over 20 years of experience segmented both cancerous lesions and enlarged lymph nodes (LN). A 5-fold cross-validation split was generated to distribute the number of enlarged lymph nodes and lesion location by their location in reference to the hyoid bone. An extension of the U-net architecture, nn-UNet v2[4] was then used to train the model using the 3D-full-res configuration and patient-stratified data splits. After training, the model was tested on both the TCIA (internal validation) and independent patient (external validation) cohorts. Model performance was evaluated for both lesion and LN level and scan level using accuracy, sensitivity, Dice similarity score (DSC).

Results

There were 119 patients from the TCGA-HNSC, with 97 being used for training and validation, and 22 being used for testing. The independent cohort involved 60 patients, with 6 used for training/validation and 54 used for external validation of the model. The model had an overall accuracy, sensitivity, and specificity of 78.9% (internal test set = 72.7%; external test set = 81.48%), 78.7% (internal test set = 72.7%; external test set = 81.1%), and 100% specificity (internal test set = n/a; external test set = 100%) when detecting lesions, respectively. The lesion DICE was .47 (internal

test set = 0.46; external test set = 0.47). The model had 84.2% accuracy, 93.0% sensitivity, 57.9% specificity, and a DICE score of 0.57 when detecting LN. The model misclassified 2 lesions as LN and 1 LN as a lesion.

Conclusion

The model shows reliable performance when used on CECT images from multiple institutions with a variety of scanning protocols. Further validation with larger cohorts is necessary for additional study.

Images/Tables

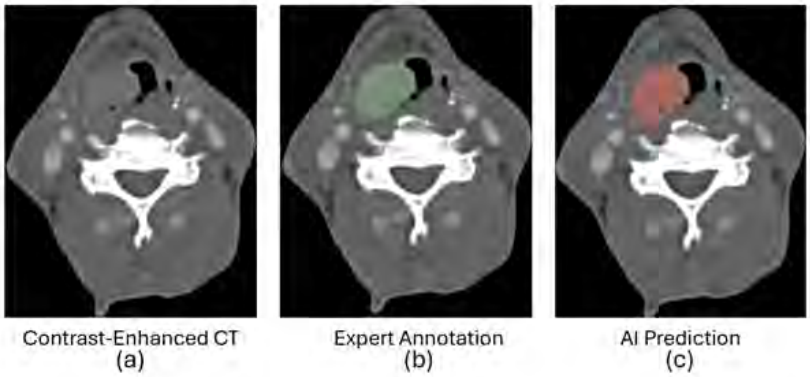

Fig 1: Internal Test Set Model Performance. (a) Shows the original contrast enhanced CT scan of the patient. (b) Shows the Expert's annotation of a lesion in green. (c) Shows the predicted location of the lesion identified by the model in red. Lesion DICE was 0.92.

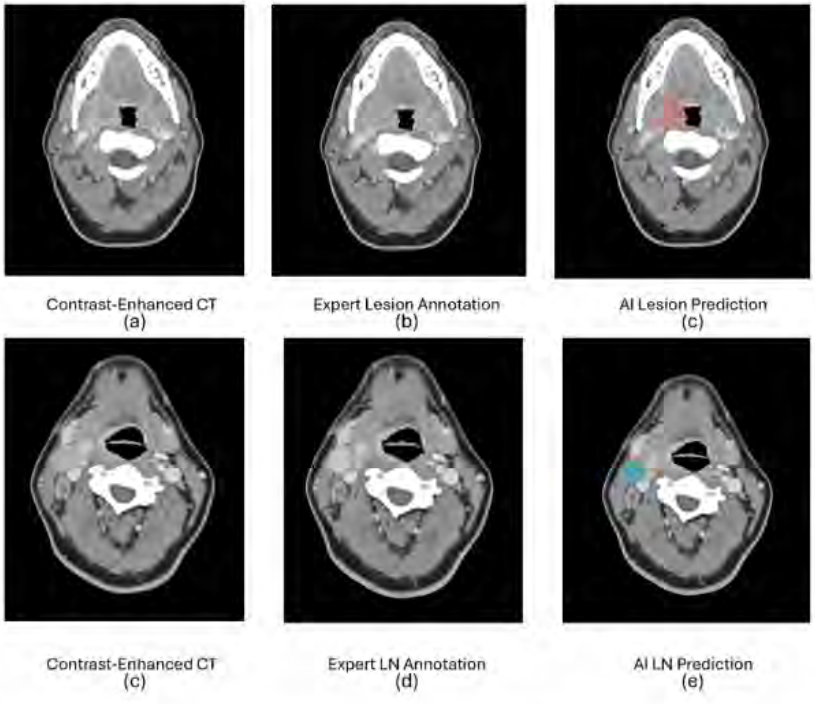

Fig 2: External Test Set Model Performance. (a) Shows the original contrast enhanced CT scan of the patient. (b) Shows the Expert's annotation of a lesion in green. (c) Shows the predicted location of the lesion identified by the model in red. Lesion DICE was 0.90. (d) Shows the Expert's annotation of an enlarged LN in yellow. (e) Shows the model's prediction of where an enlarged LN is in blue. LN DICE was 0.82.

---

837 **Accuracy and Feasibility of Portable Low-Field MRI for Acute Brain Injury: a Systematic Review and Meta-Analysis**

Mohamad Nawras MD, Thomas Esber DO, Andrew Alvarado MD, Noreen Mian BS, Tanner Graves MD, Dena Martini BS, Haitham Elsamaloty MD
University of Toledo, Toledo, OH, USA

Purpose

Acute brain injury (ABI), including ischemic stroke and intracerebral hemorrhage, is a large determinant of morbidity and mortality, particularly in intensive care unit populations. Magnetic resonance imaging (MRI) of the brain has become the cornerstone diagnostic tool for these conditions due

to its high sensitivity when compared to computed tomography (CT) [1]. However, there are many logistical factors involved with conventional MRI that may be difficult to achieve with unstable patients which puts them at a high risk for adverse events during transport. Portable low-field MRI (pMRI) addresses this very issue by offering a bedside alternative [2]. The use of pMRI has not been evaluated systematically, therefore we conducted a systematic review and meta-analysis to determine the accuracy and feasibility of pMRI.

Materials & Methods

We conducted a systematic review and meta-analysis, performing a comprehensive literature search from inception until 10/26/2025 in the following databases: PubMed, Embase, and Web of Science. We included studies that utilized pMRI for detection of ABI. The primary outcomes of our study include sensitivity and specificity of pMRI for ABI in addition to feasibility and safety of pMRI. We conducted subgroup analyses for specific type of ABI such as ischemic stroke and intracerebral hemorrhage. Pooled sensitivity, specificity, and the corresponding 95% confidence intervals (CI) were calculated using the random effect model. Heterogeneity was assessed using the Higgins I^2 index.

Results

A total of 14 studies were included in our meta-analysis which were published between the years 2020 and 2025. The pooled sensitivity of pMRI for the detection of ABI was 0.81 (95% CI: 0.72-0.88; I^2: 0.27) and the pooled specificity was 0.92 (95% CI: 0.76-0.98; I^2: 0.82) (Figure 1). Of the eight studies that reported adverse events, a total of 3 events during 445 examinations were documented. Eleven studies reported that out of a combined 802 attempted pMRI examinations, 734 patients were successfully scanned to completion.

Conclusion

Our meta-analysis demonstrates that pMRI is a promising diagnostic tool that can provide safe, reliable, and accurate imaging for the diagnosis of ABI, particularly in unstable patients. Further large-scale studies are necessary to validate our findings.

Images/Tables

Figure 1

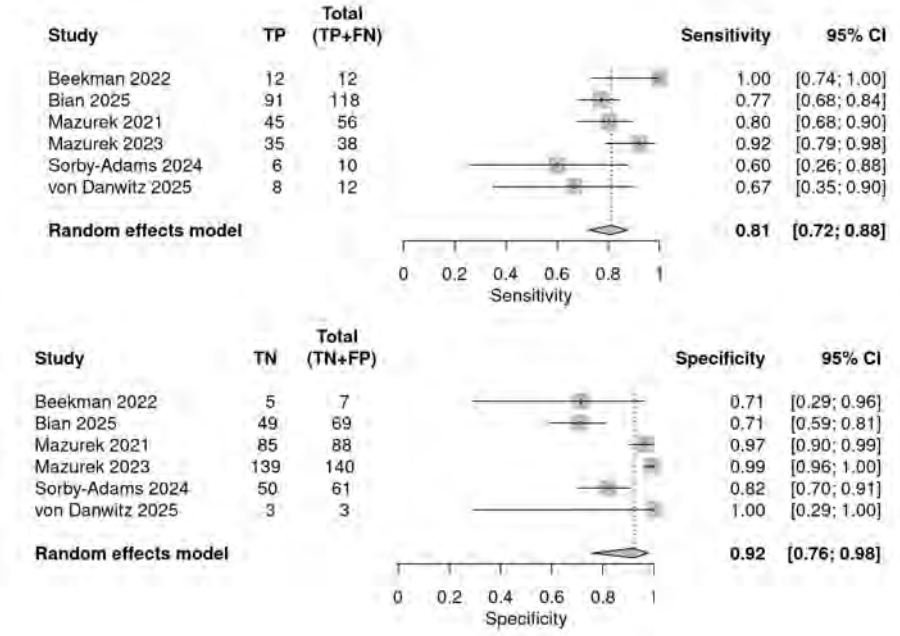

842 Using the Fazekas Score to Assess the Likelihood of Benefit from Thrombectomy in Patients with an Acute Medium Vessel Occlusion Ischemic Stroke

Andrew O Osborne MD, Cindy V Rivas, Yu Ra, Shayak Sen MD, Malak Elokour MPH, Alexis N Simpkins MD, PhD
Cedars-Sinai Medical Center, Los Angeles, CA, USA

Purpose

While endovascular thrombectomy (EVT) is established for large vessel occlusion, recent trials have not shown a benefit after EVT in the setting of medium vessel occlusion (MeVO), reporting increased symptomatic intracranial hemorrhage and mortality. These findings suggest heterogeneity within the MeVO population. The severity of white matter disease (WMD) has been associated with increased bleeding risk and worse stroke outcomes. Given the outcomes of the MeVO studies, we aimed to identify clinical factors that could influence the likelihood of benefit and safety of EVT in patients with a MeVO.

Materials & Methods

We performed a single-center retrospective review of confirmed MeVO acute ischemic stroke patients (all middle cerebral artery) between 2017-2023. Patient demographics and clinical factors were extracted (Tables 1 and 2). The Fazekas scale, a validated measure of WMD on brain imaging, was applied separately for periventricular white matter (PVWM) and deep white matter (DWM). Outcomes were assessed by discharge modified Rankin score (mRS). A good outcome was defined as an mRS 0–1. Bivariate analysis with SPSS software was used to assess significance

Results

Of the 125 subjects, the median age was 73 (interquartile range 63-86) and 6.4% had a good outcome. Age and National Institutes of Health Stroke Scale scores were predictive of favorable outcomes. When stratified by PVWM Fazekas score, a trend linked more severe PVWM disease to poor outcome (P=0.216) (Table 1). Although this did not reach statistical significance, patients with Fazekas PVWM 0–2 accounted for all 8 good outcomes, whereas none with severe PVWM disease (score = 3) achieved a good outcome at discharge (Table 1). Patients with a Fazekas DWM score of 3 did not have worse outcomes in comparison to those with a Fazekas DWM score of 0-2 (Table 2). The Fazekas score was not significantly

associated with risk of hemorrhage (Tables 1 and 2). Subgroup analysis of patients with a right hemispheric MeVO similarly had no significant difference in outcomes when stratified by severity of WMD (P = 0.59 for both Fazekas PVWM and DWM).

Conclusion

In conclusion, higher periventricular WMD burden may be associated with poor outcomes despite EVT for MeVO. While statistical significance was not achieved, likely due to limited sample size, the observed trend supports further investigation to confirm if PVWM disease burden may inform patient selection for EVT in the setting of MeVO.

Images/Tables

Table 1 Descriptive Analysis of MEVO Outcomes by PVWM Fazekas Score

Variables	n (%)	Faz PVWM 0-2	Faz PVWM 3	P value [1]
Total cohort	125	106 (84.8%)	19 (15.2%)	
Sex: (n=125)				0.012*
Male	66 (52.8%)	61 (57.5%)	5 (26.3%)	
Female	59 (47.2%)	45 (42.5%)	14 (73.7%)	
Risk factors: n=125				
Atrial Fibrillation	53 (42.4%)	42 (39.6%)	11 (57.9%)	.138
Coronary Artery/Heart Disease	23 (18.4%)	20 (18.9%)	3 (15.8%)	.750
Carotid Stenosis	2 (1.6%)	2 (1.9%)	0 (0%)	.546
Diabetes Mellitus	31 (24.8%)	28 (26.4%)	3 (15.8%)	.323
Peripheral Vascular Disease	3 (2.4%)	2 (1.9%)	1 (5.3%)	.376
Hypertension	95 (76%)	80 (75.5%)	15 (78.9%)	.744
Smoker	7 (5.6%)	5 (4.7%)	2 (10.5%)	.310
Dyslipidemia	51 (40.8%)	45 (42.5%)	6 (31.6%)	.374
Heart Failure	12 (9.6%)	11 (10.4%)	1 (5.3%)	.486
Pre-Stroke Diagnosis	22 (17.6%)	18 (17%)	4 (21.1%)	.668
Transient Ischemic Attack	5 (4%)	5 (4.7%)	0 (0%)	.334
Obesity	1 (0.8%)	1 (.9%)	0 (0%)	.671
Renal Insufficiency	5 (4%)	4 (3.8%)	1 (5.3%)	.760
Prior Medications: (n=125)				
None	59 (47.2%)	49 (46.2%)	10 (52.6%)	.607
Prior anticoagulation	41 (32.8%)	38 (35.9%)	3 (15.8%)	
Prior antiplatelets	25 (20%)	19 (17.9%)	6 (31.6%)	
Side of stroke (n=125)				
Right	48 (38.4%)	42 (39.7%)	6 (31.6%)	.163
Left	67 (53.6%)	54 (50.9%)	13 (68.4%)	
Bilateral	10 (8%)	10 (9.4%)	0 (0%)	
Stroke etiology (n=125)				
Cardioembolic	80 (64%)	66 (62.3%)	14 (73.7%)	.340
Large-artery atherosclerosis	11 (8.8%)	9 (8.4%)	2 (10.5%)	
Small-vessel disease	4 (3.2%)	4 (3.8%)	0 (0%)	
Stroke of other determined etiology	5 (4%)	5 (4.7%)	0 (0%)	
Cryptogenic	25 (20%)	22 (20.8%)	3 (15.8%)	
Type of post-stroke scan reviewed (n=125)				.287
Magnetic resonance imaging	93 (74.4%)	77 (72.6%)	16 (84.2%)	
Computed tomography	32 (25.6%)	29 (27.4%)	3 (15.8%)	
Deep involvement of stroke (n=94)				
Yes	57 (60.6%)	49 (60.5%)	8 (61.5%)	.943
No	37 (39.4%)	32 (39.5%)	5 (38.5%)	
Thrombolytic used (n=37)				.243
Alteplase	23 (62.2%)	18 (58.1%)	5 (83.3%)	
Tenecteplase	14 (37.8%)	13 (41.9%)	1 (16.7%)	
mRS at discharge (n=125)				
0-1	8 (6.4%)	8 (7.5%)	0 (0%)	.216
2-6	117 (93.6%)	98 (92.5%)	19 (100%)	
Neuroimaging within 36 hours (n=68)				
Yes				
No	4 (5.9%)	4 (7.3%)	0 (0%)	.316
	64 (94.1%)	51 (92.7%)	13 (100%)	
Fazekas PVWM (n=125)				
0	11 (8.8%)			
1	59 (47.2%)			
2	36 (28.8%)			
3	19 (15.2%)			
Fazekas DWM (n=125)				
0	22 (17.6%)			
1	49 (39.2%)			
2	31 (24.8%)			
3	23 (18.4%)			
Variables	Median (IQR)			P value [2]
Age (n=125)	72.5 (62.5, 86)	71 (62, 84)	84 (74, 90)	.004*
Initial NIHSS (n=67)	13 (9, 20)	11 (7.5, 20)	19 (15, 23)	.008*
mRS DC (n=125)	4 (3, 5)	4 (3, 5)	4 (4, 5)	.158
Time to Recanalization (min) (n=54)	182 (145, 281.5)	185 (148.9, 280)	176 (145, 185)	.554

Notes: *n*, size of sample; %, percentage; IQR, interquartile range; mRS, Modified Rankin Score; DC, Discharge; Faz, Fazekas; NIHSS: National Institute of Health Stroke Score; PVWM, Periventricular white matter; DWM, Deep white matter. [1]Chi Square test. [2]Man Whitney test. *P<0.1.

Table 2 Descriptive analysis of MEVO Outcomes by DVM Fazekas Score

Variables	n (%)	Faz DVM 0-2	Faz DVM 3	P value [1]
Total cohort	125	102 (81.6%)	23 (18.4%)	
Sex: (n=125)				
Male	66 (52.8%)	59 (57.8%)	7 (30.4%)	.017*
Female	59 (47.2%)	43 (42.2%)	16 (69.6%)	
Risk factors: n=125				
Atrial Fibrillation	53 (42.4%)	43 (42.2%)	10 (43.5%)	.908
Coronary Artery/Heart Disease	23 (18.4%)	19 (18.6%)	4 (17.4%)	.890
Carotid Stenosis	2 (1.6%)	2 (2%)	0 (0%)	.498
Diabetes Mellitus	31 (24.8%)	28 (27.5%)	3 (13%)	.148
Peripheral Vascular Disease	3 (2.4%)	2 (2%)	1 (4.3%)	.499
Hypertension	95 (76%)	78 (76.5%)	17 (73.9%)	.795
Smoker	7 (5.6%)	5 (4.9%)	2 (8.7%)	.475
Dyslipidemia	51 (40.8%)	43 (42.2%)	8 (34.8%)	.516
Heart Failure	12 (9.6%)	10 (9.8%)	2 (8.7%)	.871
Pre-Stroke Diagnosis	22 (17.6%)	16 (15.7%)	6 (26.1%)	.237
Transient Ischemic Attack	5 (4%)	2 (2%)	3 (13%)	.014*
Renal Insufficiency	5 (4%)	4 (3.9%)	1 (4.3%)	.925
Prior Medications: (n=125)				
None	59 (47.2%)	49 (48.1%)	10 (43.5%)	.692
Prior anticoagulation	41 (32.8%)	34 (33.3%)	7 (30.4%)	
Prior antiplatelets	25 (20%)	19 (18.6%)	6 (26.1%)	
Side of stroke (n=125)				
Right	48 (38.4%)	42 (41.2%)	6 (26.1%)	.324
Left	67 (53.6%)	53 (52%)	14 (60.9%)	
Bilateral	10 (8%)	7 (6.8%)	3 (13%)	
Stroke etiology (n=125)				
Cardioembolic	80 (64%)	66 (64.7%)	14 (60.9%)	.729
Large-artery atherosclerosis	11 (8.8%)	7 (6.9%)	4 (17.4%)	
Small-vessel disease	4 (3.2%)	4 (3.9%)	0 (0%)	
Stroke of other determined etiology	5 (4%)	4 (3.9%)	1 (4.3%)	
Cryptogenic	25 (20%)	21 (20.6%)	4 (17.4%)	
Type of post-stroke scan reviewed (n=125)	93 (74.4%)	74 (72.5%)	19 (82.6%)	.318
Magnetic resonance imaging	32 (25.6%)	28 (27.5%)	4 (17.4%)	
Computed tomography				
Deep involvement of stroke (n=94)				
Yes	57 (60.6%)	45 (58.4%)	12 (70.6%)	.354
No	37 (39.4%)	32 (41.6%)	5 (29.4%)	
Thrombolytic used (n=37)				
Alteplase	23 (62.2%)	18 (62.1%)	5 (62.5%)	.982
Tenecteplase	14 (37.8%)	11 (37.9%)	3 (37.5%)	
mRS at discharge 0-1 (n=125)				
0-1	8 (6.4%)	7 (6.9%)	1 (4.3%)	.656
2-6	117 (93.6%)	95 (93.1%)	22 (95.7%)	
Neuroimaging within 36 hours (n=68)				
Yes	4 (5.9%)	4 (7.3%)	0 (0%)	.316
No	64 (94.1%)	51 (92.7%)	13 (100%)	
Fazekas scoring, PVWM (n=125)				
0	11 (8.8%)			
1	59 (47.2%)			
2	36 (28.8%)			
3	19 (15.2%)			
Fazekas scoring, DWM (n=125)				
0	22 (17.6%)			
1	49 (39.2%)			
2	31 (24.8%)			
3	23 (18.4%)			
Variables	Median (IQR)			P value [2]
Age (n=125)	72.5 (62.5, 86)	71 (62, 83)	84 (71, 90)	.005*
Initial NIHSS (n=67)	13 (9, 20)	11 (7.5, 20)	17 (13, 21)	.051*
Time to Recanalization (min) (n=54)	182 (145, 282)	182 (145, 283)	182 (161, 208)	.971
mRS DC (n=125)	4 (3, 5)	4 (3, 5)	4 (4, 5)	.437

Notes: *n*, size of sample; %, percentage; IQR, interquartile range; mRS, Modified Rankin Score; DC, Discharge; Faz, Fazekas; min, minutes; NIHSS: National Institute of Health Stroke Score; PVWM, Periventricular white matter; DWM, Deep white matter; [1]Chi Square test. [2]Man Whitney test. *P<0.1.

---

864 Real-World Evaluation of AI-Assisted Vessel Occlusion Detection in a Regional Stroke Center

Juan E Ortega MD

Bayhealth Hospital, Dover, DE, USA

Purpose

This study aimed to assess the clinical impact of deploying an FDA-cleared artificial intelligence (AI) algorithm for vessel occlusion (VO) detection (Aidoc, Tel Aviv, Israel) at a regional stroke center. Previous studies have demonstrated that AI-assisted analysis of CT angiography can improve sensitivity and efficiency for detecting vessel occlusions, supporting its integration into clinical workflows.1,2We hypothesized that implementation of the AI algorithm would increase the detection rate of vessel occlusions and reduce the number of missed cases in a real-world setting.

Materials & Methods

Consecutive head and neck CTA exams were retrospectively reviewed by the solution. A retrospective review of 385 consecutive head and neck CTA exams processed by the AI algorithm was performed over a 2.5-month period (September 25–December 5, 2023). Ground truth was established by radiologist review and adjudication of discordant findings. AI performance was assessed against this ground truth using sensitivity, specificity, PPV, and NPV with 95% confidence intervals. Enhanced detection rate was analyzed after false positive review.

Results
A total of 385 cases were analyzed by the solution. The prevalence was found to be 12.5% (48/385). The Aidoc solution achieved a sensitivity of 86.0% (95% CI: 73.3-94.2) and specificity of 98.5% (95% CI: 96.6-99.5), with PPV 89.6% (95% CI: 78.2-95.4) and NPV 97.9% (95% CI: 96.0-98.9). 19 potential misses (AI+/NLP-) were identified, of which 73.7% (14/19) were confirmed as undocumented vessel occlusions. The enhanced detection (ED) rate was calculated at 37.8%.
Conclusion
The AI solution demonstrated an enhanced detection rate potentially enabling a higher diagnostic yield for AI assisted radiologists for the detection of vessel occlusions. The solution maintained high sensitivity and specificity on real-world data, supporting the role of AI-assisted detection in optimizing stroke workflows, particularly within regional centers with varied presentation patterns.
Images/Tables

Table 1.0: Performance metrics for the AI model in detecting target pathology

Accuracy Metrics		CI 95%	
		CI lower	CI upper
Sensitivity	86.0%	73.3%	94.2%
Specificity	98.5%	96.6%	99.5%
Positive Predictive Value	89.6%	78.2%	95.4%
Negative Predictive Value	97.9%	96.0%	98.9%
Accuracy	96.9%	94.6%	98.4%

---

872 **Treatment Failure in Middle Meningeal Artery Embolization Compared to Burr Hole and Craniectomy for Chronic Subdural Hematoma**
Sawyer Archer[1], Truman Archer[1], Holden Archer MD[2]
[1]Texas Tech University Health Sciences Center, Amarillo, Texas, USA. [2]University of Texas Southwestern Medical School, Dallas, Texas, USA
Purpose
Chronic subdural hematoma (CSDH) is a prevalent neurological condition, particularly among the elderly, and is commonly managed with surgical evacuation via burr hole or craniotomy. Despite widespread use, these approaches carry recurrence rates of 10–30% and substantial morbidity. Middle meningeal artery embolization (MMAE) has emerged as a minimally invasive alternative shown to reduce recurrence when used as an adjunctive therapy. However, outcomes following primary MMAE remain underexplored in large populations. This study evaluated mortality, recurrence, and reoperation rates in patients with CSDH treated with MMAE compared with conventional surgical approaches across multiple time endpoints.
Materials & Methods
A retrospective propensity-matched cohort study was conducted using a large national database. Adult patients with nontraumatic CSDH treated with either MMAE, burr hole evacuation, or craniectomy/craniotomy were included. Cohorts were identified via ICD and CPT codes for MMAE, burr hole evacuation, or craniectomy/craniotomy. Propensity matching was performed based on demographics, comorbidities, and laboratory values. Outcomes including all-cause mortality, cerebral infarction, subsequent CSDH-related procedures, and acute subdural hematoma diagnosis were compared at 1-, 3-, 6-, 12-, 24-, and 36-month intervals. Secondary analyses assessed outcomes following MMAE stratified by age (18–65, 65–80, and >80 years).
Results
After propensity matching, 2,678 patients were included in the MMAE vs burr hole comparison and 2,629 in the MMAE vs craniotomy/craniectomy comparison with balanced demographic and clinical characteristics. Compared with burr hole evacuation, patients treated with MMAE demonstrated significantly lower overall rates of future operative management (relative risk [RR] 0.20–0.60, $p<0.0001$) and lower mortality beginning at six months (RR 0.84, 95% CI 0.71–0.99, $p=0.046$). However, the MMAE cohort exhibited a modestly higher risk of cerebral infarction at one year (RR 1.18, 95% CI 1.01–1.38, $p=0.03$). Compared with craniectomy/craniotomy, MMAE was associated with significantly lower mortality (RR 0.50–0.76 across timepoints), fewer repeat embolization or operative procedures (RR 0.24–0.68), and reduced cerebral infarction risk after six months. Patients undergoing MMAE were more likely to require subsequent burr hole evacuation (RR 2.75–3.29).
Age-stratified analysis of 2,638 MMAE patients revealed consistent reoperation rates across age groups but expected age-related increases in mortality (10.4% for 18–65 years vs 17.6% for >80 years at 36 months). Stroke incidence varied modestly between groups, with no significant differences in recurrence or acute hematoma formation.
Conclusion
In this large, multicenter analysis, primary MMAE for nontraumatic CSDH was associated with significantly lower mortality and reoperation rates compared with both burr hole evacuation and craniotomy/craniectomy. Outcomes were consistent across age strata, supporting MMAE's safety and efficacy as a minimally invasive alternative to surgical evacuation. These findings reinforce MMAE's potential to redefine the standard of care for CSDH management.

895 Machine learning and functional connectivity for disambiguating unipolar and bipolar depression

Alexander Lu[1], Licia Luna MD, PhD[2]

[1]Johns Hopkins University School of Medicine, Baltimore, MD, USA. [2]Johns Hopkins University Department of Radiology and Radiological Sciences, Baltimore, MD, USA

Purpose

The challenge of accurate differentiation between unipolar depression and bipolar disorder at first clinical presentation can lead to inappropriate treatment selection and poorer long-term outcomes.[1] There is an urgent clinical need for accurate biomarkers that can inform treatment decisions. Prior neuroimaging studies have shown that resting-state functional connectivity patterns differ between unipolar and bipolar depression, with evidence for altered activity in fronto-limbic and default mode networks, as well as changes in temporal variability of the BOLD signal[2] . Despite the potential of these novel imaging biomarkers, most studies have been limited by small sample sizes with hand-crafted metrics that may not fully capture clinically relevant time-varying dynamics.[2,3] Towards this end, this work proposes the development and evaluation of recurrent neural networks for classification of resting-state functional magnetic resonance images (rs-fMRI) between healthy controls, major depressive disorder (MDD), and bipolar disorder (BPD).

Materials & Methods

The proposed approach uses a long-short term memory (LSTM) recurrent neural network to encode the time-varying nature of the BOLD signal. As input, this network operates on the BOLD signal derived from parcellated fMRI regions-of-interest (ROIs), concatenated with the embedded temporal coordinate and, optionally, embedded clinical variables (age, gender). This approach allows dynamic time series resampling, enabling data augmentation and input harmonization for time series of differing lengths and sampling frequencies.

The proposed architecture was trained and evaluated using a dataset composed of resting-state fMRI images and associated structural images from multiple open-source datasets, totaling 1277 patient images (912 healthy controls, 269 MDD, 96 BPD). All sequences were input to a preprocessing pipeline that reduced slice timing and motion artifacts, followed by denoising, resampling to 2mm isotropic voxel size, smoothing, and ROI parcellation according to the Schaefer 2018 400 ROI atlas. The proposed architecture was trained on an Nvidia RTX A6000 GPU for 60 epochs, optimizing the cross-entropy loss using the Adamw optimizer with a learning rate of 0.00003. This approach was compared against non-neural baselines, including gradient boosting classifier (GBC) and support vector classifier (SVC).

Results

The LSTM classifier achieved the highest test F1 score (0.50) compared to GBC (0.42) and SVM (0.29), as well as the highest accuracy (0.74), compared to GBC (0.528) and SVM (0.71). The addition of clinical variables (age, gender) did not improve classification accuracy, as plotted in the attached Figure 1c.

Conclusion

The classification of resting-state fMRI with the proposed LSTM architecture offers a promising approach for improved diagnostic clarity in patients presenting with a depressive episode, outperforming traditional machine learning methods. The capacity for integrating multiple data sources, leveraging time series processing, demonstrates the potential for multi-institutional deployment and generalization.

Images/Tables

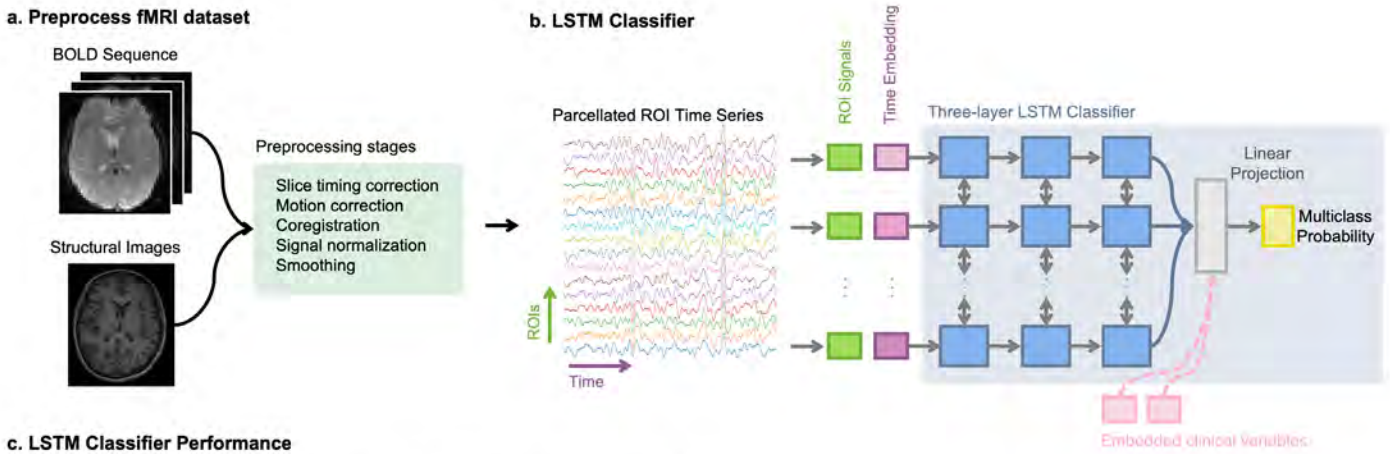

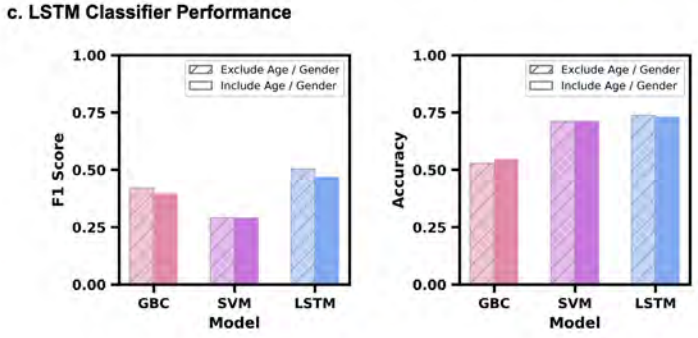

896 Maturation of the Glymphatic System in Childhood: Insights from the DTI-ALPS Index and Choroid Plexus Volume in 537 normal subjects

Arim Pak MD, Moonjung Hwang PhD, Sung-Hye You MD, PhD, Byungjun Kim MD, PhD, Bo Kyu Kim MD, PhD, Jae Ho Shin MD, PhD
Korea University Anam Hospital, Seoul, Seoul, Korea, Republic of

Purpose

The developmental trajectory of the glymphatic system in pediatric populations remains poorly characterized. This study aimed to investigate age- and sex-related maturation patterns of the glymphatic system in individuals under 20 years of age using the Diffusion Tensor Image Analysis Along the Perivascular Space (DTI-ALPS) index and choroid plexus volume (CPV).

Materials & Methods

This retrospective study included 537 neurologically normal participants (275 males, 262 females; age range, 0–20 years) who underwent brain MRI, including diffusion tensor imaging (DTI) and three-dimensional T1-weighted imaging (3D T1WI). The DTI-ALPS index, CPV, and intracranial volume (ICV) were calculated. Age-related trends and inflection points were analyzed with segmented linear regression.

Results

The DTI-ALPS index gradually increased in participants under 20 years of age. In the segmented regression model, an inflection point separating the rapid and stable maturation phases was identified at 5.45 years (DTI-ALPS = 1.439) in the total cohort, at 5.33 years in girls (DTI-ALPS = 1.439), and at 8.39 years in boys (DTI-ALPS = 1.422). The CPV-to-ICV ratio (CIR) decreased progressively until 14.58 years ($p < 0.001$) and was negatively correlated with the DTI-ALPS index in the lower ALPS range (≤ 1.61; $\beta = -0.098$, $p < 0.001$), a pattern consistent across sexes.

Conclusion

Glymphatic function measured by the DTI-ALPS index matures rapidly in early childhood, with the early rapid phase lasting longer in boys than in girls, and transitions to a stable phase by early adulthood. CIR declines until mid-adolescence. These age- and sex-specific patterns provide new insights into normal pediatric brain development.

Images/Tables

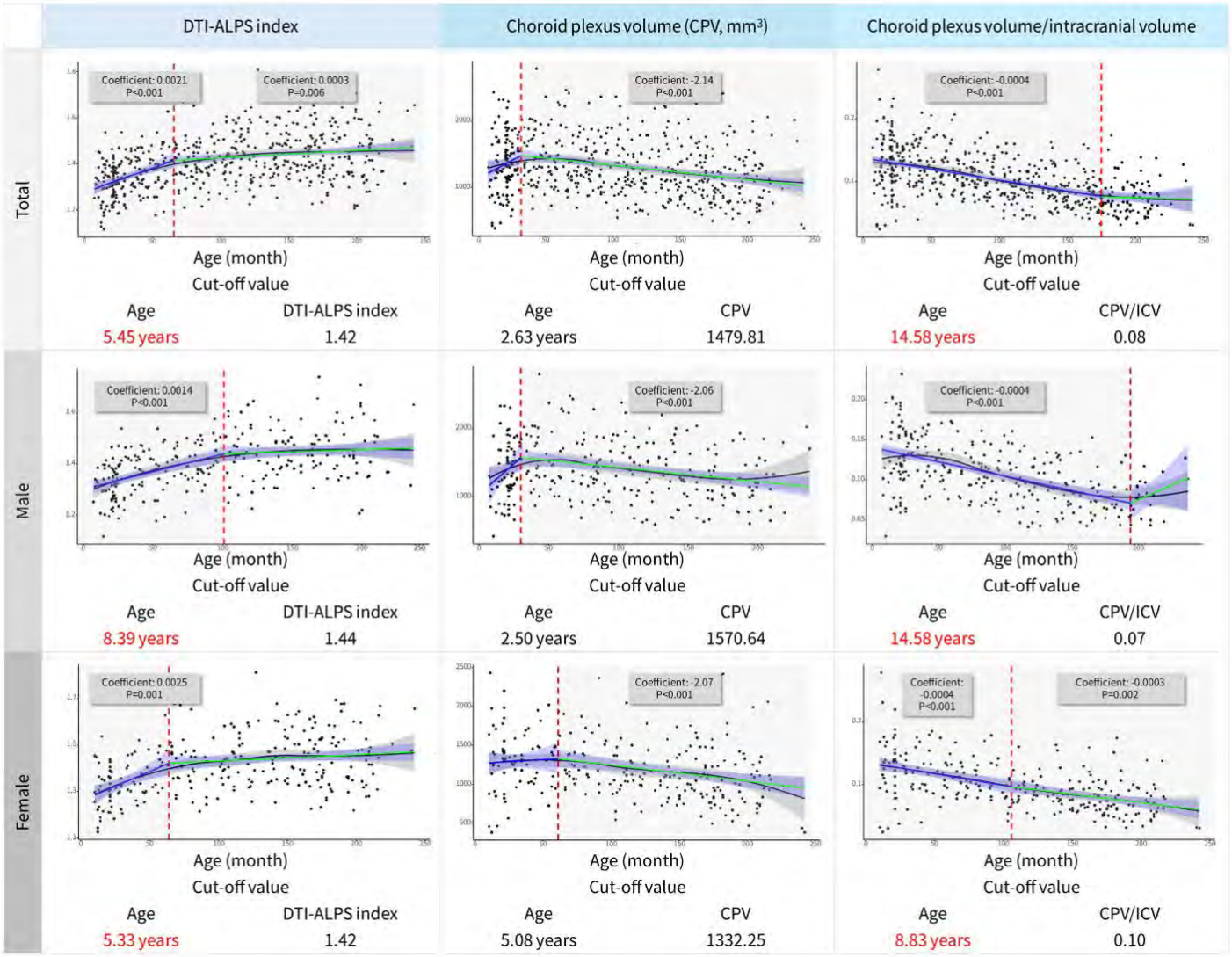

897 Association of long-term exposure to lower low-density lipoprotein cholesterol with neuroimaging metrics: a population-based cohort study

Han Lv Dr., Jing Sun Dr.
Department of Radiology, Beijing Friendship Hospital, Capital Medical University, Beijing, Beijing, China

Purpose

Limited evidence exists regarding the relationship between long-term exposure to low concentrations of low-density lipoprotein cholesterol (LDL-C) and brain structural integrity. This study aimed to examine the associations of cumulative low LDL-C exposure with a series of neuroimaging metrics.

Materials & Methods

This study included 987 participants (median age 55 years) from a population-based cohort study in China. Serum circulatory LDL-C concentrations were assessed biennially from 2006 to 2018. Prolonged LDL-C exposure was calculated using a time-weighted average (TWA) approach during that period. Brain MRI examinations were performed during 2020-2022. We used generalized linear model to investigate the multivariate-adjusted associations of TWA LDL-C levels with MRI markers of brain tissue volume, white matter microstructural integrity, and white matter hyperintensity (WMH).

Results

After full adjustments, TWA LDL-C concentrations of 70-100 mg/dL and less than 70 mg/dL were associated with lower fractional anisotropy value and higher mean diffusivity, axial diffusivity, and radial diffusivity value compared to LDL-C concentrations of 100-130 mg/dL. These associations were particularly prominent in male participants and older participants who were over 50 years. No association was found between relatively lower LDL-C levels and brain tissue volumes or WMH.

Conclusion

LDL-C concentrations of 70-100 mg/dL and < 70 mg/dL are associated with impaired microstructural integrity of brain white matter.

Images/Tables

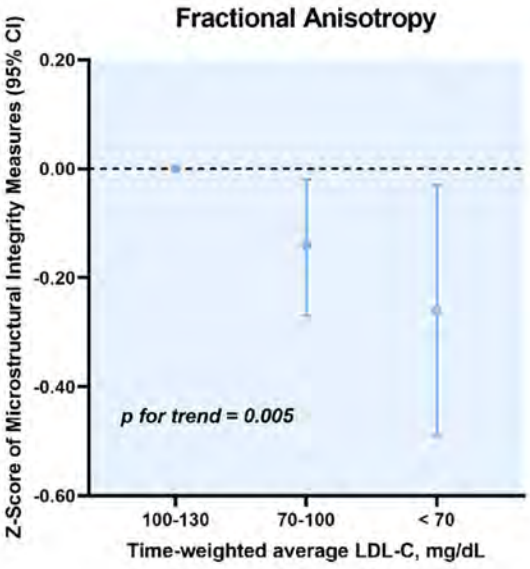

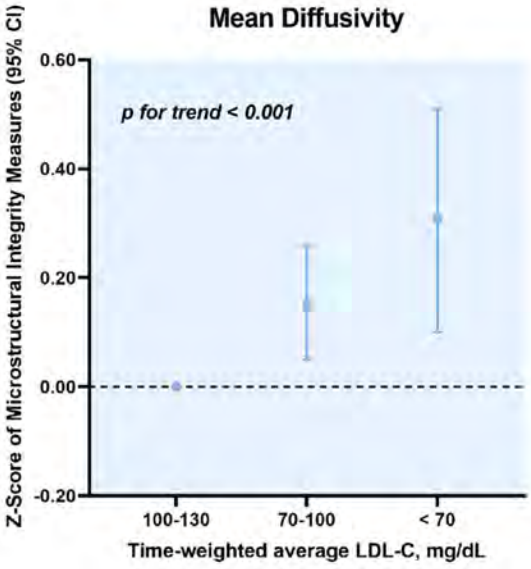

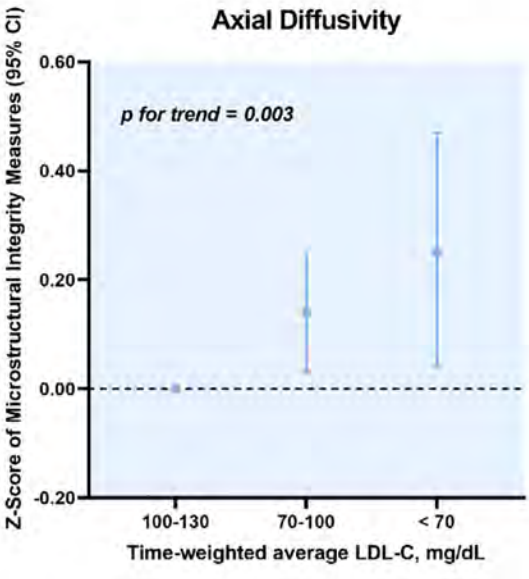

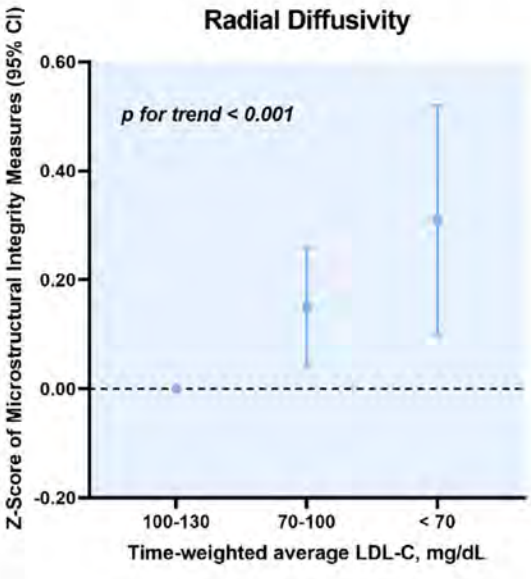

921 Comparison of Percent Signal Change in Meningeal Glymphatic Flow Using IR-ALADDIN among Young, Elderly, and Alzheimer's Disease Groups

Sung-Hye You MD, PhD, Moonjung Hwang PhD, Byungjun Kim MD, PhD, Bo Kyu Kim MD, PhD, Jae Ho Shin MD, PhD
Korea University Anam Hospital, Seoul, Seoul, Korea, Republic of

Purpose

To compare the percent signal change (PSC) of meningeal glymphatic flow among young, elderly, and Alzheimer's disease (AD) groups using inversion recovery–alternating labeling with null recovery (IR-ALADDIN), a noncontrast MRI sequence designed for visualizing meningeal lymphatic vessels.

Materials & Methods

This retrospective single-center study included 48 participants—30 young healthy volunteers, 12 cognitively normal older adults, and 6 patients with AD—examined between December 2024 and July 2025. IR-ALADDIN scans were acquired within 2 minutes 27 seconds for a single inversion time (TI = 2300 ms) using five slices (5-mm thickness). A MATLAB-based post-processing pipeline was used to calculate PSC as PSC=(Ascending - Descending)/Baseline ×100, where ascending and descending images represent posterior to anterior and anterior to posterior flow directions, respectively. Statistical comparisons were performed using the Games–Howell post hoc test.

Results

The mean PSC of meningeal glymphatic flow was 10.1 ± 6.3% in the young group, 18.7 ± 7.6% in the elderly group, and 14.3 ± 5.5% in the AD group (p = 0.001). The elderly group showed significantly higher PSC than the young group ($p < 0.01$), whereas the AD group exhibited a slightly lower trend compared with the elderly group. PSC demonstrated a moderate positive correlation with age ($r = 0.45$, $p = 0.001$).

Conclusion

IR-ALADDIN enables rapid, noncontrast quantification of meningeal glymphatic flow. PSC increased with aging, suggesting an adaptive lymphatic response to metabolic waste accumulation; however, the attenuated increase in AD may indicate impaired lymphatic compensation related to neurodegeneration.

Images/Tables

Comparison of percent signal change (%) of meningeal glymphatic flow in IR-ALADDIN

Variable	Young-age (n=30)	Old-age (n=12)	Alzheimer's disease (n=6)	p-value	Post hoc (Games–Howell)
Age (years)	26.53 ± 1.99	74.67 ± 7.05	69.83 ± 11.44	<0.001	YA < OA*** YA < AD***
Baseline signal	575.98 ± 107.47	502.60 ± 123.70	499.80 ± 117.18	0.098	NS
Ascending – descending (up)	55.15 ± 31.32	95.30 ± 47.59	68.46 ± 22.39	0.007	YA < OA*
Percent signal change (%)	10.08 ± 6.30	18.69 ± 7.55	14.27 ± 5.45	0.001	YA < OA**

924 Evaluating an Open-Source Large Language Model for Dementia FDG PET Report Annotation

Tanush Fatterpekar, Timothy M Shepherd, Siddhant Dogra
NYU Langone Health, New York, NY, USA

Purpose

With increasing use of FDG PET in dementia evaluation, large, well-labeled datasets with confidently established imaging diagnoses are needed to support research and model development.[1] Large language models (LLMs) can extract diagnosis labels from reports, but FDG PET interpretation is challenging given the lack of tissue-based reference standards and variability in radiologist confidence.[2] Reliance on commercial LLMs poses data-privacy concerns.[3] This study assessed whether a locally-deployed, open-source LLM could extract dementia-related diagnostic information, including the radiologist's expressed diagnostic confidence, from FDG PET reports compared with expert human annotation.

Materials & Methods

All 2023 FDG PET reports from a single institution were included in this retrospective study. The history and impression sections were provided to two independent readers who answered four questions:

1) Exam indication (dementia / epilepsy / other)

2) For dementia cases, whether there were abnormalities suggestive of neurodegenerative disease

3) If suggestive of neurodegenerative disease, was there a single diagnosis confidently expressed, a favored diagnosis with other possibilities or mixed confidence, or multiple differentials without a favored diagnosis?

4) If a single or a favored diagnosis was given, what was it?
The same information and questions were provided to Qwen-3-32B, an open-source LLM executed locally via vLLM. Model outputs were compared to reader annotations. Analyses included inter-reader agreement for questions where both readers gave answers, LLM performance on cases with full reader consensus, and stratified evaluation by reader and model confidence levels.

Results

Two readers independently annotated 1,016 FDG PET reports. Inter-reader agreement was 96.9% (κ = 0.89) for indication, 89.5% (κ = 0.76) for abnormality, 71.6% (κ = 0.53) for three-level confidence, and 99.1% (κ = 0.98) for diagnosis, when considering questions where both readers gave answers. When considering all cases where either reader provided a diagnosis, inter-reader diagnostic agreement was 72.8% (348/478). When confidence was binarized (favored diagnosis versus no clear diagnosis), human agreement improved to 83.6% (κ = 0.58).

LLM achieved near-human accuracy across all categorical tasks. On cases with full human consensus, model performance was 97.3% (κ = 0.90) for indication, 94.3% (κ = 0.85) for abnormality, 52.8% (κ = 0.30) for three-level confidence, 83.6% (κ = 0.40) for binarized confidence, and 99.4% (κ = 0.99) for diagnosis.

When the model expressed its highest confidence (single confident diagnosis), diagnostic predictions matched both readers in 94.3% (149/158) of cases. Including cases graded as “favored diagnosis with other possibilities or mixed confidence” yielded 61.7% (339/549) agreement of model predictions with both readers.

Conclusion

A locally executed open-source LLM (Qwen-3-32B) accurately reproduced human interpretation of dementia-related FDG PET radiology reports, achieving near-human performance for indication, abnormality, and diagnosis while preserving full data privacy. At high confidence thresholds, the model’s diagnostic predictions aligned almost entirely with both readers, reflecting reliable, well-calibrated certainty. At moderate confidence thresholds, performance decreased, paralleling regions of greater human variability. Open-source LLMs may thus enable secure, transparent large-scale curation of dementia FDG PET datasets.

Images/Tables

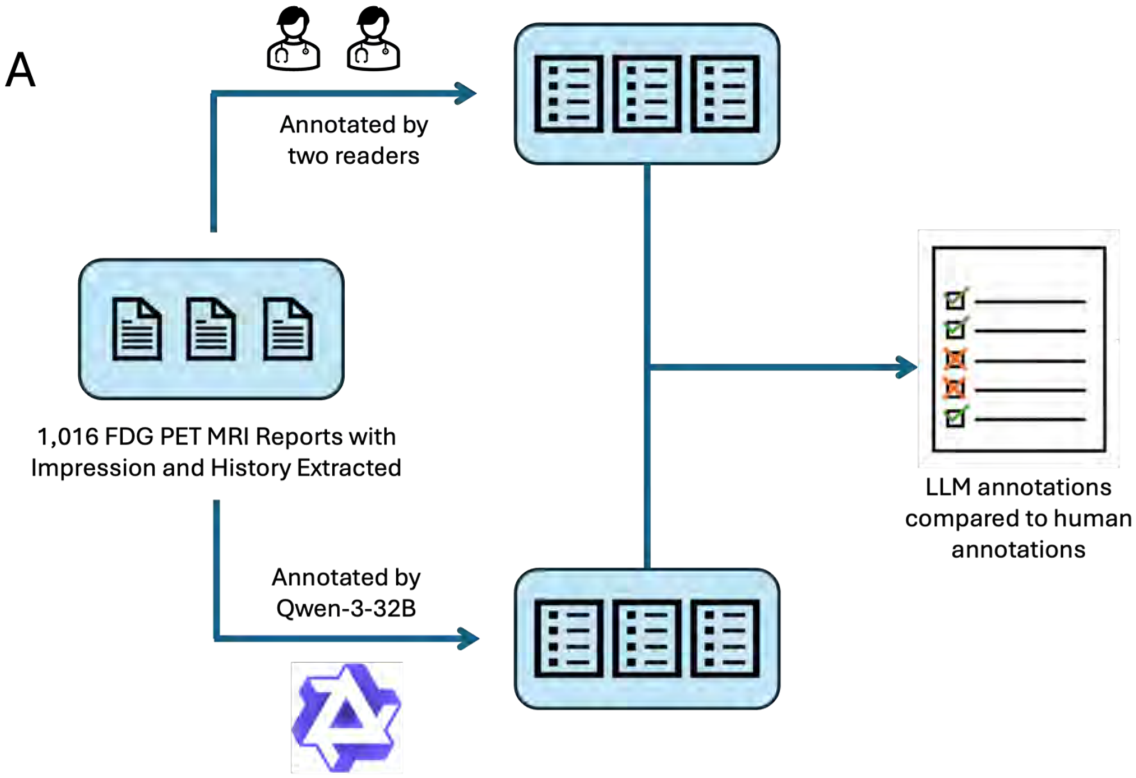

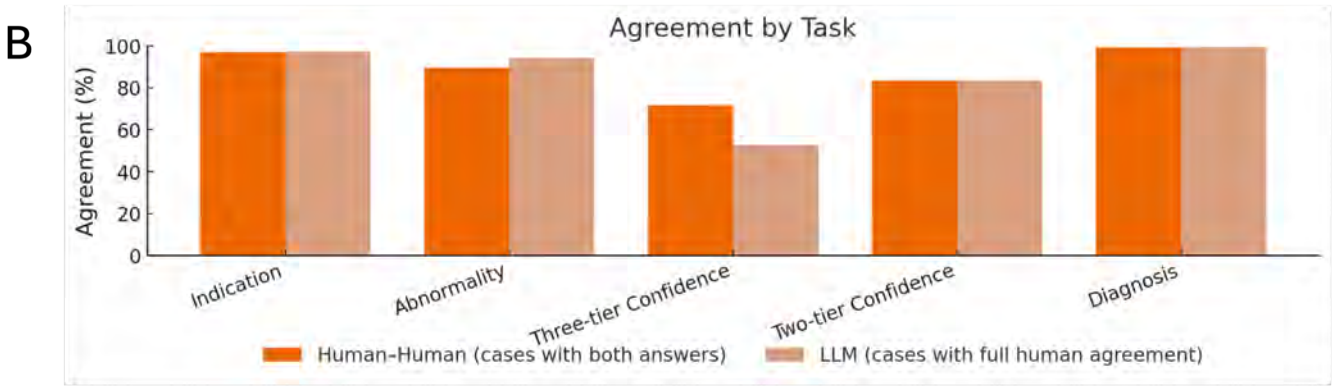

935 Empowering Neuroradiology in Underserved Settings: SRGAN-Driven Denoising and Super-Resolution for Low-Field Brain MRI

Vipul Kaliraman MBBS[1], Aditya Duhan MD[2], FNU Vaibhav MBBS[3], Pardeep Kumar MBBS[3], Ankit LNU MBBS[4], Deepak Jaglan MD[5], Rajat Kaushik MBBS[3]
[1]Maulana Azad Medical College, New Delhi, Delhi, India. [2]University of Colorado, Denver, Colorado, USA. [3]Pt. B.D. Sharma PGIMS, Rohtak, Haryana, India. [4]Northern Lincolnshire and Goole NHS Foundation Trust, Grimsby, Grimsby, United Kingdom. [5]AMA School of Medicine, Makati, Manila, Philippines

Purpose

Low-field magnetic resonance imaging (MRI) systems in resource-limited settings often produce low-resolution, noisy images due to reduced signal-to-noise ratio and Rician artifacts, compromising neuroradiologic assessment of brain pathology, including atrophy, lesions, and vascular abnormalities. This study aimed to develop and evaluate an adapted super-resolution generative adversarial network (SRGAN) framework for 4x enhancement of brain MRI, incorporating MRI-specific denoising to simulate and mitigate low-field conditions, ultimately improving diagnostic quality and promoting equitable neuroradiologic care in underserved populations.

Materials & Methods

Utilizing the Open Access Series of Imaging Studies (OASIS-1) dataset, comprising 434 T1-weighted MRI sessions from 416 subjects aged 18-96 (including 100 with mild to moderate Alzheimer's disease), we preprocessed images to grayscale, normalized intensities to [0,1], and generated low-resolution (64×64) pairs via 4x bicubic downsampling from high-resolution (256×256) slices. Data augmentation included flips, rotations, Gaussian noise, brightness/contrast adjustments, gamma correction, blur, and elastic transformations. The dataset was stratified and split into training (70%), validation (15%), and test (15%) sets.

The SRGAN model was modified for single-channel grayscale input: the generator featured an initial 9×9 convolution (64 filters), 16 residual blocks, sub-pixel 4x upsampling, and final convolution; the discriminator included eight convolutional layers with LeakyReLU and batch normalization. Losses combined adversarial, perceptual (VGG16-adapted), mean squared error, and total variation terms. Training used Adam optimization (learning rate 5e-5) with a schedule over 240 epochs.

Extensions simulated low-field Rician noise (σ levels: low 0.02-0.04, medium 0.05-0.08, high 0.08-0.12) and integrated a U-Net denoiser (encoder-decoder with skip connections) trained on noisy-clean pairs. The pipeline denoised inputs before super-resolution. Evaluation on the test set used peak signal-to-noise ratio (PSNR), structural similarity index (SSIM), mean squared error (MSE), and normalized cross-correlation (NCC), with paired t-tests, confidence intervals, and effect sizes for statistical rigor.

Results

Baseline SRGAN achieved PSNR of 26.77 dB, SSIM of 0.799, MSE of 0.002185, and NCC of 0.964 on clean test data, demonstrating effective upsampling while preserving neuroradiologic details, such as cortical sulci and ventricular contours. Under simulated Rician noise, performance declined: medium-level noise yielded PSNR of 21.90 dB (-4.87 dB), SSIM of 0.435, MSE of 0.006540, and NCC of 0.912.

The standalone denoising extension improved medium-noise inputs to a PSNR of 25.75 dB (+3.85 dB). The integrated pipeline restored super-resolved images to PSNR 24.57 dB, SSIM 0.680, MSE 0.003551, and NCC 0.941—gaining +2.67 dB PSNR and +0.245 SSIM over noisy SRGAN ($p<0.01$, Cohen's $d>0.7$). Metric correlations exceeded $r = 0.85$, confirming consistency.

Conclusion

This SRGAN adaptation with a denoising pipeline effectively enhances low-resolution, noisy brain MRI, approximating high-field quality and addressing neuroradiologic challenges in resource-limited settings. The improvements in PSNR and SSIM under simulated low-field conditions suggest the potential to detect subtle pathologies better, fostering equitable access to advanced neuroimaging. Future clinical validation in diverse populations is warranted to translate these findings into practice.

Images/Tables

939 **Many Faces of Pilocytic Astrocytoma: A Retrospective Analysis Demonstrating Diverse Radiological Presentations**

Raghav Jindal MBBS, Arpita Sahu MD
TATA Memorial Centre, Mumbai, Mumbai, Maharashtra, India

Purpose

Pilocytic astrocytoma (PA) is the most common brain glioma in children, classified as WHO Grade I. While the classical presentation is a well-circumscribed cystic lesion with an enhancing mural nodule, PA demonstrates remarkable imaging heterogeneity depending on anatomical location. This educational case series illustrates the diverse radiological presentations of PA across multiple locations to enhance diagnostic recognition.

Materials & Methods

We did a retrospective case analysis of 25 histologically proven pilocytic astrocytoma from our tertiary institutional database showing variable radiological features within and spanning multiple anatomical locations, including the optic chiasma, cerebellum, tectal plate, hypothalamus, brainstem, spinal cord, and supratentorial regions. Also, beyond the classic cystic-nodular pattern, in our analysis we found various atypical features including solid enhancement patterns, calcifications, hemorrhagic components, and multifocal presentations that posed diagnostic challenges.

Results

All cases underwent comprehensive MRI evaluation with conventional and advanced sequences, including MR spectroscopy and perfusion analysis to aid in accurate diagnosis. Cases were selected to demonstrate atypical presentations that diverge from classic imaging patterns.

Case no 1: Rare presentation showing post operative fusiform cord enlargement with associated syringomyelia, demonstrating residual intramedullary location of tumor in the cervico-dorsal region of spinal cord.

Case no 2: Illustrating the predilection for optic pathway involvement and potential for involvement of surrounding cerebral hemispheres mimicking high-grade gliomas.

Case no 3: Distinctive midline presentation involving tectal plate causing upstream obstructive hydrocephalus, often requiring CSF diversion prior to tumor management.

Case no 4: Representing medullary involvement with a very rare sight of hemorrhagic products within the tumor.

Conclusion

Pilocytic astrocytoma exhibits considerable imaging heterogeneity, extending beyond the traditional cystic lesion with an enhancing mural nodule. Recognizing location-specific presentations is essential for accurate diagnosis, particularly in cases that may resemble higher-grade gliomas. This series underscores the importance of including pilocytic astrocytoma in the differential diagnosis of pediatric brain tumors across all anatomical locations, even when imaging characteristics appear atypical. Understanding these diverse presentations is crucial for appropriate surgical planning and patient management.

Images/Tables

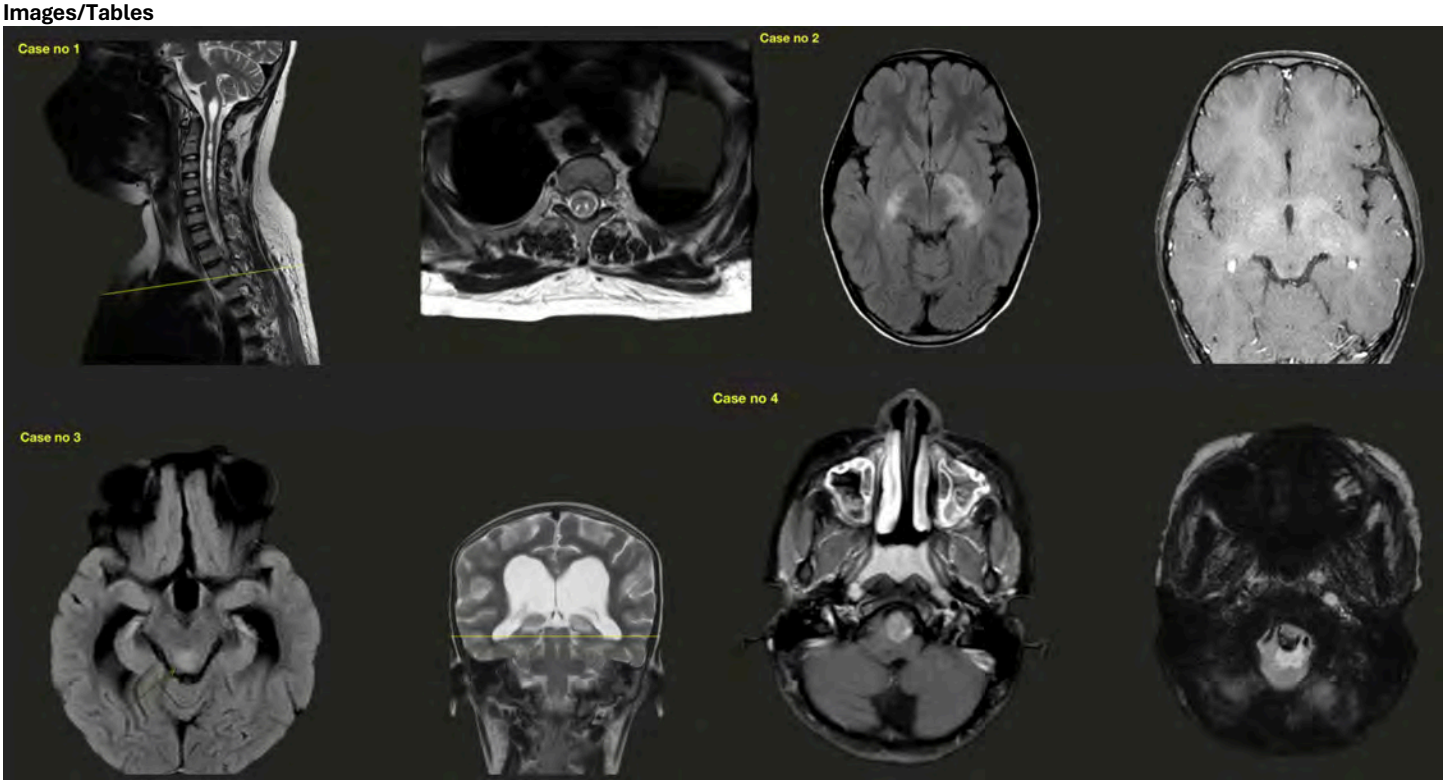

995 Real-World Clinical Performance and Diagnostic Discordance of Commercial AI Algorithms for Acute Stroke Imaging

Joao Jabbur Stern MD[1], Mahmoud Omar MD[1], Charit Tippareddy MD[1], Alex You[2], Jennifer Sommer DO[1]
[1]University Hospitals, Cleveland, OH, USA. [2]Northeast Ohio Medical University, Rootstown, Ohio, USA

Purpose

As multiple artificial intelligence (AI) vendors are now available for worklist prioritization and diagnostic assistance in acute stroke imaging, real-world comparative data across institutions are needed to guide clinical adoption. This single-institution, multi-site study retrospectively sought to compare the diagnostic accuracy and clinical efficiency of two commercially available AI platforms (RapidAI and Aidoc), against the final dictated radiology report (ground truth) for critical neurovascular findings, large vessel occlusion (LVO) and intracranial hemorrhage (ICH), in a high-volume clinical setting.

Materials & Methods

This retrospective study included 2700 patients across 12 sites (utilizing 27 CT scanners from various vendors) who underwent non-contrast head CT (NCCT) alone or non-contrast head CT plus CT angiography (CTA) of the head and neck for suspected stroke over a six-month period (04/2025 – 10/2025), during which RapidAI and Aidoc were clinically implemented. For each examination, the binary AI outputs (positive/negative) from RapidAI and Aidoc were recorded for LVO (on CTA) and ICH (on NCCT). Medium vessel occlusions (MeVO) detected by Aidoc were analyzed separately. The final radiology report served as the reference standard. Diagnostic performance (sensitivity, specificity, NPV, PPV) was calculated. Clinical efficiency was assessed by comparing timestamps (ExamEndTime, FinalReportTime, AIOutputTime). AI latency (Exam End to AI Output) was compared using a paired t-test, and diagnostic concordance was assessed using McNemar's test.

Results

Preliminary analysis included 856 NCCT and 505 CTA for stroke. A total of 209 examinations were not successfully processed by the RapidAI system due to workflow integration failures. These failures included 5 true positive LVO and 7 true positive ICH cases. Aidoc failed to process 1 true positive LVO and 3 true positive ICH cases. The preliminary cohort contained 20 LVO and 36 ICH cases. Analysis of diagnostic discordance on true positive cases revealed that for ICH, Aidoc correctly identified 6 cases that RapidAI missed. Conversely, for LVO, RapidAI correctly identified 1 case that Aidoc missed. Mean latency from Exam End to AI Output was -32 seconds for RapidAI vs. 1.97 minutes for Aidoc. The average time from AI Output to Final Report was 24.67 min for RapidAI vs. 24.42 min for Aidoc.

Conclusion

Both AI platforms demonstrated high diagnostic accuracy for acute stroke findings. While AI output latency differences did not significantly impact overall report turnaround time, a critical difference emerged in case capture and processing compliance. RapidAI's direct modality integration resulted in 209 failed cases, including 12 true positives (5 LVO, 7 ICH), highlighting susceptibility to human workflow variance and potential patient harm. In contrast, Aidoc's integration via a PACS router and orchestrator had significantly fewer processing failures, ensuring more consistent deployment. These findings suggest that AI's integration architecture could be a more crucial factor than raw processing speed for optimizing time-critical stroke triage and ensuring reliable AI utilization, particularly within a highly complex health care system spanning multiple sites and numerous scanners.

Images/Tables

Figure 1: Flowchart of data and workflow integration

Metric	RapidAI (LVO)	Aidoc (LVO)	RapidAI (ICH)	Aidoc (ICH)
Sensitivity (%)	92.8	88.2	75.0	93.7
Specificity (%)	96.0	97.9	97.5	98.1
NPV (%)	99.9	99.8	99.4	99.8
PPV (%)	22.0	34.9	42.9	54.5

Table 1: Preliminary performance statistics

1000 CT Percent Insular Ribbon Infarction (PIRI) Score Reflects Stroke Severity, Hemisphere-Specific Outcomes, and Prognosis in Insular Involvement

Utarat Kaewumporn M.D., Rehab Naeem Khalid M.D., Ok Kyu Song M.D., Alessia Guarnera M.D., Robert W. Regenhardt M.D., Ph.D., Rajiv Gupta M.D., Ph.D., Michael H Lev M.D., Joel Kevin Raj Samuel MBBS, M.D.
Massachusetts General Hospital, Harvard University, Boston, MA, USA

Purpose

The insular cortex is a key regulator of autonomic and sensorimotor function, yet most evidence linking insular injury to outcome has relied on MRI. This study assessed whether a simple CT-based Percent Insular Ribbon Infarction (PIRI) score correlates with neurological severity (NIHSS), functional outcomes (mRS), and hemisphere-specific complications in middle cerebral artery (MCA) and internal carotid artery (ICA) territory stroke involving the insular region.

Materials & Methods

Thirty-one patients (10 right-sided, 21 left-sided) with acute ischemic stroke involving the insular cortex were evaluated on admission noncontrast CT. CT PIRI (0–4) was rated by consensus between two neuroradiologists and categorized as Good (0–1), Intermediate (2), or Poor (3–4). Associations between PIRI severity, baseline NIHSS, mRS at discharge and 90 days, and in-hospital complications were analyzed using nonparametric tests and logistic regression.

Results

CT PIRI severity showed a strong correlation with baseline NIHSS (p=0.002, Kruskal-Wallis test), with median NIHSS values of [Good 7:(IQR 5-8.5)], [Intermediate 16:(IQR15-17)], and [Poor 17:(IQR13-21)]. CT PIRI was also significantly associated with worse mRS at both discharge (p = 0.01) and 90 days (p = 0.003, Kruskal–Wallis), with median mRS at discharge of [Good 2.5:(IQR2-3)], [Intermediate 4:(IQR4-5)], and [Poor 4.5:(IQR4-5)], and at 90 days of [Good 2: (IQR1-2)], [Intermediate 2: (IQR2-3)], and [Poor 6: (IQR3-6)]. Right-sided Poor PIRI demonstrated progressive worsening of mRS from discharge to 90 days, reaching a median of 6 (IQR 4.5-6) (p = 0.25 at discharge, p = 0.03 at 90 days, Kruskal–Wallis), and was associated with hospital-acquired pneumonia (HAP) (OR = 46.7, 95% CI 0.5–4311.5, p = 0.04, LRT). A trend toward association with new dysphagia was also observed (OR=11.6, 95%CI: 0.6-219.9; p=0.06, LRT). Left-sided Poor PIRI demonstrated stable mRS between discharge and 90 days (p=0.05 for both, Kruskal-Wallis test). Across all cases, patients who developed in-hospital complications of new HTN and new dysphagia showed significantly favorable 90-day mRS outcomes when Good PIRI was present (new HTN: OR = 55, 95% CI 1.7–19 244.7, p = 0.04, LRT; new dysphagia: OR = 51, 95% CI 1.2–18 562.4, p = 0.03, LRT).

Conclusion

In MCA and ICA territory stroke, CT PIRI severity independently reflects both baseline neurological severity and longitudinal outcome trajectory. Right Poor PIRI identifies patients at risk for pneumonia and progressive disability, whereas left Poor PIRI is associated with dysphagia and functional stability. Importantly, Good PIRI remained associated with favorable 90-day functional outcomes even among patients who developed in-hospital complications such as new HTN and new dysphagia. These findings support CT PIRI as a simple, reproducible biomarker linking insular injury severity with complication-adjusted outcomes.

Images/Tables

Table1: Patients Characteristics

	Total (31)	Right (10)	Left (21)	p-value	Good PIRI (11)	Intermediate PIRI (5)	Poor PIRI (15)	p-value
Age (Mean±SD)	70.3±13.3	74.8±14.0	68.2±12.6	0.14	72.7±10.9	73.6±12.5	67.5±15.2	0.64
Female, n (%)	19 (38.7)	4 (40.0)	8 (38.1)	1.0	5 (45.5)	1 (20.0)	6 (40)	0.78
NIHSS, Median(IQR1-3)	13 (7-18)	13 (8.25-16.5)	15 (7-21)	0.50	7 (5-8.5)	16 (15-17)	17 (13-21)	**0.002**
Known CAD, n(%)	10 (32.3)	4 (40)	6 (28.6)	0.69	5 (45.5)	2 (40)	3 (20)	0.73
Known AF, n(%)	4 (12.9)	2 (20)	2 (9.5)	0.58	2 (18.2)	0 (0)	2 (13.3)	0.14
Smoking, n(%)	5 (16.1)	3 (30)	3 (14.3)	0.36	2 (18.2)	2 (40)	2 (13.3)	0.42

Table2: Association Between PIRI Grades and Clinical Outcomes

Complication	Right-Good PIRI (2)	Right Intermediate PIRI (2)	Right-Poor PIRI (6)	p-value	Left-Good PIRI (9)	Left Intermediate PIRI (3)	Left-Poor PIRI (9)	p-value	Good PIRI (11)	Intermediate PIRI (5)	Poor PIRI (15)	p-value	Right (10)	Left (21)	p-value
mRS at discharge, median(IQR 1-3) (29)	3 (2.5-3.5)	5(4-4)	4(4-4)	0.25	2.5(2-3)	5(4.5-5.5)	5(4-5)	**0.057**	2.5(2-3)	4 (4-5)	4.5(4-5)	**0.013**	4(4-4)	4(2-5)	0.91
90-day mRS, n(%) median(IQR 1-3) (29)	1.5(1.25-1.75)	2(1.5-2.5)	6(4.5-6)	**0.037**	2(1.5-2.5)	3(2.5-4.5)	3(3-6)	**0.055**	2(1-2)	3(2-3)	5(3-6)	**0.003**	3(2-4.5)	3.5(2.25-6)	0.46

Table3: Logistic Regression Analysis of Association between Poor PIRI (PIRI > 50%) and complications

comparison	Variable	Unadjusted OR (95% CI)	p-value	Adjusted OR (95% CI)	p-value
All Cases	Hospital-Acquired Pneumonia (HAP)	**5.4 (0.8-38.7)**	**0.06**	**13.1 (1.1-156.0)**	**0.08**
	New dysphagia	**4.4 (0.9-20.2)**	**0.04**	**4.2 (0.6-29.6)**	**0.06**
	New HTN	2.0 (0.4-9.7)	0.37	**10.7 (0.4-278.1)**	**0.21**
Right Stroke	Hospital-Acquired Pneumonia (HAP)	4.2 (0.4-49.1)	0.23	**46.7 (0.5-4311.5)**	**0.04**
	New dysphagia	**16.2 (0.6-441.7)**	**0.04**	**11.6 (0.6-219.9)**	**0.06**
	New HTN	5.0 (0.2-136.3)	0.29	6.7 (0.1-908.1)	0.49
Left Stroke	Hospital-Acquired Pneumonia (HAP)	4.4 (0.2-121.7)	0.34	6.2 (0.2-181.6)	0.41
	New dysphagia	2.2 (0.4-12.7)	0.37	0.4 (0.1-9.7)	0.62
	New HTN	1.5 (0.2-8.7)	0.68	3.0 (0.2-58.9)	0.47

Figure 2. The axial image of insula on NCCT; 0 shows 0% insular ribbon infarction (PIRI score 0). 1 shows 0-25% insular ribbon infarction (PIRI score1). 2 shows 25-50% insular ribbon infarction (PIRI score 2). 3 shows 50-75% insular ribbon infarction (PIRI score 3). 4 shows 100% insular ribbon infarction (PIRI score 4).

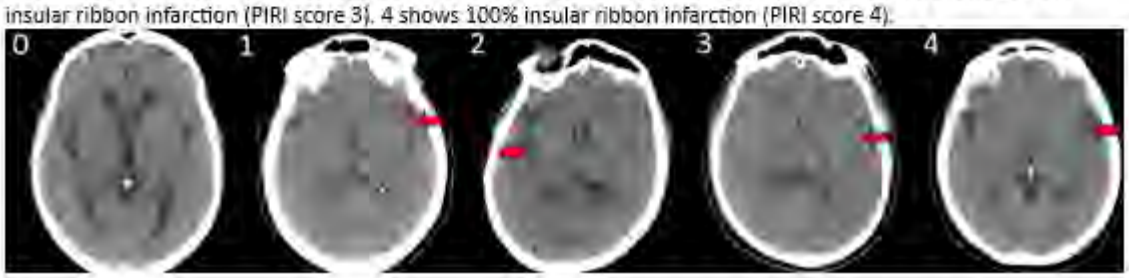

1004 **CHOROID PLEXUS VOLUME FRACTION AS A GLYMPHATIC IMAGING MARKER CORRELATES WITH CORTICAL THINNING AND WHITE MATTER MICROSTRUCTURE IN THE ALZHEIMER'S DISEASE CONTINUUM**

Ji Young Lee[1], Jin-Ju Yang[2], Yueh Lee[3], Carlos Zamora[3]

[1]Seoul St. Mary's Hospital, Seoul, NA, Korea, Republic of. [2]Hanyang Vision Research Center, Hanyang University, Seoul, NA, Korea, Republic of. [3]University of North Carolina Chapel hill, Chapel HIll, North Carolina, USA

Purpose

The choroid plexus volume fraction (CPVF) is a proposed glymphatic imaging biomarker associated with cognitive decline and cortical atrophy in Alzheimer's disease (AD). However, its relationship with white matter integrity remains unclear. This study aimed to investigate the association between CPVF and brain structural integrity, including cortical thickness and white matter volume/microstructure, across the AD continuum.

Materials & Methods

Brain MRI and clinical data were obtained from the Alzheimer's Disease Neuroimaging Initiative (ADNI), including healthy controls (HC), mild cognitive impairment (MCI), and AD patients. CPVF and structural metrics were derived from 3D T1-weighted MRI. White matter microstructure was assessed

using diffusion tensor imaging (DTI) and tract-based spatial statistics (TBSS). Partial correlation analyses were conducted to examine associations between CPVF and cortical thickness, white matter volume, and voxel-wise DTI metrics, adjusting for age, sex, APOE ε4 status, education, and white matter hyperintensity volume. Multiple comparisons were corrected using false discovery rate (FDR) and family-wise error (FWE) methods.

Results

CPVF showed moderate negative correlations with entorhinal cortical thickness ($r \approx -0.42$ to -0.47) and weak correlations with bilateral temporal, parietal, and frontal cortices ($r \approx -0.10$ to -0.20; FDR-$p < 0.05$). White matter volume exhibited moderate-to-weak negative correlations in the superior frontal, precuneus, posterior cingulate, and temporal regions ($r \approx -0.20$ to -0.30). TBSS revealed reduced FA in the corpus callosum, corona radiata, internal capsule, posterior thalamic radiation, cingulum, and superior longitudinal fasciculus. CPVF also correlated positively with mean, axial and radial diffusivity in limbic tracts, including the fornix, tapetum, sagittal stratum, and inferior fronto-occipital fasciculus (FWE-$p < 0.05$).

Conclusion

CPVF is associated with both cortical thinning and white matter degeneration in the AD continuum. While glymphatic dysfunction has been primarily linked to cortical atrophy, our findings newly demonstrate its relationship with white matter alterations, highlighting CPVF's value as a comprehensive marker of neurodegeneration.

Images/Tables

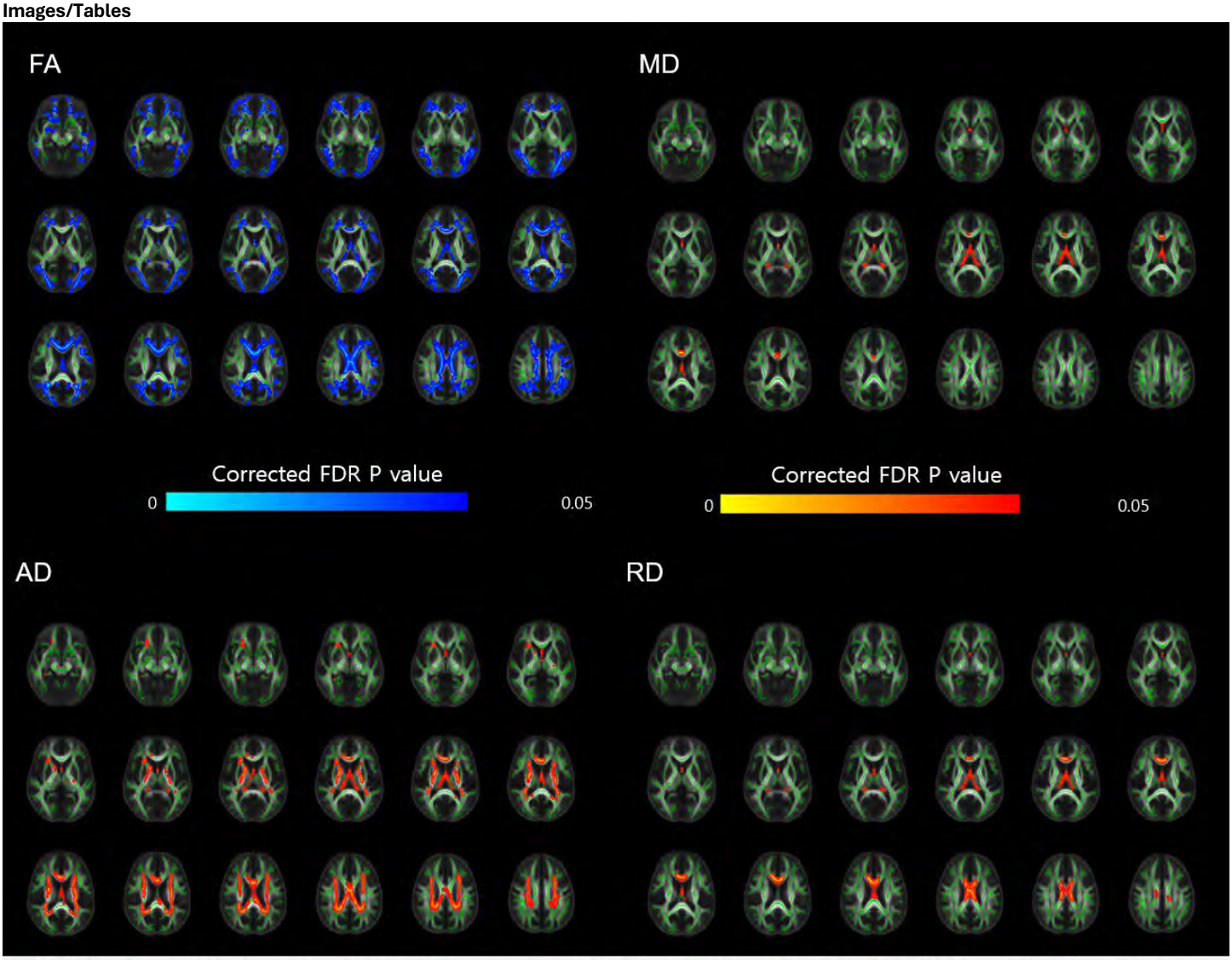

Whole-brain voxel-wise associations between choroid plexus volume fraction (CPVF) and diffusion tensor imaging (DTI) metrics. Voxel-wise regression analysis revealed significant associations between CPVF and fractional anisotropy (FA), mean diffusivity (MD), axial diffusivity (AD), and radial diffusivity (RD) across the white matter skeleton. Higher CPVF was associated with decreased FA and increased MD, AD, and RD in widespread white matter tracts.

1041 High-Resolution Cortical Parcellation Reveals Structural Correlates of Mild Cognitive Impairment in Parkinson's Disease

Arturs Silovs Medical[1], Nauris Zdanovskis Medical[1], Ardis Platkajis Medical[2], Jurgis Skilters[3], Santa Bartusevica Computer science[3], Janis Mednieks Medical[2], Aleksejs Sevcenko Medical[2], Solvita Umbrasko[3], Liga Zarina[3], Jelena Smilga[3]

[1]Riga East clinical university hospital, Riga, Latvia, Latvia. [2]Riga Stradins University, Riga, Latvia, Latvia. [3]University of Latvia, Riga, Latvia, Latvia

Purpose

Cognitive impairment (CI) is a frequent yet under-recognized non-motor manifestation of Parkinson's disease (PD). Different underlying mechanisms from those in typical Alzheimer's disease are suggested, and reliable early imaging biomarkers are lacking. Cortical parcellation using high-resolution

MRI enables quantitative assessment of structural brain changes. This study aims to investigate the relationship between cortical volumetric alterations derived from multi-modal MRI and CI severity in PD patients.

Materials & Methods

We studied 49 participants: 25 PD patients with mild cognitive impairment (PD-MCI) and 24 healthy control subjects. CI was assessed using the Montreal Cognitive Assessment (MoCA). All participants underwent 3 T MRI including a thin-slice 3D T1 sequence with voxel size 1×1×1 mm. Based on MoCA scores, subjects were categorised as either mild cognitive impairment or no cognitive impairment. Cortical segmentation and parcellation were performed using FreeSurfer v7.4.1, employing the Destrieux anatomical atlas to extract regional volumes. Statistical analyses were conducted using SPSS v29 and JASP 0.18.3. A significance threshold of $p < 0.05$ was applied.

Results

The median age of the study group was 57 years (interquartile range 45.0–63.0 years) with 25 women and 24 men. Lower overall MoCA scores were significantly associated with reduced tissue volumes in the bilateral superior temporal gyrus (p = 0.001 left, p = 0.014 right), bilateral middle temporal gyrus (p = 0.039 left, p = 0.043 right), bilateral occipital pole (p = 0.024 left, p = 0.005 right), left superior occipital gyrus (p = 0.032), and right subcallosal gyrus (p = 0.008). The strongest correlations were found for left middle temporal gyrus volume (r = 0.443) and right superior temporal gyrus volume (r = 0.445). No significant associations were observed between MoCA scores and volumetric changes in the basal ganglia, limbic system structures, or thalamus.

Conclusion

In PD patients with mild cognitive impairment, cortical volumetric reductions in the superior and middle temporal lobes, both occipital poles, left superior occipital gyrus, and right subcallosal gyrus are associated with cognitive decline. Notably, unlike in Alzheimer's disease, hippocampal and entorhinal cortex atrophy were not prominent in this cohort, aligning with prior observations. These findings highlight temporal and occipital cortical involvement in PD-MCI and warrant further investigation in larger cohorts to better define early imaging biomarkers for cognitive decline in PD.

Images/Tables

Patients	49
Gender	25 women & 24 men
Median age	57 [Interquartile range: 45.0 - 63.0]

Table 1. Patient group data.

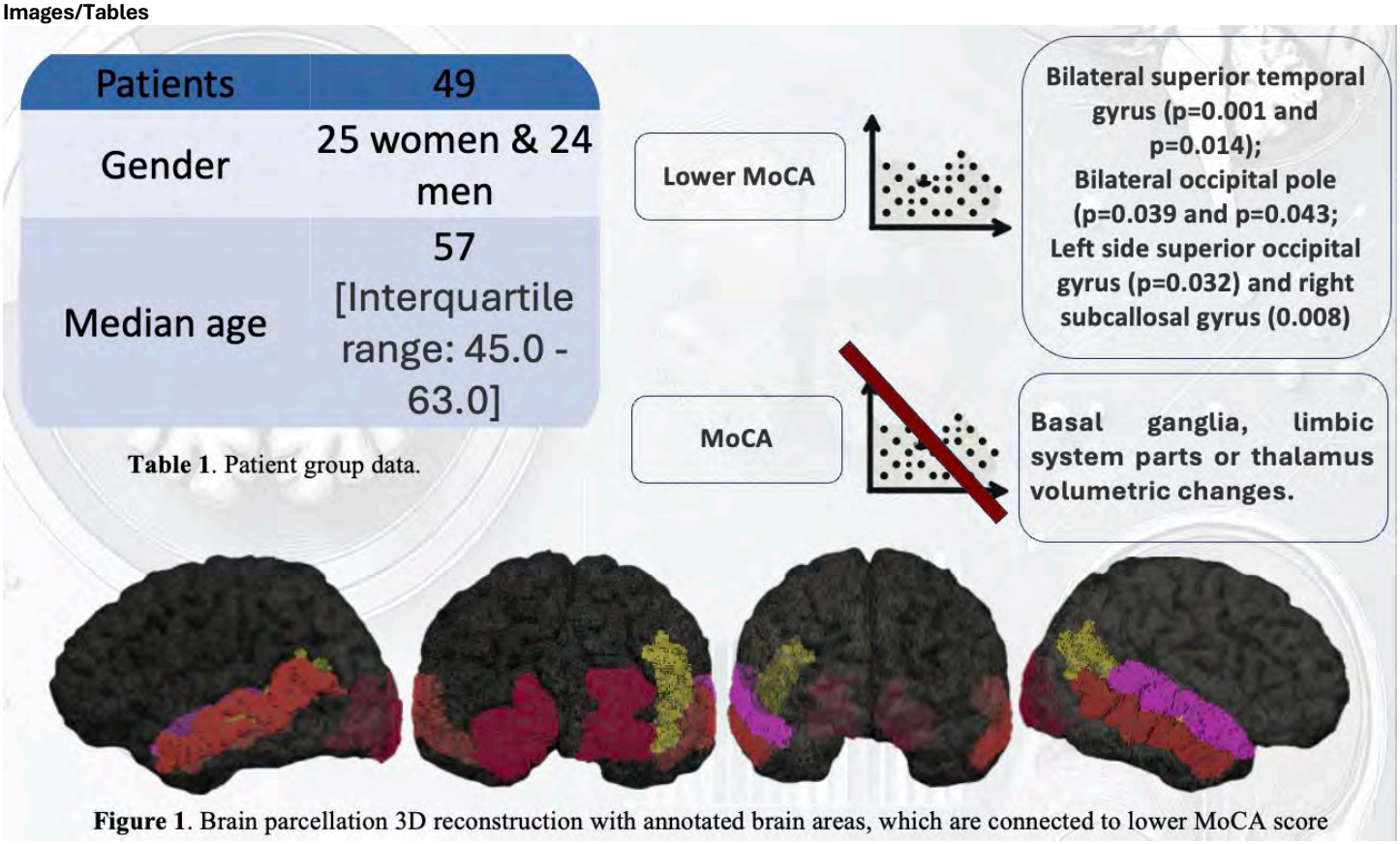

Figure 1. Brain parcellation 3D reconstruction with annotated brain areas, which are connected to lower MoCA score

---

1044 Differentiating Glioma from Brain Metastasis Using Neurite Orientation Dispersion and Density Imaging: A Systematic Review and Meta-Analysis

Amir Mahmoud Ahmadzadeh[1], Nima Broomand Lomer[2], Sadegh Ghaderi[3], Mahdi Afarideh Sani[4], Girish Bathla[5], Long Tu[6]

[1]Mashhad University of Medical Sciences, Mashhad, Khorasan Razavi, Iran, Islamic Republic of. [2]University of Pennsylvania, Philadelphia, Pennsylvania, USA. [3]Tehran University of Medical Sciences, Tehran, Tehran, Iran, Islamic Republic of. [4]Royal United Hospitals, Bath, Somerset, United Kingdom. [5]Mayo Clinic, Rochester, Minnesota, USA. [6]Yale School of Medicine, New Haven, Connecticut, USA

Purpose

Differentiating gliomas from brain metastases (BMs) remains a major diagnostic challenge due to overlapping imaging features on conventional MRI (1). Noninvasive microstructural biomarkers such as neurite orientation dispersion and density imaging (NODDI) may improve diagnostic accuracy (2). This study aims to systematically review and meta-analyze published evidence on NODDI-derived parameters for distinguishing gliomas from BMs.

Materials & Methods

This study followed PRISMA 2020 guidelines and was prospectively registered with PROSPERO (CRD420251126646). PubMed, Scopus, Embase, and Web of Science were searched through August 18, 2025. Studies were eligible if they measured either of quantitative NODDI parameters, including orientation dispersion index (ODI), isotropic volume fraction (V-ISO), and intracellular volume fraction (V-IC), in both glioma and BM. Two

reviewers independently performed study selection, data extraction, and quality assessment using the modified Newcastle-Ottawa Scale. Pooled standardized mean differences (SMDs) with 95% confidence intervals (CIs) were computed using a random-effects model in STATA 17, with Hedge's g as the effect size. Heterogeneity was quantified using the Higgins I^2 statistic, and subgroup analyses were conducted to identify potential sources of heterogeneity. Publication bias was evaluated using Funnel plots, Begg's test, and Egger's test.

Results

Ten studies were finally included. The publication dates ranged from 2020 to 2025. According to the modified NOS scale, one study was scored as very good, two as satisfactory, and others as good. The number of coil channels, b-values, time of repetition (TR), and time of echo (TE) spanned from 20 to 64, 0 to 3500 s/mm2, 2500 to 8741 ms, and 71 to 123 ms, respectively. The studies utilized data from various masks, including whole tumor, tumor core (whole tumor minus peritumoral T2 hyperintensity), contrast-enhancing tumor (CET), necrotic area, and peritumoral edema area (PEA). In pooled CET analyses, ODI (SMD = –1.43 [–2.02, –0.85]) and V-ISO (SMD = –0.98 [–1.60, –0.37]) were significantly lower in gliomas than BMs, indicating reduced dispersion and free-water fraction, while V-IC differences were nonsignificant (SMD = –0.57 [–1.17, 0.04]). For PEA, group differences were nonsignificant overall; however, in the glioblastoma subgroup, V-ISO showed a significant reduction (SMD = –0.73 [–0.96, –0.50]) with minimal heterogeneity (I^2 = 0%). Other subgroup analyses revealed that longer TE (>100 ms) and 32-channel coils (compared to 64-channel coils) yielded larger absolute effect sizes for CET V-ISO and CET V-IC, respectively. Sensitivity analysis confirmed the robustness of analyses. No significant publication bias was detected (all $p > 0.05$).

Conclusion

This meta-analysis demonstrates that NODDI-derived parameters, particularly ODI and V-ISO, provide significant microstructural contrasts between gliomas and BMs, supporting their potential as noninvasive biomarkers for differential diagnosis. The observed lower ODI values in gliomas may reflect partially preserved axonal microstructure within infiltrative tumor tissue, while elevated V-ISO in BMs likely corresponds to greater extracellular free-water content associated with disorganized cellularity and vasogenic edema. These findings encourage further multicenter validation using harmonized diffusion protocols and standardized post-processing to integrate NODDI metrics into clinical decision-making for brain tumor characterization.

Images/Tables

Differentiating Glioma vs. Brain Metastasis

A Systematic Review & Meta-Analysis of NODDI Parameters

Diagnostic Challenge & Method

The Problem

Gliomas and brain metastases (BMs) may have overlapping MRI features, making their differentiation difficult by conventional MRI.

The Method: Meta-Analysis

We synthesized data from **10 studies** to quantify the utility of NODDI parameters (ODI, V-ISO, V-IC) in the differentiation of these tumors.

Eligibility Criteria

Studies that measured any of the quantitative parameters derived from NODDI in both glioma and BM patients

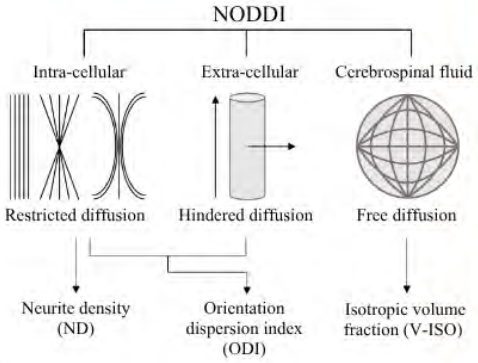

Analysis 1: Contrast-Enhancing Tumor (CET)

Comparing NODDI values within the enhancing portion of the tumor:

ODI	V-ISO	V-IC
Glioma < Metastasis	Glioma < Metastasis	No significant difference
SMD = -1.43	SMD = -0.98	SMD = -0.57
✓	✓	✗

Analysis 2: Peritumoral Edema Area (PEA)

Comparing NODDI values in the edema surrounding the tumor:

ODI	V-ISO	V-IC
No significant difference	No significant difference	No significant difference
SMD = +0.42	SMD = -1.43	SMD = +0.36
✗	✗	✗

Key Finding: Glioblastoma-Only Subgroup

When analyzing **glioblastoma (GBM)** specifically, the **PEA V-ISO** became significant, showing less free water in infiltrative edema (GBM) vs. vasogenic edema (BMs). **SMD = -0.73 ($p < 0.05$)**

Final Conclusions

- NODDI is a powerful tool for differentiating gliomas from BMs.
- **In the CET:** Look for **lower ODI** & **lower V-ISO** (suggests glioma).
- **In the PEA:** Look for **lower V-ISO** (suggests glioblastoma).

1054 Novel Visualization of Vagal Branches to the Esophageal Plexus Using High Resolution CISS MRI

Mridhula Muthukumar, Shruti Kumari, Ari Blitz
University Hospitals Cleveland, Cleveland, OH, USA

Purpose

The vagus nerve (cranial nerve X, CN X) has the most extensive distribution of any cranial nerve, providing parasympathetic innervation to the head, neck, thorax, and abdomen. As the nerves travel through the thorax, they contribute to the esophageal plexus, a network of vagal fibers that arborize along the esophageal wall. Imaging these esophageal branches holds significant diagnostic value in gastro-enterologic and autonomic disorders, such as diabetic autonomic dysfunction, paraneoplastic syndromes and idiopathic gastroparesis. Gastrointestinal vagal nerve stimulation has also shown to be an emerging target for restoring vagal tone and improving motility in patients with autonomic dysfunction. Despite the clinical relevance, direct imaging of CN X branches beyond the lung hilum remains a challenge with current imaging modalities. Standard MRI sequences with 1-mm isotropic resolution often fail to resolve these fine neural structures, and their course is usually inferred from adjacent anatomy. High-resolution isotropic 3D MRI sequences, particularly constructive interference in steady state (CISS), has excellent SNR efficiency and allows for high-spatial resolution imaging in a clinically reasonable time period. Therefore, in this study we demonstrate that 0.5-0.6 mm CISS MRI in cadavers will enable visualization of vagal branches to the esophageal plexus.

Materials & Methods

54 cadavers were scanned using the CISS MRI protocol. All scans were independently evaluated by two trained raters (one physician and one masters in anatomy) blinded to each other's interpretation in multiple sessions. Branching points from CN X were initially observed on pre-dissection MRI, then validated and identified based on anatomic dissection between two distinct anatomic landmarks. Branches identified by both raters were included in the study.

Results

CISS MRI analysis of 54 embalmed cadavers revealed direct esophageal branches arising from CN X in 5 embalmed cadavers, with a total of 5 branches identified. The esophageal branches originated from the superior thoracic segment of CN X near the tracheal bifurcation at the level of the sternal angle.

Conclusion

This is the first study showing the visualization of esophageal branches of CN X in cadavers using CISS MRI. Translation of this work and use of CISS MRI for routine clinical imaging of CN X branches at its distal targets offers significant potential for better nerve preservation during surgery and optimizing therapeutic targeting for esophageal and gastric diseases.

Images/Tables

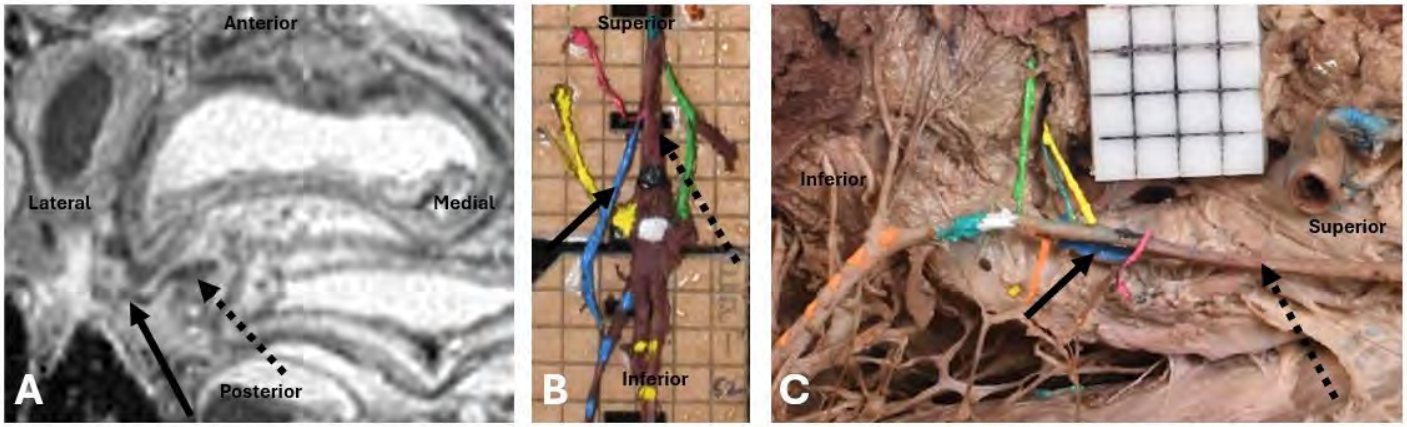

Figure 1: Representative images of right branch to esophageal plexus just above tracheal bifurcation. A) Representative Axial CISS MRI image of right branch (solid arrow) of CN X (dashed arrow) to esophageal plexus. B) Representative image of excised right branch (solid arrow) of CN X (dashed arrow) to esophageal plexus. C) Representative image of in situ right branch (solid arrow) of CN X (dashed arrow) to esophageal plexus

1069 Somatostatin Receptor-Targeted PET Imaging for Meningiomas: Insights from a Retrospective Cohort Study

Jeppe L. Haslund-Vinding MD[1], Bryce D. Beutler MD[2], David R. Raleigh MD, PhD[2], Dante Capaldi PhD[2], Nancy Ann Oberheim Bush MD, PhD[2], Javier E. Villanueva-Meyer MD[2]
[1]Rigshospitalet Neurocentret, Copenhagen, Capital Region, Denmark. [2]University of California San Francisco, San Francisco, CA, USA

Purpose

DOTA-(Tyr^3)-octreotate (DOTATATE) a synthetic peptide that binds to somatostatin receptor subtype 2 (SSTR2), which is consistently and highly expressed in meningiomas. Positron emission tomography (PET) imaging with DOTATATE has shown promise in differentiating tumor tissue, guiding surgical and radiotherapeutic planning, and detecting residual or recurrent disease in the postoperative setting. However, the relationship between DOTATATE uptake and tumor grade remains incompletely understood. We aimed to evaluate the association between DOTATATE uptake and meningioma World Health Organization (WHO) grade and identify imaging biomarkers of biological behavior and therapeutic relevance.

Materials & Methods

We retrospectively analyzed 153 patients who underwent DOTATATE imaging between January 2017 and March 2025. Clinical data, imaging characteristics (SUV_{max}, SUV_{mean}, uptake pattern), WHO grade, histopathology, and molecular profiles from the UCSF500 next-generation sequencing panel were extracted. Statistical analyses were performed to explore the association between DOTATATE uptake metrics and tumor grade.

Results
A total of 153 patients were included in the analysis, 149 of whom had intracranial meningiomas and 4 of whom had spinal lesions. A total of 123 patients had solitary lesions, 32 had multiple meningiomas, and 2 presented with distant metastases. In 86 patients, imaging was performed for known meningiomas; in 71 subjects, meningiomas were incidentally identified on PET scans obtained for unrelated neoplasms. SUV_{max} did not significantly correlate with WHO grade across the cohort. Exploratory thresholds (e.g., SUV_{max} >20) did not differentiate high-grade (WHO grade 2 or 3) from low-grade (WHO grade 1) tumors. Analysis of molecular data is ongoing.
Conclusion
No significant correlation was observed between SUV_{max} and WHO grade. However, DOTATATE PET remains a valuable tool for detecting residual disease and guiding management, irrespective of tumor grade. Future integration of imaging metrics with molecular profiling may refine risk stratification and personalize therapeutic approaches for meningioma patients.
Images/Tables

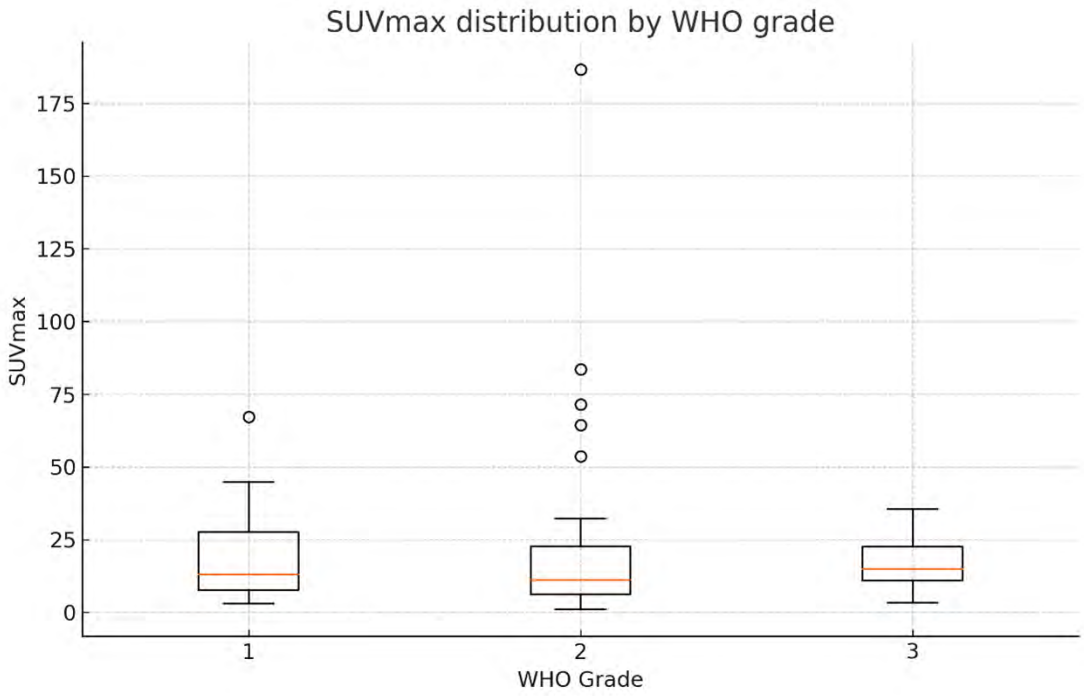

1081 ALPS-INDICES ACROSS THE ALZHEIMER'S DISEASE SPECTRUM
Omar Moustafa PhD[1], Jeremy Ford MD MS MBA[2]
[1]University of Connecticut School of Medicine, Farmington, CT, USA. [2]Massachusetts General Hospital, Boston, MA, USA
Purpose
To test whether a non-contrast diffusion tensor imaging (DTI) metric of glymphatic function—the Along-the-Perivascular-Space (ALPS) index—differs across the cognitive spectrum (healthy controls [HC], mild cognitive impairment [MCI], Alzheimer's disease [AD]) and relates to clinical severity, plasma tau, amyloid burden, and perfusion measures.
Materials & Methods
DTI data were obtained from 44 subjects classified into HC (n=15), MCI (n=19), and AD (n=10) groups. ALPS-index was calculated using DSI studio by taking the average of left and right hemisphere metrics after EDDY correction. Differences among groups were assessed using ANOVA with post hoc analysis. Spearman correlation analyses evaluated relationships between ALPS-indices and CDR scores, plasma and imaging biomarkers (pTau217, Centiloid values and regional standardized uptake value ratio (SUVR) for beta-amyloid), and arterial spin labeling (ASL) imaging measures (Whole brain CBF, Arterial transit time (ATT), and blood-brain barrier water exchange (k_W).
Results
The ALPS index declined stepwise across the diagnostic spectrum—highest in healthy controls, intermediate in MCI, and lowest in Alzheimer's disease—with an overall significant group effect ($p = 0.03$). After correction, HC > AD remained significant ($p = 0.02$), whereas MCI did not differ significantly from either group. The ALPS-index correlated negatively with clinical severity measures including CDR ($r = -0.363$, $p = 0.0154$) and CDR-SoB ($r = -0.418$, $p = 0.0066$), as well as with Plasma pTau217, ATT, k_W/CBF ratio, Centiloid values, and regional SUVRs in the cingulate and parietal cortices. In contrast, positive associations were observed with Whole Brain CBF ($r = 0.383$, $p = 0.0103$). No significant correlations were found with Vascular Risk Factors ($r = -0.10$) or Whole Brain k_W ($r = -0.16$).
Conclusion
These findings indicate a progressive reduction in the ALPS-index from healthy aging through MCI to AD, with the ALPS-index tracking clinical severity, tau pathology, amyloid burden, and perfusion. The lack of association with k_W suggests that the ALPS-index and k_W may probe different aspects of the glymphatic circuit—the former assessing perivenous efflux, and the latter estimating aquaporin-4-mediated influx and blood-brain barrier injury. Moreover, the absence of correlation between ALPS-index and vascular risk factors suggests possible specificity for AD. While these findings support DTI-ALPS as a potential contrast-free imaging biomarker for early detection and longitudinal monitoring of AD, further longitudinal studies are needed with expanded sample size.

1088 Modeling What Clinicians See: Individualized Risk Profiles After Thrombectomy Using Truncated Skew-Normal ML

Dayeong An[1], Chaochao Zhou[1], Syed Faruqui[2], Ramez Abdalla[1], Sameer Ansari[1], Donald Cantrell[1]
[1]Northwestern University, chicago, il, USA. [2]Sam Houston State University, Huntsville, tx, USA

Purpose

Mechanical Thrombectomy (MT) is the established standard-of-care for the interventional treatment of Acute Ischemic Stroke (AIS). Accurate prediction of clinical outcomes after MT is crucial for guiding post-operative management, yet it remains heterogeneous. The NeuroVascular Quality Initiative-Quality Outcomes Database (NVQI-QOD) registry provides detailed pre-operative, peri-operative, and post-operative data of neurointerventional procedures. However, healthcare data is often bounded, skewed, and heavy-tailed. We introduce a probabilistic machine learning (ML) model that predicts patient-specific distributions using a truncated skew-normal (TSN) likelihood.

Materials & Methods

AIS patients treated with MT recorded in the NVQI-QOD registry were analyzed. The feature variables were grouped into three categories: Preop (prior to MT) and Postop (post-MT). Datasets (n=5,221) were split 8:2 (train/test). We implemented XGBoost Distribution with a TSN likelihood constrained to NIHSS [0, 42]. The model outputs per-patient TSN parameters (loc, scale, skew) and is trained by minimizing the truncated negative log-likelihood (NLL). For comparison, the same model with normal likelihood was fitted. Evaluation emphasized distributional fit for clinically meaningful events.

Results

The model with a TSN had lower NLL than Normal (Preop: 3.545 vs. 3.655, Postop:2.962 vs. 3.050) and similar continuous ranked probability score (CRPS) (Preop: 3.817 vs. 3.633, Postop: 2.205 vs. 2.111), consistent with normal mass leaking outside of [0, 42]. TSN improved clinical coverage where bounds and asymmetry matter (**Fig 1**). Illustratively (**Fig 2**), a patient with baseline NIHSS 6 who achieved discharge NIHSS 0, the TSN respected the floor and concentrated probability near 0 with a right-skewed distribution while normal assigned non-trivial probability to negative NIHSS.

Conclusion

Modeling distributions rather than point estimates provides actionable probabilities for patient-specific, directionally informative forecasts. A TSN aligns with the bounded and skewed nature of stroke outcomes. A TSN aligns with the bounded and skewed nature of stroke outcomes and improves interval realism. TSN distribution improves and supports its use for clinical decision support and communication of uncertainty for MT.

Images/Tables

Fig 1. Comparison of discharge NIHSS distributions: histograms, KDEs of predicted vs. observed (Normal vs. Truncated skew-normal), residual plots, and probability distribution.

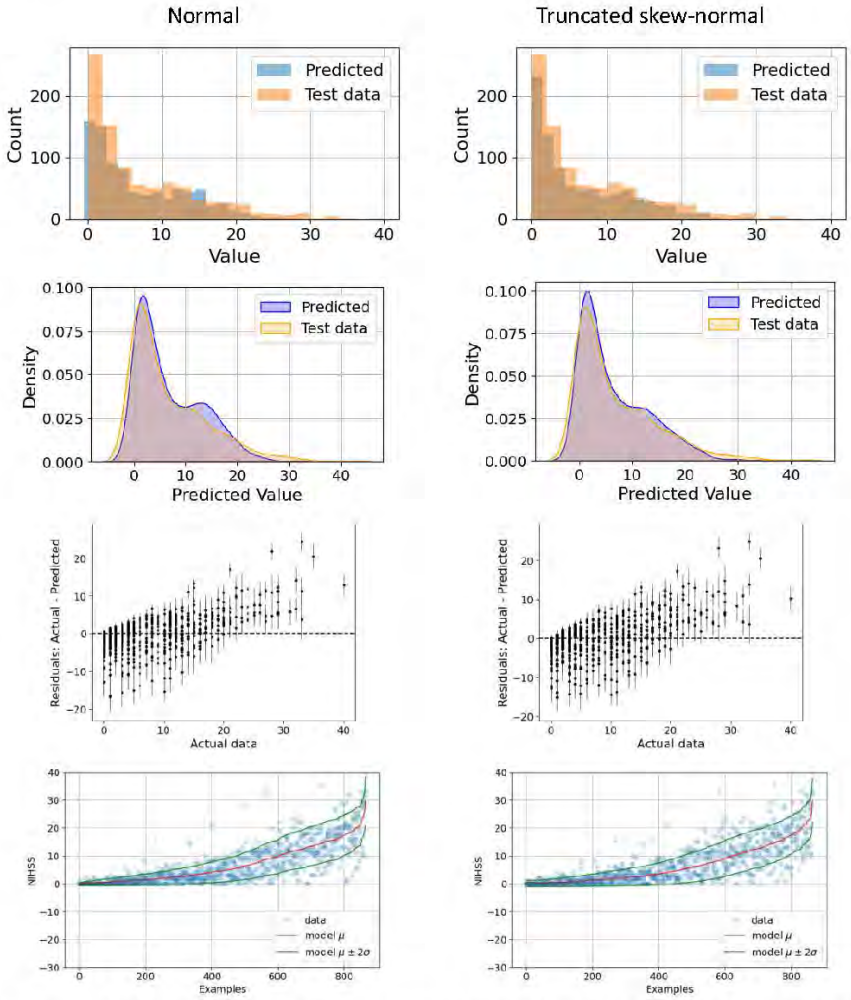

Fig 2. Single-patient example (baseline NIHSS 6, discharge NIHSS 0). While Normal allocates impossible probability < 0, Truncated skew-normal respects the NIHSS range and places mass near 0.

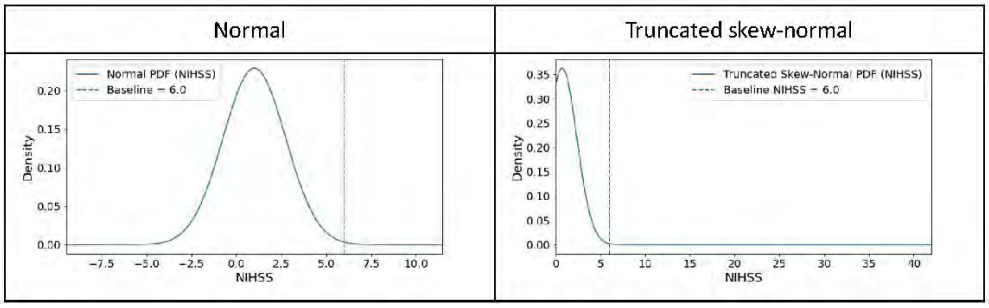

1108 Revisiting the Swallow Tail Sign: A Scoping Review

Alexander Reyes Lobo Radiologist[1], Diego Felipe Zarate Bernal Radiology resident[2], Carolina Becerra Barajas epidemiologist[1], Reynaldo Rodriguez Amaya epidemiologist[3], Laura Marcela Rodriguez Alba radiology resident[2]
[1]Universidad industrial de Santander, Bucaramanga, Santander, Colombia. [2]Universidad Militar Nueva Granada, bogota, cundinamarca, Colombia. [3]university of Auckland, auckland, auckland, New Zealand

Purpose

To scope out the literature on swallow tail sign and establish its diagnostic performance for diagnosing Parkinson disease. Additionally, a secondary objective was the recompilation of other important information about this sign and its interpretation

Materials & Methods

We conducted a scoping review using the PRISMA criteria in Pubmed and ScienceDirect. The search terms were Swallow tail sign and MRI, no time limits were set. In Pubmed a total of 34 articles were obtained, with a total of 21 articles deemed appropiate after exclution criteria. In the ScienceDirect database 1178 were selected with the search terms mentioned above. Nevertheless, most of them were not related to Neuroradiology or PD, due to this, we applied the filter of neurosciences, obtaining 265 articles. Then a new screening was performed and 44 publications were left for analysis after exclution criteria

Results

Our society is witnessing the ageing of the population worldwide while a new era of biomarkers, which are radiological findings that are capable of establishing diagnosis criteria is breaking through. One of these biomarkers is the swallow tail sign (STS) loss on MRI. This marker correlates with degenerative changes in the substantia nigra of the mesencephalon, that are present in Parkinson's disease (PD). Although this sign is widely known in some places, its use is not totally extended and some works have shown that its diagnostic value is not really high. The purpose of this review was to explore the diagnostic capacity of the loss of the swallow tail sign, and investigate other interesting data related to it

A poor visualization of the Nigrosome 1 had an overall sensitivity of 98.5% and specificity of 93.6% with a positive predictive value of 94.3% and a negative predictive value of 98,3%.

Meijer et al evaluated the STS with two different radiologists, the ability of the STS to discriminate between PD and controls resulted in an AUC of 0.72 for reader 1, and an AUC of 0.58 for reader 2. In this work it is also remarkable that there was a difference between magnets of 3 Tesla and 7 Tesla, with a diagnostic accuracy of 86% for the former and 96% for the latter. These differences suggest that the expertise of the neuroradiologist and the power of the magnet, influence the results.

According to the Chau et al, an abnormal Nigrosome 1 increases the odds of having PD approximately 10-fold, whereas the odds decrease significantly if the appearance of Nigrosome 1 is normal

Conclusion

Although there was some discordance among the analyzed studies, most articles confirmed the utility of the loss of the STS as a biomarker for PD. The overall sensitivity and specificity were high as well as the accuracy. Here, it is important to mention that even some works have shown a sensitivity as high as 100%. Therefore, MRI practicing SWI with the correct protocol is an excellent diagnostic tool for patients with suspected PD, keeping this evidence in mind, it can be assumed that the loss of the STS is a good biomarker for PD.

Images/Tables

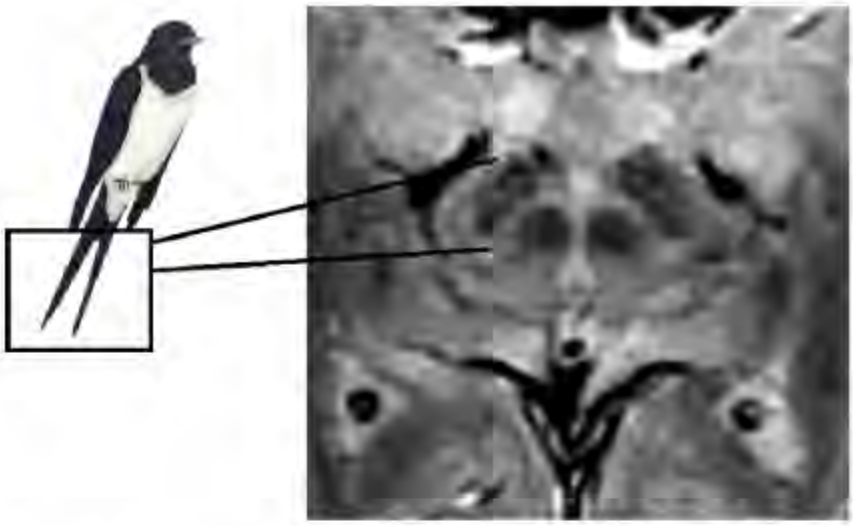

Summary of the relevant articles.

Author	Year	Sensitivity	Specificity	Predictive positive value	Diagnostic accuracy
Stezin et al	2018	98.5%	93.6%	94.3%	96%
Sotoudeh et al	2021	100%	95%	69%	--
Meijer et al	2016	AUC: 0.72 and 0.58 (readers 1 and 2 respectively)	--	--	86% (3T) 96% (7T)
Wang et al	2017	83% *	100% *	Non specified	Non specified
Liu et al	2021	90.91%	91.49%	--	91.18%
Cheng et al	2019	67.53%	90.8%	--	79.88%
Prasuhn et al	2021	37%	78%	--	61%
Wang et al	2021	94.59%	92.49%	--	93.75%
Michler et al	2021	81.5%	75%	84.6%	79.1%
Gupta et al	2022	75.55%	97.7%	--	86.66%
Chau et al	2020	94%	90%	--	
Schwarz et al	2018	100%	93%	--	98%
De Pietro et al	2021	94%	56%	81%	81%

AUC: area under the curve. * Percentages calculated from the data of the article.

1126 Preoperative and Intraoperative Visualization of Cerebral Perforator Vessels Using HR-CBCT (DynaCT Micro)

William J Lee B.A., Omar Choudhri M.D.
University of Pennsylvania, Philadelphia, PA, USA

Purpose

To evaluate the efficacy of high-resolution cone-beam CT (HR-CBCT; DynaCT Micro) in visualizing cerebral perforator vessels in preoperative and intraoperative uses. Cerebral perforator vessels are small vessels that branch off into deep areas of the brain and perform the critical function of supplying blood to inner brain structures [1]. They can be difficult to visualize due to their small size and variable anatomy; however, occlusion of perforator vessels can cause severe defects such as hemiplegia, ischemic stroke, sensory loss, or visual disturbances[1-3]. It is thus imperative to visualize these perforators during microsurgical procedures to prevent such complications.

Materials & Methods

We conducted a retrospective study of 20 patients (10 men, 10 women; mean age: 55.3 ± 14.8 years) who underwent microsurgical treatment at the University of Pennsylvania between July 2022 and November 2024. Patients underwent preoperative CTA, preoperative HR-CBCT, and intraoperative HR-CBCT. Four CAQ-certified neuroradiologists with varying levels of experience (PGY-7, PGY-9, PGY-35) independently evaluated the visibility of the recurrent artery of Heubner (RAH), anterior choroidal artery (AChA), and lateral lenticulostriate artery (LSA) and rated confidence for each identified vessel. Effective radiation doses were estimated from DLP and DAP values using ICRP-derived conversion factors (k = 0.0025 mSv/mGy-cm, 0.0056 mSv/mGy-cm^2) [4 5].

Results

HR-CBCT demonstrated superior visualization of perforator vessels compared to CTA (RAH: 75% vs. 7%; AChA: 100% vs. 40%; LSA: 100% vs. 48%; all p < 0.0001). Reader confidence was significantly higher using HR-CBCT for assessment of the AChA and LSAs (both p<0.0001). Intraoperative HR-CBCT, despite differences in imaging acquisition and presence of surgical artifacts, only recorded a minor reduction in perforator visualization (RAH: 65% vs 75%, p = 0.37; AChA: 97% vs 100%, p=1; LSA: 97% vs 100%, p=1). The presence of surgical artifacts from surgical clips, instruments, or bone flaps did not impact reader ability to visualize perforators (p = 0.90), nor did it significantly affect reader confidence in visualizing RAH (p =0.89), LSA (p=0.88), and AChA (p=1.00). Mean effective dose of radiation did not differ significantly between CTA (1.92±1.6 mSv) and HR-CBCT (1.48±0.06 mSv; p = 0.70).

Conclusion

HR-CBCT provides superior visualization of small cerebral perforator arteries compared with conventional CTA, both in preoperative and intraoperative settings. Vessel visualization remains preserved intraoperatively, even in the presence of surgical or metallic artifacts or bone flaps. HR-CBCT also displays higher inter-observer agreement and reduced dependence on reader experience, suggesting potential to flatten the learning curve in perforator vessel identification. Radiation exposure associated with HR-CBCT is comparable to CTA, indicating that the superior spatial resolution does not incur a significant dose penalty. Collectively, these findings support HR-CBCT as an efficient imaging modality to visualize cerebral perforator vessels to assist in surgical planning and intraoperative monitoring.

Images/Tables

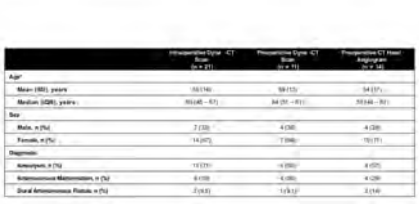

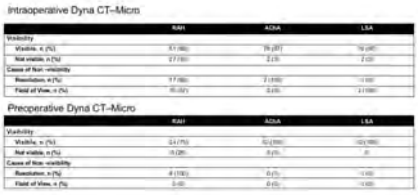

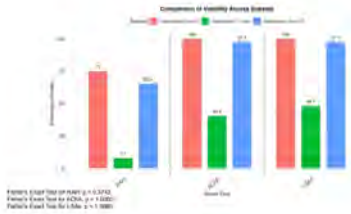

1127 Diffusion Tensor Imaging Along the Perivascular Space as a Marker of Glymphatic Dysfunction in Traumatic Brain Injury: A Meta-analysis

Nima Broomand Lomer M.D[1], Amir Mahmoud Ahmadzadeh M.D.[2], Mohammad Amin Ashoobi M.D[3], Ragini Verma PhD[1]

[1]University of Pennsylvania, Philadelphia, Pennsylvania, USA. [2]Mashhad University of Medical Sciences, Mashhad, Mashhad, Iran, Islamic Republic of. [3]Guilan University of Medical Sciences, Rasht, Guilan, Iran, Islamic Republic of

Purpose

The glymphatic system plays a crucial role in clearing metabolic waste and maintaining brain homeostasis [1]. Animal studies have revealed that glymphatic system disruption plays a key role in the pathophysiological cascade of traumatic brain injury (TBI) [2]. Diffusion tensor imaging along the perivascular space (DTI-ALPS) has emerged as a promising non-invasive biomarker for quantifying glymphatic dysfunction [3]. This meta-analysis aimed to synthesize current evidence on alterations of DTI-ALPS values in TBI and to explore associations with clinical and methodological factors.

Materials & Methods

This study was conducted according to the PRISMA 2020 guidelines. A systematic search of PubMed, Embase, Scopus, and Web of Science (up to August 8, 2025) identified studies reporting DTI-ALPS metrics in TBI and healthy control (HC) cohorts. Eligible studies included human participants with any TBI severity and provided mean ± SD for DTI-ALPS or provided enough data to calculate these values. Pooled standardized mean differences (SMD; Hedges' g) between TBI and HC groups were calculated using a random-effects model. Heterogeneity was quantified using Higgins I^2, and subgroup/meta-regression analyses were incorporated to explore the effect of potential moderators including age, time since injury, diffusion protocol, and study quality. Correlation meta-analyses evaluated relationships between DTI-ALPS and demographic or clinical measures (age, Glasgow Coma Scale [GCS]). Publication bias was assessed via Begg's test and funnel-plot asymmetry.

Results

Eleven moderate- to high-quality studies (694 TBI patients, 503 HCs) met inclusion criteria. DTI-ALPS values were significantly reduced in TBI patients compared with HCs (SMD = –0.77; 95% CI: –1.38 to –0.15; I^2 = 93%). Reductions were more pronounced in chronic stage than acute stage TBI cohorts (SMD = –1.38 vs 0.14; p = 0.01), and meta-regression confirmed progressive decline over time since injury (β = –0.0095 per day; p = 0.025). Single-shell DTI studies yielded stronger effects than multi-shell acquisitions (SMD = –1.18 vs –0.08; p = 0.04). High-quality studies reported greater differences than moderate-quality ones (SMD = –0.98 vs 0.16; p = 0.05). No significant correlations were observed between DTI-ALPS and age (r = –0.27) or GCS (r = 0.07). Begg's test indicated no considerable publication bias (p = 0.12). Hemisphere-specific comparison showed no lateral asymmetry (left vs. right: SMD = –0.11; p > 0.05). Cognitively, lower ALPS indices correlated with poorer memory and executive scores (negative correlations with MoCA and RAVLT; positive correlations with WCST and Digit Span tests) according to the findings of individual studies.

Conclusion

TBI is associated with significantly reduced DTI-ALPS values relative to healthy controls. Lower ALPS indices are linked to poorer memory and executive performance, suggesting a progressive glymphatic dysfunction that contributes to long-term neurocognitive decline after TBI. These results highlight DTI-ALPS as a promising noninvasive biomarker for assessing glymphatic impairment and its chronic consequences. Nonetheless, considerable methodological heterogeneity underscores the need for standardized diffusion protocols and longitudinal studies to establish its clinical and prognostic value.

Images/Tables

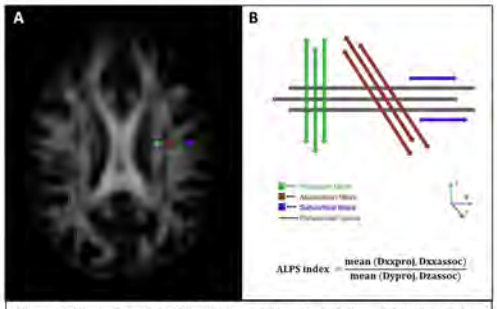

Figure 1. Illustration of the DTI-ALPS method and calculation of the ALPS index. (A) Axial fractional anisotropy (FA) map at the level of the lateral ventricle body demonstrating regions of interest (ROIs) placed along the projection (green), association (brown), and subcortical (purple) fibers adjacent to the perivascular spaces. (B) Schematic diagram showing the spatial relationship between the perivascular spaces (gray lines, oriented along the x-axis) and the three main fiber systems: projection fibers (green, z-axis), association fibers (brown, y-axis), and subcortical fibers (purple, x-axis). The ALPS index quantifies diffusivity along the perivascular space relative to orthogonal directions and is calculated as shown in the figure. This metric reflects water diffusivity along perivascular spaces, serving as an indirect marker of glymphatic function.

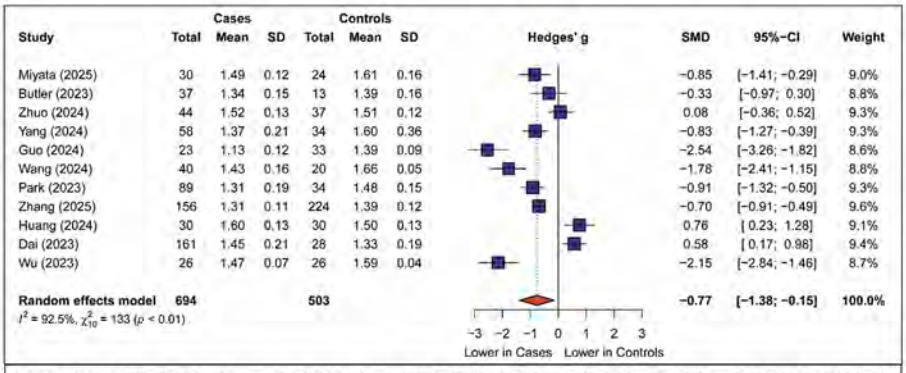

Figure 2. Forest plot showing the pooled standardized mean difference (Hedges' g) in DTI-ALPS values between patients with traumatic brain injury (TBI) and healthy controls. Individuals with TBI exhibited significantly lower DTI-ALPS indices compared with controls, reflecting a moderate-to-large effect size (SMD = −0.77; 95% CI: −1.38 to −0.15). Considerable heterogeneity was present across studies (I^2 = 93%), warranting cautious interpretation of these results. Subgroup and univariable meta-regression analyses were performed to explore potential sources of heterogeneity. The reduction in DTI-ALPS values was more pronounced in chronic-stage compared with acute-stage TBI cohorts (SMD = −1.38 vs 0.14; p = 0.01). Moreover, meta-regression demonstrated a significant progressive decline in ALPS indices with increasing time since injury (β = −0.0095 per day; p = 0.025). Number of directions was also identified as a potential moderator of heterogeneity (β = 0.0138; p = 0.045).

Table 1. Characteristics of the included studies

Author (Year)	Country	TBI (M/F)	HC (M/F)	GCS	Time since injury	MRI Scanner	b value (s/mm²)	Directions
Miyata (2025)	Japan	30 (28/2)	24 (20/4)	NR	25.7 ± 10.5 years	3.0 T Siemens	1000	30
Butler (2023)	USA	37 (28/9)	13 (7/6)	12.3 ± 2.9	148.7 ± 39 days	3.0 T Siemens	1500, 3000	98
Zhuo (2024)	USA	44 (24/20)	37 (17/20)	14.7 ± 0.5	13.8 ± 8.1 days	3.0 T Siemens	1000, 2500	45, 90
Yang (2024)	China	58 (33/25)	34 (19/15)	14.3 ± 0.7	9.8 ± 7 days	3.0 T Siemens	1000, 2000, 3000	30
Guo (2024)	China	23 (17/6)	33 (25/8)	9.1 ± 3.7	131.7 ± 95.7 days	3.0 T Siemens	1000	32
Wang (2024)	China	40 (30/10)	20 (10/10)	Median: 14.5	Median: 19 months	3.0 T GE	1000	30
Park (2023)	Korea	89 (72/17)	34 (27/7)	Median: 12	NR	3.0 T Philips	800	32
Zhang (2025)	USA	156 (NR)	224 (NR)	NR	NR	3.0 T GE	1000	60
Huang (2024)	China	30 (19/11)	30 (12/18)	NR	Median: 14 days	3.0 T GE	1000,1800, 2500	20, 40, 60
Dai (2023)	China	161 (121/40)	28 (15/13)	14.7 ± 1.1	5.6 ± 7.3 days	3.0 T Siemens	1000	20
Wu (2023)	China	26 (17/9)	26 (15/11)	Median: 14	NR	3.0 T GE	1000	30

NR: Not reported.

Table 2. Results of meta-regression analysis

Moderator	N	β (95% CI)	p value	Adjusted R^2
Max b-value	8	0.0005 [-0.0001; 0.0012]	0.1263	11.65%
Number of directions	8	0.0138 [0.0003; 0.0274]	**0.0453**	24.21%
Age (years)	10	-0.0377 [-0.1203; 0.0450]	0.3719	0.00%
Male percentage	10	-1.8060 [-8.2596; 4.6476]	0.5833	0.00%
Time since injury (days)	7	-0.0095 [-0.0178; -0.0012]	**0.0254**	42.82%
GCS	8	0.2924 [-0.0890; 0.6737]	0.1330	16.82%

P-value of significant subgroup analyses are shown in bold.
N: Number of studies for each univariable meta-regression analysis.

1133 **Did AI really change the game? Multialgorithm post implementation surveillance of AI models for assessing critical neuro and vascular findings: Surveillance breeds conformity.**

Giridhar Dasegowda MD, Darrin A McFall, Omer Hamza MD, Ahmed E Abdelmonem MD, Marianne Nabbout MD, Suryakala Buddha MD, Sanjaya Viswamitra MBBS
UAMS, Little Rock, AR, USA

Purpose

Prior studies have reported the performance of radiology AI models during training and validation. However, there is lack of literature in understanding the true impact of radiology AI models after their implementation. Our study was conducted to analyse post implementation monitoring of the AI models.

Materials & Methods

Our retrospective, multialgorithm study included a total of 497 consecutive CT Angiogram of head and neck studies for 1988 findings including intracerebral hemorrhage (ICH), subdural hematoma (SDH), aneurysm, and large vessel occlusion (LVO). The radiology reports were compared to the AI output from a commercial vendor to assess the real time agreement for the critical neuro and vascular findings. We documented demographic data, quality of the CT scans, output of AI algorithm and reported findings by the fellowship trained neuroradiologist. The Cohen's Kappa agreement between the radiology reports and the AI output were used to evaluate the performance.

Results

The imaging studies belonged to 231 men and 266 women with a mean age of 58±18 years. The AI algorithm failed to process 34% of the findings (n = 669/1988). In these studies where AI failed to provide output, the positive findings (with missed percentage) reported by the radiologist were as follows: 15 SDH (0.07%), 12 ICH (0.06%), 2 aneurysms (0.02%) and 7 LVO (0.05%). Issues related to poor image quality, motion artifacts and technical difficulties were the common reasons for failing. For the studies where AI provided output, the Cohen's kappa agreement between the radiologist and the AI output varied from 0.73 for ICH to 0.45 for aneurysm. The agreement for SDH and LVO was 0.54 and 0.61 respectively.

Conclusion

Our study provides a framework for conducting post implementation surveillance of radiology algorithms. The study also highlights the common errors/pitfalls with AI output. While the implemented AI models provided focused outputs to improve efficiency, the radiologists must be aware of these pitfalls for accurate interpretation.

Images/Tables

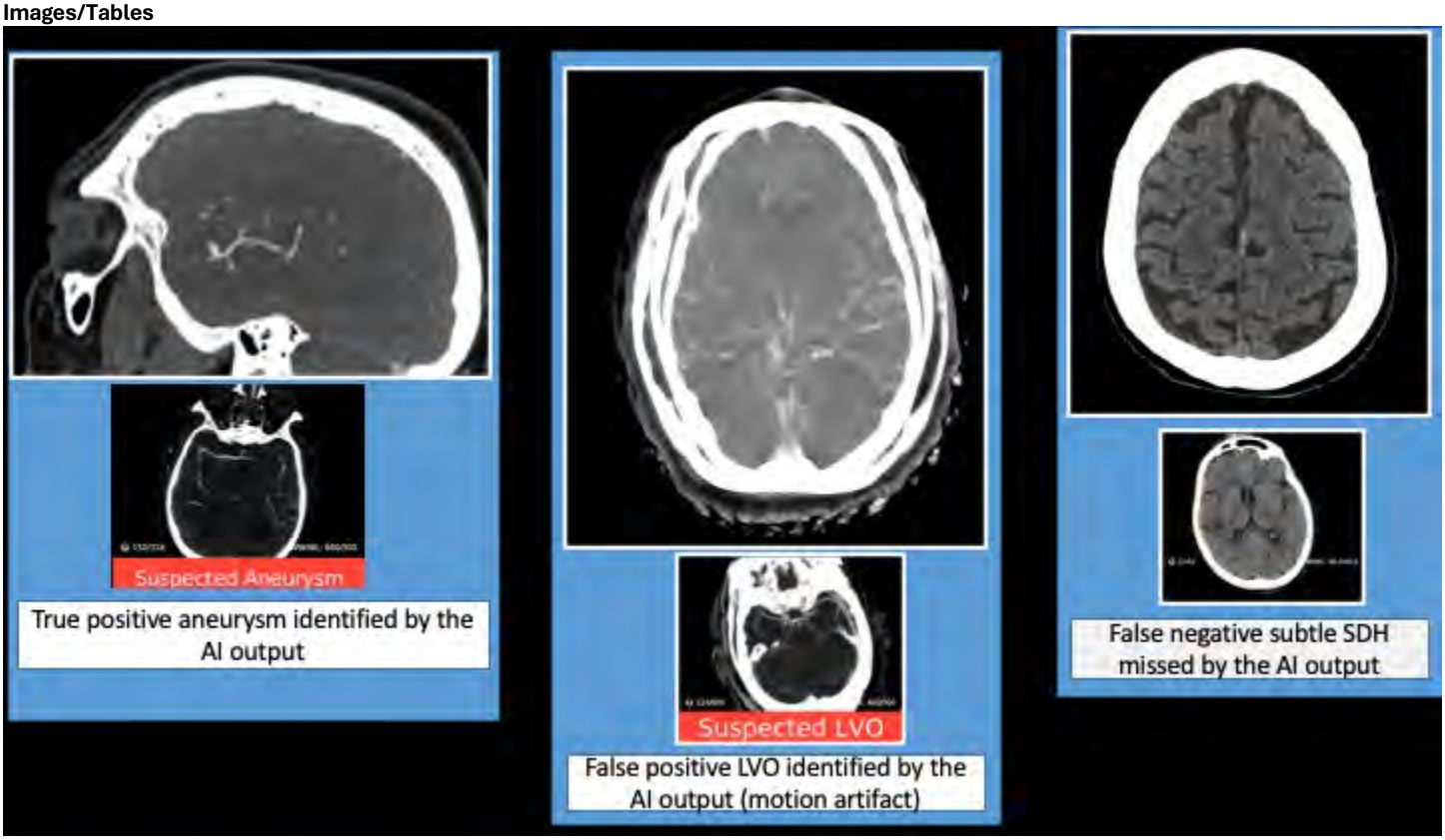

1150 SliceDx: An AI-Powered Web-Based Diagnostic Platform for Neuroradiology with Structured Imaging Characterization and Case Collaboration Capabilities

Joshua D Brown MD, PhD
Emory University, Atlanta, GA, USA

Purpose

Accurate diagnosis in neuroradiology requires synthesizing complex imaging characteristics across brain, spine, and head and neck regions. Traditional educational resources rarely allow users to systematically narrow differentials based on specific imaging and clinical features, making it difficult for trainees and even experienced radiologists to efficiently reason through rare or complex cases. **SliceDx** is a web-based platform designed to enhance diagnostic accuracy and learning by enabling users to filter neuroradiology diagnoses using structured imaging features and clinical classifications. The platform also supports case sharing and collaborative discussion, allowing users to leverage collective expertise without geographical or institutional limitations.

Materials & Methods

SliceDx was developed using the Next.js framework and TypeScript, with a PostgreSQL database supporting structured diagnostic data and role-based authentication. Diagnoses are organized across neuroanatomical systems and regions, each linked to definable imaging features (e.g., signal characteristics, enhancement patterns, morphology) and clinical descriptors (e.g., demographic associations, clinical course). AI-assisted tools support characteristic tagging, case indexing, and guided differential narrowing. A collaboration module allows users to upload de-identified cases and optionally request discussion or input from peers.

Results

SliceDx currently includes a foundational neuroradiology diagnostic database with structured imaging features and clinical associations. Users can refine differential diagnoses by interactively selecting imaging characteristics and anatomical context, allowing systematic narrowing based on reasoning patterns similar to expert diagnostic logic. The collaboration feature enables users to contribute cases that can be searched, filtered, and compared using the same structured imaging descriptors, supporting both education and shared diagnostic problem-solving. This feature facilitates clinical collaboration and enables users to seek guidance from experts across different institutions, breaking down geographical and organizational barriers. AI tools streamline case tagging and improve consistency in feature labeling across users.

Conclusion

SliceDx provides a unified neuroradiology diagnostic platform centered on structured feature-based differential refinement. The system enhances diagnostic reasoning for both trainees and practicing radiologists and establishes a framework for scalable growth through user contributions. The ability to share and discuss cases extends the educational and clinical value of the platform while preserving the core emphasis on systematic imaging-based diagnosis.

Images/Tables

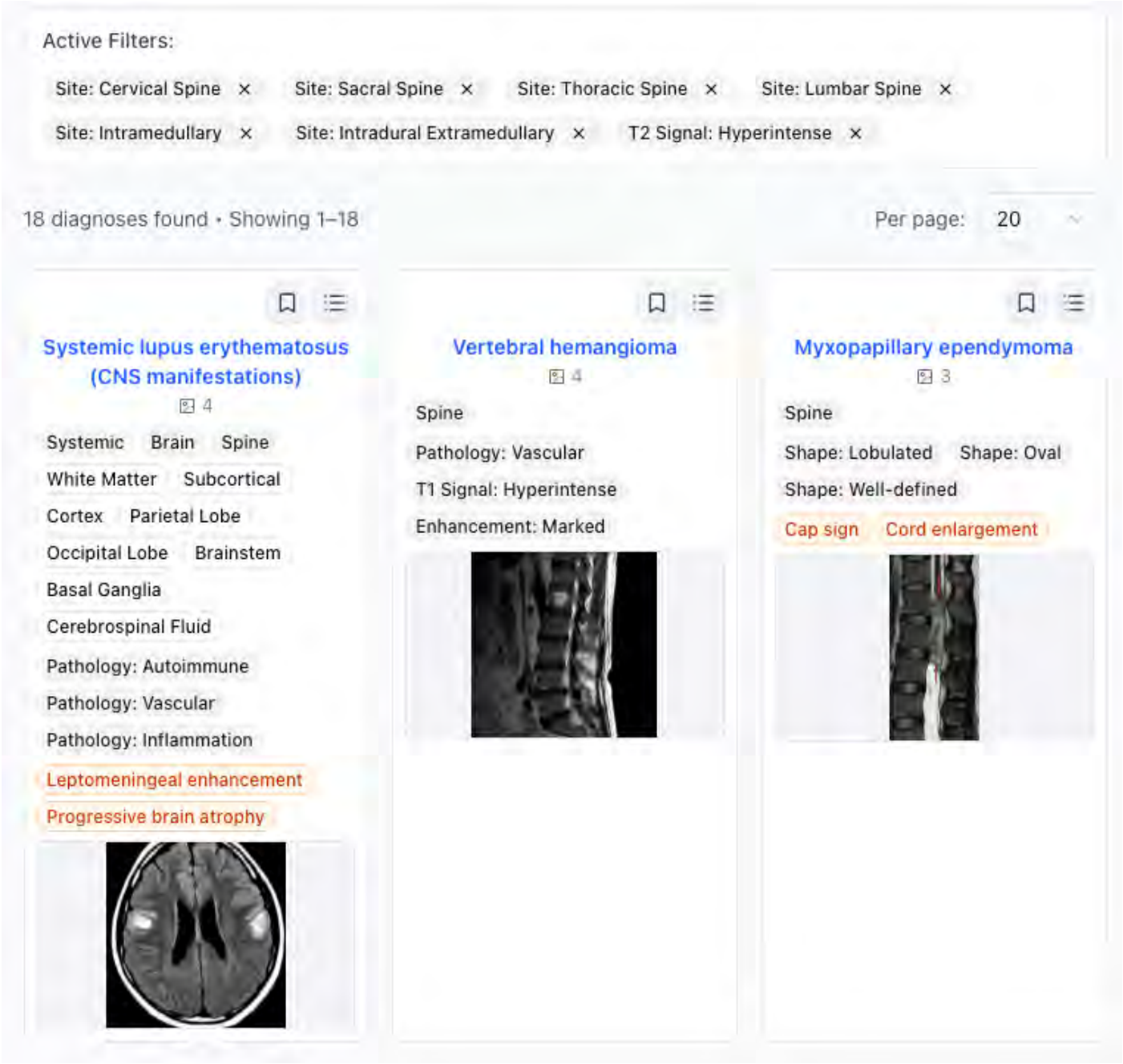

1172 **Assessment of Ascending Pharyngeal Artery Enlargement on Post-Contrast MRI as a Marker of Sigmoid-Jugular Dural AVFs: Implications for Evaluating Incidental ASL Hyperintensity at the Left Skull Base**

Wilson Chavez, Yusef Qazi, Christopher J Shin, Nicholas A Telischak, Lotfi Hacein-Bey, Tarik F Massoud
Stanford University School of Medicine, Satnford, CA, USA

Purpose

Incidental arterial spin-labeling hyperintensity (ASL+) at the left jugular bulb (JB) and sigmoid sinus (SS) is uncommon but can create diagnostic uncertainty. Although often attributed to benign jugular venous reflux, it may also mimic a skull base dural arteriovenous fistula (dAVF), which warrants further evaluation. To avoid performing angiographic studies on all ASL+ patients, we assess whether post-contrast MRI features can help identify dAVFs in the lateral venous sinus outflow tract. Enlargement of the ascending pharyngeal artery (APhA) has been previously suggested as a helpful indicator because it frequently supplies posterior skull base dAVFs. Here, we test the hypothesis that enlargement of APhA alone may not reliably predict dAVF presence, given evidence that multiple external carotid artery (ECA) branches may supply dAVFs shunting into the SS and JB.

Materials & Methods

We retrospectively analyzed brain and skull base MRIs for 30 adults with lateral venous sinus outflow tract dAVFs and 30 healthy controls (HCs). We reviewed fat-suppressed, post-contrast SPGR sequences (0.9-mm isotropic) and then digitally measured the maximum axial diameter for bilateral APhAs at the mid-C2 level. We divided dAVF types into three groups based on shunted pouch angioarchitecture (Kiyosue) and distance from the JB: Groups 1 (transverse sinus), Group 2 (transvers-sigmoid sinus), and Group 3 (sigmoid/JB/condylar veins). We computed descriptive statistics for patient demographics, all morphometrics, and dAVF groups. We compared APhA sizes and sidedness within and between HCs and dAVF patients using t-tests, and performed multiple statistical association and conditional correlation tests (Pearson, Spearman rank, point-biserial,

ANOVA, Kruskal-Wallis H, and chi-squared) in dAVF patients to assess relationships between binary/categorical/continuous parameters of APhA width, side, age, sex, and dAVF group. Statistical significance was set at P<0.05.

Results

HCs were F:M=15:15 aged 63±2.8 years; and dAVF patients were F:M=11:19 aged 60.8±2.8 years. In dAVF patients there were 15 right and 15 left fistulas; and 8, 11, and 11 patients in fistula-type Groups 1-3, respectively. Mean width of APhAs was 1.4±0.2mm in HCs; and 1.3±0.3mm and 1.2±0.3mm in dAVF patients, contralateral and ipsilateral to the fistula, respectively. There were no statistical differences (P>0.05) in APhA calibers between these cohorts, nor between right and left APhAs segregated by dAVF sides. In dAVF patients, there was a statistically significant positive correlation between right and left APhA widths (r=0.632, P=0.0002); and in Group 3, there was a statistically significant association between sex and right APhA width (r=–0.706, P=0.015), with females having larger arteries.

Conclusion

APhA caliber on post-contrast SPGR-MRI is similar in HCs and patients with lateral sinus outflow dAVFs. In the absence of adjunctive CTA/MRA/DSA, scrutiny of the APhA in isolation on non-angiographic MRI may be useful in some patients with distal sigmoid/JB/condylar dAVFs, but more generally we find that it is unlikely to be helpful in distinguishing the presence/absence of a dAVF. In upcoming studies, we aim to extend these initial results to studying morphometrics for multiple ECA branches, multimodality angiographic correlations, and secondary subset analysis of ASL+ versus dAVF patients.

1176 Designing Effective Neuroradiology Educational Videos: Lessons from Six Years of YouTube Data

Laura N Okechukwu BS ` [1], Miguel L Devonish MD, MBA[2], Jacqueline C Junn MD[2], Gennaro D'Anna MD[3], Brent D Weinberg MD[2]

[1]Temple University, Philadelphia, PA, USA. [2]Emory University School of Medicine, Atlanta, GA, USA. [3]CDI Centro Diagnostico Italiano, Milano, Lombardia, Italy

Purpose

YouTube has emerged as a validated medical-education platform, with systematic review data demonstrating measurable benefits in learner engagement, content accessibility, and knowledge retention in radiology[1]. Online platforms such as YouTube are increasingly leveraged for medical education, but optimal strategies for content design remain under-explored in subspecialty fields like neuroradiology. The purpose of our study was to to analyze six years of engagement data from a dedicated neuroradiology education channel and identify video characteristics that optimize reach, retention, and global learner engagement.

Materials & Methods

Video-level YouTube analytics (January 2018-December 2024) were extracted for all LearnNeuroradiology uploads. Variables included duration, views, watch time, average view duration, average percentage viewed, and interaction metrics (likes, shares, subscribers). Videos were categorized (brain, spine, head & neck, Board Review, Case Review, Basic Neuroradiology, Other). Descriptive statistics, category-level comparisons, and correlation analyses were performed.

Results

Among 334 videos, median duration was 5.3 min (IQR 182-640). Median average view duration was 2.5 min, with median completion 46.3%. Short Board Review videos achieved the highest retention (mean 60%). Brain and Head & Neck videos attracted the greatest views (10K-15K mean) but with lower completion (33-40%). Spine and Basic Neuroradiology achieved balanced reach and retention. Case Reviews, although longest (median 11.7 min), sustained high watch hours per video. Correlation analysis showed video duration strongly predicted absolute viewing time (r=0.86 with avg. view duration) but inversely correlated with completion (r= -0.77).

Conclusion

Neuroradiology video engagement is optimized when content-tailored strategies are used: concise formats for Board Review, segmentation for Brain/Head & Neck, and narrative depth for Case Reviews. A one-size-fits-all approach to video length is insufficient; instead, content categories should guide design of digital educational materials.

Images/Tables

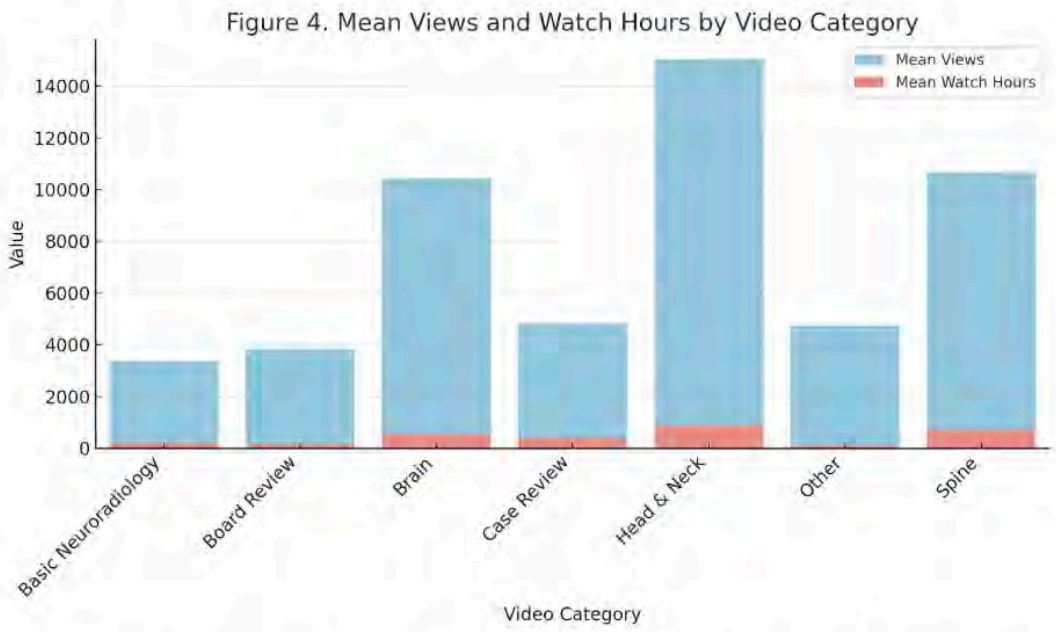

Figure 4. Mean Views and Watch Hours by Video Category. Brain and Head & Neck videos generated the highest mean views, while Case Reviews and Spine content produced disproportionately high watch hours, reflecting deep engagement by smaller audiences.

1178 Translational Relevance of Calvarial Diploic Venous Lakes: A CT-MRI Study of Their Spatial Morphometrics and Feasibility Demonstration of a New Digital Subtraction Diploic Venography (DSDV) Technique

Christopher J Shin, Nicholas S Bates, Johannes H Decker, Tarik F Massoud
Stanford University School of Medicine, Stanford, CA, USA

Purpose

Prior experimental and computational studies have established diploic veins (DV) as potential physiological receptacles and conduits for surgical drainage of cerebrospinal fluid (CSF). Clinical translation has been limited in part by the absence of morphometric data to guide safe and effective catheter targeting of the larger diploic lakes (DLs). In this study we generate normative MRI data for DV/DL spatial morphometrics, quantifying their size, distribution, and proximity to calvarial surgical landmarks. We also test a new CT digital subtraction technique (DSDV) to demonstrate the DV/DLs as standalone structures. This analysis will help identify and visualize potential surgically-accessible and hydraulically-viable sites for future intraosseous CSF diversion systems.

Materials & Methods

We retrospectively analyzed 40 normal adult brain MRIs. We reviewed fat-suppressed, post-contrast volumetric SPGR sequences (0.9-mm isotropic) in orthogonal planes to identify and measure diploic venous structures. DLs were defined as venous channels >3mm in width. We recorded age, sex, DV or DL types, orthogonal and maximal vessel diameters, cross-sectional DL areas, nearest external landmark (pterion, asterion, lambda, or other sutural point), and Euclidean distances from those landmarks. We computed descriptive statistics for all morphometrics, Pearson's correlation coefficients for linear relationships between age and size, and Welch's t-tests to compare male and female morphometrics. We also calculated the probability of encountering a DV/DL within ≤10, ≤20, and ≤30mm of a surgical landmark. We tested initial feasibility of DSDV by using sets of contrast-enhanced head CTs along with same patient CT angiogram images and subsequent MPR reformatting of DV/DLs in 3D space.

Results

For the 26 females and 14 males, we measured 18 (45%) DLs and 22 (55%) DVs. The mean widest vessel diameter was 5.6±9.4mm, and the mean cross-sectional area was 13.5±31.3mm^2. Spatially, most DV/DLs were located near recognizable calvarial landmarks: 33.3% within 10mm, 82.1% within 20mm, and 84.6% within 30mm of the nearest landmark. Pterion was the most common site for nearby DL/DVs (n=26, mean 10.9±6.8mm; all within 20mm). There were no significant demographic trends. For females vs. males, respectively: (1) The mean widest diameter for all diploic channels was 5.3mm vs. 3.7mm (p=0.44), and mean cross-sectional area 14.4mm^2 vs. 8.9mm^2 (p=0.46). (2) For DLs, the mean diameter was 10.5mm vs. 5.2mm (p=0.27), and mean area 49.5mm^2 vs. 17.1mm^2 (p=0.26). (3) For DVs, the mean diameter was 2.2mm vs. 2.1mm (p=0.66) and mean area was 3.6mm^2 vs. 3.2mm^2 (p=0.71). Age-related effects were negligible (widest diameter r=0.12, p=0.44; cross-sectional area r=0.15, p=0.36). We will demonstrate examples of DSDV images in this presentation.

Conclusion

DV/DLs demonstrate morphological variability but consistent proximity to key surface landmarks, particularly pterion and asterion. Such consistency provides a foundation for identifying locations that balance surgical accessibility with reliable DV/DL communication. By quantifying dimensions and landmark-based encounter probabilities of DV/DLs, we address an important translational barrier to intraosseous CSF diversion—defining reproducible, hydraulically viable calvarial targets. Integration of these spatial morphometrics and our new DSDV imaging technique with additional permeability/flow modeling may guide optimal site selection and future device design.

1180 Spatial distribution of perivascular spaces as a marker of disease severity in idiopathic intracranial hypertension

Rafael Buongermini[1], Jim Xie[2], Marko Tien[2], Emma Blanchette[2], Benjamin Morgan[1], Yash Patel[2], Edward Margolin[3], Shivaprakash Hiremath[1], Alexandre Boutet[1]

[1]Toronto Western Hospital–University Health Network, Toronto, Ontario, Canada. [2]Temerty Faculty of Medicine, University of Toronto, Toronto, Ontario, Canada. [3]University Health Network, Toronto, Ontario, Canada

Purpose

Idiopathic intracranial hypertension (IIH) causes raised intracranial pressure without identifiable cause and can lead to permanent visual loss if untreated. Growing evidence suggests that glymphatic dysfunction, affecting cerebrospinal fluid transport and clearance, contributes to IIH pathophysiology. Because perivascular spaces (PVS) reflect glymphatic activity, we investigated their relationship with IIH severity and their potential value as imaging markers of advanced disease.

Materials & Methods

Forty-seven patients with clinically diagnosed IIH (mean age = 32.6 ± 10.2 years; 44 women) and 47 age- and sex-matched controls were prospectively included. All subjects underwent MRI which included 3D T1-weighted and FLAIR sequences. PVS were manually segmented and normalized to MNI152 space to generate individual binary masks. Group-level analyses produced cumulative frequency, outcome-weighted, and odds ratio maps to explore associations between PVS distribution, optic disc edema, quantitative visual parameters (visual field mean deviation, peripapillary retinal nerve fiber layer thickness), and presence of visual loss. Normalized PVS volumes were compared between groups, and multivariable linear regression was used to assess associations with clinical measures.

Results

Mean PVS volume was higher in patients with IIH compared with controls (164.7 ± 104.5 mL vs 121.4 ± 83.6 mL; p = 0.015). Patients with more severe optic disc edema or visual loss showed a wider distribution of PVS, extending beyond the areas usually seen in milder cases, particularly within the amygdala, posterior internal capsules, and superior basal ganglia. These regions overlapped with those more frequently affected in IIH on OR maps. Within the IIH group, there were no significant associations between PVS volume and pRNFL, VFMD, or visual loss.

Conclusion

Patients with idiopathic intracranial hypertension show both an overall increase in perivascular space volume and, more notably, a distinct spatial pattern that likely reflects underlying glymphatic congestion. While total PVS volume alone does not appear to correlate strongly with disease severity, the presence of PVS in certain brain regions was more frequent among patients with significant visual impairment. These findings suggest that the distribution of PVS could serve as an additional imaging marker of more severe forms of IIH and may help identify patients who are more likely to benefit from treatment.

1181 Mapping MBA Training in Neuroradiology Shows a Bidirectional Leadership Pipeline Effect Amid Nationwide Underrepresentation: A Cross-Sectional Study

Christopher J Shin, Tarik F Massoud

Stanford University School of Medicine, Stanford, CA, USA

Purpose

To quantify the prevalence, timing, and distribution of MBA degrees among academic neuroradiologists in the US and to evaluate whether business training follows a leadership pipeline effect—accumulating at higher academic ranks rather than being acquired early in career trajectories. We also investigate sex, institutional, and regional disparities to contextualize these findings within the rapid national expansion of MD/MBA dual-degree programs.

Materials & Methods

We reviewed faculty rosters from the top 50 US medical schools to identify all neuroradiology faculty (n=795). For each individual, we recorded academic rank, sex, institutional type (public vs. private), region, and academic degrees. For a subset of MBA-trained neuroradiologists (n=16) we further analyzed degree timing including year of MD, MBA, and promotion to professor rank, to estimate the typical interval between clinical and business training. We used descriptive statistics to summarize overall prevalence, and chi-squared and Fisher's exact tests (significance <0.05) to assess associations between MBA status and rank, sex, institution type, and region.

Results

Sixteen of 795 neuroradiologists (2.0%) held an MBA. MBA prevalence increased stepwise with seniority, with 0.6% among assistant professors, 1.8% among associate professors, and 4.4% among full professors (p=0.006). Among all MBA-trained neuroradiologists, 62.5% were full professors, 25% were associate professors, and 12.5% were assistant professors. For 16 neuroradiologists with available year data, the mean interval between MD and MBA was 14.7 years, showing that business training is typically pursued mid-career. Qualitative review showed that MBAs were typically pursued either to enable promotion into leadership roles or to formalize management skills after promotion. This bidirectional pattern suggests obtaining an MBA supports leadership development mainly in response to, or in anticipation of, administrative duties, rather than as proactive early-career preparation. There was a nonsignificant higher MBA representation among men (2.4%) than women (0.9%) (p=0.26). MBA prevalence was comparable between private (1.8%) and public (2.2%) institutions (p=0.92), reflecting a field-wide underrepresentation rather than institutional disparity. There was no significance in regional representation (p=0.57), indicating that MBA underrepresentation spans across all geographic regions.

Conclusion

Despite the nationwide expansion of MD/MBA dual-degree programs—from 33 in 2002 to 92 in 2022—formal business degree training remains rare in academic neuroradiology. The significant association between MBA status and higher academic rank supports a bidirectional leadership pipeline effect, wherein business education both facilitates and follows advancement into administrative roles. The long lag between MD and MBA completion suggests that such training is most often obtained mid-career, perhaps reflecting a reactive model of leadership preparation that emerges only after neuroradiologists assume managerial duties. Sex and institutional/regional analyses collectively demonstrate that MBA underrepresentation is system-wide rather than localized, reflecting a broader cultural separation between business fluency and neuroimaging practice. As radiology departments confront increasing operational and strategic complexity, these findings underscore an urgent opportunity to integrate leadership and management curricula earlier to align radiology/neuroradiology training with the evolving demands of academic medicine. Doing so would better equip neuroradiologists not only to participate in clinical care but to shape the organizations and policies that define modern medical practice.

1190 Partially Ossified Sacral Posterior Arch Defects as Natural Low-Resistance Pathways for Percutaneous Transosseous Thecal Sac Access: A CT Morphometric Study and Concept Proposal

Siddhant S Dhawan, Christopher J Shin, Tarik F Massoud
Stanford University School of Medicine, Stanford, CA, USA

Purpose

Alternative image-guided percutaneous access to the dural sac is sometimes needed when standard lumbar puncture (LP) is difficult or not feasible. Reported transosseous approaches include CT-guided spinal needle access achieved by drilling through intact lumbar laminae, and fluoroscopy-guided placement of a 17G needle through bone overlying the sacral canal. Notably, however, posterior vertebral arch fusion defects in the upper sacrum are common (≈40%), often presenting as partial defects in the laminae. These shallow, incompletely ossified channels retain thin bony bridging near the spinal canal and may provide more accessible pathways for drill-free, transosseous passage of coaxial low/large-gauge spinal needle combinations with minimal bone traversal. We therefore characterize lumbosacral partial laminar defects to assess their potential as natural entry routes for future image-guided dural sac puncture procedures.

Materials & Methods

We retrospectively analyzed lumbosacral spine axial CT scans for 57 healthy adults and identified 18 laminae containing measurable partial laminar defects ("fenestrations" and "clefts", >3mm and <3mm wide, respectively). For each, we recorded vertebral level, defect width, laminar width, and residual bone thickness at defect base. We then derived a barrier ratio (base thickness divided by full laminar width) and categorized defects by thickness-based feasibility tiers: ultra-thin (≤1.0mm), thin (1.01–2.0mm), moderate (2.01–3.0mm), and thick (>3.0mm). We computed descriptive statistics for demographics and morphometrics by spinal level, and Pearson correlation coefficients (significance, $P<0.05$) for the relationship between defect width and base thickness.

Results

There were 15 subjects (F:M=10:5; aged 43.7±13.9 years) whose thecal sac terminations were from upper S1 to low S2. Average laminar thickness gradually increased down lumbar levels, measuring 6.6±1.6 mm (L3), 7.0±1.4mm (L4), and 7.5±1.5mm (L5), before decreasing through the sacrum to 5.8±0.9mm (S1) and 4.4±1.0mm (S2). We found 18 partial defects (2 fenestrations and 16 clefts): 1 at L5, 12 at S1, and 5 at S2. Mean width for partial fenestrations and clefts was 5.1±0.9mm and 1.6±0.7mm, respectively. Defect base bone thickness was moderate, a mean 3.0±1.2mm. Cumulative distribution analysis showed that no defects had a base thickness ≤1.0mm, while 22.2% measured ≤2.0mm and 66.7% measured ≤3.0mm. Corresponding mean barrier ratios were 0.5±0.2 at S1, 0.77 at S2, and 0.7±0.2 at L5, indicating that S1 partial defects had the thinnest laminar osseous barriers, whereas L5 and S2 partial defects preserved thicker bone at defect bases. No significant correlation was found between defect width and base thickness ($P=0.58$), indicating that defect width does not reliably predict bone thickness separating it from the thecal sac.

Conclusion

Partial posterior arch fusion defects are much more common at S1 than in the lumbar spine, and all are wider than the outer diameter of standard spinal needles. These consistent, predictable, natural, and morphologically favorable bone windows offer anatomically thin osseous barriers as feasible routes for percutaneous transosseous thecal sac access without requiring full-thickness laminar drilling. Our morphometric data lay the groundwork for future potential image-guided transosseous sacral puncture techniques as alternatives to LP, leveraging pre-existing anatomical features that can be incorporated into procedural planning.

1195 Conditional Hybrid GAN with CNN-Vision Transformer Discriminator for Class-Specific 2D Brain MRI Synthesis

Taofeeq Oluwatosin Togunwa MD, Ivo Dinov PhD
University of Michigan Medical School, Ann Arbor, Michigan, USA

Purpose

High-quality synthetic MRI can mitigate data scarcity, class imbalance, and privacy constraints that limit robust Artificial Intelligence (AI) development in neuroimaging. Convolutional Conditional GANs (cGANs) capture local texture but struggle with long-range anatomical dependencies; while pure transformer models are data-hungry and unstable on small medical sets. We propose a conditional Hybrid-cGAN that fuses convolutional and transformer features in the discriminator to improve anatomical fidelity, stability, and class control for brain MRI generation. The objective was to test whether local-global feature fusion and an adaptive transformer fine-tuning schedule yield realistic, diverse, and class-faithful synthetic images.

Materials & Methods

Data was obtained from Msoud et al. (2021) 2D brain MRI collection, constrained to axial slices from four classes: glioma, meningioma, pituitary, and no-tumor. We used 2,492 training, 534 validation, and 535 test images. The generator followed a class-conditional design. The discriminator combined (1) a CNN backbone for localized spatial features and (2) a pretrained ViT-Base/16 branch to model non-local context. Features were fused before the adversarial head. We employed a progressive unfreezing policy where the ViT branch was kept frozen initially, and partially, then fully unfrozen, only after loss plateaus, enabling the CNN to anchor early training while gradually introducing global attention. Performance was tracked with Fréchet Inception Distance (FID), Kernel Inception Distance (KID), and Multi-Scale SSIM (MS-SSIM). We also monitored class-conditional MS-SSIM to assess within-class diversity control. Model selection used the best validation FID.

Results

The Hybrid-cGAN achieved its best model at epoch 150 by FID. On the validation set, metrics were FID (152.77), KID (0.0914), and mean class-conditional MS-SSIM (0.8942). On the independent test set, performance remained consistent with FID (149.81), KID (0.0861), and mean class-conditional MS-SSIM (0.9063), indicating realistic appearance with preserved diversity rather than mode collapse. Qualitatively, generated samples displayed reasonably coherent global head morphology and conceivable tumor-parenchyma relationships across all four classes, with crisp boundaries and reduced background artifacts compared with early-epoch models. FID and KID declined as MS-SSIM rose following the two unfreezing milestones, supporting the value of the progressive transformer schedule for adversarial stability.

Conclusion

A conditional hybrid discriminator that integrates CNN locality with ViT global context, coupled with staged transformer unfreezing, produces anatomically coherent and class-controllable synthetic brain MRIs on a modest-sized dataset. The approach maintained generalization from validation to test and improved realism while preserving diversity, addressing common limitations of purely convolutional GANs on medical images. While the images are not completely indistinguishable from real scans, the strength of this work lies in its methodical innovation using a principled

training schedule and architecture, to address common pitfalls of purely convolutional or transformer GANs. We anticipate stronger performance from future work scaling the approach through multi-sequence inputs and 3D volumes. This framework could potentially support privacy-preserving dataset augmentation and expansion and simulation of under-represented tumor phenotypes in neuroradiology workflows.

Images/Tables

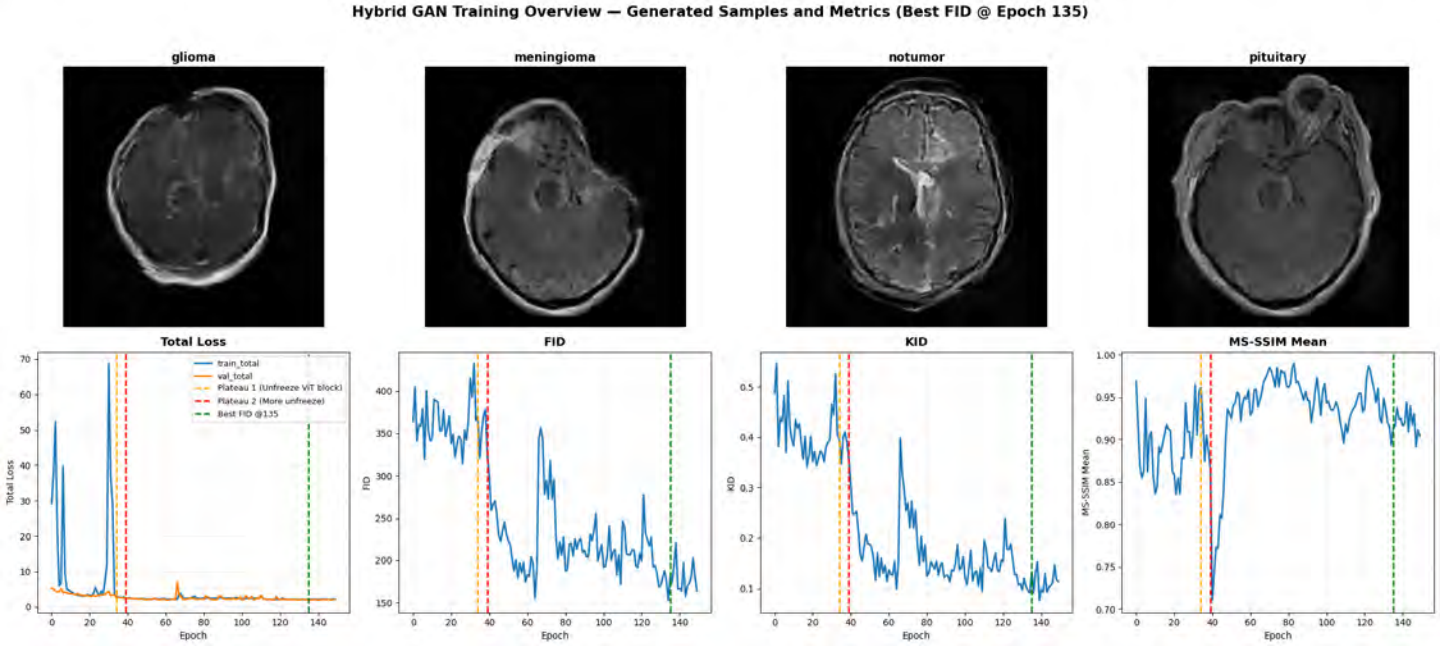

1198 Late Window Malignant Core Infarct Volume Underestimated by CTP Compared to Color-Coded CTA Collateral Assessment

Rehab Khalid MBBS[1], Joel Samuel Gnanam MD[1], Ok Kyu Song MD[1], Alessia Guarnera MD[2], Rajiv Gupta MD, PhD[1], Michael Lev MD[1], David Vu MD[3], Utarat Kaewumporn MD[4]

[1]Massachusetts General Hospital, Boston, MA, USA. [2]Sant'Andrea Hospital, Sapienza University of Rome, Rome, Rome, Italy. [3]Scripps, La Jolla, California, USA. [4]Bangkok Hospital, Bangkok, Bangkok, Thailand

Purpose

Patients with very large ischemic cores (>100 mL) presenting in late (>12 hour) time windows are unlikely to have good outcomes from endovascular thrombectomy, whereas those with smaller cores (<50 mL), are far more likely to experience favorable outcomes. Rapid assessment of infarct core severity is therefore critical for triage in acute large-vessel-occlusion (LVO) stroke. We hypothesized that the collateral pattern on CTA, categorized as malignant versus non-malignant can serve as a surrogate for infarct core size, that collateral-based assessment better reflects true infarct extent than CTP-derived estimates, and that color-coded collateral maps may enhance workflow and reader confidence.

Materials & Methods

In this pilot study, twenty presumed wake-up LVO stroke cases (estimated ≥10–12 hours since last known well) with both CTA source imaging and color-coded collateral maps were reviewed by four blinded readers: one non-radiologist, one clinical neuroradiology fellow, and two attending neuroradiologists.

Each reader completed two sessions separated by a 24-hour washout period. In the first session, readers alternated between CTA-source imaging and color-coded-CTA in sets of ten cases to balance order effects. In the second session, the same sets were presented in the opposite modality order, with randomized case order within each set.

For each case, collaterals were classified as malignant (>100 ml) or symmetric (<50ml), and reader confidence (1–5) and interpretation time (seconds) were recorded. Ground truth was established by a neuroradiologist with three decades of experience using concurrent CTA collateral, CTA parenchymal, CTP and most importantly unenhanced head CT review. CTP maps were generated using a validated perfusion package (core = CBF<30%, penumbra = Tmax >6 s).

Results

Collateral grading on CTA source imaging closely reflected infarct severity, demonstrating 96.9% sensitivity, 53.9% specificity, and 62.5% accuracy for identifying malignant cores, while color-coded CTA achieved 90.6%, 64.8%, and 70.0%, respectively. Both modalities were highly sensitive for malignant cores, with color improving specificity and overall accuracy.

Collateral assessment also more accurately represented true infarct extent than perfusion-based estimates. Among the four malignant cases, both CTA source imaging and color-coded CTA correctly identified all (100% sensitivity), whereas CTP correctly identified only one (126 mL) and underestimated the remaining three (35, 75, and 98 mL). Across all 20 cases, collateral grading showed higher agreement with expert-determined ground truth than CTP. Among 16 cases with core volumes <50 mL, all were correctly classified on both gray-scale and colorized CTA, while CTP misclassified one (60 mL). Color-coded CTA yielded comparable reader confidence (4.27 vs 4.31) and similar interpretation times (12.3 vs 12.1 s) relative to standard CTA.

Conclusion

Collateral pattern on CTA source and color-coded imaging mirrored infarct core severity and outperformed CTP-derived estimates in identifying malignant cores. Color-coded maps provided comparable confidence and efficiency without compromising diagnostic accuracy. This pilot study

establishes a foundation for shifting from perfusion-based to collateral-based approaches in estimating infarct core, underscoring the need for larger, multicenter studies to validate these findings and refine imaging triage in acute stroke care.

Images/Tables

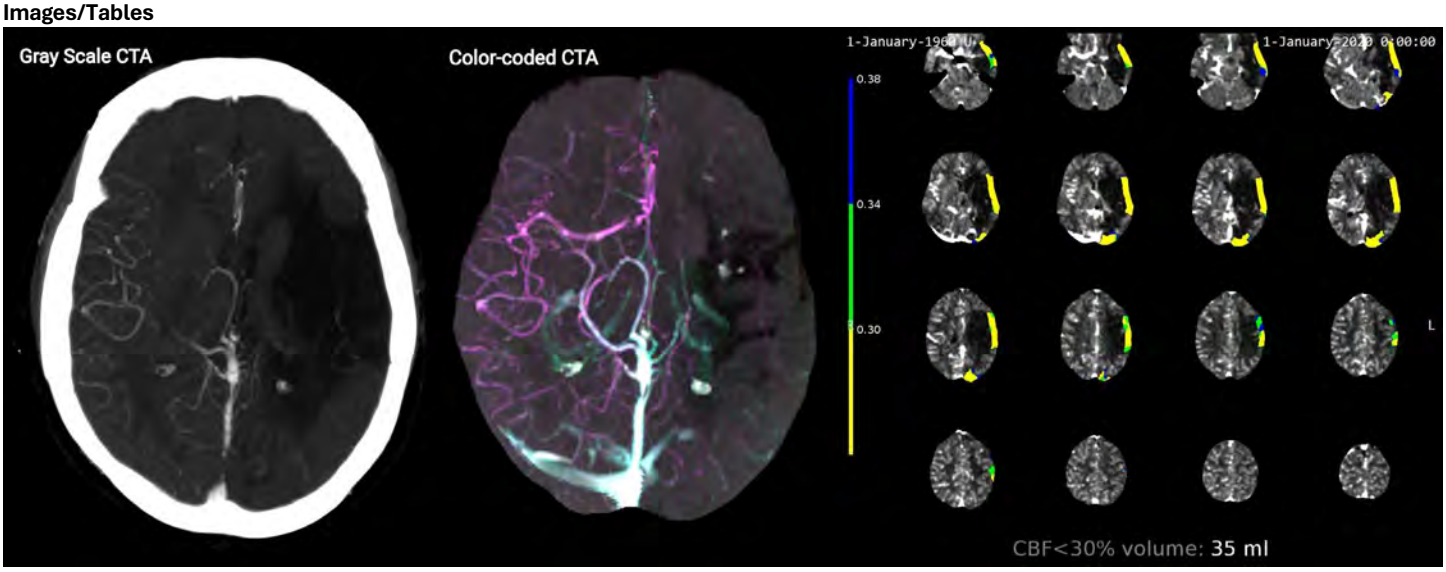

1214 Integrating Interactive Scrollable Cases at a National Radiology Conference is Possible and Desirable by Attendees

Tabassum Kennedy
Madison, WI, USA

Purpose

While there has been emphasis and progress made towards integrating interactive case-based learning in radiology training programs, there has been a lag to adoption at the national level in radiology society conferences. Radiology conferences remain based primarily on power point presentations with finely curated image selection with an emphasis on conveying presenter mastery. The current generation of learners seek alternative methods of instruction with opportunities for active engagement in the learning process. The purpose of this study was to assess the feasibility of implementing a case-based model of instruction utilizing scrollable cases in a workshop format at a national radiology conference.

Materials & Methods

Two workshops were organized at the American Society of Head and Neck Radiology conference utilizing the platform Collective Minds. Each workshop was facilitated by experts to guide learners through scrollable cases within the platform that also integrated live polling. A pre and post workshop survey was deployed to gauge attendee engagement. The pre survey consisted of 4 questions and the post survey consisted of 8 questions.

Results

There were 68 responses for the pre survey and 72 responses for the post workshop survey. Of the 72 responses from the post survey, 99% of respondents felt “more engaged in the learning process” when compared to traditional lecture-based formats and 99% of respondents “would like to see more interactive case-based sessions at future conferences”. Some suggestions for improvement included loading fewer images to facilitate the scrolling process as well as improving the wifi bandwidth to facilitate faster downloading of cases.

Conclusion

Incorporating sessions with scrollable cases that facilitate the learning process is possible at a national Radiology conference. Learners felt more engaged in the workshops when compared to traditional lecture-based formats. Instructors should consider curating the series when facilitating a session with scrollable images. Conference organizers should consider wifi accessibility when organizing workshops in order to provide an optimal experience for attendees.

Images/Tables

894 Distinct Molecular and Survival Manifestations in IDH-wildtype Glioblastomas without Contrast Enhancement: Interrelationship with Molecular Glioblastomas

Yae Won Park, Pae Sun Suh, Sung Soo Ahn, Seung-Koo Lee
Yonsei University College of Medicine, Seoul, Seoul, Korea, Republic of

Purpose

To compare the clinical, pathological, and surgical characteristics, as well as prognosis, between IDH-wildtype glioblastomas without and with contrast enhancement (CE), with a specific focus on the interrelationship between CE and molecular glioblastomas.

Materials & Methods

Retrospective review was performed in 983 IDH-wildtype glioblastoma patients (70 without CE, 913 with CE from volumetric measurement) from a single institution between 2005–2023. Patient characteristics and overall survival (OS) were compared. Survival analysis was performed within patients without CE. The interaction between CE and molecular glioblastoma was assessed.

Results

Patients without CE were younger with higher KPS and more often classified as molecular glioblastoma (50.0% vs. 1.1%, $P < 0.001$), showing less frequent p53 expression (6.6% vs. 21.7%, $P = 0.005$), lower Ki-67 index (5% vs. 20%, $P < 0.001$), more frequent gliomatosis cerebri (18.6% vs. 9.3%, $P = 0.013$), less leptomeningeal metastases (1.4% vs. 11.4%, $P = 0.009$), and smaller non-enhancing tumor volumes (37.2 vs. 82.9cm^3, $P < 0.001$). Their median OS was longer than in patients with CE (26.8 vs. 19.5 months; $P = 0.013$). Among patients without CE, *MGMT* promoter unmethylation (HR = 1.80, $P = 0.012$) and molecular glioblastoma (HR = 0.30, $P = 0.002$) were independent prognostic factors. Interaction analysis also showed that molecular glioblastoma had a lower risk compared with histological glioblastoma (HR = 0.49, P for interaction = 0.039) within patients without CE.

Conclusion

IDH-wildtype glioblastoma patients without CE represent a distinct subgroup with more favorable prognosis. Recognition of *MGMT* status and molecular glioblastoma is essential for risk stratification in these patients.

References

Vollmuth P, Karschnia P, Sahm F, Park YW, Ahn SS, Jain R. A Radiologist's Guide to IDH-Wildtype Glioblastoma for Efficient Communication With Clinicians: Part I-Essential Information on Preoperative and Immediate Postoperative Imaging. *Korean J Radiol.* 2025; 26(3):246-268.
Tesileanu CMS, Dirven L, Wijnenga MMJ, et al. Survival of diffuse astrocytic glioma, IDH1/2 wildtype, with molecular features of glioblastoma, WHO grade IV: a confirmation of the cIMPACT-NOW criteria. *Neuro Oncol.* 2020; 22(4):515-523.

786 Interobserver Variability and Comparison of SWI with T2* in the Diagnosis of Cerebral Amyloid Angiopathy and ARIA Scoring at 7T MRI.

Can Ozutemiz MD, Rojin Ahmadi MD, Mark Folkertsma MD, Scott Lunos MS, Dongming Cai MD, Phd, Christopher D Streib MD
University of Minnesota, Minneapolis, MN, USA

Purpose

To compare SWI and T2* sequences obtained at 7T MRI regarding their ability to identify hemorrhagic elements in the diagnosis of cerebral amyloid angiopathy (CAA) with integration of ARIA scoring and to assess interobserver variability.

Materials & Methods

Between August 2022 and March 2025, 153 7T MRI exams were obtained in 118 patients due to transient focal neurologic deficits, dementia, or ARIA scoring, to rule out microbleeds and CAA. These are retrospectively reviewed, and 17 were excluded (Patient was younger than 50, lack of SWI/T2* or proven stroke). 136 exams included for analysis. All exams obtained before the pTx upgrade with the Siemens 7T Terra machine. Two board-certified neuroradiologists independently assessed both SWI (Voxel size: 0.2x0.2x1.4mm, Time: 6:28, TR/TE: 22/15ms, GRAPPA:3), T2* (Voxel size: 0.2x0.2x1.5mm, Time: 9:35, TR/TE: 1080/20ms, GRAPPA: 3) and FLAIR sequences and scored the following; Gross intracranial parenchymal hemorrhage (ICH) (Present or no), cortical/subcortical microbleeds and deep microbleeds using ARIA scoring (0=none,1-4=mild, 5-9= moderate, >9= severe), cortical superficial siderosis (CSS) and convexity subarachnoid hemorrhage (0=none, 1=1 focal area, 2=2 focal area, 3=3 or more focal area), and new imaging biomarkers including intragyral hemorrhage sign (IGH) and striated cortex sign (SCS). White-matter-hyperintensities (WMH), distribution, ARIA-E scoring, and presence of atrophy were assessed. If a discrepancy arose between observers, a consensus decision was reached two months after the initial blind assessment. Descriptive and weighted kappa analyses were performed to compare T2* with SWI and between two separate observers.

Results

Agreement between the raters and agreement between the T2* and SWI sequences are provided in Tables 1 and 2, respectively. In 118 cases, T2* was available, and almost perfect agreement was observed. In 134 cases, SWI was available, and substantial agreement was observed regarding IGH and SCS; otherwise, almost perfect agreement was present between the raters in the remaining parameters. In 136 cases with FLAIR, interobserver agreement was almost perfect. In 115 exams where both SWI and T2* were available, there was almost perfect agreement among hemorrhagic parameters, except for the IGH sign (k = 0.62), indicating substantial agreement. SCS could not be assessed due to its low frequency (was positive only in a single case at SWI and not observed in T2*). Descriptive findings based on the consensus agreement is as follows; ICH-SWI: 10.4%, ICH-T2*:11%. Cortical/Subcortical microbleeds-SWI: None=45.5%, mild=22.3%, moderate=12.7%, severe= 19.4%, Cortical/Subcortical microbleeds-T2*: None=62.6%, mild=26.8%, moderate=6.7%, severe=3.7%. Deep microbleeds-SWI: None=45.5%, mild=22.3%, moderate=12.7%, severe= 19.4%, Deep microbleeds-T2*: None=66.1%, mild=25.4%, moderate=5.9%, severe=2.5%. CSS-SWI: None=75.3%, 1=3%, moderate=2.2%, severe= 19.4%, CSS-T2*: None=74.5%, mild=4.2%, moderate=1.7%, severe=19.5%. IGH-SWI: None=75.5%, 1=5.9%, moderate=5.9%, severe= 12.7%, IGH-T2*: None=84.7%, mild=5.9%, moderate=2.5%, severe=6.7%

Conclusion

Interobserver variability is almost perfect at 7T MRI using ARIA hemorrhage parameters in patients with suspected CAA or dementia. Regarding SWI and T2*, there is almost a perfect correlation in the diagnosis of parenchymal hemorrhages, cortical/subcortical microbleeds, deep microbleeds, and CSS.

References
1. Koemans EA, Voigt S, Rasing I, et al. Striped occipital cortex and intragyral hemorrhage: Novel magnetic resonance imaging markers for cerebral amyloid angiopathy. *Int J Stroke* 2021;16:1031-1038
2. Cogswell PM, Andrews TJ, Barakos JA, et al. ASNR Alzheimer, ARIA, and Dementia Study Group. Alzheimer Disease Anti-Amyloid Immunotherapies: Imaging Recommendations and Practice Considerations for Monitoring of Amyloid-Related Imaging Abnormalities. *AJNR Am J Neuroradiol*. 2025;46(1):24-32
3. Özütemiz C, Hussein HM, Ikramuddin S, et al. Occult Amyloid-β-Related Angiitis: Neuroimaging Findings at 1.5T, 3T, and 7T MRI. *AJNR Am J Neuroradiol*. 2024; 45(8):1013-1018

Images/Tables

mean (SD) age = 73.0 (12.2) range=30-95.7

female n (%) = 67 (57%), male n (%) = 51 (43%)

Table 1. 7T MRI: Agreement between Raters

Type	Measure	N images	Kappa (95% CI)
T2*	Gross ICH	118	1.00 (1.00-1.00)
	Cortical/subcortical MB	118	0.91 (0.86-0.96) [w]
	Deep MB	117	0.85 (0.76-0.95) [w]
	cSS	118	0.96 (0.92-0.99) [w]
	cSAH	118	0.92 (0.80-1.00) [w]
	IGH Sign	118	0.86 (0.74-0.99) [w]
	SCS	118	nc
SWI	Gross ICH	134	0.96 (0.89-1.00)
	Cortical/subcortical MB	134	0.96 (0.93-0.99) [w]
	Deep MB	134	0.86 (0.77-0.95) [w]
	cSS	134	0.95 (0.90-1.00) [w]
	cSAH	134	0.93 (0.84-1.00) [w]
	IGH Sign	134	0.74 (0.63-0.84)
	SCS	134	0.66 (0.04-1.00)
FLAIR	WMHs	136	0.96 (0.92-1.00)
	WMH Distribution	96	0.81 (0.70-0.91)
	PVS	136	0.97 (0.93-1.00) [w]
	ARIA-E	136	1.00 (1.00-1.00)
	Atrophy	136	0.85 (0.78-0.92) [w]

[w] Weighted Kappa. nc = Not calculable, all 0

Table 2. 7T MRI: Agreement between T2 and SWI (Consensus ratings)

Measure	N images	Kappa (95% CI)
Gross ICH	115	1.00 (1.00-1.00)
Cortical/subcortical MB	115	0.90 (0.85-0.95) [w]
Deep MB	115	0.90 (0.83-0.97) [w]
cSS	115	0.97 (0.94-1.00) [w]
cSAH	115	1.00 (1.00-1.00)
IGH Sign	115	0.62 (0.46-0.78)
SCS	115	nc

[w] Weighted Kappa. nc = Not calculable, all 0

MB: microbleeds, ICH: intracerebral hemorrhage, cSS: cortical superficial siderosis, cSAH: convexity subarachnoid hemorrhage, IGH : Intragyral Hemorrhage sign, SCS: Striated cortex sign, WMH: white matter hyperintensity, PVS: perivascular spaces

795 Dynamic Functional Connectivity with Hemispheric reorganization in Left Frontal and Temporal Lobe Tumors

Dr. Samra Iftikhar MBBS, FCPS Diagnostic Radiology[1], Dr. Saeed Rahmani MD, HMBA[2], Antonio Napolitano PhD[3], Amirali Aali MD[1], Jennifer Moliterno MD[4], Todd Constable PhD[5], Dr. Luca Pasquini MD,PhD[1]

[1]Clinical Neuroplasticity Laboratory, Yale University School of Medicine, New Haven, Connecticut, USA. [2]Clinical Neuroplasticity Laboratory, Yale University School of Medicine,Department of Radiology and Biomedical Imaging,Yale University, New Haven, Connecticut, USA. [3]Medical Physics Department, Bambino Gesu Children's Hospital,, Rome, Lazio, Italy. [4]Department of Neurosurgery, yale University School of Medicine, New Haven, Connecticut, USA. [5]Department of Neurosurgery, Yale University School of Medicine, New Haven, Connecticut, USA

Purpose

Brain tumors disrupt neural networks, triggering adaptive reorganization through functional plasticity. While resting state(rs) functional connectivity (FC) reveals synchronized activity between brain regions under normal and pathological conditions, dynamic FC(dFC) captures temporal fluctuations in network topology that may reflect ongoing compensatory mechanisms in tumor patients (1,2). Few studies have investigated dFC in brain tumors, despite evidence that inter network connectivity changes may indicate subject level plasticity (2).We characterized temporal dynamics of graph theoretic network properties and hemispheric lateralization in patients with left frontal (LFLT) and temporal lobe (LTLT) tumors compared to healthy controls.

Materials & Methods

We analyzed preoperative rs-fMRI from 71 patients (41 left frontal,30 left temporal tumors) and 53 age/sex/matched healthy controls. Using an 80s sliding window approach advanced every 40 seconds, we computed graph theory metrics across eight consecutive time windows(T1-T8).FC was assessed among 132 atlas defined regions of interest,with graphs constructed at 20% density threshold.We applied ComBat harmonization to control for multi-site acquisition effects and used linear mixed-effects models with AR(1) covariance to test group differences while controlling for repetition time (TR) and age.A dynamic connectivity laterality index quantified hemispheric reorganization over time.

Results

Compared to healthy controls, both tumor groups demonstrated mostly disrupted network topology across most windows, lower global efficiency (HC>LFLT Δ=0.036, p=.001; HC>LTLT Δ=0.033, p=.002), lower local efficiency (HC>LFLT Δ=0.036, p=.002, HC>LTLT Δ=0.033, p=.004), longer characteristic path length (HC<LFLT Δ=-3.871, p=.006; HC<LTLT Δ=-3.296, p=.020), higher betweenness centrality (HC<LFLT Δ=-41.27, p<.001; HC<LTLT Δ=-38.55, p<.001), higher eccentricity (HC<LFLT Δ=-11.64, p<.001,HC<LTLT Δ=-10.06, p<.001), and lower closeness centrality (HC>LFLT Δ=0.034, p<.001,HC>LTLT Δ=0.032, p=.002). Modularity showed window specific effects, with patients displaying higher segregation than controls only at the final window (T8), HC < LFLT Δ = −0.043, p=.028 & LTLT > LFLT Δ=0.024, p=.006. The connectivity laterality index revealed stable rightward reorganization, HC maintained balanced lateralization (mean=0.482), while both patient groups showed persistent leftward to rightward shifts (LFLT mean=0.462, p<.001, LTLT mean=0.451, p<.001), with temporal tumors demonstrating the greatest rightward compensation.

Conclusion

Dynamic resting-state analysis showed that left-hemispheric tumors cause a sustained disturbance of brain network organization that evolves during the scan. Compared with healthy controls, patients shifted from a more integrated to a more modular, segregated architecture, especially in the later time windows, suggesting that tumor affected networks tend to settle into less efficient states, something a single static connectivity map would miss. Tumor location influenced this pattern as patients with LFLT had smaller changes and some late improvement in efficiency, consistent with partial adaptive capacity, while patients with LTLT showed a steadier drift toward higher modularity and assortativity, indicating more persistent disruption of language dominant networks. Connectivity laterality index also followed a consistent order (controls >LFLT>LTLT) across all windows, supporting stable rightward/bilateral reorganization rather than brief, flexible shifts. Overall, these findings show that dynamic connectivity metrics reveal clinically relevant, location specific limits in functional plasticity and could help guide preoperative planning or rehabilitation strategies aimed at preserving network integration.

References

(1) Preti MG, Bolton TA, Van De Ville D. The dynamic functional connectome: state-of-the-art and perspectives. Neuroimage. 2017;160:41–54. doi:10.1016/j.neuroimage.2016.12.061.

(2) Cai S, Liang Y, Wang Y, et al. Shared and malignancy-specific functional plasticity of dynamic brain properties for patients with left frontal glioma. *Cereb Cortex*. 2024;34(1):bhad445. doi:10.1093/cercor/bhad445

Images/Tables

Metric	HC vs LFLT	HC vs LTLT	Window pattern (dynamic rs-fMRI)	Interpretation
Global efficiency	HC>LFLT Δ=0.036, p=.001	HC>LTLT Δ=0.033, p=.002	Diagnosis x Window; late small deviations (T7–T8)	Tumor networks less integrated, changes over scan
Local efficiency	HC>LFLT Δ=0.036, p=.002	HC>LTLT Δ=0.033, p=.004	Diagnosis× Window, T7 HC≯LFLT, T8 HC≯LTLT	Location-specific/partial adaptation
Char. path length	HC<LFLT Δ=−3.871, p=.006	HC<LTLT Δ=−3.296, p=.020	Stable across windows	Less efficient information transfer
Betweenness	HC<LFLT Δ=−41.27, p<.001	HC<LTLT Δ=−38.55, p<.001	Higher across windows	Greater hub load / rerouting
Eccentricity	HC<LFLT Δ=−11.64, p<.001	HC<LTLT Δ=−10.06, p<.001	Higher across windows	Less compact networks
Closeness	HC>LFLT Δ=0.034, p<.001	HC>LTLT Δ=0.032, p=.002	Mostly stable; minor late changes	Reduced accessibility of nodes
Modularity (T8)	HC<LFLT Δ=−0.043, p=.028	LTLT>LFLT Δ=0.024, p=.006	T8 only	Late drift to segregation, strongest temporal
Laterality index	HC 0.482 vs LFLT 0.462, p<.001	HC 0.482 vs LTLT 0.451, p<.001	HC > LFLT > LTLT **all windows**	Stable rightward/bilateral reorganization

---

445 **Optimizing Intrinsic Parallel Diffusivity in NODDI Enhances White-Matter Disease Stratification in Alzheimer's Disease**

Saeed Rahmani MD, MPH, MHPE, HMBA[1], Antonio Napolitano Ph.D[2], Tommaso Scacco Ph.D[2], Luca Pasquini MD, Ph.D[1]

[1]Department of Radiology and Biomedical Imaging, Yale University School of Medicine, New Haven, Connecticut, USA. [2]Medical Physics Department, Bambino Gesù Children's Hospital, Rome, Lazio, Italy

Purpose

To test whether optimizing the intrinsic parallel diffusivity (d‖) in the NODDI model (1) improves sensitivity to white-matter degeneration in Alzheimer's disease (AD), enabling discrimination among AD, mild cognitive impairment (MCI), and cognitively normal (CN) groups, and to explore associations with α-synuclein seed amplification assay (SAA) (2).

Materials & Methods

Multi-shell diffusion MRI from ADNI3/4 was analyzed (b=0/500/1000/2000 s/mm^2; 127 directions; 2-mm isotropic; n=143: AD=26, MCI=59, CN=58). Preprocessing included denoising, Gibbs-ringing removal, bias-field correction, Synb0-DisCo-assisted susceptibility distortion correction (topup) (3), motion/eddy correction, brain masking, and tensor fitting to derive FA. NODDI fitting (MDT) was repeated across 26 d‖ values (0.5–3.0 μm^2/ms) to generate voxelwise log-likelihood maps, from which "best-d‖", optimized NDI (oNDI), and optimized ODI (oODI) were derived (1); SMT was used for cross-model validation (intrinsic diffusivity and intra-neurite volume fraction) (4). Tract-Based Spatial Statistics (TBSS) with permutation testing (TFCE, p<0.05, corrected) compared CN vs MCI, CN vs AD, and MCI vs AD on FA, oNDI, traditional NDI (fixed d‖=1.7 μm^2/ms), and SMT metrics. In the SAA subset (n=79), groups were ASYN1 (detected) vs ASYN0 (not detected) evaluated in all subjects, and stratified by CN and "patients" (AD+MCI).

Results

Compared with FA and traditional NDI, oNDI demonstrated broader and more robust WM skeleton differences **(Figure 1)**:

- CN>MCI and CN>AD: widespread reductions in oNDI and traditional NDI relative to CN, with oNDI showing greater sensitivity than FA (TFCE-corrected p<0.05).
- MCI>AD: oNDI, but not FA or traditional NDI, revealed significant WM tract reductions in AD compared with MCI, indicating improved stage discrimination.
- Best-d‖ maps showed regions with AD<CN (contrary to the initial hypothesis of higher d‖ in AD); these trends were not confirmed by SMT intrinsic diffusivity.

In SAA analyses, ASYN1 showed regional WM reductions versus ASYN0 on FA and oNDI (all-subjects analysis), with patterns persisting, though more focally, within CN and within patients (AD+MCI); intrinsic diffusivity maps showed no group differences.

Conclusion

Voxelwise optimization of d‖ in NODDI yields an oNDI metric that improves detection of AD-related WM degeneration and distinguishes AD from MCI where FA and traditional NDI do not. Associations between oNDI and α-synuclein positivity further support oNDI as a biologically relevant microstructural biomarker. These findings motivate incorporating d‖ optimization into clinical-research pipelines for neurodegeneration staging and trial enrichment.

References

1. Zhang H, Schneider T, Wheeler-Kingshott CA, Alexander DC. NODDI: practical in vivo neurite orientation dispersion and density imaging of the human brain. Neuroimage. 2012 Jul 16;61(4):1000-16.
2. Tosun D, Hausle Z, Iwaki H, Thropp P, Lamoureux J, Lee EB, MacLeod K, McEvoy S, Nalls M, Perrin RJ, Saykin AJ. A cross-sectional study of α-synuclein seed amplification assay in Alzheimer's disease neuroimaging initiative: prevalence and associations with Alzheimer's disease biomarkers and cognitive function. Alzheimer's & Dementia. 2024 Aug;20(8):5114-31.
3. Schilling KG, Blaber J, Huo Y, Newton A, Hansen C, Nath V, Shafer AT, Williams O, Resnick SM, Rogers B, Anderson AW. Synthesized b0 for diffusion distortion correction (Synb0-DisCo). Magnetic resonance imaging. 2019 Dec 1;64:62-70.
4. Kaden E, Kelm ND, Carson RP, Does MD, Alexander DC. Multi-compartment microscopic diffusion imaging. NeuroImage. 2016 Jun 6;139:346.

Images/Tables

Figure 1. TBSS results of randomise contrasts